

ADVANCED FUNCTIONAL POLYPEPTIDES
FOR BIOLOGICAL, ENERGY AND ELECTRONIC APPLICATIONS

A Dissertation

by

TAN PHAM-DUY NGUYEN

Submitted to the Office of Graduate and Professional Studies of
Texas A&M University
in partial fulfillment of the requirements for the degree of

DOCTOR OF PHILOSOPHY

Chair of Committee,	Karen L. Wooley
Committee Members,	Daniel L. Alge
	David E. Bergbreiter
	Marcetta Y. Darensbourg
Head of Department,	Simon W. North

December 2020

Major Subject: Chemistry

Copyright 2020 Tan Pham-Duy Nguyen

ABSTRACT

Synthetic polypeptides constitute a class of polyamides that may impart the biocompatibility, (bio)degradability and conformational properties of proteins, while also allowing for expanded composition and structure to tune structure-property-performance parameters. This dissertation is focused on the development of peptide-based materials for biological, energy and electronic applications, exploiting their inherent degradability and conformations to direct the properties of the polymer networks. For the biological application, PEGylated β -sheet-forming polypeptides were synthesized for use as extracellular matrices in three-dimensional cell cultures. For the energy and electronic applications, simple natural amino acid synthons were transformed into functional polypeptides for use as active materials in secondary and redox flow batteries. These projects aim to expand scientific perceptions of peptide-based materials beyond the scope of traditional biological applications and to raise public awareness of mindful development of future energy storage systems to incorporate sustainability features in material designs.

DEDICATION

To my parents, brother and partner

ACKNOWLEDGEMENTS

Five years in graduate school are a long journey with many ups and downs. But every relationship established, every challenge encountered and every lesson learned were invaluable opportunities that helped me grow, both personally and scientifically.

I would first like to thank my Ph.D. advisor, Professor Karen L. Wooley, for her continued support throughout my graduate study at Texas A&M University. She welcomed me into her group, provided me with the freedom to develop my own proposals, supported my diversity and inclusion initiatives, guided me through research obstacles, challenged me with scientific quests and assisted me through the hardship of the pandemic. This dissertation would never come to a fruitful completion without her trust in me and in the ideas I proposed. I will always keep in my heart the three words she told me during the darkest moments of my Ph.D. journey—"Hang in there!"

I would like to thank my undergraduate advisor, Professor Marilyn R. Mackiewicz, for her mentorship and friendship throughout my Ph.D. journey, for inspiring me to pursue a career in academia and for teaching me that mentorship lasts a lifetime.

I would like to thank my committee members, Professor Marcetta Y. Darensbourg, Professor David E. Bergbreiter and Professor Daniel Alge for their time and support throughout the course of my Ph.D. research.

The majority of this dissertation was conducted in collaboration with wonderful scientists at TAMU and outside institutes. Therefore, I would like to thank all my collaborators and contributors, especially Dr. Soon-Mi Lim, Ms. Alexandra Easley and

Professor Jodie L. Lutkenhaus, and Dr. Zhiming Liang and Dr. Harsha Attanayake from the research group of Professor Susan A. Odom.

Within the Wooley group, I would like to recognize Dr. Jingwei Fan, Dr. Xun He, Dr. Rachel A. Letteri and Dr. Ashlee A. Jahnke for their mentorship, friendship, advice and guidance. I have learned many useful research skills and techniques from these talented scientists. I would also like to thank all past and present members of the Wooley group for being such great peers and making the lab environment so enjoyable to be in, especially Ms. Mariela Vazquez, Dr. Nari Kang and Mr. David K. Tran for being my best buddies of graduate school.

Lastly, I would like to thank my father, mother and brother for their continued support for my graduate research. Especially, I would like thank my partner for his understanding, support, patience, trust and love through this incredible journey.

CONTRIBUTORS AND FUNDING SOURCES

Contributors

The work done in this dissertation was supervised by a committee consisting of Professor Karen L. Wooley (Departments of Chemistry, Chemical Engineering, and Materials Science and Engineering, TAMU), Professor Marcetta Y. Darensbourg (Department of Chemistry, TAMU), Professor David E. Bergbreiter (Department of Chemistry, TAMU) and Professor Daniel Alge (Department of Biomedical Engineering, TAMU).

In **Chapter II**, the cell study was performed by Dr. Soon-Mi Lim of the Department of Chemistry. The thermal characterization was done by Mr. David K. Tran (Department of Chemistry, TAMU). The Soft Matter Facility at Texas A&M University is also gratefully acknowledged.

In **Chapter III**, the electrochemical measurements were conducted by Ms. Alexandra Easley (Department of Materials Science & Engineering, TAMU) under the supervision of Professor Jodie L. Lutkenhaus (Departments of Chemical Engineering and Materials Science & Engineering, TAMU). The x-ray photoelectron spectroscopy and scanning electron microscopy were measured by Dr. Nari Kang (Department of Materials Science & Engineering, TAMU). The cell viability study was done by Ms. Sarosh Khan and Dr. Soon-Mi Lim (Department of Chemistry, TAMU). The electron paramagnetic resonance spectroscopy was obtained by Ms. Shaoyang Wang (Department of Chemical Engineering, TAMU). The thermogravimetric analysis was performed by Mr. David K.

Tran. The modulated differential scanning calorimetry was collected by Ms. Alexandra Easley. The high-resolution mass spectrometry and liquid chromatography were performed by Dr. Yohannes Rezenom (Department of Chemistry, TAMU). The Mass Spectrometry Center and Materials Characterization Facility at Texas A&M University are also gratefully acknowledged.

In **Chapter IV**, the redox flow batteries were constructed by Dr. Zhiming Liang and Dr. Harsha Attanayake from the research group of Professor Susan A. Odom of the Department of Chemistry at the University of Kentucky.

All other work conducted for this dissertation was completed by the student independently.

Funding Sources

The work done in **Chapter II** was made possible *via* the support of the National Science Foundation (DMR-1507429 and DMR-1905818) and the Welch Foundation through the W. T. Doherty-Welch Chair in Chemistry (A-0001).

The work done in **Chapter III** was financially supported by the National Science Foundation (DMR-1507429, DMR-1905818 and DMREF-1629094), the Welch Foundation through the W. T. Doherty-Welch Chair in Chemistry (A-0001), the U.S. Department of Energy Office of Science (DE-SC0014006) and the National Science Foundation Graduate Research Fellowship.

The work done in **Chapter IV** was supported by the National Science Foundation (DMR-1507429, DMR-1905818, DMREF-1629094 and ENG-3200001992) and the Welch Foundation through the W. T. Doherty-Welch Chair in Chemistry (A-0001).

NOMENCLATURE

6HHC	6-Chlorohexyl hydrocinnamate
ATR-FTIR	Attenuated total reflectance-Fourier transform infrared spectroscopy
CB	Super P [®] Carbon Black
CD	Circular dichroism
CDCl ₃	Deuterated chloroform
CD ₃ OD	Deuterated methanol
CHLG	γ -(6-Chlorohexyl)-L-glutamate
CV	Cyclic voltammetry/cyclic voltammogram
DCM	Dichloromethane
CD ₂ Cl ₂	Deuterated dichloromethane
DLAG	DL-Allylglycine
DMEM	Dulbecco's modified eagle medium
DMF	<i>N,N'</i> -Dimethylformamide
DMSO	Dimethyl sulfoxide
DMSO- <i>d</i> ₆	Deuterated dimethyl sulfoxide
D ₂ O	Deuterium oxide
DP	Degree of polymerization
DPBS	Dulbecco's phosphate buffered saline
DSC	Differential scanning calorimetry

DTT	1,4-Dithiothreitol
\mathcal{D}	Dispersity
ECM	Extracellular matrix
ESI	Electrospray ionization
$\hat{\gamma}$	Shear strain
G'	Storage modulus
G''	Loss modulus
HC- <i>bis</i> (MTEMPO)	Hydrocinnamate- <i>bis</i> (MTEMPO)
HC- <i>bis</i> (PA)	Hydrocinnamate- <i>bis</i> (propionic acid)
HRMS	High-resolution mass spectrometry
IHHC	6-Iodoethyl hydrocinnamate
ITO	Indium tin oxide
LC	Liquid chromatography
LSCM	Laser scanning confocal microscopy
M_n	Number-average molar mass
M_w	Weight-average molar mass
MDSC	Modulated differential scanning calorimetry
MTEMPOL	1-Methoxy-2,2,6,6-tetramethylpiperidin-4-ol
MW	Molecular weight
MWCO	Molecular weight cut-off
NAM	Normal amine mechanism
NCA	<i>N</i> -Carboxyanhydride

NMP	<i>N</i> -Methyl-2-pyrrolidone
NMR	Nuclear magnetic resonance
ω	Angular frequency
PBPI	1-(6-((3-Phenylpropanoyl)oxy)hexyl)-[4,4'-bipyridin]-1-ium iodide
PC	Propylene carbonate
PEG	Poly(ethylene glycol)
PHC	Propargyl hydrocinnamate
PLG	γ -Propargyl-L-glutamate
PVDF	Polyvinylidene difluoride
SEC	Size exclusion chromatography
SEM	Scanning electron microscopy
SPPS	Solid-phase peptide synthesis
TFA- <i>d</i>	Deuterated trifluoroacetic acid
T_g	Glass transition temperature
TGA	Thermogravimetric analysis
THF	Tetrahydrofuran
UV-vis	Ultraviolet-visible
VGCF	Vapor-grown carbon fiber
XPS	X-ray photoelectron spectroscopy

TABLE OF CONTENTS

	Page
ABSTRACT	ii
DEDICATION	iii
ACKNOWLEDGEMENTS	iv
CONTRIBUTORS AND FUNDING SOURCES.....	vi
NOMENCLATURE.....	ix
TABLE OF CONTENTS	xii
LIST OF FIGURES.....	xv
LIST OF TABLES	xxv
CHAPTER I INTRODUCTION	1
Polypeptides: Synthesis and Characterization.....	2
Polypeptides from N-Carboxyanhydride (NCA) polymerizations.....	2
Peptide Secondary Structures	5
Peptide-based Hydrogels.....	8
Polymer-based Batteries.....	11
History of Batteries	11
Organic Radical Batteries.....	12
Redox Flow Batteries	15
Characteristics of Batteries.....	17
Scope of the Dissertation.....	18
CHAPTER II POLYPEPTIDE HYDROGEL SCAFFOLDS FOR CELL THERAPEUTICS	21
Introduction	21
Experimental Section	22
Materials	22
Synthesis of PEGylated Alkenyl-functionalized Polypeptides	23
Chemical Characterization	24
Cell Cultures.....	25

Hydrogel Preparation	25
Rheological Measurements	26
Thermal Analysis	27
Hydrogel 3D Cell Culture	28
Cell Viability Determination	28
Results and Discussion.....	30
Synthesis of PEGylated Alkenyl-functionalized Polypeptides	30
Rheological Measurements	31
3D Cell Cultures	35
Conclusion.....	39
CHAPTER III POLYPEPTIDE ORGANIC RADICAL BATTERIES.....	41
Introduction	41
Experimental Section	43
Materials	43
Synthesis of Viologen Polypeptides.....	44
Synthesis of BiTEMPO Polypeptide.....	49
Synthesis of Viologen Analog.....	55
Synthesis of BiTEMPO Analog	58
Chemical Characterization	61
Thermal Analysis	62
Electrochemical Characterization.....	62
Degradation Study	66
Cell Viability Study.....	67
Results and Discussion.....	69
Syntheses of Redox-active Polypeptides.....	69
Electrochemical Characterization.....	73
Degradation of Viologen and BiTEMPO Polypeptides	76
Cell Viability Study.....	79
Conclusion.....	81
CHAPTER IV POLYPEPTIDE REDOX FLOW BATTERIES	83
Introduction	83
Experimental Section	84
Materials.....	84
Syntheses of Redox-active Polypeptides and their Small-molecule Analog.....	87
Chemical Characterization	88
Electrochemical Characterization.....	88
Results and Discussion.....	90
Syntheses of Redox-active Polypeptides and their Small-molecule Analog.....	90

Crossover Tests	92
Flow Cell Cycling	93
Conclusion.....	96
CHAPTER V CONCLUSIONS	98
REFERENCES	101
APPENDIX A SUPPLEMENTARY DATA FOR CHAPTER II	123
Attenuated Total Reflectance-Fourier Transform Infrared	123
Nuclear Magnetic Resonance Spectroscopy	124
Rheology	126
Fluorescence Confocal Microscopy	130
APPENDIX B SUPPLEMENTARY DATA FOR CHAPTER III	136
Syntheses of Small-molecule Analogs	136
Size Exclusion Chromatography	137
Circular Dichroism	137
Ultraviolet-visible Spectroscopy	138
Electron Paramagnetic Resonance Spectroscopy	138
Attenuated Total Reflection-Fourier Transform Infrared Spectroscopy	139
X-ray Photoelectron Spectroscopy	145
Nuclear Magnetic Resonance Spectroscopy	149
Electrochemical Characterization	171
Degradation Study	179
Cell Viability Study	189
APPENDIX C SUPPLEMENTARY DATA FOR CHAPTER IV	193

LIST OF FIGURES

	Page
Figure 1. Properties and applications of peptide-based materials.....	1
Figure 2. Different methods of peptide synthesis: (A) Solid phase peptide synthesis and (B) ring-opening polymerization of <i>N</i> -carboxyanhydrides.....	3
Figure 3. Pathways for ring-opening polymerization of NCAs: (A) Normal amine mechanism (NAM), (B) activated monomer mechanism (AMM), (C) normal amine mechanism with added N ₂ flow.....	4
Figure 4. (A) Secondary structures of peptides and their characteristic (B) circular dichroism ellipticity and (C) infrared spectroscopy wavelengths. *(+) indicates positive ellipticity and (-) indicates negative ellipticity at designated wavelengths.	7
Figure 5. Schematic illustrations of peptide amphiphile gelation <i>via</i> (A) micellar percolation of PEG- <i>block</i> - α -helical polypeptides and (B) fibrillar entanglement of PEG- <i>block</i> - β -sheet-forming polypeptides.....	10
Figure 6. Illustrative designs of a (A) secondary battery and (B) flow battery.	13
Figure 7. Commonly used (A) backbones for polymers with (B) common redox-active pendant groups.....	14
Figure 8. Summary of Ph.D. dissertation.	19
Figure 9. (A) Synthesis of PEGylated polypeptides. (B) Illustration of β -sheet formation of PEG ₄₅ - <i>b</i> -PDLA _n	22
Figure 10. (A) Strain sweep ($T = 37\text{ }^{\circ}\text{C}$, $\omega = 10\text{ rad}\cdot\text{s}^{-1}$) and (B) frequency sweep tests ($T = 37\text{ }^{\circ}\text{C}$, $\hat{\gamma} = 0.2\%$) of P-30-4% hydrogels.....	32
Figure 11. Mechanical strengths of P-20 and P-30 hydrogels studied.....	33
Figure 12. (A) Time sweep ($T = 37\text{ }^{\circ}\text{C}$, $\hat{\gamma} = 0.2\%$, $\omega = 10\text{ rad}\cdot\text{s}^{-1}$), (B) shear-thinning and (C) self-healing ($T = 37\text{ }^{\circ}\text{C}$, $\hat{\gamma} = 0.2\%$, $\omega = 10\text{ rad}\cdot\text{s}^{-1}$) measurements P-30-4% hydrogels.	34

Figure 13. Preparation of hydrogel 3D cell cultures.	36
Figure 14. Fluorescence images (10×) of (A) the P-20-4% hydrogel after 7 d, and (B) the P-30-4% hydrogel after 1 d, 5 d and 7 d (Scale bars = 1 mm). (C) Fluorescence images (10×) of marked locations on i. P-20-4% and ii. P-30-4% hydrogels (Scale bars = 100 μm).	38
Figure 15. Schematic design of polypeptide-based organic radical battery during charging (<i>left</i>) and discharging (<i>right</i>) processes.	43
Figure 16. Synthesis strategy for redox-active polypeptides	70
Figure 17. Detailed synthetic schemes for redox-active polypeptides.	71
Figure 18. Molecular structures of viologen and polypeptide analogs.	73
Figure 19. Cyclic voltammograms of (A) the viologen polypeptide and (B) the biTEMPO polypeptide thin films on ITO-coated glass in a three-electrode beaker cell configuration. The supporting electrolyte was 0.5 M LiCF ₃ SO ₃ in propylene carbonate. Lithium metal was used as counter and reference electrodes.	73
Figure 20. Electrochemical characterization of (A) viologen polypeptide composite half cell, (B) biTEMPO polypeptide composite half cell and (C) viologen/biTEMPO polypeptide full cell, including their i. cyclic voltammograms, ii. charge-discharge curves and iii. cycling response. (A) and (B) utilized a polypeptide composite electrode 0.5 M LiCF ₃ SO ₃ in PC + filter paper lithium metal configuration while (C) utilized a viologen polypeptide composite electrode 0.5 M LiCF ₃ SO ₃ in PC + filter paper biTEMPO polypeptide composite electrode configuration. The composite electrodes were composed of 30 wt% active polypeptide with 60 wt% CB and 10 wt% PVDF on ITO-coated glass. In Aiii. and Biii., the C rates were varied, while in Ciii. the C-rate was constant at 1 C.	75
Figure 21. Liquid chromatography coupled with ESI-HRMS (LC-ESI-HRMS) was used to separate and identify the degradation products of the viologen and biTEMPO polypeptides (data from positive-ion mode shown).	78
Figure 22. Cell viability study of viologen polypeptide, biTEMPO polypeptide, viologen analog, biTEMPO analog and their degradation products.	80

Figure 23: (A) Illustrative design of peptide-based redox flow battery during charging and discharging. (B) Molecular structures of the redox-active polypeptides and their small-molecule analogs.....	85
Figure 24. Crossover study of (A) the redox-active polypeptides and (B) their small-molecule analogs using Daramic 175 and FAPQ 375 PP membranes. Solid lines = viologen species, dashed lines = biTEMPO species.....	93
Figure 25. Rate study of the (A) polypeptide and (B) small-molecule analog NAORFBs.....	94
Figure 26. Constant current cycling of the (A) polypeptide and (B) small-molecule analog NAORFBs.....	95
Appendix Figure 1. ATR-FTIR spectra of the synthesized species.....	123
Appendix Figure 2. ^1H NMR and ^{13}C NMR spectra of DLAG NCA.....	124
Appendix Figure 3. ^1H NMR spectra of PEG ₄₅ - <i>b</i> -PDLAG ₂₀ (P-20).....	125
Appendix Figure 4. (A) Strain sweep ($T = 37\text{ }^\circ\text{C}$, $\omega = 10\text{ rad}\cdot\text{s}^{-1}$) and (B) frequency sweep tests ($T = 37\text{ }^\circ\text{C}$, $\gamma = 0.2\%$) of P-20-1% hydrogels.....	126
Appendix Figure 5. (A) Strain sweep ($T = 37\text{ }^\circ\text{C}$, $\omega = 10\text{ rad}\cdot\text{s}^{-1}$) and (B) frequency sweep tests ($T = 37\text{ }^\circ\text{C}$, $\gamma = 0.2\%$) of P-20-2% hydrogels.....	126
Appendix Figure 6. (A) Strain sweep ($T = 37\text{ }^\circ\text{C}$, $\omega = 10\text{ rad}\cdot\text{s}^{-1}$) and (B) frequency sweep tests ($T = 37\text{ }^\circ\text{C}$, $\gamma = 0.2\%$) of P-20-4% hydrogels.....	127
Appendix Figure 7. (A) Strain sweep ($T = 37\text{ }^\circ\text{C}$, $\omega = 10\text{ rad}\cdot\text{s}^{-1}$) and (B) frequency sweep tests ($T = 37\text{ }^\circ\text{C}$, $\gamma = 0.2\%$) of P-20-8% hydrogels.....	127
Appendix Figure 8. (A) Strain sweep ($T = 37\text{ }^\circ\text{C}$, $\omega = 10\text{ rad}\cdot\text{s}^{-1}$) and (B) frequency sweep tests ($T = 37\text{ }^\circ\text{C}$, $\gamma = 0.2\%$) of P-30-1% hydrogels.....	128

Appendix Figure 9. (A) Strain sweep ($T = 37\text{ }^{\circ}\text{C}$, $\omega = 10\text{ rad}\cdot\text{s}^{-1}$) and (B) frequency sweep tests ($T = 37\text{ }^{\circ}\text{C}$, $\gamma = 0.2\%$) of P-30-2% hydrogels.....	128
Appendix Figure 10. (A) Strain sweep ($T = 37\text{ }^{\circ}\text{C}$, $\omega = 10\text{ rad}\cdot\text{s}^{-1}$) and (B) frequency sweep tests ($T = 37\text{ }^{\circ}\text{C}$, $\gamma = 0.2\%$) of P-30-8% hydrogels.....	129
Appendix Figure 11. Images (10 \times) of P-20-4% hydrogel cell culture after 7 d of incubation, including a green fluorescence (<i>top-left</i>), brightfield (<i>bottom-left</i>), red fluorescence (<i>top-right</i>) and merged fluorescence image (<i>bottom-right</i>). Scale bars = 1 mm.....	130
Appendix Figure 12. Images (10 \times) of P-30-4% hydrogel cell culture after 1 h of incubation, including a green fluorescence (<i>top-left</i>), brightfield (<i>bottom-left</i>), red fluorescence (<i>top-right</i>) and merged fluorescence image (<i>bottom-right</i>). Scale bars = 1 mm.....	131
Appendix Figure 13. Images (10 \times) of P-30-4% hydrogel cell culture after 5 d of incubation, including a green fluorescence (<i>top-left</i>), brightfield (<i>bottom-left</i>), red fluorescence (<i>top-right</i>) and merged fluorescence image (<i>bottom-right</i>). Scale bars = 1 mm.....	132
Appendix Figure 14. Images (10 \times) of P-30-4% hydrogel cell culture after 7 d of incubation, including a green fluorescence (<i>top-left</i>), brightfield (<i>bottom-left</i>), red fluorescence (<i>top-right</i>) and merged fluorescence image (<i>bottom-right</i>). Scale bars = 1 mm.....	133
Appendix Figure 15. High magnification images (40 \times) of P-20-4% (top) and P-30-4% (bottom) hydrogel cell cultures after 7 d in gel-dense areas (A and C) and at gel-glass interfaces (B and D). Scale bars = 100 μm . Each figure includes a green fluorescence (<i>top-left</i>), brightfield (<i>bottom-left</i>), red fluorescence (<i>top-right</i>) and merged fluorescence image (<i>bottom-right</i>).	134
Appendix Figure 16. Cell quantification of P-20-4% and P-30-4% hydrogel cell cultures after 7 d.....	135
Appendix Figure 17. Synthesis of viologen analog.	136
Appendix Figure 18. Synthesis of biTEMPO analog.....	136
Appendix Figure 19. (A) SEC traces of PCHLG ₅₀ (4) and PPLG ₅₀ (12), and (B) their tabulated dispersity and molar mass values.	137

Appendix Figure 20. Normalized CD spectra of viologen polypeptide (6) and biTEMPO polypeptide (14) in ACN (0.1 mg·mL ⁻¹).	137
Appendix Figure 21. (A) UV-vis spectra of biTEMPO polypeptide (1 mM of repeating unit) and 4-OH-TEMPO (1 mM) in CHCl ₃ . (B) UV-vis calibration curve of 4-OH-TEMPO in CHCl ₃	138
Appendix Figure 22. EPR spectra of biTEMPO polypeptide (1 mM of repeating unit) and 4-OH-TEMPO (1 mM) in CHCl ₃	138
Appendix Figure 23. ATR-FTIR spectra of the synthesized species.	139
Appendix Figure 24. ATR-FTIR spectra of the synthesized species (cont'd).	140
Appendix Figure 25. ATR-FTIR spectra of the synthesized species (cont'd).	141
Appendix Figure 26. ATR-FTIR spectra of the synthesized species (cont'd).	142
Appendix Figure 27. ATR-FTIR spectra of the synthesized species (cont'd).	143
Appendix Figure 28. ATR-FTIR spectra of the synthesized species (cont'd).	144
Appendix Figure 29. XPS spectra of PPLG ₅₀ -g-MTEMPO (13).	145
Appendix Figure 30. XPS spectra of biTEMPO polypeptide (14).	146
Appendix Figure 31. XPS spectra of HC- <i>bis</i> (MTEMPO) (21).	147
Appendix Figure 32. XPS spectra of biTEMPO analog (22).	148
Appendix Figure 33. ¹ H NMR and ¹³ C NMR spectra of MBPI (2).	149
Appendix Figure 34. ¹ H NMR and ¹³ C NMR spectra of CHLG (3).	150
Appendix Figure 35. ¹ H NMR and ¹³ C NMR spectra of CHLG NCA (4).	151
Appendix Figure 36. ¹ H NMR and ¹³ C NMR spectra of PCHLG ₅₀ (5).	152
Appendix Figure 37. ¹ H NMR and ¹³ C NMR spectra of PIHLG ₅₀ (6).	153

Appendix Figure 38. ^1H NMR and ^{13}C NMR spectra of viologen polypeptide (7).....	154
Appendix Figure 39. ^1H NMR and ^{13}C NMR spectra of MTEMPOL (8).	155
Appendix Figure 40. ^1H NMR and ^{13}C NMR spectra of diMTEMPO disulfide (9).....	156
Appendix Figure 41. ^1H NMR and ^{13}C NMR spectra of Thio-MTEMPO (10).....	157
Appendix Figure 42. ^1H NMR and ^{13}C NMR spectra of PLG HCl (11).....	158
Appendix Figure 43. ^1H NMR and ^{13}C NMR spectra of PLG NCA (12).....	159
Appendix Figure 44. ^1H NMR and ^{13}C NMR spectra of PPLG ₅₀ (13).	160
Appendix Figure 45. ^1H NMR spectrum of PPLG ₅₀ -g-MTEMPO (14).	161
Appendix Figure 46. ^1H NMR spectrum of biTEMPO polypeptide (15).	162
Appendix Figure 47. ^1H NMR and ^{13}C NMR spectra of CHHC (16).....	163
Appendix Figure 48. ^1H NMR and ^{13}C NMR spectra of IHHC (17).	164
Appendix Figure 49. ^1H NMR and ^{13}C NMR spectra of PBPI (18).	165
Appendix Figure 50. ^1H NMR and ^{13}C NMR spectra of viologen analog (19).....	166
Appendix Figure 51. ^1H NMR and ^{13}C NMR spectra of PHC (20).	167
Appendix Figure 52. ^1H NMR and ^{13}C NMR spectra of HC- <i>bis</i> PA (21).	168
Appendix Figure 53. ^1H NMR and ^{13}C NMR spectra of HC- <i>bis</i> (MTEMPO) (22).....	169
Appendix Figure 54. ^1H NMR and ^{13}C NMR spectra of biTEMPO analog (23).....	170
Appendix Figure 55. Electrochemical characterization set-ups discussed in the manuscript. (A) The three-electrode solution beaker cell: glassy carbon working electrode and lithium metal counter/reference electrodes. (B)The three-electrode beaker cell: polypeptide composite working electrode and lithium metal counter/reference electrodes. (C) The half sandwich cell:	

viologen or biTEMPO polypeptide composite working electrode and lithium metal reference electrode with a filter paper separator. (D) The full sandwich cell: viologen polypeptide composite working electrode and biTEMPO polypeptide composite reference electrode with a filter paper separator.....	171
Appendix Figure 56. Solution state cyclic voltammetry of (A) viologen analog and (B) biTEMPO analog at 1 mM in 0.5 M LiCF ₃ SO ₃ in PC electrolyte. A glassy carbon electrode was utilized as the working electrode in a three-electrode beaker cell with lithium metal reference and counter electrodes.....	172
Appendix Figure 57. Peak current vs. square-root of scan rate from the cyclic voltammograms for (A) polypeptide thin film electrodes and (B) polypeptide composite electrodes of i. Viol ⁺ /Viol ²⁺ and ii. Viol ⁰ /Viol ⁺ for the viologen polypeptide and iii. for the biTEMPO polypeptide. The viologen polypeptide composite electrode did not exhibit a lower redox peak at scan rates greater than 10 mV·s ⁻¹	174
Appendix Figure 58. Peak separation vs. square-root of scan rate from the cyclic voltammograms for (A) polypeptide thin film electrodes and (B) polypeptide composite electrodes of i. the viologen polypeptide and ii. the biTEMPO polypeptide. The viologen polypeptide composite electrode did not exhibit a lower redox peak at scan rates greater than 10 mV·s ⁻¹	175
Appendix Figure 59. Scanning electron micrographs of (A) the viologen polypeptide composite electrode and (B) the biTEMPO polypeptide composite electrode i. before and ii. after 50 charge-discharge cycles in the full sandwich cell configuration (viologen polypeptide composite electrode 0.5 M LiCF ₃ SO ₃ in PC + filter paper biTEMPO polypeptide composite electrode).....	176
Appendix Figure 60. Solution state CV of the electrolyte (1) after soaking the electrode in the electrolyte solution, and after electrochemical testing of (2) PVDF/CB composite electrodes. The tests were carried out for the electrolyte tested with (A) the viologen polypeptide composite electrodes and (B) the biTEMPO polypeptide composite electrodes.....	177
Appendix Figure 61. Solution state CV of the electrolyte after testing the full cells (with both composite electrodes). The CV was conducted in a three-electrode beaker cell with a glassy carbon	

working electrode and lithium metal counter and reference electrodes. The electrolyte was 0.5 M LiCF ₃ SO ₃ in PC unless otherwise stated. For the full sandwich cell, the separator was soaked in 15 mL of electrolyte after electrochemical testing and the resulting solution was used for solution state CV testing.....	177
Appendix Figure 62. Differential capacity curves from galvanostatic cycling curves filter paper sandwich cell at 1C. An adjacent-averaging filter with a 5-point window was applied in OriginPro 2020 to remove noise in the data.	178
Appendix Figure 63. High resolution mass spectrometry (HRMS, positive ESI) of the degradation products of (from top to bottom) viologen polypeptide, viologen analog and PBLG ₅₀	179
Appendix Figure 64. HRMS (negative ESI) of the degradation products of (from top to bottom) viologen polypeptide, viologen analog and PBLG ₅₀	180
Appendix Figure 65. HRMS (positive ESI) of the degradation products of (from top to bottom) biTEMPO polypeptide, biTEMPO analog, 4-OH-TEMPO and PBLG ₅₀	181
Appendix Figure 66. HRMS (negative ESI) of the degradation products of (from top to bottom) biTEMPO polypeptide, biTEMPO analog, 4-OH-TEMPO and PBLG ₅₀	182
Appendix Figure 67. Separation of the degradation products of (from top to bottom) viologen polypeptide, viologen analog and PBLG ₅₀ using liquid chromatography-mass spectrometry (LC-HRMS, positive ESI).	183
Appendix Figure 68. Separation of the degradation products of (from top to bottom) viologen polypeptide, viologen analog and PBLG ₅₀ using LC-HRMS (negative ESI). FeCl ₄ ⁻ contaminants eluted at 1.31 min in all samples. I ⁻ and I ₃ ⁻ residues eluted at 1.62 min for viologen polypeptide and viologen analog.....	184
Appendix Figure 69. Separation of the degradation products of (from top to bottom) biTEMPO polypeptide, biTEMPO analog, 4-OH-TEMPO and PBLG ₅₀ using LC-HRMS (positive ESI).	185
Appendix Figure 70. Separation of the degradation products of (from top to bottom) biTEMPO polypeptide, biTEMPO analog, 4-OH-	

TEMPO and PBLG ₅₀ using LC-HRMS (negative ESI). FeCl ₄ ⁻ contaminants eluted at 1.31 min in all samples.	186
Appendix Figure 71. ¹ H NMR spectra of L-glutamic acid, viologen analog and viologen polypeptide after acid degradation with 1 M HCl at 110 °C.	187
Appendix Figure 72. ¹ H NMR spectra of L-glutamic acid, biTEMPO analog and biTEMPO polypeptide after acid degradation with 1 M HCl at 110 °C.	188
Appendix Figure 73. Cytotoxicity effects of viologen and biTEMPO polypeptides on MC3T3 cells, fibroblast cells and coronary venular endothelial cells (CVECs).	189
Appendix Figure 74. Cytotoxicity effects of the degradation products of viologen and biTEMPO polypeptides on MC3T3 cells, fibroblast cells and CVECs.	190
Appendix Figure 75. Cytotoxicity effects of viologen and biTEMPO analogs on MC3T3 cells, fibroblast cells and coronary venular endothelial cells (CVECs).	191
Appendix Figure 76. Cytotoxicity effects of the degradation products of viologen and biTEMPO analogs on MC3T3 cells, fibroblast cells and CVECs.	192
Appendix Figure 77. Crossover study of (A) viologen-TFSI and (B) biTEMPO polypeptides using Daramic 175 and FAPQ 375 PP membranes.	193
Appendix Figure 78. Crossover study of (A) viologen-TFSI and (B) biTEMPO analogs using Daramic 175 and FAPQ 375 PP membranes.	194
Appendix Figure 79. ATR-FTIR spectra of (A) 0.5 M TEATFSI/ACN, (B) 50 mM viologen-TFSI polypeptide/ACN, and 50 mM viologen-TFSI polypeptide in 0.5 M TEATFSI/ACN (C) before cycling, (D) after rate study and (E) after 500 cycles at 10 mA·cm ⁻² . The y-axis of the spectra is transmittance (%).	195
Appendix Figure 80. ATR-FTIR spectra of (A) 0.5 M TEATFSI/ACN, (B) 50 mM biTEMPO polypeptide/ACN, and 50 mM biTEMPO polypeptide in 0.5 M TEATFSI/ACN (C) before cycling, (D) after	

rate study and (E) after 500 cycles at $10 \text{ mA}\cdot\text{cm}^{-2}$. The y-axis of
the spectra is transmittance (%). 196

LIST OF TABLES

	Page
Table 1. Performance of polymer-based batteries.....	42
Table 2. Degradation conditions used for the viologen and biTEMPO polypeptides.....	77
Appendix Table 1. Comparison of the oxidation/reduction peak potential (E_o/E_R), the peak separation (ΔE_p), half-wave potential ($E_{1/2}$), oxidation/reduction peak width (W_o/W_R), and oxidation/reduction peak area (A_o/A_R) for the biTEMPO analog, biTEMPO polypeptide thin film and biTEMPO polypeptide composite electrode.....	172
Appendix Table 2. Comparison of the oxidation/reduction peak potential (E_o/E_R), the peak separation (ΔE_p), half-wave potential ($E_{1/2}$), oxidation/reduction peak width (W_o/W_R), and oxidation/reduction peak area (A_o/A_R) for both peaks of the viologen analog, viologen polypeptide thin film and viologen polypeptide composite electrode.....	173

CHAPTER I

INTRODUCTION

Peptides are chains of α -amino acids linked together *via* peptide linkages. With highly ordered structures, they possess the ability to self-assemble into a wide range of nanoarchitectures, in addition to their inherent biological origins, bioactivity, biocompatibility and (bio)degradability, making them promising candidates not only for biological and biomedical purposes,^{1,2} but also for electrical and electronic applications **(Figure 1)**.³⁻⁵ With the chemical structures similar to natural proteins, peptide-based materials usually exhibit low or even no cytotoxicity. They have been demonstrated to be biodegraded by certain types of enzymes (*e.g.*, trypsin, chymotrypsin, etc.) in both *in vitro* and *in vivo* experiments,⁶⁻¹⁰ in addition to acidic and basic degradations made possible by the amide linkages. These hydrolytic processes found the basis for the design and the development of new naturally derived (bio)degradable materials. In addition, side chain modifications make it possible to incorporate unnatural residues and moieties with

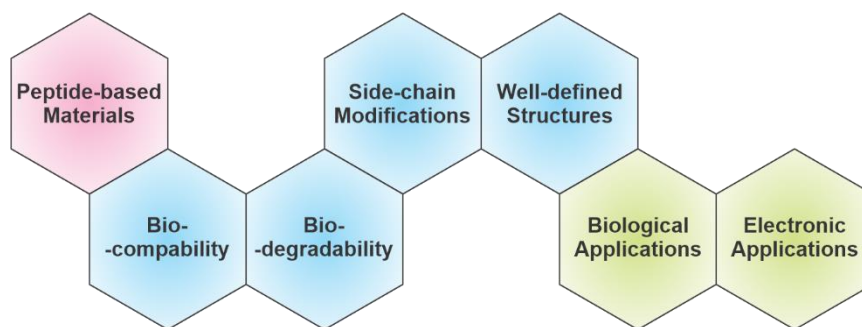


Figure 1. Properties and applications of peptide-based materials.

functionalities beyond the twenty proteinaceous amino acids, playing an important role in tuning conformational and functional properties of peptides. Together with the peptide backbones, they contribute to the overall control of peptide three-dimensional (3D) structures. This can also be made possible *via* chain length extension, side chain modification and amino acid chirality, providing scientists with immense opportunities to tune structure-property-performance parameters and develop designer peptides and smart peptide-based materials that suit specific applications.

Polypeptides: Synthesis and Characterization

Polypeptides from N-Carboxyanhydride (NCA) polymerizations

Conventionally, synthetic peptides are prepared using the Merrifield synthesis, also known as the solid phase peptide synthesis (SPPS). Even though this method is advantageous in controlling peptide sequences, it is limited to the low-yield production of short peptides, yet requires time-consuming processes and wasteful purifications (**Figure 2A**).^{11,12} On the contrary, the ring-opening polymerization (ROP) of *N*-carboxyanhydride (NCA) monomers, though lacking the ability to control peptide sequence, offers a more practical approach for large-scale preparation of peptides with high molar mass while allowing for the facile installation of functional groups beyond the scope of the twenty natural proteinogenic amino acids (**Figure 2B**).

The first synthesis of NCA monomers was reported by Leuchs and co-workers in 1906 *via* phosgenation of α -amino acids.¹³ It was not until the late 1990s when Deming *et al.* reported the first controlled polymerization of NCA using organometallic catalysts.

Since then, the field of NCA ROP witnessed the advancement of numerous living polymerization methodologies, ranging from the traditional nucleophilic initiation (*i.e.*, amine and alcohol)^{14–16} to, among others, the use of N₂ flow¹⁷ and fluorinated alcohol¹⁸ as means of polymerization acceleration. These techniques, altogether, enabled researchers to prepare peptide-based materials with well-defined architectures, chain lengths and dispersity. The polypeptides synthesized in this dissertation were prepared *via* amine initiation with added N₂ flow for accelerated ROP.

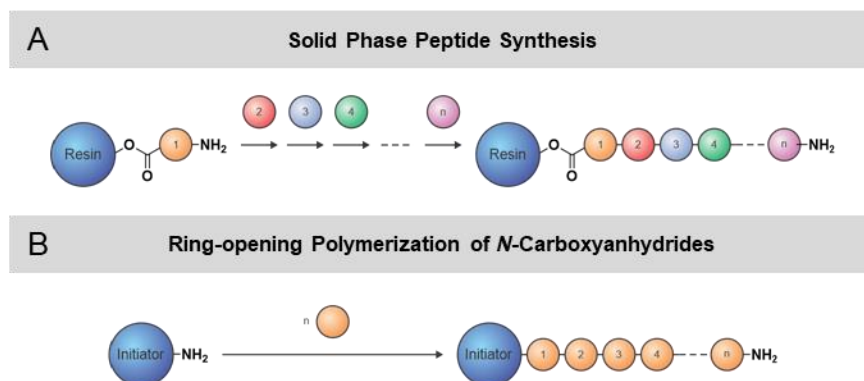


Figure 2. Different methods of peptide synthesis: **(A)** Solid phase peptide synthesis and **(B)** ring-opening polymerization of *N*-carboxyanhydrides.

With regards to amine initiation, there are two widely accepted mechanisms of NCA ROP, *i.e.*, normal amine mechanism (NAM) and activated monomer mechanism (AMM) (**Figure 3**). In the NAM, the initiator acts as a nucleophile (*e.g.*, primary amine), attacking the carbonyl group of the NCA monomers at 5-C to open its ring structure (**Figure 3A**). The subsequent release of CO₂ produces a primary amine at the ω-end, which continue to nucleophilically attack another NCA monomer to propagate the chain

growth. In contrast, the AMM involves the use of an initiator with basic character, which deprotonates the nitrogen (3-N) of the NCA monomer, resulting in the formation of the corresponding amine anion (**Figure 3B**). This anion then acts as a nucleophile to attack the carbonyl group of another NCA monomer at 5-C, followed by the release of CO₂ to yield a dimer with both a reactive *N*-acylated NCA at the α -end and a primary amine at the ω -end, which further propagates in a polycondensation manner. The α -NCA end can react with either another amine anion *via* AMM or ω -amine *via* NAM, while the ω -amine

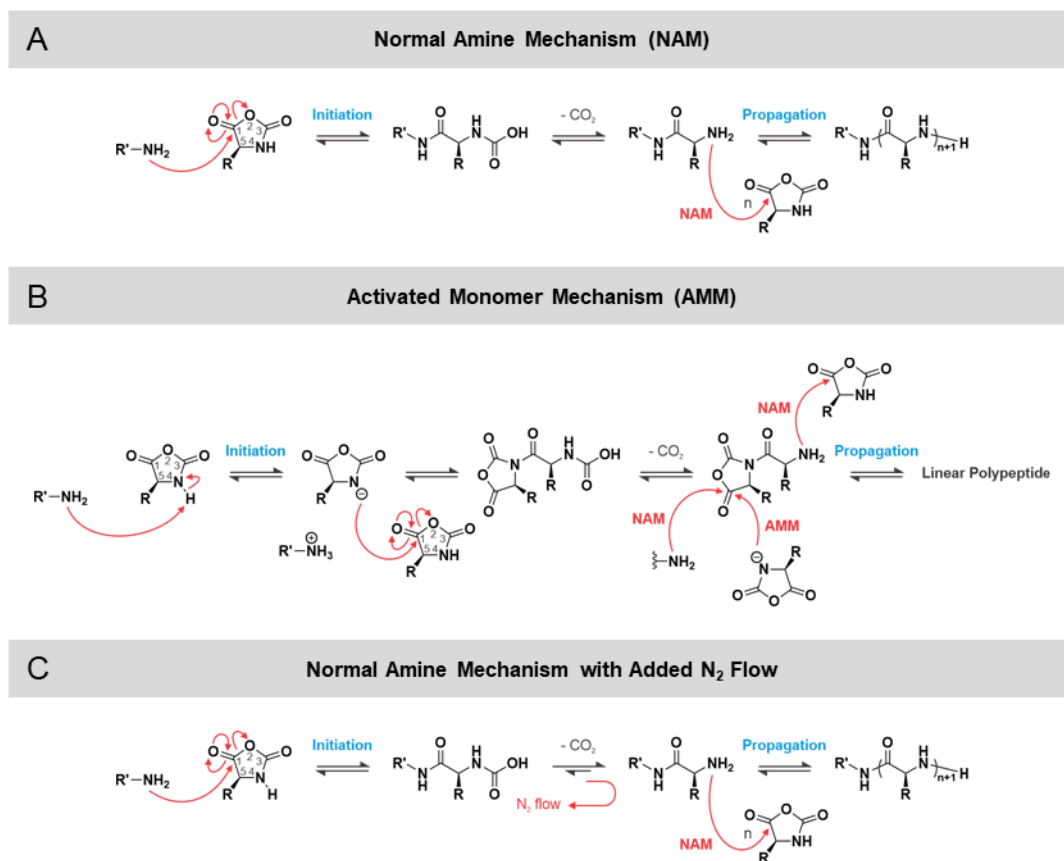


Figure 3. Pathways for ring-opening polymerization of NCAs: **(A)** Normal amine mechanism (NAM), **(B)** activated monomer mechanism (AMM), **(C)** normal amine mechanism with added N₂ flow.

end only proceeds *via* NAM. As a result, polymerizations following the AMM pathway usually produce polypeptides with broad molar mass distributions.

Since amines possess both nucleophilic and basic characters, the NAM and AMM always coexist, complicating the polymerization process.¹⁹ In addition, NCA ROP *via* amine initiation is usually slow, taking up to several days.¹⁹ The competition between NAM and AMM pathways in addition to prolonged reaction time usually leads to polypeptides with high molar mass distribution and ill-defined structures due to side reactions such as chain termination and monomer degradation. Significant advances were made over the past two decades in the field of synthetic polypeptides to eliminate side reactions, notably the AMM, and to accelerate the polymerization rates of amine-initiated NCA ROP. In 2013, our group reported a facile method to prepare well-defined polypeptides by applying continuous N₂ flow during polymerization (**Figure 3C**).¹⁷ The removal of CO₂ from the reaction mixture not only significantly accelerated the polymerization rate by driving the equilibrium forward from the carbamic acid intermediate to generate ω -primary amines, but also suppressed the AMM, as evidenced by successful chain extensions.¹⁷

Peptide Secondary Structures

Unlike non-peptidic materials, the backbone of peptides or polypeptides, together with the side chains of the amino acid residues, can construct well-defined secondary structures. Peptide secondary structures are local organizations of the amino acids that constitute the primary sequence of the macromolecules. Depending on intra- and/or

intermolecular hydrogen bonds between the amino acids, a peptide chain can be a random coil, α -helix or β -sheet (**Figure 4A**).

In an α -helix, the main chain is tightly coiled into a rod-like structure with an inner radius of 2.3 Å while the side chains extend outward in a helical array.^{11,12,20} This structure is derived from a hydrogen bonding network between the oxygen of the carbonyl group of each peptide bond in the strand and the amino hydrogen of the peptide bond of the fourth following peptide bond in the sequence. As a result, longer sequences will make the α -helical structures more stable. On average, each helical turn constitutes 3.6 amino acids (1.5 Å each).^{11,12,20} An α -helix can be right-handed (α_R , clockwise) or left-handed (α_L , counter-clockwise).²¹ Peptides formed predominantly from α -helix-forming L-amino acids assemble into a right-handed conformation while those from α -helix-forming D-amino acids assemble into the left-handed structure.²² Coexistence of L- and D-residues in a peptide chain can reduce the helical content from either α -helix handedness and can lead to the loss of helicity to form a random coil structure.²²

A β -sheet is a collection of peptide chains (β -strands) fully extended with the side chains of adjacent amino acids pointing in opposite directions. The distance between two adjacent amino acids in a strand is 3.5 Å and that between two adjacent strands is 4.7 Å.^{11,12,20} The hydrogen bonding network in β -sheets is created between the carbonyl oxygens of one strand and the amino hydrogen of the adjacent strand, with each pair of β -strands being either parallel or antiparallel depending on the strand directions.^{11,12,20} In addition, hydrophobic interactions between the β -sheets play an important role in the formation, stabilization and assembly of peptide fibrils.²³ Unlike in an α -helix, the

stereochemistry of β -sheet-forming amino acids does not have an impact on the structure of the β -sheets formed, but rather on the handedness of the assembled fibrils.²⁴

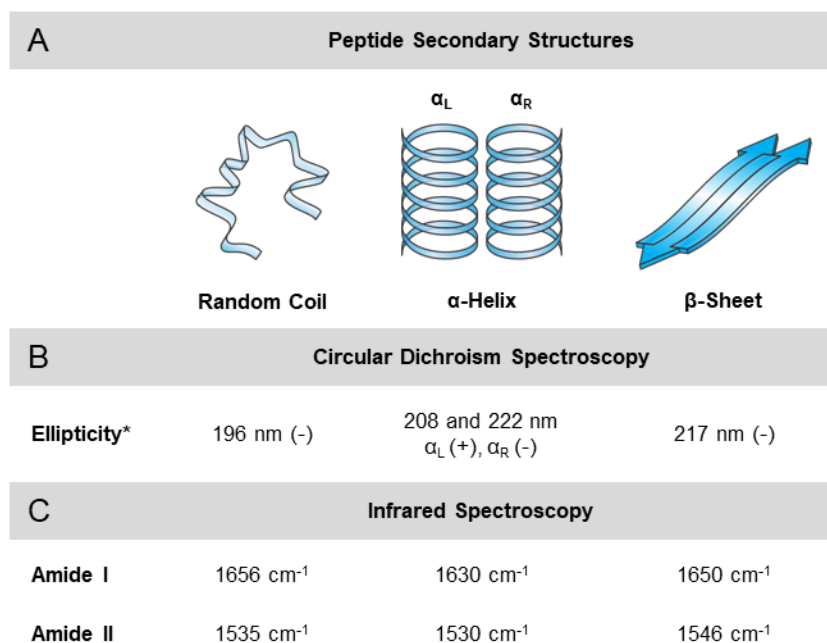


Figure 4. (A) Secondary structures of peptides and their characteristic (B) circular dichroism ellipticity and (C) infrared spectroscopy wavelengths. *(+) indicates positive ellipticity and (-) indicates negative ellipticity at designated wavelengths.

Peptide secondary structures can be determined spectroscopically by circular dichroism (CD) and infrared (IR) techniques. All peptide secondary structures exhibit CD bands with distinctive shapes and magnitudes in the far-ultra-violet region (190-250 nm). Specifically, a right-handed α -helix possesses two minima at 208 and 222 nm, whereas a single negative minimum at 196 or 217 nm is indicative of a random coil or β -sheet structure, respectively (Figure 4B).^{25,26} A left-handed α -helix possesses two maxima at the same wavelength as the right-handed counterpart. Compared to the CD technique that

relies on samples in solutions, IR spectroscopy can be used to probe the conformations of peptides in the solid state, as coatings/films on surfaces or in bulk. Generally, peptides exhibit two amide stretching bands, amide I and amide II (**Figure 4A**). The amide I band can be found at 1656, 1630 or 1650 cm^{-1} for random coil, α -helix or β -sheet, respectively, while amide band II at 1535, 1530, or 1646 cm^{-1} .^{27,28}

Peptide-based Hydrogels

Peptide-based hydrogels are soft materials with 3D networks formed *via* physical or chemical cross-linking of the peptide chains.²⁹ They inherit the innate biocompatibility and (bio)degradability of peptides with enhanced mechanical stability, injectability and elasticity, making them suitable for a wide range of biological applications such as cell therapeutics,³⁰ biosensors,³¹ drug release,³² tissue engineering³³ and wound healing.^{34,35} Driven by hydrophobic forces, coulombic interactions, hydrogen bonding and π - π stacking, among others, some polypeptides can spontaneously undergo supramolecular assembly into nanofibrils and/or nanoribbons *via* aggregations of polymer secondary structures.^{29,36} Others need to be triggered by stimuli (*i.e.*, heat, metal-ligand chelation, enzyme, pH, etc.) to induce the formation of nanostructures or change in conformation that allows for gel formation.³⁷

Among peptide-based materials that can undergo hydrolysis (*i.e.*, dipeptides, amphiphilic block copolymers, etc.), peptide amphiphiles (PAs), a member of the amphiphile family (molecules consisting of both hydrophilic and hydrophobic sections), have emerged as an attractive class of materials suitable for applications across various

fields of science and technology and advanced the field of peptide-based hydrogels beyond the scope of biological applications.³⁶ They can self-assemble into a variety of aggregates such as fibers, nanospheres, vesicles and nanosheets, to name a few.^{36,38-40} Some PAs are composed of solely amino acids arranging into hydrophobic and hydrophilic ends (*i.e.*, amphiphilic peptides).³⁶ Others are peptide chains conjugated with adjacent segments, peptidic or non-peptidic, with reversed solvent effect (*i.e.*, lipidated peptides, supramolecular PAs and poly(ethylene glycol) (PEG)-functionalized peptides).³⁶

In PA systems, peptide secondary structures are the major driving force for gelation. As a result, the gelation behaviors can be readily controlled by tuning structure-property-performance parameters. Common methods include changing peptide sequence and stereochemistry, varying block lengths, and installing moieties that allow for hydrogen bonding or host-guest/supramolecular interactions.^{36,41} Most importantly, a delicate solvophilic-solvophobic balance should be achieved and maintained in order for the PAs to undergo and sustain hydrogelation.⁴² Due to the phase separation derived from supramolecular assembly, excessive interactions between either domains would break this balance, leading to either material liquefaction (longer hydrophilic segment) or precipitation (longer hydrophobic segment).

Attachment of PEGs to hydrophobic peptides has been demonstrated as a particularly useful method to provide aqueous solubility and stability to peptide amphiphiles for use as hydrogelators. This can be done using a variety of techniques, including carbodiimide coupling,⁴³ azide-alkyne "click" chemistry,⁴⁴ thiol-ene "click" chemistry⁴⁵ and Michael addition,⁴⁶ to name a few. In this regards, hydrogels derived

from NCA ROP are considered a more practical synthetic approach for the preparation of PEGylated polypeptides, using amine- or diamine-functionalized PEGs as initiators.^{47–49} Some examples of this type of peptide amphiphiles include PEG-*block*-peptide diblock copolymers and peptide-*block*-PEG-*block*-peptide triblock copolymers.^{8,36,41,50} These macromolecules have been reported to undergo nano- and/or microphase separation of the block components when triggered with heat, which allows for sol-gel transition *via* physical association of the hydrophobic peptide domains.^{8,36,41,50}

Depending on the secondary structures of the peptide segments, the PEGylated polypeptides can undergo different nanostructure transformations during thermal gelation. When α -helical structures dominate the hydrophobic domains, micellar structures were often observed (**Figure 5A**).³⁷ With an increase in temperature, the dehydration of PEG domains enhanced the hydrophobic interactions, leading to the percolation of micelles into gel networks. Amphiphiles with dominating β -sheet-forming polypeptide segments tend

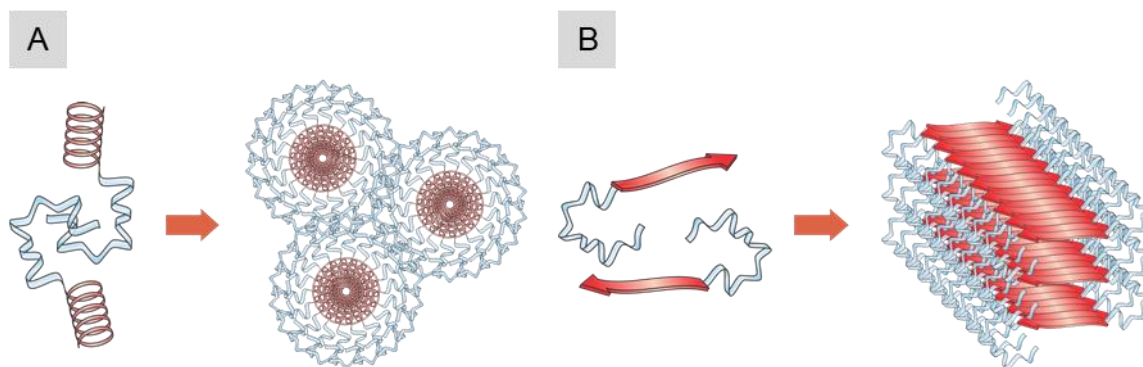


Figure 5. Schematic illustrations of peptide amphiphile gelation *via* (A) micellar percolation of PEG-*block*- α -helical polypeptides and (B) fibrillar entanglement of PEG-*block*- β -sheet-forming polypeptides.

to supramolecularly assemble into nanofibril or nanoribbon structures in aqueous solution (**Figure 5B**). An increase in temperature pushes the hydrophilic-hydrophobic balance toward the hydrophobic direction, stabilizing the hydrophobic domains by reducing the packing distance due to PEG dehydration, thus enhancing the physical crosslinking *via* stronger hydrophobic interactions.

Polymer-based Batteries

History of Batteries

The existence of batteries dates back 2000 years, during the domination of the Parthian Empire in the Fertile Crescent area in the Middle East between 190 BC and 224 AD, in the form of a clay pot containing an iron rod surrounded by a cylindrical tube made of wrapped copper sheets.^{51,52} Even though batteries are a simple concept, achieving batteries with large voltage windows, high capacity and long cycling stability remains a scientific challenge. The creation of the battery as we know it today is the result of hundreds of years of evolution, involving one invention after another and multinational interdisciplinary scientific collaboration to balance performance, weight, cost, among other factors.

Batteries are composed of two electrodes of different chemical potentials connected by an ionically conductive material called an electrolyte. When the electrodes are connected to an external device to form a closed circuit, electrons travel from the electrode with a more negative potential (anode) to that with the more positive potential (cathode). In the 19th and early 20th centuries, zinc-manganese oxide arose as a good

electrode material candidate for non-rechargeable primary batteries, and lead-acid and nickel oxide-cadmium for rechargeable secondary ones. In the late 20th century, nickel-metal hydrides and lithium ions emerged as the main modern portable sources of energy in high-end applications.^{53,54} In parallel with the development of secondary batteries, redox flow batteries also attracted significant scientific attention and are considered a promising candidate for grid-scale electrochemical energy storage. **Figure 6** provides illustrative designs of a typical secondary battery (**Figure 6A**) and flow battery (**Figure 6B**).

Organic Radical Batteries

Proposed by Michael Stanley Wittingham, Akira Yoshino and John B. Goodenough in 1976, lithium-ion batteries (LIBs) are considered the most established secondary technology for energy storage among current electrochemical energy storage systems in general and among current secondary battery systems in particular. In a conventional secondary battery, the active materials are loaded into solid composite anodes and cathodes, which are separated by a liquid electrolyte-loaded membrane (**Figure 6A**). Despite recent technology advances to make lighter, safer and more affordable LIBs, drawbacks are still present in current battery manufacturing, including the declining reserve, unethical sourcing, toxicity and limited recycling of raw materials,^{55,56} attracting significant research towards more sustainable alternatives. All of these drawbacks can be tackled by using organic materials. One alternative battery system receiving increased attention in recent years is organic radical batteries (ORBs),

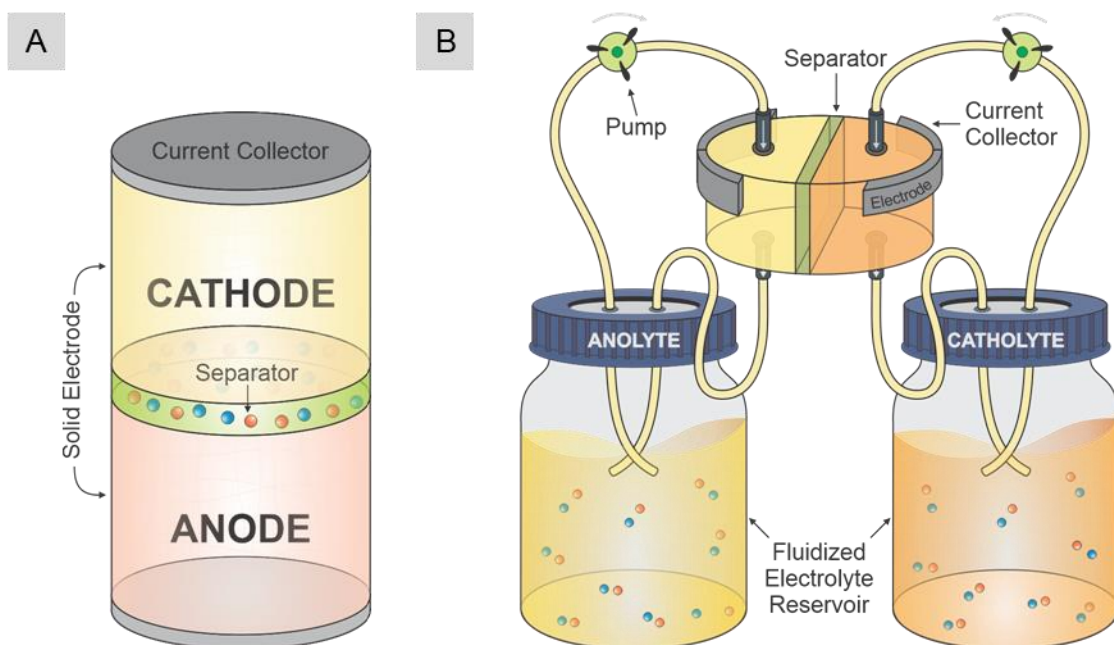


Figure 6. Illustrative designs of a (A) secondary battery and (B) flow battery.

which promise increased environmental friendliness, independence from limited inorganic resources, and fast charging rates.⁵⁷⁻⁶³ One of the most studied types of organic sources used in ORBs are redox polymer backbones carrying pendant redox active groups with two common electrochemically active pendant groups 2,2,6,6-tetramethyl-4-piperidine-1-oxyl (TEMPO) and viologen.⁶⁴⁻⁶⁷

Currently, the field of ORBs mainly focuses on increasing the theoretical capacity and voltage difference between the cathode and anode polymers, without addressing the increasing need for material sustainability.⁶⁸⁻⁷³ To the best of our knowledge, none of the redox-active polymers reported for battery applications employed degradable polymer backbones, which will be important for improved closed-loop materials utilization.⁶⁷ Specifically, most non-conjugated redox-active polymers bear aliphatic backbones that

are challenging to degrade, as seen in **Figure 7**.⁷⁴ The first example of redox-active polymers with degradable backbones for energy storage is that of TEMPO-containing deoxyribonucleic acid-lipid complexes as cathode materials, where the TEMPO moieties were incorporated onto DNA backbones *via* electrostatic interactions between positively charged lipids and anionic phosphate linkages.⁷⁵ Additionally, TEMPO were also reported to be conjugated onto polypeptides *via* esterification and amidation of

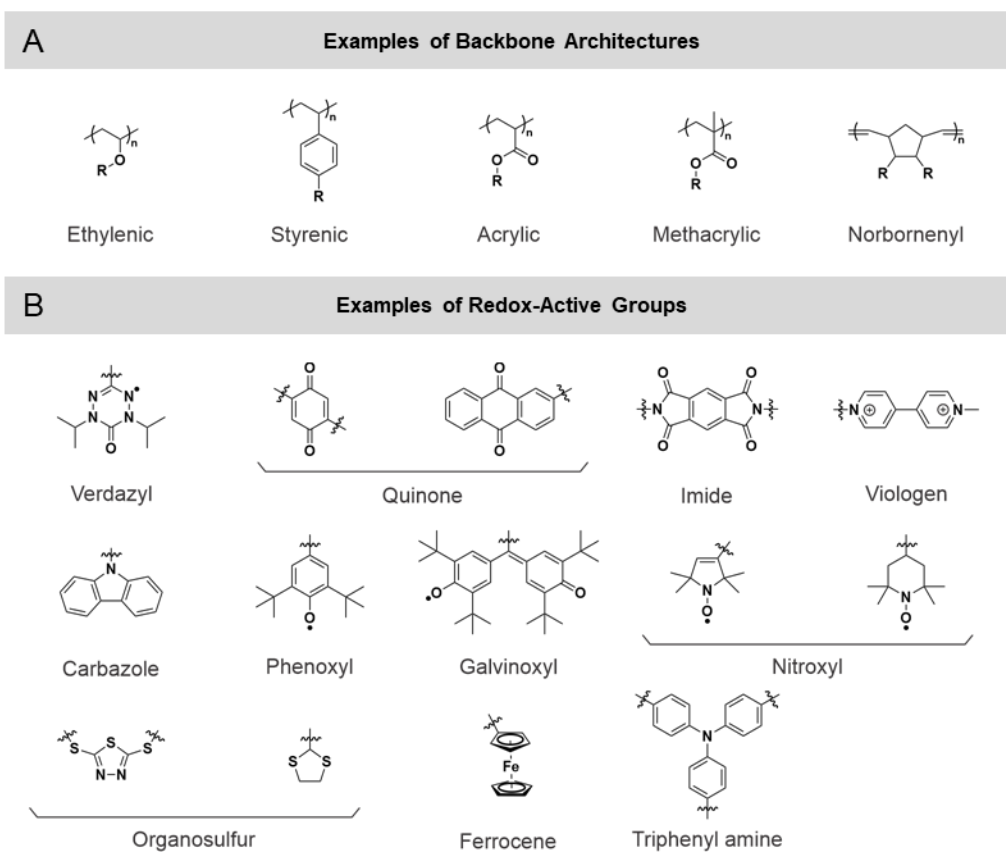


Figure 7. Commonly used (A) backbones for polymers with (B) common redox-active pendant groups.

poly-L-glutamic acid with 4-hydroxy-TEMPO and 4-amino-TEMPO, respectively. However, the electrochemical properties of these TEMPO-decorated polypeptides were not considered.⁷⁶

Furthermore, there has been a limited number of studies in which a fully organic battery has been presented.^{69,70,73,77,78} Typically, studies by Sano *et al.* have demonstrated a fully organic battery with viologen- and TEMPO-containing polymethacrylates as anode and cathode, respectively.⁷³ In addition, Suga *et al.* reported the use of a poly(TEMPO-substituted norbornene) cathode with a poly(galvinoxystyrene) anode.⁷⁰ Additionally, Wild *et al.* demonstrated two chemistries, poly(2-vinylthianthrene) and poly(2-methacrylamide-11,11,12,12-tetracyano-9,10-anthraquinonedimethane), as cathode and anode materials, respectively, for a fully organic battery.⁷⁷ These prior works highlight that, although fully organic batteries have been demonstrated, none has investigated backbone degradability or demonstrated active material recyclability.

Redox Flow Batteries

Secondary batteries, metal-based or polymer-based, even though representing the biggest and most developed group of electrochemical energy storage, are still faced with high-cost production, active material degradation and short lifetime, thus preferred for small-scale electronics.⁷⁹ In parallel with the development of secondary batteries, the past few decades also witnessed the fast growing evolution of redox flow batteries, one of the most promising candidates for grid-scale electricity energy storage for their design flexibility, low cost of production and enhanced safety feature.^{80,81} In these systems, the

redox-active compounds are fluidized in external reservoirs and pumped into an electrochemical cell, where they undergo redox reactions and exchange electrons with current collectors (**Figure 6B**). As a result, the capacity of RFBs is controlled by the concentration of redox-active materials, not their molar mass and mass loading as in the case of secondary batteries. This feature provides RFBs with flexible scalability for different energy storage applications. In addition, similar to secondary batteries, RFBs are also rendered as rechargeable fuel cells due to the reversibility of the electrochemical reactions of the redox-active materials.

Several challenges have recently emerged, including the high cost, solubility and toxicity of metal-based materials, membrane crossover during cell operation, and lack of advancement of inexpensive, stable and highly conductive membranes that are suitable for RFB commercialization.^{80,82,83} This has led to a surge in the search for alternative RFB chemistries, especially the utilization of small-molecule organic redox-active materials in both aqueous (aqueous organic RFBs, AORFBs) and organic electrolytes (non-aqueous organic RFBs, NAORFBs).^{84–86} This advancement, even though reducing the dependence of RFBs on the use of scarce metal resources and demonstrated to exhibit good electrochemical and chemical stability, was still faced with limited solubility of redox species in electrolyte solutions (millimolar scale) and membrane crossover of the active materials.^{82,87,88} Recently, redox-active polymers normally used in ORBs were demonstrated to be usable in RFBs.^{79,81,89–94} These macromolecules, however, still require further development to incorporate backbone degradability to provide future RFBs with sustainability features.

Characteristics of Batteries

In a battery, two important parameters are the theoretical voltage and theoretical capacity. The theoretical voltage or cell voltage (U [V]) of a battery is the difference in (standard) potentials of the electrodes:

$$U = \text{Cathode potential} - \text{Anode potential} \quad \text{Equation 1.}$$

The theoretical capacity (C_{theo} [A·h]) is defined as the maximum electric charge that can be stored in a battery when all active materials contribute fully. A different unit of capacity is Coulomb (1 C = 1 A·s, 1 A·h = 3600 A·s). To compare different electrode materials, the specific capacity (C_{spec} [A·h·g⁻¹]) of an electrode in a secondary battery is usually provided *per* mass of active material, using the following equation:

$$\begin{aligned} C_{spec} &= \frac{n \times F}{M_w} = \frac{n \times 96485}{M_w} [\text{A} \cdot \text{s} \cdot \text{g}^{-1}] \\ &= \frac{n \times 26.801}{M_w} [\text{A} \cdot \text{h} \cdot \text{g}^{-1}] \end{aligned} \quad \text{Equation 2,}$$

where n is the number of transferred electrons *per* redox reaction, F is the Faraday constant and M_w is the molar mass of the structural unit. The specific capacity of a full secondary battery cell can be calculated as follows:

$$\frac{1}{C_{spec_{cell}}} = \frac{1}{C_{spec_{cathode}}} + \frac{1}{C_{spec_{anode}}} \quad \text{Equation 3.}$$

In a redox flow battery, the cell voltage is also calculated using **Equation 3**. The volumetric capacity of each of the anolyte and catholyte in a RFB can be calculated as follows:

$$C_{spec} = \frac{m \times n \times F}{M_w \times V} = M \times n \times F \text{ [A} \cdot \text{s} \cdot \text{L}^{-1}]$$

$$= M \times n \times 26.801 \text{ [A} \cdot \text{h} \cdot \text{L}^{-1}]$$

Equation 4,

where n is the number of transferred electrons *per* redox reaction, F is the Faraday constant, and m , M_w and M are the mass loading, molar mass and molar concentration of the structural unit, respectively. The volumetric capacity of the RFB is the same as that of the electrolyte with limiting concentration. In addition, for both systems, the coulombic efficiency (η_c [%]), the ratio of the obtained discharging and charging capacity, is calculated as follows:

$$\eta_c = \frac{C_{discharge}}{C_{charge}}$$

Equation 5.

Scope of the Dissertation

This dissertation is focused on the development of peptide-based materials for biological, energy and electronic applications, exploiting their inherent degradability and conformations to direct the properties of the polymer networks (**Figure 8**). For the biological application, PEGylated β -sheet-forming polypeptides were prepared for use as hydrogel scaffolds in 3D cell cultures (**Chapter II**). For the energy and electronic applications, simple natural amino acids were transformed into functional polypeptides that can be used as active materials in secondary and redox flow batteries (**Chapters III and IV**, respectively).

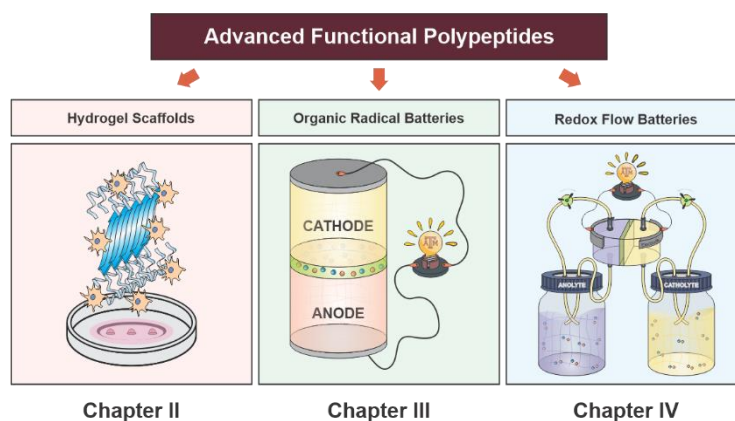


Figure 8. Summary of Ph.D. dissertation.

Three-dimensional cell cultures play an important role for a wide range of biological applications, such as tissue engineering and spinal cord injury treatment. In Chapter II, a library of thermoresponsive diblock poly(ethylene glycol)₄₅-*block*-poly(DL-allylglycine)_n (PEG₄₅-*b*-PDLAG_n) was prepared for use as extracellular matrices for cell cultures (**Figure 8**). The PEG block is essential in providing aqueous solubility while the β -sheet-forming hydrophobic PDLAG segment offers physical crosslinking *via* π - π stacking of the allyl groups on the peptide side chains to construct supramolecularly-assembled networks for gelation. The length of the PDLAG segment was varied to establish different hydrophilic-hydrophobic ratios to examine the gelation, cell encapsulation and cell viability properties of the resulting PEGylated polypeptides. Their gelation kinetics were studied in detail, utilizing a combination of rheology, Live/Dead® assay and fluorescence confocal microscopy. Rheological measurements of the polymers in cell media under physiological conditions were conducted to determine gelation times and mechanical strengths of the hydrogels formed. As a demonstration of cell encapsulation capability, mouse fibroblast cells were cultivated in polypeptide hydrogels

without mineralization or pH adjustment. The effect of the polypeptide hydrogels on cell viability was assessed using the Live/Dead® assay followed by fluorescence confocal microscopy to monitor cell proliferation.

Over the past few decades, lithium-ion batteries have revolutionized technologies that substantially impact the global health, wealth and well-being of society, enabling the proliferation of portable devices and electric vehicles. However, this rapid technology growth has exceeded the ability to address issues associated with the ethical and environmental challenges of mining lithium, cobalt and other mineral ore resources, their safe usage, and their non-hazardous disposal, requiring alternative innovative approaches to harness the potential of organic-based electroactive materials. In **Chapter III**, an all-polypeptide-based secondary battery is demonstrated, in which redox-active viologens and nitroxide radicals are incorporated as redox-active groups along polypeptide backbones to function as anode and cathode materials, respectively (**Figure 8**). These polypeptides perform as stable active materials during battery operation, and subsequently degrade on-demand in acidic conditions to generate amino acids, other building blocks and degradation products. In addition, the high solubility of the viologen- and nitroxide radical-containing polypeptides in organic solvents made them promising candidates for NAORFBs. In **Chapter IV**, an NAORFB was assembled with viologen polypeptide anolyte and biTEMPO polypeptide catholyte reservoirs separated by an anion exchange membrane (**Figure 8**). Together with the secondary battery counterpart, this all-polypeptide-based redox flow battery aims to address the need for alternative chemistries for green and sustainable batteries in the future circular economy.

CHAPTER II

POLYPEPTIDE HYDROGEL SCAFFOLDS FOR CELL THERAPEUTICS

Introduction

Extracellular matrix (ECM) is a complex fibrous network that provides bioactivity and mechanical support for cells in three-dimensional (3D) environments.^{95,96} However, current understanding about cell-matrix interactions relies on traditional two-dimensional (2D) cultures, where cells are grown as monolayers on flat stiff substrates (*e.g.*, glass or plastic), where cells are cultivated in unnatural environments with homogeneous concentration of nutrients and growth factors. Such surfaces do not accurately resemble the physiological condition and architecture of native ECMs, affecting cellular processes and yielding flat and elongated morphologies.⁹⁷⁻⁹⁹ Among the techniques developed for 3D cell cultures (*e.g.*, hanging drop, microfluidic, etc.),¹⁰⁰ hydrogel scaffolds constructed from supramolecular assembly of synthetic peptides have attracted significant scientific attentions due to their innate biocompatibility, feasible tunability of structure-property-performance parameters, and structural and mechanical similarity to native ECMs.¹⁰¹⁻¹⁰⁸ They provided the embedded cells with 3D spatial support for cell proliferation, porosity for cell migration, and facile transportation of nutrients and growth factors.^{101-103,109-114} Inspired by the design of peptide amphiphiles previously reported as hydrogelators for 3D cell cultures, we introduce herein the use of thermoresponsive β -sheet-forming PEGylated alkenyl-functionalized polypeptides, poly(ethylene glycol)₄₅-*block*-poly(DL-allylglycine)_n (PEG₄₅-*b*-PDLAG_n, **Figure 9**), to fabricate ECM mimics.

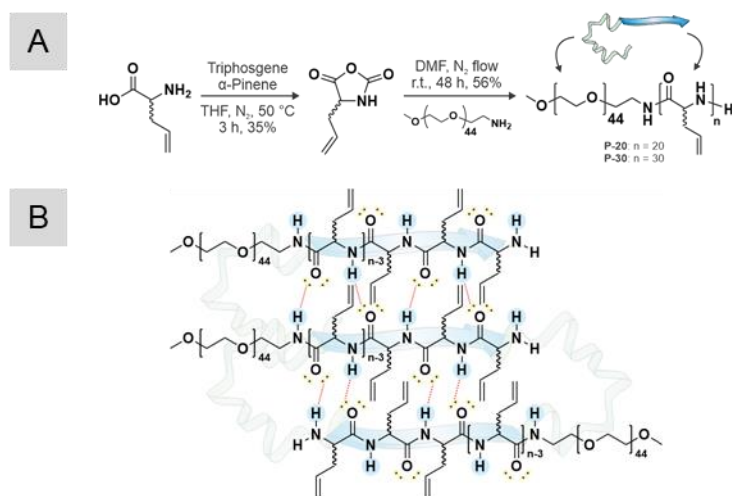


Figure 9. (A) Synthesis of PEGylated polypeptides. (B) Illustration of β -sheet formation of PEG₄₅-*b*-PDLAG_n.

Experimental Section

Materials

N,N-Dimethylformamide (DMF) and tetrahydrofuran (THF) were collected *via* the solvent purification system. Ethyl acetate, hexanes, dichloromethane (DCM), α -pinene and triphosgene were purchased from Sigma-Aldrich (USA). DL-Allylglycine (DLAG) was purchased from Carbosynth, Ltd (UK). α -Methoxy- ω -amino polyethylene glycol (mPEG₄₅-NH₂, $M_n = 2000 \text{ g}\cdot\text{mol}^{-1}$) was purchased from Rapp Polymere (Germany). All chemicals were used as received, except for mPEG₄₅-NH₂ which was dried *in vacuo* for 48 h before using. Ultrapure water (water) was collected from a Milli-Q® integral water purification system (18 M Ω ·cm). Mouse fibroblast (NIH/3T3) cells were purchased from ATCC (USA). All reagents for cell cultures were purchased from Thermo Fisher Scientific (USA) unless otherwise described.

Synthesis of PEGylated Alkenyl-functionalized Polypeptides

1. Synthesis of DL-Allylglycine N-Carboxyanhydride (DLAG NCA, 1)

Into a 250-mL three-necked round bottom flask equipped with a glass Pasteur pipette as an N₂ inlet and a condenser connected to a base trap were charged DLAG (5.2 g, 44 mmol), anhydrous THF (150 mL) and α -pinene (17 mL). The suspension was heated at 50 °C with N₂ bubbling, followed by the dropwise addition of a triphosgene solution in THF (20 mL, 1.3 mmol·mL⁻¹). **CAUTION: Phosgene and its derivatives are extremely hazardous. All manipulations must be performed using a reaction apparatus that provides for quenching phosgene released from the reaction set-up and is placed in a well-ventilated chemical fume hood with proper personal protective equipment and necessary precautions to avoid exposure.** The reaction was stirred for 3 h during which the suspension slowly became homogeneous. After cooling in an ice bath, the crude mixture was gravity-filtered into a 250-mL round bottom flask. The filtrate was then concentrated *in vacuo* using a double liquid N₂ trap system with one trap being loaded with pellet sodium hydroxide. The concentrated oil was precipitated into 1 L of hexanes. The white floating solid was collected *via* vacuum filtration and recrystallized thrice from ethyl acetate/hexanes to afford white needle-like crystals (2.15 g, 15.2 mmol, 35%). ¹H NMR (400 MHz, CDCl₃) δ 6.52 (br, 1H), 5.75 (m, 1H), 5.28 (m, 2H), 4.40 (m, 1H), 2.72-2.53 (m, 2H). ¹³C NMR (101 MHz, CDCl₃) δ 168.9, 152.5, 130.0, 121.61, 57.3, 36.0. FTIR: 3345, 3095, 3017, 2934, 1842, 1827, 1748, 1290, 926 cm⁻¹. MS (m/z): [M-H]⁻ calcd. 140.0348, found 140.0345.

2. Synthesis of Poly(ethylene glycol)₄₅-*block*-poly(DL-allylglycine)_n (PEG₄₅-*b*-PDLAG_n)

Two PEGylated polypeptides with different hydrophobic block lengths—**P-20** ($n = 20$) and **P-30** ($n = 30$) were synthesized. Shown below is the representative procedure for the synthesis of **P-30**. Inside an argon-filled glovebox, a flame-dried 250-mL Schlenk flask was charged with DLAG NCA (2.72 g, 19.3 mmol), mPEG₄₅-NH₂ (1.25 g, 616 μ mol) and DMF (150 mL). The flask was then sealed, moved to a fume hood and connected to a Schlenk line through a N₂ flowmeter with a drierite column as an N₂ outlet. The reaction was vigorously stirred under 100 mL·min⁻¹ N₂ flow at r.t. for 48 h and monitored using FTIR. When the reaction was complete, the mixture was concentrated *in vacuo*, precipitated into 500 mL ethyl ether ($\times 3$), dialyzed against nanopure H₂O for 3 d and lyophilized to obtain the polymer as a white powder (1.69 g, 56%). ¹H NMR (400 MHz, TFA-*d*) δ 5.62 (br, 22H), 5.13 (br, 44H), 4.64 (br, 22H), 3.83 (br, 183), 3.63 (s, 3H), 2.53 (br, 44H). FTIR: 3426-3149, 3079, 2871, 1697, 1627, 1515, 1103, 701 cm⁻¹. The polypeptides exhibited similar thermal characteristics with onset degradation at *ca.* 370 °C, a T_c value of *ca.* -40 °C, a T_m value of *ca.* 10 °C and a T_g value of *ca.* -60 °C.

Chemical Characterization

Attenuated total reflectance-Fourier transform infrared (ATR-FTIR) spectra were recorded for powder samples on an IR Prestige 21 system (Shimadzu Corp., Japan) and analyzed using IRsolution v. 1.40 software. ¹H and ¹³C nuclear magnetic resonance (NMR) spectra were recorded on a Bruker 400 spectrometer. Chemical shifts were

referenced to the solvent resonance signals. High resolution electrospray ionization mass spectrometry (ESI-HRMS) experiments were performed using a Thermo Scientific Q Exactive Focus (Thermo Scientific, USA) in both positive and negative mode. The sample was injected into a 10 μL loop and methanol was used as a mobile phase at a flow rate of 100 $\mu\text{L}\cdot\text{min}^{-1}$. The Q Exactive Focus HESI source was operated in full MS in positive mode. The mass resolution was tuned to 70000 FWHM at m/z 200. The spray voltage was set to 3.75 kV for positive mode and 3.3 kV for negative mode, and the sheath gas and auxiliary gas flow rates were set to 7 and 0 arbitrary units, respectively. The transfer capillary temperature was held at 250 $^{\circ}\text{C}$ and the S-Lens RF level was set at 50 V. Exactive Series 2.8 SP1/Xcalibur v. 4.0 software was used for data acquisition and processing.

Cell Cultures

All cell cultures were maintained in the cell culture incubator (37 $^{\circ}\text{C}$, 5% v/v CO_2). Fibroblast cells were maintained in Dulbecco's modified Eagle Medium (DMEM/F-12) supplemented with 10% fetal bovine serum and 1% PSA to obtain final concentrations of 100 $\text{U}\cdot\text{ml}^{-1}$ penicillin, 100 $\text{mg}\cdot\text{mL}^{-1}$ streptomycin and 0.25 $\text{mg}\cdot\text{mL}^{-1}$ amphotericin B (cell medium).

Hydrogel Preparation

For rheological measurements

The polypeptides were dried *in vacuo* for 2 h prior to hydrogel preparation. Cell medium was then added into glass vials containing glass vials containing pre-weighed

PEG₄₅-*b*-PDLAG_n to obtain the final concentrations of 1, 2, 4 and 8 % w/v. The vials were then placed in an ice bath and the mixtures homogenized by ultrasonication for 2 min in a cold room (4 °C), using a Model 150 V/T ultrasonic homogenizer from Biologics, Inc. (USA, power output: 20 W, output frequency: 20 kHz, tip diameter: 3.81 mm).

For 3D cell cultures

The polypeptides were dried under vacuum for 2 h prior to hydrogel preparation. Glass vials containing pre-weighed PEG₄₅-*b*-PDLAG₂₀ and PEG₄₅-*b*-PDLAG₃₀ were sterilized under UV irradiation in the biosafety cabinet for 1 h. Cell medium was then added into the vials to obtain a concentration of 6% w/v. The vials were then placed in an ice bath and the mixture homogenized by ultrasonication as described above. The tip was sterilized with EtOH/H₂O (70% v/v) prior to ultrasonication.

Rheological Measurements

Rheological measurements of homogenized polypeptide mixtures in cell media were determined on a TA Instruments DHR-2 rheometer using a 40-mm diameter parallel plate geometry and 500 µm gap size. All rheological tests were performed at 37 °C to mimic cell physiological temperature unless otherwise noted. Hydrogel mixtures (800 µL) were transferred onto the measuring system immediately after ultrasonication. The reported values are the average of three replicates.

- a) Strain sweep measurements: After soaking for 1 h, the storage modulus (G') and loss modulus (G'') were then measured with increasing strains ($\hat{\gamma}$) from 0.01 to 100% at $\omega = 10 \text{ rad}\cdot\text{s}^{-1}$.
- b) Frequency sweep measurements: After soaking for 1 h, the storage modulus (G') and loss modulus (G'') were measured with increasing angular frequencies (ω) from 0.1 to 100 $\text{rad}\cdot\text{s}^{-1}$ at $\hat{\gamma} = 0.2\%$.
- c) Time sweep measurements: After the mixtures were exposed to $\hat{\gamma} = 500\%$ and $\omega = 10 \text{ rad}\cdot\text{s}^{-1}$ for 1 min, the storage modulus (G') and loss modulus (G'') were measured with $\hat{\gamma} = 0.2\%$ and $\omega = 10 \text{ rad}\cdot\text{s}^{-1}$ for 1 h.
- d) Shear-thinning measurements: After the mixtures were exposed to $\hat{\gamma} = 500\%$ and $\omega = 10 \text{ rad}\cdot\text{s}^{-1}$ for 1 min, the viscosity was measured with increasing shear rates from 0.1 to 100 s^{-1} . The measurements took place at 15 °C and 25 °C.
- e) Self-healing study: After the mixtures were allowed to undergo hydrogelation for 15 min with $\gamma = 0.2\%$ and $\omega = 10 \text{ rad}\cdot\text{s}^{-1}$, the storage modulus (G') and loss modulus (G'') were measured with two alternating cycles of 15 min of $\hat{\gamma} = 0.2\%$ and $\omega = 10 \text{ rad}\cdot\text{s}^{-1}$, and 2 min of $\hat{\gamma} = 500\%$ and $\omega = 10 \text{ rad}\cdot\text{s}^{-1}$.

Thermal Analysis

Thermogravimetric analysis (TGA) was performed under N_2 atmosphere using a Mettler-Toledo model TGA 2 (Mettler-Toledo, Inc., Columbus, OH) with a heating rate of $10 \text{ }^\circ\text{C}\cdot\text{min}^{-1}$. Glass transition temperatures (T_g) were measured by differential scanning

calorimetry (DSC) on a Mettler-Toledo DSC 3®. The samples were ramped from -80 °C to 150 °C with a heating rate of 5 °C·min⁻¹. All thermal measurements were analyzed using Mettler-Toledo STARe v. 7.01 software. The T_g was taken as the inflection point of the second heating cycle.

Hydrogel 3D Cell Culture

Homogenized polypeptide solutions in cell medium were stored at 4 °C immediately after ultrasonication until mixed with cells. Cells were trypsinized and centrifuged at 100 × g for 5 min and resuspended in cell medium. A mixture of cells at 1.0 × 10⁶ cells·mL⁻¹ was mixed with the cold homogenized polypeptide solution to obtain the final polypeptide concentration of 4% w/v. Cells were gently mixed with the polymer solution and small droplets (*ca.* 10 μL) of the cell mixture with the polymer were plated on 35-mm glass bottom dishes from MatTek (USA). The hydrogel droplets were allowed to form in the cell culture incubator for 1 h, followed by the addition of cell medium. Cell viability was measured after 1 h, 5 d and 1 week. The cell medium was changed every 2 d.

Cell Viability Determination

Live/Dead® cell viability assays for mammalian cells were purchased from Thermo Fisher (USA) and used as described on the manufacturer protocol. The Live/Dead® reagent was prepared by mixing 1 μL of Calcein AM and 4 μL of ethidium homodimer-1 (EthD-1) into 1 mL of Dulbecco's phosphate buffered saline (DPBS).

Calcein AM (ex/em: 495 nm/515 nm) induces green fluorescence in live cells, while EthD-1 (ex/em: 495 nm/635 nm) is excluded by the membrane of live cells and only emits red fluorescence in dead cells. Cell medium was aspirated and the hydrogel droplets were incubated with the Live/Dead® reagents at r.t. for 30 min prior to confocal imaging. Cell fluorescence was imaged using a laser scanning confocal microscope (Olympus FV 1000) with 10× objective or 20× objective combined with 2× zoom (40× magnification equivalent). Mosaic images were acquired with the Multi Area Time Lapse function of Olympus FV 1000. The image size *per* pixel was 2.48 μm/pixel for the images acquired with 10x objective at 512 x by 512 pixels.

ImageJ software was used to count cells numbers in green channel and red channel separately. After converting each image to 8-bit, the cell numbers in each channel were counted with the Particle Analysis Plugins with Max Entropy or Otsu threshold. Cell viability was calculated from the number of green cells over the total number of green and red cells. The calculated viability of cells in **P-20-4%** and **P-30-4%** hydrogels were 97±2% and 96±3%, respectively. The average size of cells was calculated from the overall fluorescence area divided by the number of cells in green channel. Because of the high viability (> 95%) and significantly larger area of green fluorescence compared to red fluorescence in cells, it is reasonable to estimate the average cell size from the green fluorescence images.

Results and Discussion

Synthesis of PEGylated Alkenyl-functionalized Polypeptides

The PEGylated polypeptides were prepared *via* ring-opening polymerization of DLAG NCA by amine-functionalized PEG. As previously reported, the alkenyl-functionalized amino acid, DLAG, was cyclized *via in situ* phosgenation to produce the corresponding NCA monomer.^{5,50,115} Subsequent ring-opening polymerization of DLAG NCAs with PEGylated amines afforded PEG₄₅-*b*-PDLAG_n with varying polypeptide block lengths (**Figure 9A**).⁵ The PEG block is essential in providing aqueous solubility while the β -sheet-forming hydrophobic PDLAG segment offers physical crosslinking *via* π - π stacking of the allyl groups on the polypeptide side chains to construct supramolecularly-assembled networks for gelation (**Figure 9B**). Two polymers, **P-20** and **P-30**, with varying PDLAG segment lengths ($n = 20$ and 30 , respectively), were synthesized to establish different solvophilic-solvophobic ratios to examine the gelation behavior, cell encapsulation and cell viability of the resulting PEGylated polypeptides.

The degrees of polymerization of the PEGylated polypeptides were determined by ¹H NMR spectroscopy by comparison of the intensities of methylene proton resonances of the PEG chain at *ca.* 3.5 ppm with the intensities of DLAG methine proton at *ca.* 5.7 ppm, or the alkenyl protons at *ca.* 5.0 ppm, or the methylene protons at *ca.* 2.3 ppm (**Appendix Figure 3**). Due to gelation in most organic solvents, size exclusion chromatography was not employed to determine the dispersity of the polymers.

The secondary structure of the polymers both in their pristine form and as cryogels from 4% w/v solution in water and cell medium was studied with attenuated total

reflection-Fourier transform infrared (ATR-FTIR) spectra (**Appendix Figure 1**). **P-20** and **P-30** exhibited similar β -sheet secondary structure in all tested forms. Representative FTIR spectra of **P-30** cryogels suggested that the nutrients and growth factors in the cell medium did not affect the conformation of the polypeptides.

Rheological Measurements

Direct loading of cells during hydrogelation is considered one of the most effective ways for cell encapsulation. In this manner, the polypeptides are required to assemble into crosslinked networks in a relatively short period of time (within 1 h) with reasonable strength (≥ 100 Pa) to ensure homogenous distribution of the embedded cells. From each of the synthesized polymers, four pre-gel solutions with varying concentrations (1, 2, 4 and 8% w/v) were prepared *via* homogenization in cell media at 4 °C using ultrasonication. By using vial tilting method, hydrogelation did not readily occur after homogenization for all mixtures prepared. To evaluate the suitability of the hydrogels for 3D cell cultures, their rheological viscoelasticity was measured after 1 h of incubation at physiological temperature (**Figure 10** and **Appendix Figure 4** to **Appendix Figure 10**). Due to the hygroscopic nature of PEGylated polymers, the polypeptides were extensively dried *in vacuo* and immediately used for the preparation of pre-gel solutions to prevent potential impact of excessive water content. All rheology measurements were conducted at 37 °C unless otherwise specified.

First, strain sweep and frequency sweep tests were conducted to determine gel formations, and to measure linear-viscoelastic (LVE) regions and mechanical strengths of

the prepared hydrogel mixtures (**Figure 10** and **Appendix Figure 4** to **Appendix Figure 10**). Immediately after homogenization at 4 °C, the pre-gel solutions were allowed to undergo hydrogelation on the rheology stage for 1 h prior to strain sweep and frequency sweep measurements. Water was added around the outer edge of the Peltier plate and the solvent trap was placed over the geometry to prevent hydrogel dehydration during incubation and data acquisition.

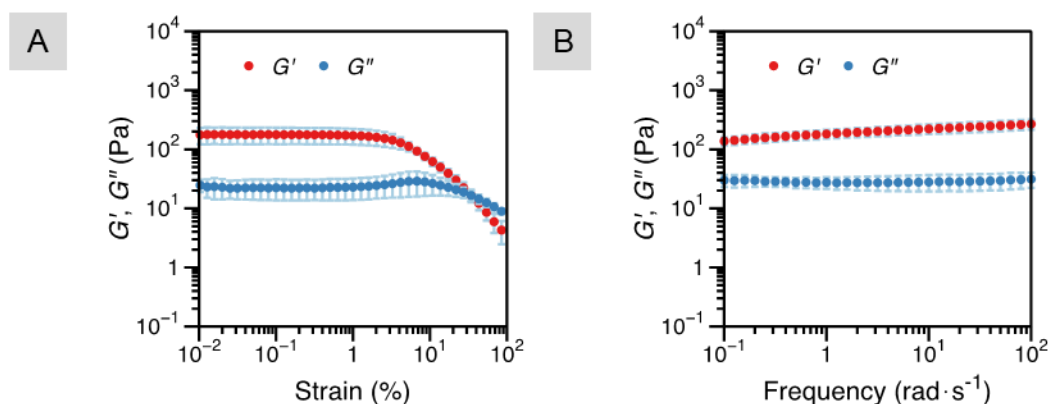


Figure 10. (A) Strain sweep ($T = 37\text{ }^{\circ}\text{C}$, $\omega = 10\text{ rad}\cdot\text{s}^{-1}$) and (B) frequency sweep tests ($T = 37\text{ }^{\circ}\text{C}$, $\hat{\gamma} = 0.2\%$) of **P-30-4%** hydrogels.

Hydrogels typically have storage moduli (G') that exceed loss moduli (G''). With the strain sweep measurements collected at an angular frequency of $10\text{ rad}\cdot\text{s}^{-1}$, **P-20** formed weak gels at 4 and 8% w/v (21 and 30 Pa, respectively) while remaining as liquids at lower concentrations ($< 10\text{ Pa}$) (**Appendix Figure 4** to **Appendix Figure 7**). **P-30**, on the contrary, afforded self-supporting hydrogels at 4 and 8% w/v ($> 100\text{ Pa}$) (**Figure 10** and **Appendix Figure 10**) while remaining in liquid phase at lower densities (**Appendix Figure 8** and **Appendix Figure 9**). These observations were confirmed by the frequency

sweep tests (**Appendix Figure 4** to **Appendix Figure 9**), conducted using 0.2 % strain. The mechanical strengths, reported as the first G' values of strain sweep measurements, of the **P-20** and **P-30** hydrogels prepared are summarized in **Figure 11**.

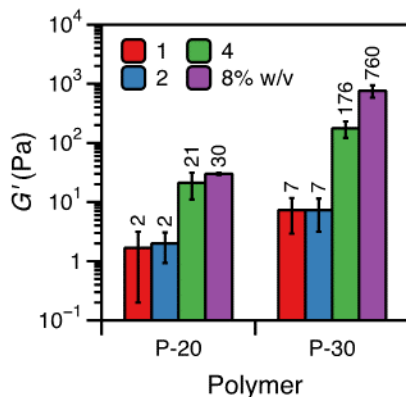


Figure 11. Mechanical strengths of **P-20** and **P-30** hydrogels studied.

Even though high polymer contents in hydrogels provide stronger 3D spatial support for the cells, the resulting dense matrices could inhibit cell proliferation and limit transportation of nutrients and growth factors, thus result in cell apoptosis. As a result, hydrogels containing 8% w/v of **P-30** were considered too dense for 3D cell cultures. Since low concentrations of **P-20** (1, 2 and 4% w/v) and **P-30** hydrogels (1 and 2% w/v) did not afford self-supporting strengths within 1 h, they were deemed inadequate for use as ECMs. To this end, hydrogels containing 4% w/v of **P-30** (**P-30-4%**) were selected for further rheology studies and to construct hydrogel 3D cell cultures.

Oscillatory time sweep of the **P-30-4%** hydrogel was measured to further study its gel formation kinetics (**Figure 12A**). The **P-30-4%** pre-gel solution was pipetted on the rheology stage immediately after homogenization at 4 °C, and the storage and loss moduli

were recorded over 1 h at 37 °C with $\hat{\gamma} = 0.2\%$ and $\omega = 10 \text{ rad}\cdot\text{s}^{-1}$. The G' values were higher than G'' at all times, once again confirming gel-like rheological behaviors of the **P-30-4%** hydrogel (**Figure 12A**). The hydrogel reached a self-supporting strength of *ca.* 100 Pa within 10 min of incubation and reached a stiffness of *ca.* 180 Pa after 60 min.

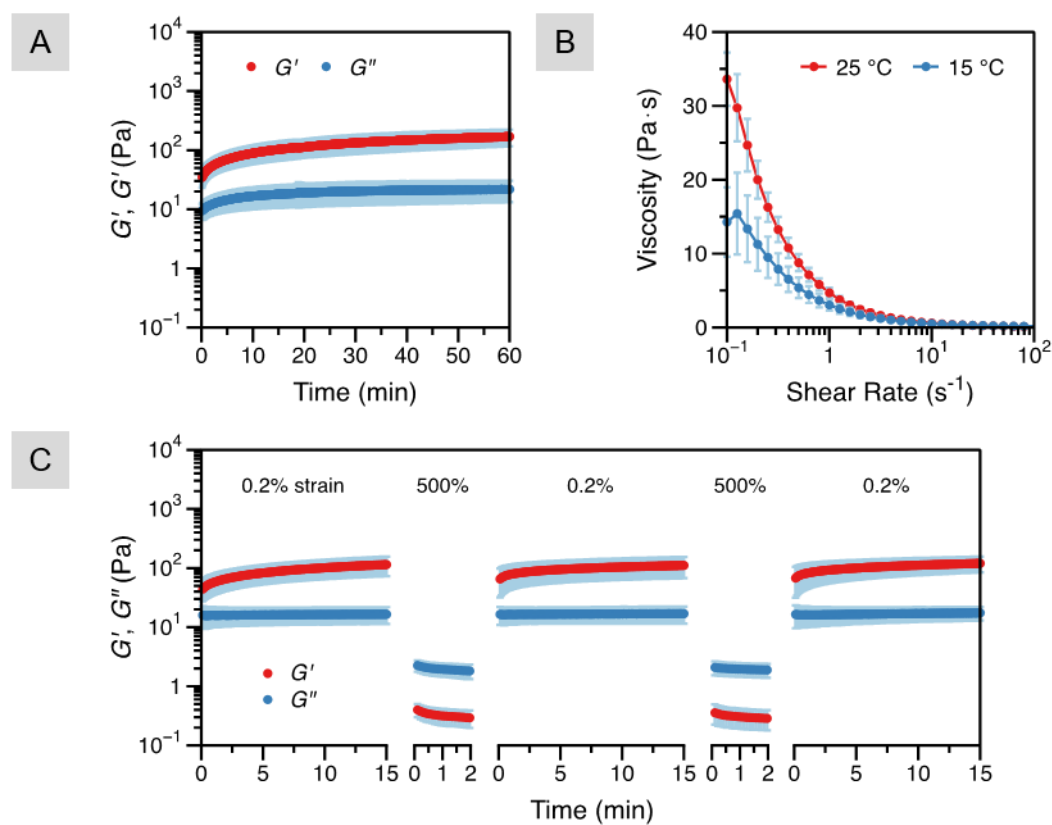


Figure 12. (A) Time sweep ($T = 37 \text{ }^\circ\text{C}$, $\hat{\gamma} = 0.2\%$, $\omega = 10 \text{ rad}\cdot\text{s}^{-1}$), (B) shear-thinning and (C) self-healing ($T = 37 \text{ }^\circ\text{C}$, $\hat{\gamma} = 0.2\%$, $\omega = 10 \text{ rad}\cdot\text{s}^{-1}$) measurements **P-30-4%** hydrogels.

The injectability and self-healing property of the **P-30-4%** hydrogels were then studied to assess their suitability for cell delivery. First, the injectability of the **P-30-4%**

pre-gel solutions was evaluated with shear thinning and at 15 and 25 °C. Their viscosity of the pre-gel solutions was measured with increasing shear rate, immediately after homogenization, reaching *ca.* 3 and 5 Pa·s at 5 s⁻¹ at 15 and 25 °C, respectively (**Figure 12B**). Such shear thinning indicates that the hydrogels are injectable at both temperatures investigated as confirmed practically by plating the pre-gel solutions as small droplets *via* 10 µL pipet tips. Next, to assess the ability of the hydrogels to reassemble after exposure to disruption, time sweep measurements were conducted with repeated intervals of gelation-disruption. The hydrogels were allowed to form with $\gamma = 0.2\%$ and $\omega = 10 \text{ rad}\cdot\text{s}^{-1}$, followed by 2 cycles of high strain (500%) for 15 min and low strain (0.2%) for 2 min. **Figure 12C** suggested that the hydrogels were liquefied ($G'' > G'$) when exposed to high strain and managed to recover to their original gel strengths at the end of each cycle.

3D Cell Cultures

The 3D cell culture matrices were prepared by directly adding mixtures of mouse fibroblast (NIH/3T3) cells into the polypeptide pre-gel solutions (1/1 v/v). In addition to **P-30-4%**, hydrogels containing 4% w/v **P-20 (P-20-4%)** were also fabricated as a control to compare weak and strong scaffolds and their effects on cell viability and proliferation. Small droplets of the cell-polypeptide mixtures were then plated on glass bottom dishes (**Figure 13**), allowed to undergo hydrogelation in a 5% CO₂ incubator at 37 °C, and periodically maintained by refreshing cell culture medium. The cells were expected to distribute homogeneously and grow in 3D within the hydrogel architecture.

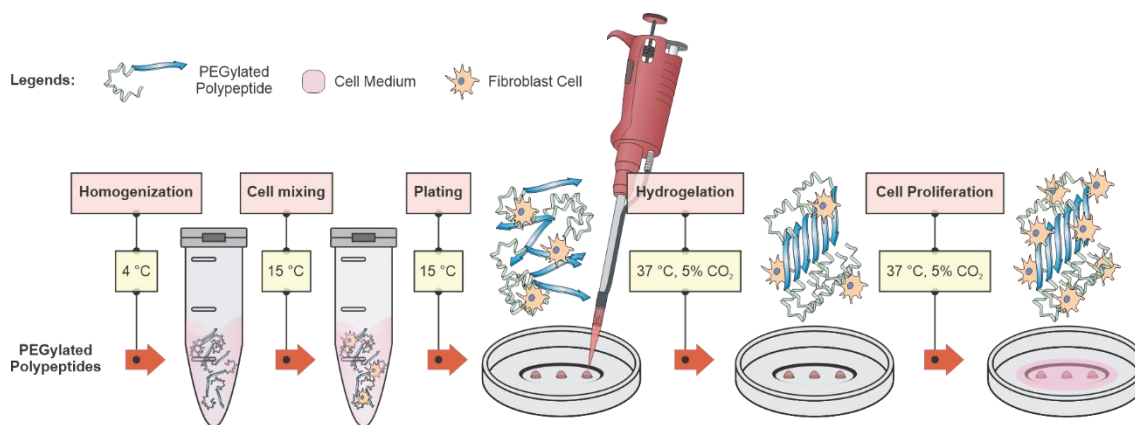


Figure 13. Preparation of hydrogel 3D cell cultures.

To examine cell viability, the **P-20-4%** and **P-30-4%** hydrogel droplets were stained with Live/Dead® reagents, calcein AM and ethidium homodimer (EthD-1) after 1 h, 5 d and 7 d of cultivation, and observed with fluorescence confocal microscopy. Calcein AM is a membrane-permeable non-fluorescence acetomethoxy derivative of calcein—a green fluorescence dye. Its selective permeability in live cells allows it to penetrate the cells’ membranes into cytoplasm where it is hydrolyzed by esterase into calceins that bind to intracellular calcium and give out strong green fluorescence. Dead cells lacking active esterase cannot hydrolyze calcein AM and or be detected by green fluorescence. EthD-1 is a membrane-impermeable fluorescence dye. After cells die, their plasma membranes are disrupted, allowing EthD-1 to enter their intracellular fluid and emit strong red fluorescence upon binding to nucleic acids. As a result, green fluorescence is detected only from viable cells and red fluorescence only from dead cells.

Fluorescence images provided evidence for the viable environments of the **P-20-4%** and **P-30-4%** hydrogels (**Figure 14**). Due to the fragility of the **P-20-4%** matrices,

most plated hydrogel droplets were disintegrated into small patches during media changes. As a result, it was impossible to image the individual droplets at early time points. The cultures were allowed to incubate for 7 d with media refreshment every 2 d. Fluorescence images of the **P-20-4%** hydrogels after 7 d showed a layer of cells with high viability (**Figure 14A**), extending from the remaining hydrogel patches to the surrounding glass substrate. The **P-30-4%** droplets were, on the contrary, able to form self-supporting hydrogels after 1 h and maintain their initial shapes over subsequent media changes. Fluorescence images of the **P-30-4%** hydrogels after 1 h showed that the live cells resided around the edge of the droplets with more dead cells concentrated towards the center (**Figure 14B**). It is hypothesized that the abrupt change in the environment stiffness lead to more cell apoptosis at the center of the droplets, compared to at the edge, where the cells were exposed to lower gel density. Over the following 5 d, the cells adapted to the matrix environment, proliferated and occupied the entirety of the droplets with very minimal cell death. At day 7, the cells continued to grow outward and escaped to the outside environment. Similar to **P-20-4%**, fluorescence images of the **P-30-4%** cultures also showed an extended layer of cells, with the gel areas significantly spread out compared to the droplets at 1 h and 5 d. This suggested that as the cells overgrew to the outer environments, they broke the gels, carried the small patches onto the surrounding glass substrate and continued to proliferate. Cell counting of the two hydrogel cell cultures after 7 d confirmed that the two PEGylated polypeptides investigated indeed

supported cell viability with *ca.* 100% live cell ratio in all areas counted (**Appendix Figure 16A**).

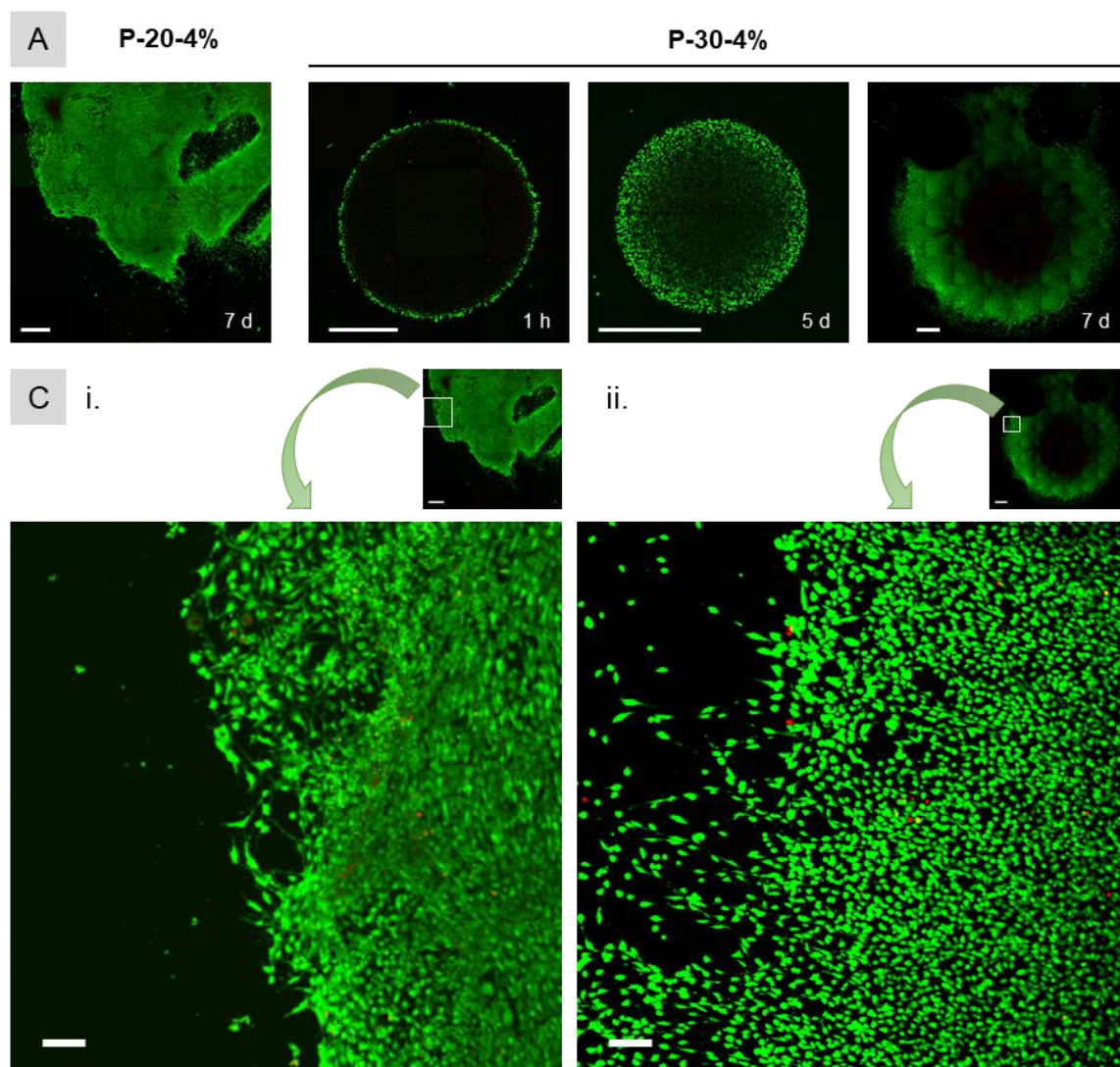


Figure 14. Fluorescence images (10 \times) of (A) the P-20-4% hydrogel after 7 d, and (B) the P-30-4% hydrogel after 1 d, 5 d and 7 d (Scale bars = 1 mm). (C) Fluorescence images (10 \times) of marked locations on i. P-20-4% and ii. P-30-4% hydrogels (Scale bars = 100 μ m).

Even though the hydrogels formed from two polymers with different lengths of the hydrophobic segment exhibited different physical properties, the cells afforded similar morphological structures in both of the gels after 1 week of incubation. In both networks, the cells afforded spherical shapes when surrounded by hydrogel and formed elongated shape after escaping from the hydrogel and proliferating on a hard glass surface, with the average cell areas decreasing with increased number of live cells (**Appendix Figure 16B**). Such plasticity showed consistent results with the literature where cells cultured on stiff surfaces tended to have flattened shapes.¹¹⁶⁻¹¹⁸

Conclusion

In conclusion, we reported in this study the use of amphiphilic PEGylated alkenyl-functionalized polypeptides, PEG₄₅-*b*-PDLA_{G_n}, as hydrogelators for encapsulation of fibroblast cells. Rheological measurements suggested that the optimal polypeptide for hydrogelation was PEG₄₅-*b*-PDLA_{G₃₀}, which formed stable hydrogels at 4% w/v (**P-30-4%**) within 1 h of incubation at physiological temperature without the need for mineralization or pH adjustment. Advantageously, **P-30-4%** did not form hydrogels at lower temperatures (15 and 25 °C), allowing for the delivery of the pre-gel materials *via* pipetting or injection. Mouse fibroblast cells were encapsulated during hydrogelation simply by adding the polypeptide pre-gel solution in cell medium to cell suspension. Fluorescence images showed that the cells cultured in **P-30-4%** hydrogels had high viability with no significant apoptosis observed after 7 d. Images with higher magnification revealed that the embedded cells adapted to the environment with different

phenotypes (spherical *vs.* elongated) depending on their corresponding location on the gels (gel areas *vs.* glass substrates, respectively).

CHAPTER III

POLYPEPTIDE ORGANIC RADICAL BATTERIES

Introduction

Organic radical batteries (ORBs) promise increased environmental friendliness, independence from limited inorganic resources and fast charging rates as compared to their lithium-ion battery counterparts.^{55,56,64,67,74,119–121} However, a key global challenge, even with the beneficial aspects of organic polymer materials, is the conscientious design of functional plastics with an end-of-life consideration.¹²² Indeed, the most-studied active materials in ORBs are polymers that carry redox-active pendant groups, such as 2,2,6,6-tetramethyl-4-piperidine-1-oxyl (TEMPO) and 4,4'-bipyridine derivatives (viologen),^{65,66,72,73,122,123} along non-degradable, aliphatic backbones.^{70,73} Although few studies have investigated redox-active degradable polymers and others have explored fully polymeric batteries (**Table 1**),^{67,74,75,124–127} none have combined these two concepts to create fully polymeric batteries that degrade on-demand, which is a first step in the future design of sustainable, recyclable batteries.^{67,74,75,124,125,127} Therefore, we hypothesized that redox-active pendant groups along a polypeptide backbone might provide a suitable materials platform for degradable organic radical batteries.⁷⁶

Here, we report an on-demand degradable, polypeptide-based battery (**Figure 15**). Anodic and cathodic polypeptides containing redox-active pendant groups were designed and synthesized, their redox activities were determined, and their behaviors in all-polypeptide batteries were established. Initially, each polypeptide was assembled into a

Table 1. Performance of polymer-based batteries.

Anode	Cathode	Output Potential (V)	C _{spec} (mA·h·g ⁻¹) [*]	E _{spec} (mW·h·g ⁻¹)	Degradable
Poly(vinylidenebenzothienophenesulfone)	Poly(TEMPO methacrylate)	2.6	~200 ^b	541	No
Viologen Polypeptide	BiTEMPO Polypeptide	1.3 and 1.6	33	56 [‡]	Yes
Polyviologen hydrogel	Poly(TEMPO acrylamide)	1.1 and 1.5	165	248 [‡]	No
Poly(2-Methacrylamide-TCAQ)	Poly(2-vinylthianthrene)	1.3	105	137 [‡]	No
Poly(antraquinone-substituted ethyleneimine)	Poly(TEMPO acrylamide)	1.1	80	88 [‡]	No
Poly(viologen dibromide)	Poly(TEMPO acrylamide)	1.2	~100 [†]	120	No
Poly(galvinoxylstyrene)	Poly(TEMPO-substituted norbornene)	0.7	32	22 [‡]	No
Poly(nitronylnitroxylstyrene)	Poly(galvinoxylstyrene)	0.6	29	17 [‡]	No

TCAQ = 11,11,12,12-Tetracyano-9,10-anthraquinonedimethane

^{*} Value taken from first charge/discharge cycle.[†] The value was not provided in text but estimated from graph.[‡] Value calculated by multiplying specific capacity by output voltage (largest voltage if two are listed).

lithium metal half-cell battery to elucidate their respective fundamental energy storage characteristics. Then, we constructed a fully polypeptide-based battery. As a demonstration of recyclability, hydrolytic degradation was conducted under acidic conditions with determination of the degradation products. In addition, effects of the intact redox-active polypeptides and their degradation products on viabilities of three different cell types were quantified. By merging degradable polypeptide backbones with the energy storage properties of the redox-active moieties, this bioinspired polypeptide-based battery begins to address the challenges of conventional lithium-ion batteries (*e.g.*, use of scarce resources, safety concerns, high carbon emissions, and high-cost recycling).

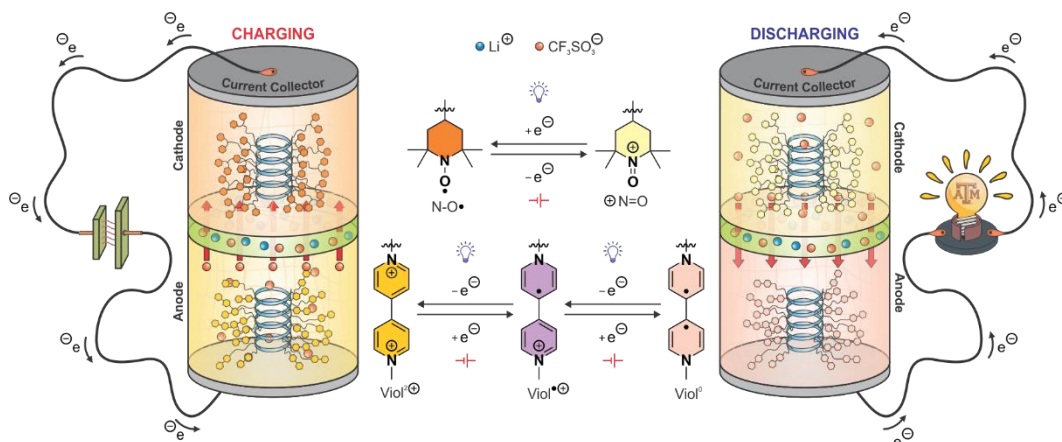


Figure 15. Schematic design of polypeptide-based organic radical battery during charging (*left*) and discharging (*right*) processes.

Experimental Section

Materials

1. For Chemical Processes

Acetonitrile (ACN), 3,3-dithiodipropionic acid, 4,4'-dipyridine, *meta*-chloroperoxybenzoic acid (*m*-CPBA, $\leq 77\%$), dichloromethane (DCM), *N,N'*-dicyclohexylcarbodiimide (DCC), 4-dimethylaminopyridine (DMAP), 2,2-dimethoxy-2-phenylacetophenone (DMPA) *N,N*-dimethylformamide (DMF), dimethylsulfoxide (DMSO), 4-hydroxy-2,2,6,6-tetramethylpiperidine-1-oxyl (4-OH-TEMPO, TEMPOL), diphosgene, hexanes, *n*-hexylamine, hydrocinnamic acid, iodomethane, iron (II) sulfate heptahydrate ($\text{FeSO}_4 \cdot 7\text{H}_2\text{O}$), L-glutamic acid, methanol, propargyl alcohol, sodium iodide (NaI), triethylamine (TEA), trifluoroethanol (TFE), trimethylsilyl chloride (TMSCl) and triphosgene were purchased from Sigma-Aldrich (USA). DL-Dithiothreitol (DTT) was purchased from Tokyo Chemical Industry. 6-Chloro-1-hexanol and acetic anhydride were purchased from Alfa-Aesar (USA). All reagents were used as received, except for

propargyl alcohol, which was distilled under an atmosphere of N₂ prior to use. Ultrapure water (water) was collected from a Milli-Q® integral water purification system (18 MΩ·cm).

2. For Electrochemical Processes

Lithium triflate (LiCF₃SO₃), methanol, *N*-methyl-2-pyrrolidinone (NMP), propylene carbonate (PC) and poly(acrylic acid) (PAA, $M_v \sim 4,000,000 \text{ g}\cdot\text{mol}^{-1}$) were purchased from Sigma-Aldrich (USA). DCM and chloroform were purchased from VWR (USA). Super P® Carbon Black (CB) was purchased from TIMCAL Graphite & Carbon. Vapor-grown carbon fiber (VGCF) was purchased from Showa Denko K.K. (Japan). Polyvinylidene fluoride (PVDF, MW = 600,000 g·mol⁻¹) was purchased from MTI Corp. (USA). ITO-coated glass substrates (ITO-coated glasses) were purchased from Delta Technologies (USA), and cleaned by subsequent sonication in soap water, water, acetone and isopropyl alcohol, followed by drying with N₂ and ozone plasma treatment for 10 min. Lithium metal was purchased from Alfa-Aesar (USA).

Synthesis of Viologen Polypeptides

1. Synthesis of 1-Methyl-4,4'-bipyridylium Iodide (MBPI, 2)

A solution of 4,4'-bipyridine (9.2 g, 59 mmol) and methyl iodide (4.5 mL, 72 mmol) in dichloromethane was stirred while being heated at reflux for 2 h. After the mixture was allowed to cool to r.t., the precipitate was collected *via* filtration, washed twice with diethyl ether and recrystallized from methanol/diethyl ether at -20 °C to provide

2 as a yellow solid (16.7 g, 56.0 mmol, 95%). ^1H NMR (400 MHz, DMSO- d_6 , ppm) δ 9.14 (d, 2H, $J = 8$ Hz), 8.87 (d, 2H, $J = 4$ Hz), 8.62 (d, 2H, $J = 4$ Hz), 8.05 (d, 2H, $J = 8$ Hz), 4.39 (s, 3H). ^{13}C NMR (101 MHz, DMSO- d_6 , ppm) δ 151.81, 150.98, 146.12, 140.80, 124.91, 121.82, 47.56. FTIR: 3150-2850, 3022, 1649, 1599, 1547, 1495, 1416, 1333, 1283, 1221, 1192, 995, 810, 712 cm^{-1} . MS (m/z) $[\text{M}]^+$ calcd. 171.0917, found 171.0913.

2. Synthesis of (6-Chlorohexyl)-L-Glutamate (CHLG, **3**)

6-Chloro-1-hexanol (15 mL, 0.11 mol) and tetrahydrofuran (15 mL) were added to a 250-mL round bottom flask charged with L-glutamic acid (10.1 g, 68.6 mmol). The mixture was cooled in an ice bath, followed by dropwise addition of sulfuric acid (4 mL). After warming to r.t., the reaction was allowed to continue for 24 h. Afterwards, ice-cold saturated aqueous sodium bicarbonate solution was slowly added to the reaction mixture. The product started to precipitate when the pH reached *ca.* 7 (monitored with pH paper). The crude product was collected *via* filtration, dissolved in water/isopropanol (100 mL, 2/8 v/v) at 50 °C and recrystallized at 4 °C to afford **3** as a white solid (15.2 g, 51.0 mmol, 83%). ^1H NMR (400 MHz, DMSO- d_6 /TFA- d , 2/1 v/v, ppm) δ 3.85 (t, 2H, $J = 6.5$ Hz), 3.78 (m, 1H), 3.42 (t, 2H, $J = 6.5$ Hz), 2.43-2.20 (m, 2H), 1.90 (m, 2H), 1.54 (quint, 2H, $J_{12} = 6.7$ Hz, $J_{23} = 7.0$ Hz), 1.41 (quint, 2H, $J_{12} = 6.7$ Hz, $J_{23} = 7.0$ Hz), 1.23-1.15 (m, 4H). ^{13}C NMR (101 MHz, DMSO- d_6 /TFA- d , 2/1 v/v, ppm) δ 172.06, 170.86, 64.35, 51.52, 45.42, 32.25, 29.49, 28.25, 26.23, 24.96. FTIR: 3250-2400, 3179, 3000-2500, 1742, 1726,

1612, 1584, 1557, 1501, 1416, 1356, 1319, 1265, 1182, 1148, 1090, 1049, 974, 929, 881, 829, 802, 758, 714, 648 cm^{-1} . MS (m/z) $[\text{M}+\text{H}]^+$ calcd. 266.1159, found 266.1163.

3. Synthesis of (6-Chlorohexyl)-L-Glutamate N-Carboxyanhydride (CHLG NCA, **4**)

Inside an argon-filled glovebox, a 50-mL Schlenk flask was charged with **3** (4.9 g, 18 mmol) and anhydrous tetrahydrofuran (100 mL). The flask was then sealed, moved to a fume hood and placed under N_2 atmosphere, followed by dropwise addition of diphosgene (1.2 mL, 9.9 mmol). To protect the Schlenk lines from contamination during phosgenation reaction, a column charged with pellet sodium hydroxide was utilized to connect the Schlenk line and flask. **CAUTION: Phosgene and its derivatives are extremely hazardous. All manipulations must be performed using a reaction apparatus that provides for quenching phosgene released from the reaction set-up and is placed in a well-ventilated chemical fume hood with proper personal protective equipment and necessary precautions to avoid exposure.** After 24 h of reaction at r.t., the solvent was removed *in vacuo* using a double liquid nitrogen trap system where one trap was loaded with pellet sodium hydroxide. The concentrated oil was dissolved into ethyl acetate (50 mL) and washed with ice-cold aqueous media (water, saturated sodium bicarbonate $\times 2$, brine and water, 50 mL each). The organic layer was dried over MgSO_4 , concentrated and precipitated against hexanes ($\times 3$) to afford **4** as a yellow oil. The actual mass of **4** was calculated by subtracting the mass of residual ethyl acetate from that of the collected oil, resulting in a yield of 3.6 g (12 mmol, 66%). The mole ratio between **4** and ethyl acetate was calculated from ^1H NMR. ^1H NMR (400 MHz,

CDCl₃, ppm) δ 6.48 (s, 1H), 4.41 (t, 1H, $J = 4.8$ Hz), 4.11 (t, 2H, $J = 5.3$ Hz), 3.54 (t, 2H, $J = 5.3$ Hz), 2.55 (t, 2H, $J = 5.3$ Hz), 2.27-2.10 (m, 2H), 1.78 (quint, 2H, $J_{12} = 5.4$ Hz, $J_{23} = 5.6$ Hz), 1.66 (quint, 2H, $J_{12} = 5.4$ Hz, $J_{23} = 5.6$ Hz), 1.47 (quint, 2H, $J_{12} = 5.6$ Hz, $J_{23} = 6.8$ Hz). ¹³C NMR (101 MHz, CDCl₃, ppm) δ 172.93, 169.69, 152.02, 65.47, 57.26, 45.18, 32.58, 30.05, 28.55, 27.14, 26.61, 25.43. FTIR: 3500-3100, 2940, 2862, 1857, 1782, 1728, 1371, 1242, 1175, 1105, 1045, 916, 758, 631 cm⁻¹. MS (m/z) [M-H]⁻ calcd. 290.0801, found 290.0801.

4. Synthesis of Poly((6-Chlorohexyl)-L-Glutamate)₅₀ (PCHLG₅₀, 5)

Inside an argon-filled glovebox, a flame-dried 25-mL Schlenk flask was charged with the monomer **4** (1.7 g, 6.0 mmol), DMF (18 mL) and a solution of hexylamine (330 μ L, 0.36 mmol·mL⁻¹ in DMF, 0.12 mmol, monomer:initiator = 50:1). The reaction flask was then sealed, moved to a fume hood and connected to a Schlenk line through a N₂ flowmeter with a drierite column as an N₂ outlet. The reaction was stirred for 12 h under 100 mL·min⁻¹ N₂ flow at r.t. and monitored using FTIR. When the reaction was complete, the mixture was concentrated *in vacuo*, dissolved into DCM (10 mL) and precipitated into ice-cold methanol thrice to afford **5** as a waxy white solid (1.4 g, 91%). ¹H NMR (400 MHz, TFA-*d*, ppm) δ 4.72 (m), 4.16 (m), 3.48 (m), 2.57 (m), 2.24 (m), 2.08 (m), 1.72 (m), 1.51-1.23 (m), 0.82 (b). ¹³C NMR (101 MHz, TFA-*d*, ppm) δ 178.47, 175.60, 68.95, 55.59, 46.37, 33.97, 32.20, 29.72, 29.08, 29.05, 28.01, 26.65. FTIR: 3286, 3000-2800, 1730, 1652, 1547, 1451, 1313, 1248, 1171, 1119, 1080, 978, 799, 729, 647 cm⁻¹. The

polymer exhibited an onset degradation temperature at *ca.* 310 °C and a T_g value of *ca.* 7 °C.

5. Synthesis of Poly((6-Iodo)-L-Glutamate)₅₀ (PIHLG₅₀, **6**)

Poly((6-chlorohexyl)-L-glutamate)₅₀ (**5**, 0.83 g, 3.4 mmol) and NaI (5.1 g, 34 mmol) were added into a 250-mL round bottom flask charged with acetone (50 mL). The reaction was stirred for 3 d while being heated at reflux and monitored by ¹H NMR spectroscopy. Upon completion, the solvent was evaporated, followed by the addition of chloroform (50 mL). The chloroform solution was then stored at 4 °C for 12 h to precipitate residual NaI, which was then removed *via* gravity filtration. The filtrate was washed with ice-cold water (50 mL × 3), dried over MgSO₄ and evaporated *in vacuo* to obtain **6** as a yellow wax (0.86 g, 76%). ¹H NMR (400 MHz, CDCl₃/TFA-*d*, 2/1 v/v, ppm) δ 4.64 (m), 4.14 (m), 3.20 (m), 2.54 (m), 2.16-2.01 (m), 1.83 (b), 1.67 (b), 1.45-1.37 (m), 0.88 (b). ¹³C NMR (101 MHz, CD₃Cl₃/TFA-*d*, 2/1 v/v, ppm) δ 177.92, 175.09, 68.64, 55.23, 35.04, 32.04, 31.82, 29.79, 28.98, 26.42, 8.01. FTIR: 3283, 3000-2800, 1728, 1651, 1547, 1451, 1395, 1328, 1249, 1207, 1169, 1120, 1080, 1029, 968, 797, 723 cm⁻¹. The polymer exhibited an onset degradation temperature at *ca.* 273 °C and a T_g value of *ca.* 6 °C.

6. Synthesis of Viologen Polypeptide (**7**)

Inside an argon-filled glovebox, **6** (0.52 g, 1.5 mmol) and **1** (3.1 g, 16 mmol) were added into a 100-mL Schlenk flask charged with DMF (50 mL). The reaction was stirred

for 2 d at 70 °C under N₂ atmosphere. Upon completion, the reaction mixture was dialyzed against water for 3 d and lyophilized to obtain **7** as a reddish brown solid (0.87 g, 89%). ¹H NMR (400 MHz, D₂O, ppm) δ 9.22 (m), 9.08 (m), 8.60 (m), 8.57 (m), 4.50 (b), 4.12 (b), 2.94-1.24 (m). ¹³C NMR was attempted but also provided unassignable spectra with high signal-to-noise ratio. FTIR: 3287, 3000-2800, 1728, 1651, 1547, 1450, 1395, 1327, 1250, 1173, 1117, 1080, 980, 831, 799, 719, 646 cm⁻¹. The polymer exhibited an onset degradation temperature at *ca.* 240 °C and a *T_g* value of *ca.* 142 °C.

Synthesis of BiTEMPO Polypeptide

1. Synthesis of 1-Methoxy-2,2,6,6-tetramethylpiperidin-4-ol (MTEMPOL, **8)**

4-hydroxy-1-oxyl-2,2,6,6-tetramethylpiperidine (9.2 g, 53 mmol), ferrous sulfate heptahydrate (17.8 g, 64.0 mmol) and DMSO (200 mL) were added to a 250-mL two-neck round-bottom flask, which was equipped with a thermometer and placed in a water bath, to maintain the reaction temperature at r.t. A solution of 30% aqueous hydrogen peroxide (8.3 mL, 81 mmol) was then added dropwise over 1.5 h using a syringe pump, followed by an additional 1.5 h of reaction. Upon completion, the reaction was cooled using an ice bath, followed by the slow addition of water (150 mL) then an aqueous sodium hydroxide solution (70 mL, 2.7 mmol/mL). The mixture was stirred for 1 h and extracted DCM (200 mL × 3). The organic layers were combined, dried over MgSO₄ and concentrated to obtain a yellow liquid. Purification by flash column chromatography eluting with hexanes/ethyl acetate (9/1 v/v gradually increasing to 8/2 v/v) yielded **8** as a white solid (8.4 g, 45 mmol, 84%). ¹H NMR (400 MHz, DMSO-*d*₆, ppm) δ 4.42 (d, 1H, *J* = 4 Hz), 3.72 (m, 1H), 3.53

(s, 3H), 1.66 (d, 2H, $J = 4$, 12 Hz), 1.27 (t, 2H, $J = 12$ Hz), 1.12 (s, 6H), 1.05 (s, 6H). ^{13}C NMR (101 MHz, DMSO- d_6 , ppm) δ 64.90, 60.74, 59.46, 48.07, 32.92, 20.65. FTIR: 3500-3100, 3050-2800, 1450, 1371, 1358, 1335, 1302, 1254, 1215, 1175, 1043, 1026, 951, 895, 721, 611 cm^{-1} . MS (m/z) $[\text{M}+\text{H}]^+$ calcd. 188.1645, found 188.1644.

2. Synthesis of DiMTEMPO Disulfide (9)

A 500-mL round-bottom was charged with **8** (5.2 g, 30 mmol), 3,3'-dithiodipropionic acid (2.6 g, 12 mmol), DCC (5.7 g, 28 mmol) and DCM (200 mL). After stirring at 40 °C under reflux for 1 h, DMAP (0.30 g, 2.5 mmol) was added. The mixture was stirred for another 48 h, gravity-filtered, concentrated and purified by flash column chromatography eluting with hexanes/ethyl acetate (9/1 v/v gradually increasing to 8/2 v/v) to afford **9** as a colorless viscous oil (4.3 g, 7.9 mmol, 64%). ^1H NMR (400 MHz, DMSO- d_6 , ppm) δ 4.95 (m, 1H), 3.55 (s, 1H), 2.89 (t, 2H, $J = 4$ Hz), 2.66 (t, 2H, $J = 4$ Hz), 1.82 (d, 2H, $J = 4$, 12 Hz), 1.45 (d, 2H, $J = 12$ Hz), 1.16 (s, 6H), 1.11 (s, 6H). ^{13}C NMR (101 MHz, DMSO- d_6 , ppm) δ 170.64, 66.27, 66.05, 59.45, 43.57, 33.61, 32.92, 20.44. FTIR: 3050-2850, 1734, 1721, 1348, 1238, 1211, 1186, 1165, 1142, 1032, 997, 951, 930, 893, 827, 750, 716, 679 cm^{-1} . MS (m/z) $[\text{M}+\text{H}]^+$ calcd. 549.3027, found 549.3022.

3. Synthesis of Thio-MTEMPO (10)

A 5-mL round bottom flask equipped was charged with **9** (3.9 g, 7.1 mmol), DTT (2.2 g, 14 mmol) and DCM (1 mL). The reaction mixture was bubbled with N_2 for 1 h,

followed by the addition of TEA (4 mL, 29 mmol). After stirring for 24 h, the crude product was washed with 1 M HCl (100 mL \times 2) and brine (100 mL). The organic layer was dried over MgSO₄, filtered, concentrated and purified by flash column chromatography eluting with DCM to afford **10** as a colorless liquid (3.5 g, 13 mmol, 90%). ¹H NMR (400 MHz, DMSO-*d*₆, ppm) δ 4.95 (m, 1H), 3.55 (s, 1H), 2.64 (m, 2H), 2.57 (m, 2H), 2.44 (t, 1H, *J* = 8 Hz) 1.82 (dd, 2H, *J* = 4, 12 Hz), 1.45 (t, 2H, *J* = 12 Hz), 1.16 (s, 6H), 1.11 (s, 6H). ¹³C NMR (101 MHz, DMSO-*d*₆, ppm) δ 170.79, 66.09, 65.04, 59.46, 43.60, 38.07, 32.62, 20.45, 19.25. FTIR: 3050-2750, 1730, 1470, 1429, 1360, 1306, 1242, 1175, 1038, 1001, 955, 883, 837, 719 cm⁻¹. MS (m/z) [M+H]⁺ calcd. 276.1628, found 276.1625.

4. Synthesis of γ -Propargyl-L-Glutamate Hydrochloride (PLG HCl, **11**)

In a 1-L round bottom flask, L-glutamic acid (10.8 g, 73.4 mmol) was suspended in distilled propargyl alcohol (400 mL, 7 mol) under N₂ for 1 h at r.t., followed by the dropwise addition of TMSCl (30 mL, 0.2 mol) over 1 h. The suspension was stirred until it became homogeneous (*ca.* 36 h). The resulting solution was then precipitated into diethyl ether (1.5 L) and the crude product was collected *via* vacuum filtration. The obtained solid was dissolved in MeOH (200 mL), filtered and precipitated into diethyl ether (1.5 L). The precipitate was collected *via* vacuum filtration, washed with diethyl ether and dried *in vacuo* to afford **11** as a white solid (13.3 g, 60.0 mmol, 82%). ¹H NMR (400 MHz, CD₃OD, ppm) δ 2.14-2.31 (m, 2H), 2.58-2.72 (m, 2H), 2.94 (t, 1H, *J* = 2.5 Hz), 4.06 (t, 1H, *J* = 6.7 Hz), 4.74 (d, 2H, *J* = 2.5 Hz). ¹³C NMR (101 MHz, CD₃OD,

ppm) δ 26.51, 30.34, 53.13, 54.84, 76.42, 78.57, 171.35, 172.78. FTIR: 3350-2350, 3294, 3152, 3050-2500, 1748, 1722, 1611, 1489, 1454, 1421, 1362, 1325, 1264, 1223, 1173, 1144, 1121, 1084, 1043, 1003, 957, 837, 791, 685, 662 cm^{-1} . MS (m/z) $[\text{M}+\text{H}]^+$ calcd. 186.0766, found 186.0752.

5. Synthesis of γ -Propargyl-L-Glutamate *N*-Carboxyanhydride (PLG NCA, **12**)

Into a 250-mL three-necked round bottom flask equipped with a glass Pasteur pipette as an N_2 inlet and a condenser connected to a base trap were charged **11** (4.0 g, 18 mmol) and anhydrous THF (150 mL). The suspension was heated at reflux with N_2 bubbling, followed by the dropwise addition of a triphosgene solution in THF (10 mL, 6.0 mmol/mL). **CAUTION: Phosgene and its derivatives are extremely hazardous. All manipulations must be performed using a reaction apparatus that provides for quenching phosgene released from the reaction set-up and is placed in a well-ventilated chemical fume hood with proper personal protective equipment and necessary precautions to avoid exposure.** The reaction was stirred for 6 h during which the suspension slowly became homogeneous. After cooling in an ice bath, the crude solution was gravity-filtered. The filtrate was then washed with ice-cold aqueous media (water, saturated aqueous sodium bicarbonate, brine and water). The organic layer was dried over MgSO_4 , filtered, concentrated and purified by precipitation against hexanes ($\times 3$) to obtain a yellow viscous oil. The actual mass of **12** was calculated by subtracting the mass of residual ethyl acetate from that of the collected oil, resulting in a yield of 1.7 g (8.0 mmol, 45%). The mole ratio between **12** and ethyl acetate was calculated from ^1H

NMR. ^1H NMR (400 MHz, CDCl_3 , ppm) δ 2.11-2.34 (m, 2H), 2.52 (t, 1H, $J = 2.5$ Hz), 2.61 (t, 2H, $J = 7.1$ Hz), 4.43 (dt, 1H, $J = 5.8, 1.0$ Hz), 4.71 (d, 2H, $J = 2.5$ Hz), 6.61 (br, 1H). ^{13}C NMR (101 MHz, CDCl_3 , ppm) δ 26.7, 29.4, 52.6, 56.8, 75.5, 77.2, 152.3, 169.5, 171.8. FTIR: 3500-3100, 3050-2850, 2129, 1856, 1776, 1730, 1439, 1371, 1306, 1275, 1244, 1163, 1103, 1016, 991, 920, 795, 756 cm^{-1} . MS (m/z) $[\text{M-H}]^-$ calcd. 210.0408, found 212.0401.

6. Synthesis of Poly(γ -Propargyl-L-Glutamate)₅₀ (PPLG₅₀, **13**)

Inside an argon-filled glovebox, a flame-dried 25-mL Schlenk flask was charged with the monomer **12** (0.69 g, 3.3 mmol), DMF (7 mL) and a solution of hexylamine (180 μL , 0.36 $\text{mmol}\cdot\text{mL}^{-1}$ in DMF, 0.065 mmol, monomer:initiator = 50:1). The reaction flask was then sealed, moved to a fume hood and connected to a Schlenk line through a N_2 flowmeter with a drierite column as an N_2 outlet. The reaction was stirred for 12 h under 100 $\text{mL}\cdot\text{min}^{-1}$ N_2 flow and monitored using FTIR. When the reaction was complete, the mixture was concentrated *in vacuo*, dissolved into DCM (10 mL) and precipitated into ice-cold diethyl ether thrice to afford **13** as a white solid (0.50 g, 3.0 mmol, 92%). ^1H NMR (400 MHz, $\text{CDCl}_3/\text{TFA-}d$, 2/1 v/v, ppm) δ 4.49 (s), 4.42 (b), 3.07 (b), 2.31 (s), 2.28 (b), 1.98 (b), 1.82 (b), 1.31 (b), 1.08 (b), 0.67 (b). ^{13}C NMR (101 MHz, $\text{CDCl}_3/\text{TFA-}d$, 2/1 v/v, ppm) δ 176.69, 175.28, 78.17, 77.90, 55.67, 55.42, 31.97, 28.89. FTIR: 3500-3150, 3100-2850, 2127, 1736, 1649, 1545, 1447, 1389, 1315, 1246, 1159, 1119, 1082, 1024, 991, 934, 795, 644 cm^{-1} . The polymer exhibited an onset degradation temperature at *ca.* 253 $^\circ\text{C}$ and a T_g value of 7 $^\circ\text{C}$.

7. Synthesis of Poly(γ -Propargyl-L-Glutamate)_{50-graft}-MTEMPO (PPLG_{50-g}-MTEMPO, **14**)

A 40-mL glass vial was charged with **13** (92.0 mg, 0.550 mmol), **9** (0.61 g, 2.2 mmol) and DMPA (0.15 g, 0.58 mmol) and DMF (10 mL). The vial was then sealed with a septum and the solution was bubbled with N₂ for 30 min, followed by irradiation for 2 h using a UV reaction chamber (equipped with Philips UV bulbs, 9W, 350–400 nm). Upon completion, the mixture was precipitated into ice-cold methanol (50 mL \times 3) and acetonitrile (50 mL \times 3) to afford **14** as a white solid (0.33 g, 84%). Overlapping ¹H NMR signals made distinct peak assignments difficult (see **Appendix Figure 45**). ¹³C NMR was attempted but also provided unassignable spectra with high signal-to-noise ratio. FTIR: 3292, 3050-2800, 1730, 1651, 1547, 1454, 1360, 1315, 1240, 1165, 1082, 1037, 999, 953, 893, 833, 719 cm⁻¹. The polymer exhibited an onset degradation temperature at *ca.* 288 °C and a *T_g* value of *ca.* 27 °C.

8. Synthesis of BiTEMPO Polypeptide (**15**)

A solution of *m*-CPBA (0.53 g, 3.1 mmol) in DCM (10 mL) was added slowly into an ice-cold 250-mL round-bottom flask containing **14** (0.14 g, 0.19 mmol) and DCM (30 mL). The reaction was stirred for 4 h at r.t. and washed with ice-cold aqueous media (saturated aqueous sodium bicarbonate \times 2, brine and water, 50 mL each). The organic layer was dried over MgSO₄, filtered, concentrated and precipitated (\times 3) into ice-cold hexanes to afford **15** as a light orange solid (0.13 g, 87%). Overlapping ¹H NMR signals

made distinct peak assignments difficult (see **Appendix Figure 46**). ^{13}C NMR was attempted but also provided unassignable spectra with high signal-to-noise ratio. The oxidation efficiency was determined with UV-Vis, electron paramagnetic resonance and X-ray photoelectron spectroscopies. FTIR: 3292, 3050-2800, 1732, 1651, 1547, 1464, 1364, 1314, 1238, 1174, 1123, 1049, 1007, 860, 735, 681 cm^{-1} . The polymer exhibited an onset degradation temperature at *ca.* 240 °C and a T_g value of *ca.* 115 °C.

Synthesis of Viologen Analog

1. Synthesis of 6-Chlorohexyl Hydrocinnamate (CHHC, 16)

Hydrocinnamic acid (10.0 g, 66.6 mmol), 6-chlorohexanol (15 mL, 0.11 mol) and THF (15 mL) were added to a 500-mL round bottom flask in an ice bath, followed by the slow addition of sulfuric acid (4 mL). The reaction mixture was allowed to warm to r.t. and stirred for 24 h. Afterwards, ice-cold saturated aqueous sodium bicarbonate was slowly added to the reaction mixture to neutralize the solution (monitored by pH paper). The crude product was then extracted with DCM (100 mL \times 3). The combined organic layers were dried over MgSO_4 , concentrated and purified by flash column chromatography eluting with hexanes/ethyl acetate (8/2 v/v gradually increasing to 7/3 v/v) to obtain **16** as a colorless oil (14.6 g, 54.3 mmol, 82%). ^1H NMR (400 MHz, $\text{DMSO-}d_6$, ppm) δ 7.29-7.16 (m, 5H), 3.98 (t, 2H, $J = 6.6$ Hz), 3.61 (t, 2H, $J = 6.6$ Hz), 2.84 (t, 2H, $J = 7.5$ Hz), 2.61 (t, 2H, $J = 7.5$ Hz), 1.68 (quint, 2H, $J = 6.6, 7.5$ Hz), 1.52 (quint, 2H, $J = 6.6, 7.5$ Hz), 1.40-1.21 (m, 4H). ^{13}C NMR (101 MHz, $\text{DMSO-}d_6$, ppm) δ 172.21, 140.47, 128.28, 126.04, 64.68, 45.30, 35.04, 31.89, 31.30, 27.96, 25.88, 24.60. FTIR: 3050-2800, 1730,

1604, 1497, 1454, 1358, 1292, 1240, 1159, 1078, 1047, 978, 904, 735, 698, 648 cm^{-1} . MS (m/z) $[\text{M}+\text{H}]^+$ calcd. 269.1308, found 269.1306.

2. Synthesis of 6-Iodohexyl Hydrocinnamate (IHHC, **17**)

A 250-mL round bottom flask was charged with **16** (5.4 g, 20 mmol), NaI (5.6 g, 37 mmol) and acetone (50 mL). The mixture was stirred for 3 d while being heated at reflux. The solvent was then removed *in vacuo*, followed by the addition of DCM (50 mL), and removal of insoluble salts *via* gravity filtration. The filtrate was washed with ice-cold water (50 mL \times 3), dried over MgSO_4 and purified by flash column chromatography eluting with hexanes/ethyl acetate (8/2 v/v gradually increasing to 7/3 v/v) to obtain **17** as a dark orange oil (6.7 g, 19 mmol, 93%). ^1H NMR (400 MHz, $\text{DMSO-}d_6$, ppm) δ 7.29-7.16 (m, 5H), 3.98 (t, 2H, $J = 6.6$ Hz), 3.26 (t, 2H, $J = 6.6$ Hz), 2.85 (t, 2H, $J = 7.5$ Hz), 2.62 (t, 2H, $J = 7.5$ Hz), 1.73 (quint, 2H, $J = 6.6, 7.5$ Hz), 1.51 (quint, 2H, $J = 6.6, 7.5$ Hz), 1.36-1.20 (m, 4H). ^{13}C NMR (101 MHz, $\text{DMSO-}d_6$, ppm) δ 172.20, 140.46, 128.27, 126.04, 63.67, 35.04, 32.73, 30.29, 29.44, 27.91, 24.23, 8.91. FTIR: 3100-2800, 1730, 1602, 1497, 1454, 1425, 1389, 1358, 1290, 1240, 1207, 1159, 1076, 1030, 949, 905, 748, 698 cm^{-1} . MS (m/z) $[\text{M}+\text{Na}]^+$ calcd. 383.0484 found 383.0473.

3. Synthesis of 1-(6-((3-Phenylpropanoyl)oxy)hexyl)-[4,4'-bipyridin]-1-ium Iodide (PBPI, **18**)

A 250-mL round bottom flask was charged with **17** (1.2 g, 3.3 mmol), 4,4'-bipyridine (1.1 g, 7.7 mmol) and acetonitrile (50 mL). The reaction was stirred at 70 $^\circ\text{C}$

for 24 h and monitored by ^1H NMR. Upon completion, the mixture was concentrated and precipitated into diethyl ether. The crude product was collected *via* vacuum filtration, dissolved in acetonitrile and precipitated again into diethyl ether ($\times 2$) to obtain **18** as a yellow solid (1.5 g, 2.9 mmol, 86%). ^1H NMR (400 MHz, DMSO- d_6 , ppm) δ 9.24 (d, 2H, $J = 8.0$ Hz), 8.87 (dd, 2H, $J = 2.8, 6.2$ Hz), 8.64 (d, 2H, $J = 8.0$ Hz), 8.05 (dd, 2H, $J = 2.8, 6.2$ Hz), 7.29-7.16 (m, 5H), 4.63 (t, 2H, $J = 7.5$ Hz), 3.99 (t, 2H, $J = 6.5$ Hz), 3.32 (s, 3H), 2.83 (t, 2H, $J = 7.5$ Hz), 2.61 (t, 2H, $J = 7.5$ Hz), 1.94 (b, 2H), 1.53 (b, 2H), 1.30 (b, 4H). ^{13}C NMR (101 MHz, DMSO- d_6 , ppm) δ 172.20, 152.25, 150.98, 145.27, 140.84, 140.44, 128.29, 126.06, 125.38, 121.90, 63.62, 60.30, 35.01, 30.51, 30.27, 27.83, 25.00, 24.74. FTIR: 3150-2750, 1728, 1638, 1600, 1547, 1524, 1495, 1466, 1416, 1362, 1340, 1296, 1269, 1221, 1179, 1150, 1076, 970, 914, 862, 814, 766, 731 cm^{-1} . MS (m/z) $[\text{M}]^+$ calcd. 389.2229, found 389.2231.

4. Synthesis of Viologen Analog (19)

A 50-mL round bottom flask was charged with **18** (1.1 g, 2.1 mmol) and acetonitrile (20 mL), followed by the addition of iodomethane (0.5 mL, 8 mmol). The reaction mixture was stirred at 80 $^\circ\text{C}$ for 24 h. After being cooled to r.t., the precipitate was collected *via* centrifugation and washed with diethyl ether to obtain **19** as an orange solid (1.1 g, 1.7 mmol, 81%). ^1H NMR (400 MHz, DMSO- d_6 , ppm) δ 9.40 (d, 2H, $J = 6.8$ Hz), 9.30 (d, 2H, $J = 6.8$ Hz), 8.81 (d, 2H, $J = 6.8$ Hz), 8.78 (d, 2H, $J = 6.8$ Hz), 7.29-7.16 (m, 5H), 4.68 (t, 2H, $J = 6.6$ Hz), 4.44 (s, 3H), 3.99 (t, 2H, $J = 6.6$ Hz), 2.84 (t, 2H, $J = 7.5$ Hz), 2.61 (t, 2H, $J = 7.5$ Hz), 1.96 (b, 2H), 1.54 (b, 2H), 1.36-1.20 (b, 4H). ^{13}C NMR (101

MHz, DMSO-*d*₆, ppm) δ 172.20, 148.48, 148.10, 146.59, 145.73, 140.46, 128.29, 126.54, 126.07, 63.62, 60.78, 48.07, 35.02, 30.55, 30.26, 27.83, 24.99, 24.72. FTIR: 3130-2800, 1726, 1636, 1557, 1504, 1450, 1352, 1271, 1227, 1182, 1144, 1076, 1049, 980, 843, 816, 756, 731, 706 cm⁻¹. MS (m/z) [M]²⁺ calcd. 202.1226 (without iodide), found 202.25.

Synthesis of BiTEMPO Analog

1. Synthesis of Propargyl Hydrocinnamate (PHC, **20)**

Hydrocinnamic acid (10.0 g, 66.6 mmol) and propargyl alcohol (40 mL, 0.7 mol) were added to a 250-mL round bottom flask. The mixture was cooled to ice-cold temperature, followed by the slow addition of TMSCl (13 mL, 0.10 mol). The reaction was allowed to warm to r.t. and stirred for 24 h. Afterwards, ice-cold saturated aqueous sodium bicarbonate was slowly added to the reaction mixture to neutralize the solution (monitored by pH paper). The crude product was then extracted with DCM (100 mL \times 3). The combined organic layers were dried over MgSO₄, concentrated and purified by flash column chromatography eluting with hexanes/ethyl acetate (8/2 v/v gradually increasing to 7/3 v/v) to obtain **20** as a colorless oil (10.8 g, 57.4 mmol, 86%). ¹H NMR (400 MHz, CD₂Cl₂, ppm) δ 7.31-7.18 (m, 5H), 4.67 (d, 2H, *J* = 2.5 Hz), 2.95 (t, 2H, *J* = 7.6 Hz), 2.67 (t, 2H, *J* = 8 Hz), 2.52 (t, 2H, *J* = 2.5 Hz). ¹³C NMR (101 MHz, CD₂Cl₂, ppm) δ 171.82, 140.45, 128.44, 128.27, 126.25, 77.41, 74.48, 51.80, 35.46, 30.68. FTIR: 3296, 3100-2800, 2116, 1738, 1605, 1497, 1454, 1375, 1240, 1146, 1078, 1045, 1024, 988, 941, 893, 737, 698, 638 cm⁻¹. MS (m/z) [M+H]⁺ calcd. 189.0916, found 189.0928.

2. Synthesis of Hydrocinnamate-*bis*(propionic acid) (HC-*bis*PA, **21**)

A 40-mL glass vial was charged with **20** (3.9 g, 21 mmol), 3-mercaptopropionic acid (8 mL, 0.09 mol) and DMPA (1.1 g, 4.3 mmol). The vial was sealed with a septum, and the solution was bubbled with N₂ for 30 min then irradiated for 2 h using a UV reaction chamber (equipped with Philips UV bulbs, 9W, 350–400 nm), resulting in a yellow solution upon completion. DCM (50 mL) was then added into the crude product. The solution was then washed with water (50 mL × 3). The organic layer was dried over MgSO₄ and purified by flash column chromatography eluting with DCM/MeOH (0 vol% MeOH gradually increasing to 5 vol% MeOH) to obtain **21** as a colorless liquid (4.7 g, 12 mmol, 56%). ¹H NMR (400 MHz, CD₂Cl₂, ppm) δ 7.30-7.18 (m, 5H), 4.33-4.19 (m, 2H), 3.04 (quint, 1H, *J* = 6.6 Hz), 2.94 (t, 2H, *J* = 7.6 Hz), 2.87-2.64 (m, 12H). ¹³C NMR (101 MHz, CD₂Cl₂, ppm) δ 178.24, 173.11, 141.11, 129.00, 128.82, 126.78, 65.91, 45.61, 36.18, 35.39, 35.33, 35.21, 31.33, 28.14, 26.81. FTIR: 3500-2250, 3150-2500, 1736, 1703, 1603, 1497, 1454, 1416, 1404, 1341, 1244, 1192, 1146, 1078, 930, 735, 698, 648 cm⁻¹. MS (m/z) [M-H]⁻ calcd. 399.0942, found 399.0942.

3. Synthesis of Hydrocinnamate-*bis*(MTEMPO) (HC-*bis*(MTEMPO), **22**)

A 100-mL round bottom flask was charged with **21** (1.5 g, 3.7 mmol), **7** (1.5 g, 8.7 mmol), DCC (1.7 g, 8.7 mmol), DMAP (0.1 g, 0.8 mmol) and DCM (50 mL). The reaction mixture was stirred for 24 h at r.t. Afterwards, the precipitate was gravity-filtered and the filtrate was purified by flash column chromatography eluting with hexanes/ethyl acetate (8/2 v/v gradually increasing to 7/3 v/v) to obtain **22** as a colorless liquid (2.2 g, 3.0 mmol,

71%). ^1H NMR (400 MHz, CD_2Cl_2 , ppm) δ 7.31-7.18 (m, 5H), 5.0 (d, 2H, $J = 2.5$ Hz), 4.33-4.18 (dd, 1H, $J = 53, 5.2$ Hz), 4.30-4.21 (dd, 1H, $J = 31, 5.2$ Hz), 3.59 (s, 6H), 3.01 (quintet, 1H, $J = 6.5, 6.5$ Hz), 2.95 (t, 2H, $J = 7.6$ Hz), 2.85-2.74 (m, 6H), 2.66 (t, 2H, $J = 7.6$ Hz), 2.56 (m, 4H), 1.83 (dd, 4H, $J = 12, 4.0$ Hz), 1.52 (t, $J = 12$ Hz, 4H), 1.20 (s, 12H), 1.16 (s, 12H). ^{13}C NMR (101 MHz, CD_2Cl_2 , ppm) δ 172.89, 171.66, 171.57, 141.15, 129.01, 128.83, 126.78, 67.58, 65.87, 60.41, 45.45, 44.49, 36.21, 35.30, 33.37, 31.37, 28.62, 27.18, 23.22, 21.00. FTIR: 3050-2800, 1730, 1454, 1420, 1375, 1360, 1294, 1240, 1173, 1080, 1038, 999, 953, 893, 831, 737, 698 cm^{-1} . MS (m/z) $[\text{M}+\text{Na}]^+$ calcd. 761.3840, found 761.3826.

4. Synthesis of BiTEMPO Analog (23)

A solution of *m*-CPBA (0.53 g, 8.7 mmol) in DCM (10 mL) was slowly added into an ice-cold 250-mL round-bottom flask containing **22** (0.53 g, 0.72 mmol) and DCM (50 mL). The reaction was stirred for 4 h at r.t. and washed with ice-cold aqueous media (saturated aqueous sodium bicarbonate $\times 2$, brine and water, 50 mL each). The organic layer was dried over MgSO_4 , filtered, concentrated and purified by flash column chromatography eluting with DCM/MeOH (0 vol% MeOH gradually increasing to 5 vol% MeOH) to obtain **23** as an orange solid (0.3 g, 0.4 mmol, 53%). ^1H NMR (400 MHz, TFA-*d*, ppm) δ 7.22-7.19 (m, 5H), 5.98 (m, 1H), 5.31 (m, 1H), 4.85 (b, 1H), 4.63 (m, 1H), 4.21-3.97 (m, 2H), 3.76-3.47 (m, 5H), 3.12-2.76 (m, 12H), 2.32 (m, 2H), 2.07 (m, 2H), 1.78-1.50 (m, 24H). FTIR: 3050-2800, 1732, 1497, 1464, 1420, 1364, 1315, 1238, 1177,

1125, 1051, 984, 862, 752, 700, 696 cm^{-1} . MS (m/z) $[\text{M}+\text{H}]^+$ calcd. 773.3353, found 773.3375.

Chemical Characterization

Attenuated total reflectance-Fourier transform infrared (ATR-FTIR) spectra were recorded for powder samples on an IR Prestige 21 system (Shimadzu Corp., Japan) and analyzed using IRsolution v. 1.40 software. Circular dichroism (CD) spectra were recorded on a Chirascan CD spectrometer from Applied Photophysics, Ltd. (Leatherhead, UK) equipped with a 150-Watt xenon arc lamp. The polymer solutions for CD measurements were $0.1 \text{ mg}\cdot\text{mL}^{-1}$ ACN. CD spectra were acquired between 180 and 280 nm, using a wavelength step of 1.0 nm, in a quartz cell with a path length of 1.0 cm, and analyzed using Pro-Data v. 5 software. Electron paramagnetic resonance (EPR) spectra were recorded on an X-Band Bruker EMS spectrometer with an Oxford ESR900 liquid helium cryostat. X-ray photoelectron spectroscopy (XPS) measurements of the polypeptide/analog thin films were recorded on an Omicron XPS system with Argus detector using Omicron's 400 dual Mg/Al X-ray source. The thin films were prepared by drop-casting $300 \mu\text{L}$ of each polymer/analog solution ($4 \text{ mg}\cdot\text{mL}^{-1}$ in CHCl_3) on ITO-coated glass. After drop-casting, the thin films were dried at ambient conditions for 24 h, followed by drying under vacuum at r.t. for 24 h before XPS measurements. ^1H and ^{13}C nuclear magnetic resonance (NMR) spectra were recorded on a Bruker 400 spectrometer. Chemical shifts were referenced to the solvent resonance signals. High resolution electrospray ionization mass spectrometry (ESI-HRMS) experiments were performed

using a Thermo Scientific Q Exactive Focus (Thermo Scientific, USA) in both positive and negative mode. The sample was injected into a 10 μL loop and methanol was used as a mobile phase at a flow rate of 100 $\mu\text{L}\cdot\text{min}^{-1}$. The Q Exactive Focus HESI source was operated in full MS in positive mode. The mass resolution was tuned to 70000 FWHM at m/z 200. The spray voltage was set to 3.75 kV for positive mode and 3.3 kV for negative mode, and the sheath gas and auxiliary gas flow rates were set to 7 and 0 arbitrary units, respectively. The transfer capillary temperature was held at 250 $^{\circ}\text{C}$ and the S-Lens RF level was set at 50 V. Exactive Series 2.8 SP1/Xcalibur v. 4.0 software was used for data acquisition and processing.

Thermal Analysis

Thermogravimetric analysis (TGA) was performed under nitrogen atmosphere using a Mettler-Toledo model TGA 2 (Mettler-Toledo, Inc., Columbus, OH) with a heating rate of 10 $^{\circ}\text{C}\cdot\text{min}^{-1}$. Measurements were analyzed using Mettler-Toledo STAR^e v. 7.01 software. Glass transition temperatures (T_g) were measured by modulated differential scanning calorimetry (MDSC) on a Q200 DSC (TA Instruments) with a heat-cool-heat cycle. The samples were ramped from -20 $^{\circ}\text{C}$ to 200 $^{\circ}\text{C}$ at a rate of 5 $^{\circ}\text{C}\cdot\text{min}^{-1}$ with amplitude of 1.272 $^{\circ}\text{C}$ for a period of 60 s with nitrogen purge at 50 $\text{mL}\cdot\text{min}^{-1}$. The T_g was taken as the inflection point of the second heating cycle.

Electrochemical Characterization

All electrochemical measurements were performed in an argon-filled glovebox with a Solartron Electrochemical Interface 1287 potentiostat/galvanostat (Ametek, Inc.,

USA) unless otherwise noted. All calculations for polymers were done based on the molar mass of the repeat units.

1. Fabrication and Electrochemical Characterization of Polypeptide Thin Films in Three Electrode Beaker Cells

Polypeptide thin films were prepared by drop-casting 300 μL of the polypeptide solution onto clean ITO-coated glass. The polypeptide solution was composed of 4 mg of polypeptide in 1 mL of MeOH/H₂O (1/1 v/v) for viologen polypeptide or CHCl₃ for biTEMPO polypeptide. After drop-casting, the thin films were dried at ambient conditions for 24 h, followed by drying under vacuum at r.t. for 24 h before electrochemical testing. Composite electrodes for both polymers were fabricated by preparing a solution of CB (60 wt%), biTEMPO polypeptide or viologen polypeptide (30 wt%) and PVDF binder polymer (10 wt%) in NMP (1 mL for 13.3 mg slurry). 300 μL of the slurry was then drop-cast onto a clean ITO-coated glass substrate. After drop-casting the slurry onto the substrates, the electrodes were dried at 40°C under ambient pressure for two days before drying under vacuum at r.t. for 24 h.

The polypeptide thin films on ITO-coated glass were utilized in a three-electrode beaker cell as the working electrode with lithium metal counter and reference electrodes, and 20 mL of 0.5 M LiCF₃SO₃ in PC for the electrolyte. The thin films were conditioned using three cyclic voltammetry (CV) cycles at 10 $\text{mV}\cdot\text{s}^{-1}$ followed by CV at different scan rates (10, 25, 50 and 100 $\text{mV}\cdot\text{s}^{-1}$).

2. Electrochemical Characterization of Analog Solutions in Three-electrode Beaker Cells

Solution state CV was conducted for the viologen and biTEMPO analogs. The analogs were dissolved at 1 mM in 20 mL of 0.5 M LiCF₃SO₃ in PC electrolyte. In the three-electrode beaker cell for solution state CV, a glassy carbon working electrode was used with lithium metal counter and reference electrodes (**Appendix Figure 55A**). After three conditioning cyclic voltammetry (CV) cycles at 10 mV·s⁻¹, CV was performed at different scan rates (10, 25, 50 and 100 mV·s⁻¹). All electrochemical measurements were performed in an argon filled glovebox with a Solartron Electrochemical Interface 1287 potentiostat/galvanostat unless otherwise noted.

3. Theoretical Capacity Calculation

The theoretical capacities of the polypeptides were calculated using **Equation 2** with M_w as the molar mass of the polymer repeat unit of each of the redox-active polypeptides, using the discharged states for both pendant groups (TEMPO and viologen²⁺). For the viologen polypeptide, the iodide ions were considered in the molar mass of the repeat unit. The theoretical capacities were 81.4 mA·h·g⁻¹ for the viologen polypeptide and 69.4 mA·h·g⁻¹ for the biTEMPO polypeptide. The theoretical capacity of the full cell composed of a biTEMPO polypeptide-based cathode and a viologen polypeptide-based anode was calculated using **Equation 3**.

4. Fabrication and Electrochemical Characterization of Polypeptide Composite Electrodes in Three-electrode Beaker Cells

Composite electrodes for both polypeptides were fabricated by preparing a slurry of viologen polypeptide or biTEMPO polypeptide (30 wt%), CB (60 wt%) and PVDF binder polymer (10 wt%) in NMP (1 mL for 13.3 mg slurry). 300 μ L of the slurry was then drop-casted onto a clean ITO-coated glass. After drop-casting, the electrodes were dried at 40 $^{\circ}$ C for 2 d before drying under vacuum at r.t. for 24 h. The composite electrodes were utilized in a half sandwich cell as working electrodes with a lithium metal reference electrode and filter paper pre-soaked with 0.5 M LiCF₃SO₃ in PC as the separator (**Appendix Figure 55C**). The fabricated electrodes were also utilized in a three-electrode beaker cell as working electrodes with lithium metal reference and counter electrodes and 20 mL of 0.5 M LiCF₃SO₃ in PC as electrolyte (**Appendix Figure 55B**).

CV (at 10 mV \cdot s⁻¹) and galvanostatic charge-discharge (5 cycles each at 1, 2, 5, 10 and 20 C followed by 25 cycles at 1 C) were performed. 1 C is defined as the current required to discharge the active material in 1 h. The current (I) for each C-rate was calculated using the theoretical capacity and coated mass (X) of the polypeptide (as shown below for a biTEMPO composite electrode at 1 C).

$$I \text{ (mA)} = \left(\frac{71.3 \text{ mA} \cdot \text{h}}{\text{g polypeptide}} \right) (X \text{ g polypeptide}) \left(\frac{1}{1 \text{ h}} \right) 1 \text{ h} \quad \text{Equation 6.}$$

5. Fabrication and Electrochemical Characterization of Fully Polypeptide Sandwich Cells

Fully polypeptide electrochemical sandwich cells were assembled with viologen polypeptide composite anodes, biTEMPO polypeptide composite cathodes and electrolyte-soaked filter paper separators (**Appendix Figure 55D**). The electrolyte was 0.5 M LiCF₃SO₃ in PC. Before assembling the sandwich cell, the viologen polypeptide electrodes were conditioned with three cyclic voltammetry (CV) cycles at 10 mV·s⁻¹ in a three-electrode beaker cell containing 0.5 M LiCF₃SO₃ in propylene carbonate (PC) electrolyte with lithium metal counter and reference electrodes. CV of the full sandwich cell was conducted at 10 mV·s⁻¹ before galvanostatic charge-discharge at 1 C for 250 cycles. Electrochemical characterization of the polypeptides as composite electrodes in three-electrode and full beaker cell configurations was also conducted (**Appendix Figure 55D**). The current (*I*) for each C-rate was calculated using the theoretical capacity and coated mass of the biTEMPO polypeptide using **Equation 6**.

Degradation Study

Viologen polypeptide and biTEMPO polypeptide were exposed to 0.01 M, 1 M and 6 M HCl at 2.5 mg·mL⁻¹ over 24 h at r.t., 50, 80 and 110 °C. Poly(γ -benzyl-L-glutamate)₅₀, small-molecule analogs of the polypeptides and 4-OH-TEMPO were hydrolyzed at 2.5 mg·mL⁻¹ with 1 M HCl over 24 h at 110 °C to guide the breakdown of the polypeptide backbones and sidechains.

Analysis of the degradation products was performed using ESI-HRMS and liquid chromatography (LC) coupled with ESI-HRMS (LC-ESI-HRMS). A Thermo Scientific Ultimate 3000 Series LC (Thermo Scientific, Waltham, MA) coupled with a Qexactive Focus mass spectrometer (Thermo Scientific, Waltham, MA) was used for analysis. A Scherazo SM-C18 (150 × 2 mm, 3 μm particle size) column (Imtakt, Japan) was used for chromatographic separation. The mobile phase consisted of 20 mM NH₄HCO₂ in H₂O (eluent A) and 100 mM NH₄HCO₂ in H₂O/ACN (1/1 v/v, eluent B). Flow rate was set at 0.3 mL·min⁻¹ and 10 μL of each sample was injected. The column compartment was held at 30 °C. Chromatographic gradient elution was set by first equilibrating the column for 3 min at 5% B. Eluent B was then gradually increased from 5% to 100% for 18 min and held at 100% for 3 min. The eluent was then set to the initial mobile phase condition (5% B) in 0.1 min and kept constant for 3 minutes. The conditions for the mass spectrometry were similar as described above, except that the capillary temperature was set to 350 °C and that the sheath gas and auxiliary gas flow rates were set to 35 and 8 arbitrary units, respectively.

Cell Viability Study

Preosteoblast cells (MC3T3 cells) were purchased from ATCC (Manassas, VA) and cultured in Alpha Minimum Essential Medium with ribonucleosides but without ascorbic acid supplemented with 10% fetal bovine serum and 1% Penicillin-Streptomycin (Millipore Sigma, St. Louis, MO) with the final concentrations of 100 U·mL⁻¹ penicillin, 100 μg·mL⁻¹ streptomycin. Bovine coronary venular endothelial cells (CVECs) were

kindly gifted by Professors Cynthia J. Meininger and Andreea Trache at Texas A&M Health Science Center. CVECs were cultured in Dulbecco's Modified Eagle Medium: Nutrient Mixture F-12 (DMEM/F-12) supplemented with 10% Fetal Bovine Serum and 1% antibiotic (final concentration as 100 U·mL⁻¹ penicillin, 100 U·mL⁻¹ streptomycin, 0.25 mg·mL⁻¹ amphotericin B (Lonza, Walkersville, MD) and 20 units·mL⁻¹ heparin (Midwest Vet Supply, Lakeville, MN). Mouse fibroblast cells (NIH/3T3) were purchased from ATCC (Manassas, VA) and cultured in Dulbecco's Modified Eagle Medium (DMEM) supplemented with 10% fetal bovine serum and 1% Penicillin-Streptomycin (Millipore Sigma, St. Louis, MO) with final concentrations of 100 U·mL⁻¹ penicillin, 100 µg·mL⁻¹ streptomycin. Reagents were purchased from Thermo Fisher Scientific (Waltham, MA) unless otherwise described.

CellTiter 96 AQ One Solution Cell Proliferation Assay was purchased from Promega and used without modification, as described previously. Cells were grown to confluency. Viologen polypeptide, biTEMPO polypeptide, viologen analog and biTEMPO analog were dissolved in sterile DMSO at 10 mg·mL⁻¹ whereas their degraded products were dissolved in sterile PBS buffer pH 7.6 at similar concentrations. All testing substances were filtered *via* sterile syringe filter and added to the cells at concentrations indicated in **Figure 22** and **Appendix Figure 73** to **Appendix Figure 76** (0.05 µg·mL⁻¹ to 100 µg·mL⁻¹). Control cells were incubated with fresh culture medium. The plates were then incubated at 37 °C for 72 h. Subsequently, a 20-µL aliquot of MTS reagent was added to each well and incubated for another 2 h. The absorbance was recorded at 490

nm. Cell viability below 50% was considered indicative of cytotoxicity. Data are expressed as mean \pm s.d. of three determinations.

Results and Discussion

Syntheses of Redox-active Polypeptides

From L-glutamic acid as a common starting amino acid, two divergent five-step synthetic pathways were utilized to prepare distinct anodic and cathodic L-glutamate-based polypeptides—viologen polypeptide and biTEMPO polypeptide, respectively (Figure 2). Both pathways began with esterification reactions to install chloro or alkynyl groups at the γ -position¹²⁸ (which were later utilized for incorporation of the final redox-active moieties), followed by cyclization to establish monomer structures and then polymerization to produce poly(L-glutamate)s (**Figure 16**). The viologen polypeptide synthesis involved activation of the chloro side chain functionality to allow for efficient installation of the dicationic oxidized form of the viologens. Separately, the biTEMPO polypeptide synthesis involved the opposite sequence of installation of TEMPO precursors onto the alkynyl side chain, followed by activation to the nitroxide radical state (**Figure 16**). Specifically, the chloro- and alkynyl-containing polypeptides were synthesized, as described in **Figure 17**, *via* ring opening polymerization (ROP) of γ -(6-chlorohexyl)-L-glutamate *N*-carboxyanhydrides (CHLG NCAs, **4**) and γ -propargyl-L-glutamate *N*-carboxyanhydrides (PLG NCAs, **12**), prepared from chloro- and propargyl-decorated L-glutamic acids, respectively, as the first two steps of the five-step sequence. The ROP reactions were monitored using attenuated total reflectance-Fourier transform

infrared (ATR-FTIR) spectroscopy by the decrease in intensity of the NCA anhydride absorption at *ca.* 1780 cm^{-1} . Upon completion, poly(γ -(6-chlorohexyl)-L-glutamate) (PCHLG, **5**) and poly(γ -propargyl-L-glutamate) (PPLG, **13**) were obtained with degrees of polymerization (DP) of *ca.* 50, as confirmed by ^1H NMR spectroscopy (**Appendix Figure 36** and **Appendix Figure 44**), and narrow dispersities ($D = 1.09$ and 1.13, respectively, **Appendix Figure 19**).

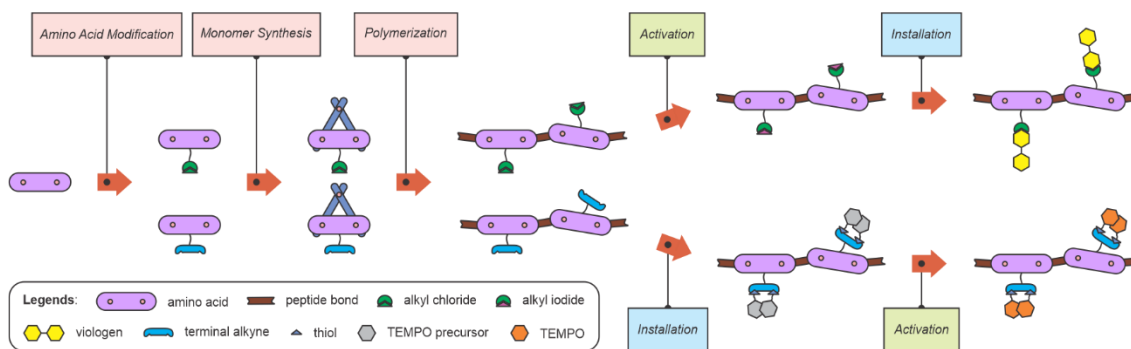


Figure 16. Synthesis strategy for redox-active polypeptides

The viologen polypeptide was obtained *via* $\text{S}_{\text{N}}2$ substitution of halide-containing side chains by the viologen precursor, 1-methyl-4,4'-bipyridylium iodide (MBPI, **2**), prepared *via* methylation of 4,4'-bipyridine (**Figure 17**). Installation of **1** was initially attempted directly from the chloro-containing polypeptide (PCHLG₅₀, **5**), but negligible conversion was observed. The utilization of an additional activation step to replace the chlorine atoms with iodine *via* Finkelstein reaction and obtain the iodo-containing polypeptide (PIHLG₅₀, **6**), prior to the installation step, succeeded in yielding the viologen polypeptide **7** with quantitative conversion as determined by ^1H NMR spectroscopy (**Appendix Figure 36** to **Appendix Figure 38**).

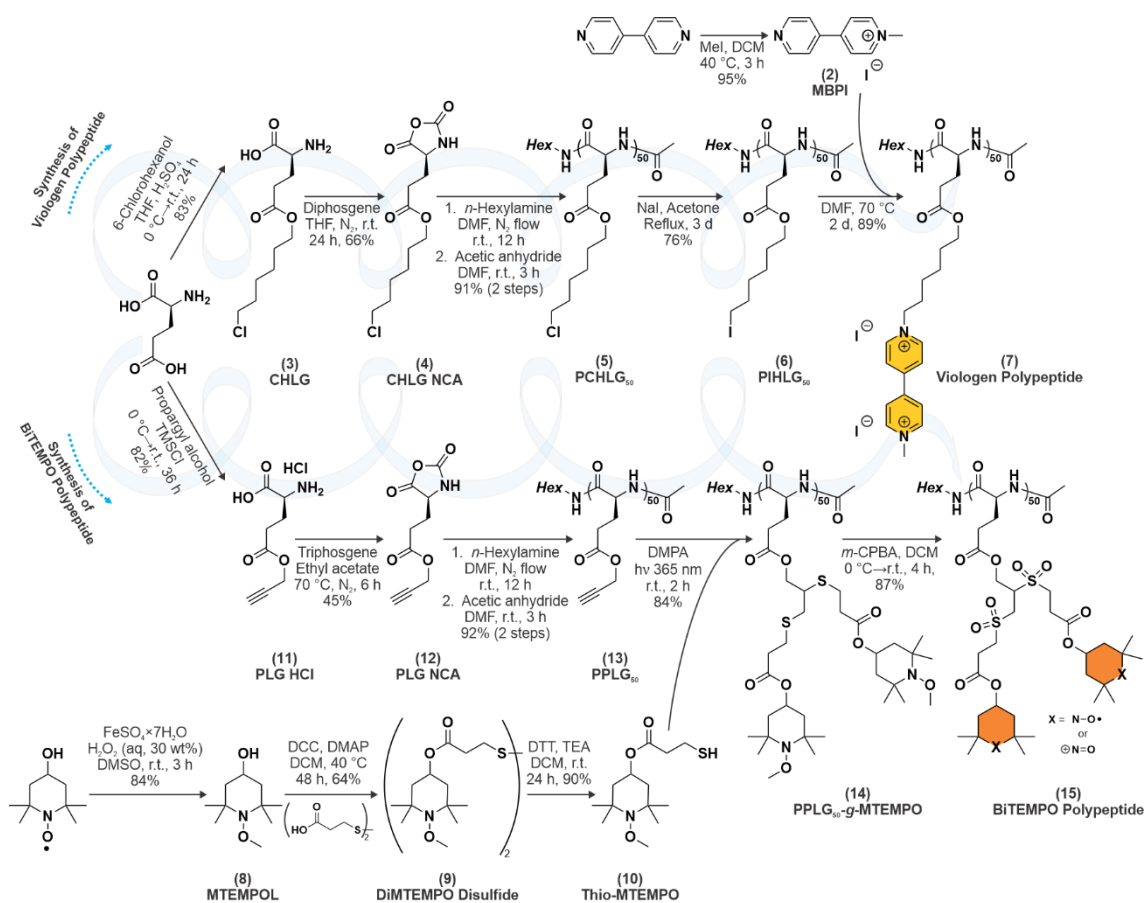


Figure 17. Detailed synthetic schemes for redox-active polypeptides.

For the biTEMPO polypeptide synthesis, terminal alkynes were incorporated as the side chain functionality to allow for thiol-yne “click” chemistry with thiol-decorated TEMPO precursors, followed by deprotection for activation. Methyl-protected methoxyamine derivatives were installed as TEMPO precursors to prevent reduction of the TEMPO-based nitroxide radicals to hydroxylamine in the presence of thiols. The esterification of the methylated 4-hydroxy-TEMPO **8** with 3,3'-dithiodipropionic acid and reduction of the disulfide bond with 1,4-dithiothreitol afforded the thiol-decorated methyl-protected TEMPO **10**. This thiol was then “clicked” onto PPLG₅₀ **13** under UV irradiation

in the presence of 2,2-dimethoxy-2-phenylacetophenone (DMPA), followed by oxidative cleavage with *meta*-chloroperoxybenzoic acid (*m*-CPBA) to afford the biTEMPO polypeptide **15**. The efficiency of this final activation step was evaluated using X-ray photoelectron spectroscopy (**Appendix Figure 29** to **Appendix Figure 32**), indicating that the thioethers (162-164 eV) of **14** were quantitatively oxidized to sulfones (167-169 eV) in **15** and that *ca.* 30% of the nitroxide radicals (401 eV) were oxidized to oxoammonium (405 eV). The latter finding was confirmed with UV-vis spectroscopy (**Appendix Figure 21**) and electron paramagnetic resonance (EPR) spectroscopy (**Appendix Figure 22**).

ATR-FTIR (**Appendix Figure 23** to **Appendix Figure 28**) and circular dichroism (CD) spectroscopy (**Appendix Figure 20**) were employed to confirm the secondary structures of the polypeptides over multiple steps of post-polymerization modification. Both the viologen and biTEMPO polypeptides exhibited α -helical conformations, as evidenced by the absorbances in the FTIR spectra at 1650 cm^{-1} (amide I region) and 1547 cm^{-1} (amide II region) and by the two bands at 208 and 222 nm in the CD spectra. This is expected, as polypeptides can have secondary structures including helices, sheets, coils, etc.¹²⁹⁻¹³¹

In addition to the redox-active polypeptides, small-molecule analogs of the peptide repeat units (**Figure 18**) were synthesized to guide structural determination, verify redox potentials and identify degradation products. Synthetic details of these molecules can be found in **Appendix Figure 17** and **Appendix Figure 18**.

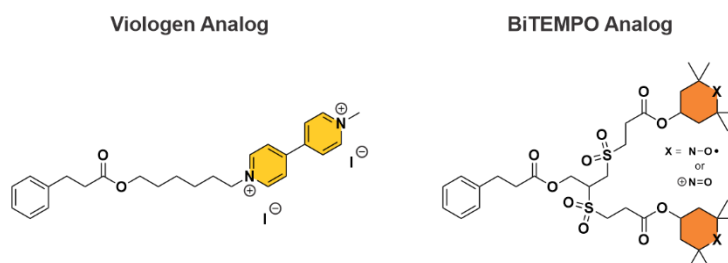


Figure 18. Molecular structures of viologen and polypeptide analogs.

Electrochemical Characterization

Cyclic voltammetry (CV) of viologen and biTEMPO polypeptide thin films (1 μm thick, 0.5-0.6 $\text{mg}\cdot\text{cm}^{-2}$) assessed the basic electrochemical response of the polypeptides (**Figure 19**). The viologen polypeptide exhibited two quasi-reversible redox peaks at 2.09 V and 2.54 V vs. Li/Li^+ (**Figure 19A**). The lower potential (2.09 V) is assigned to the reversible reaction between viologen^{+•} ($\text{Viol}^{+\bullet}$) and viologen⁰ (Viol^0), and the higher potential (2.54 V) is associated with the reversible reaction between viologen²⁺ (Viol^{2+})

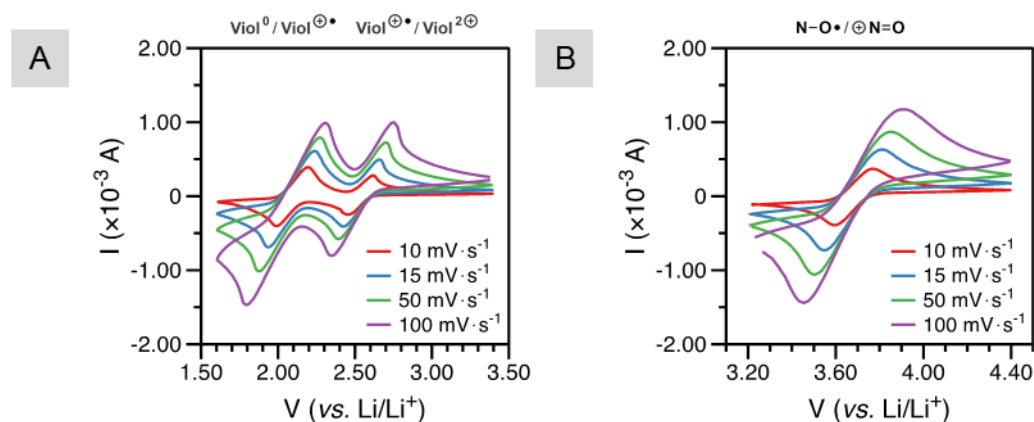


Figure 19. Cyclic voltammograms of (A) the viologen polypeptide and (B) the biTEMPO polypeptide thin films on ITO-coated glass in a three-electrode beaker cell configuration. The supporting electrolyte was 0.5 M LiCF_3SO_3 in propylene carbonate. Lithium metal was used as counter and reference electrodes.

and Viol^{\bullet} .^{70,73,123} The biTEMPO polypeptide exhibited one quasi-reversible redox peak at 3.69 V vs. Li/Li^+ , which is associated with the reversible reaction between the nitroxide radical (N-O^{\bullet}) and oxoammonium cation ($^+\text{N=O}$) (**Figure 19B**).⁶⁸ The peak current and peak separation for both the viologen and biTEMPO polypeptide thin films scaled with scan rate^{1/2}, indicative of a diffusion-limited reaction (**Appendix Figure 57** and **Appendix Figure 58**).^{68,132} Solution state cyclic voltammetry of the viologen and biTEMPO analogs (**Appendix Figure 56**) exhibited a similar response.

We next fabricated polypeptide composite electrodes (with carbon black (CB)/polyvinylidene fluoride (PVDF), 7 μm thick, 0.4-0.5 mg polypeptide $\cdot\text{cm}^{-2}$) for evaluation in lithium metal half cells. The theoretical capacities for the viologen and biTEMPO polypeptides are 85.7 and 71.3 $\text{mA}\cdot\text{h}\cdot\text{g}^{-1}$, respectively (**Equation 1**). The viologen polypeptide composite electrode (**Figure 20A**) exhibited two quasi-reversible redox couples at 2.08 V and 2.56 V vs. Li/Li^+ and a discharge capacity of 46.9 $\text{mA}\cdot\text{h}\cdot\text{g}^{-1}$ (*per g* of polypeptide) at 1 C (where 1 C is defined as the current required to reach full charge in 1 h), which decreased to 29.2 $\text{mA}\cdot\text{h}\cdot\text{g}^{-1}$ after 30 cycles (62% capacity retention). The biTEMPO polypeptide composite electrode exhibited one quasi-reversible redox peak at 3.68 V vs. Li/Li^+ and a discharge capacity of 23.9 $\text{mA}\cdot\text{h}\cdot\text{g}^{-1}$ at 1 C, which faded to 12.7 $\text{mA}\cdot\text{h}\cdot\text{g}^{-1}$ after 30 cycles (53 % capacity retention) (**Figure 20B**). The main mechanism of capacity fade is dissolution of the polypeptides into the electrolyte, as verified by solution-state CV of the electrolyte after galvanostatic cycling (**Appendix Figure 60**).¹³³

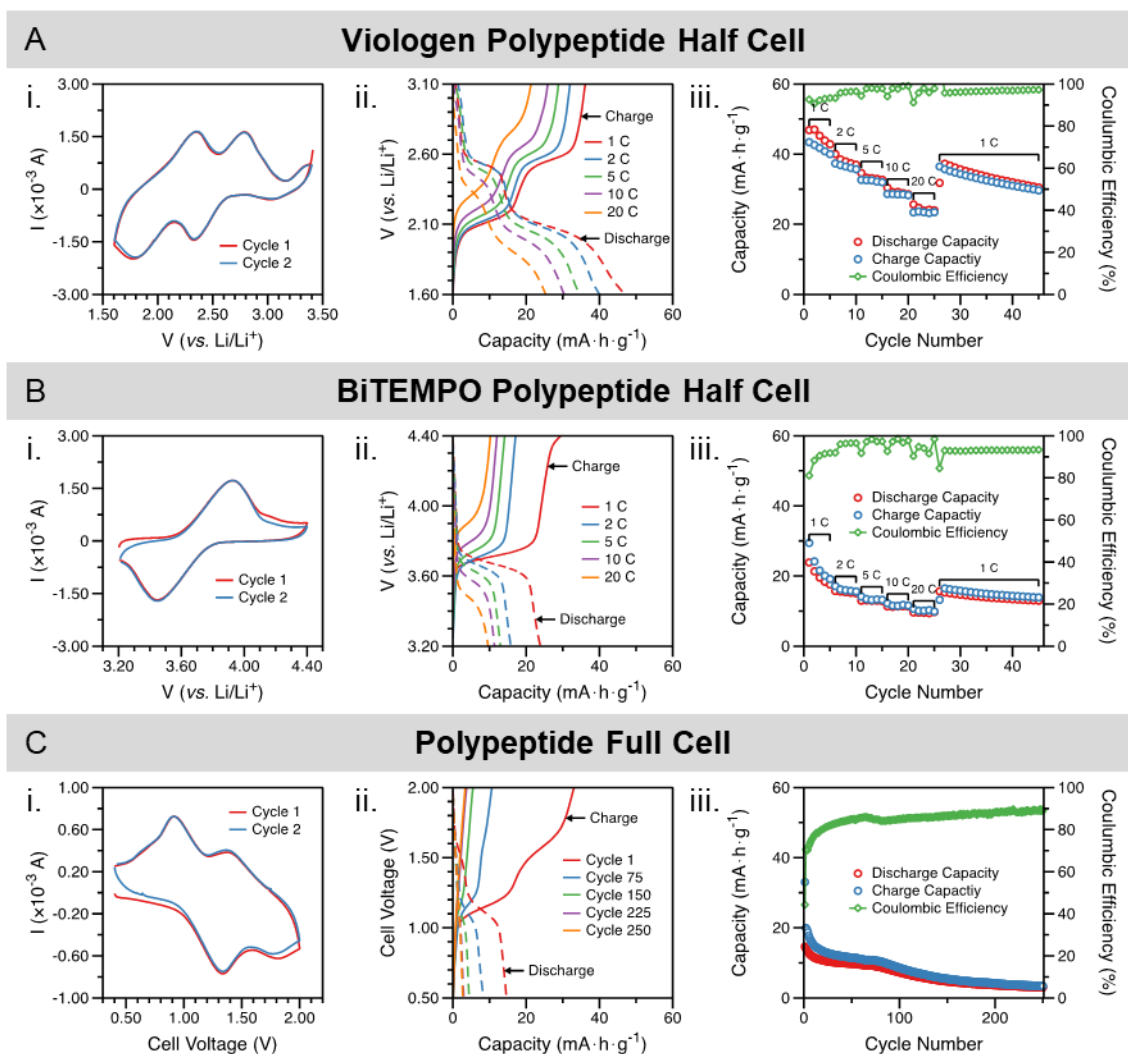


Figure 20. Electrochemical characterization of (A) viologen polypeptide composite half cell, (B) biTEMPO polypeptide composite half cell and (C) viologen/biTEMPO polypeptide full cell, including their **i.** cyclic voltammograms, **ii.** charge-discharge curves and **iii.** cycling response. (A) and (B) utilized a polypeptide composite electrode | 0.5 M LiCF₃SO₃ in PC + filter paper | lithium metal configuration while (C) utilized a viologen polypeptide composite electrode | 0.5 M LiCF₃SO₃ in PC + filter paper | biTEMPO polypeptide composite electrode configuration. The composite electrodes were composed of 30 wt% active polypeptide with 60 wt% CB and 10 wt% PVDF on ITO-coated glass. In **Aiii.** and **Biii.**, the C rates were varied, while in **Ciii.** the C-rate was constant at 1 C.

Finally, full polypeptide-based cells with viologen polypeptide composite anodes and biTEMPO polypeptide composite cathodes were prepared using filter paper soaked with electrolyte as the separator in a sandwich cell configuration. The theoretical capacity for the full polypeptide-based cell was calculated to be $38.9 \text{ mA}\cdot\text{h}\cdot\text{g}^{-1}$ (*per g* of biTEMPO polypeptide) according to **Equation 2**. Cyclic voltammetry resulted in two pairs of peaks centered around $E_{1/2} = 1.3$ and 1.6 V , consistent with the difference in redox potentials of the polypeptide composite anode and cathode. Cycling stability of the polypeptide-based battery was determined over 250 cycles of galvanostatic charging at 1 C. In the charge-discharge curves, two plateaus occurred at 1.1 V and 1.7 V (**Appendix Figure 62**). The charge capacity of the full cell at 1 C faded from an initial value of $33.0 \text{ mA}\cdot\text{h}\cdot\text{g}^{-1}$ (85% of the theoretical capacity) to $3.4 \text{ mA}\cdot\text{h}\cdot\text{g}^{-1}$ after 250 cycles (**Figure 20C**). The Coulombic efficiency was less than 100% for all cycles due to the dissolution of viologen and biTEMPO polypeptides into the electrolyte.¹³⁴ There was no visible delamination or morphological change in either composite electrode after 50 cycles (**Appendix Figure 59**).

Degradation of Viologen and BiTEMPO Polypeptides

The viologen and biTEMPO polypeptides are designed to contain amide linkages in the backbone and ester linkages in the side chains, which are prone to degradation in enzymatic, basic and acidic conditions. Hydrolysis of the redox-active polypeptides was evaluated under acidic conditions (0.01 M, 1 M and 6 M HCl) at r.t., $50 \text{ }^\circ\text{C}$, $80 \text{ }^\circ\text{C}$ and $110 \text{ }^\circ\text{C}$ (**Table 2**). No degradation was observed with 0.01 M HCl at any temperature

examined, nor with 1 M and 6 M HCl at r.t. and 50 °C. Partial degradation of the side chains was observed with 1 M and 6 M HCl at 80 °C. Complete degradation of the backbone and side chains for both polypeptides was observed with 1 M and 6 M HCl at 110 °C (**Figure 21**). Degradation of poly(γ -benzyl-L-glutamate)₅₀ (PBLG₅₀) - a model polypeptide - and the small-molecule viologen and biTEMPO analogs was also investigated in 1 M HCl at 110 °C to guide the identification of the degradation products generated from the backbones and side chains of the redox-active polypeptides, respectively. High resolution electrospray ionization mass spectrometry (ESI-HRMS, **Appendix Figure 63** to **Appendix Figure 66**) was utilized to identify the degradation species (DS), which were then verified by ¹H NMR spectroscopy (**Appendix Figure 71** and **Appendix Figure 72**).

[HCl] \ T	50 °C	80 °C	110 °C
0.01 M	No degradation	No degradation	No degradation
1 M	Partial degradation (side chains)	Partial degradation (side chains)	Complete degradation
6 M	Partial degradation (side chains)	Partial degradation (side chains)	Complete degradation

Table 2. Degradation conditions used for the viologen and biTEMPO polypeptides.

The viologen polypeptide backbone degraded into L-glutamic acid (**DS-1**) and n-hexylamine (**DS-2**) in their protonated forms, while the side chains were cleaved to yield **DS-3** and chlorinated derivative **DS-4** (**Figure 21** and **Appendix Figure 63**). In a similar manner, the biTEMPO polypeptide backbone also generated **DS-1** and **DS-2**, while the side chains were cleaved into **DS-5** and **DS-6** - the two degradation products of 4-hydroxy-

TEMPO (**Figure 21** and **Appendix Figure 65**), in addition to **DS-7** - the linker between glutamate units and TEMPO moieties (**Appendix Figure 66**). ^1H NMR spectra suggested that L-glutamic acid was regenerated in near quantitative amounts for both the viologen and biTEMPO polypeptides (**Appendix Figure 71** and **Appendix Figure 72**).

Liquid chromatography (LC) was employed successfully to separate degradation products of the redox-active polypeptides, their small-molecule analogs and the model polypeptide backbone PBLG₅₀ (**Appendix Figure 67** to **Appendix Figure 70**). The order of elution for the degraded viologen polypeptide in positive-ion mode from first to last was **DS-1**, **DS-3**, **DS-2**, and then **DS-4**. Similarly, the order of elution for the degraded biTEMPO polypeptide was **DS-1**, **DS-5**, **DS-2**, and **DS-6**. The linker **DS-7** was detected separately in the negative-ion mode (**Appendix Figure 70**). Together, these results demonstrate the on-demand degradation of the polypeptides and identification and separation of the degradation products.

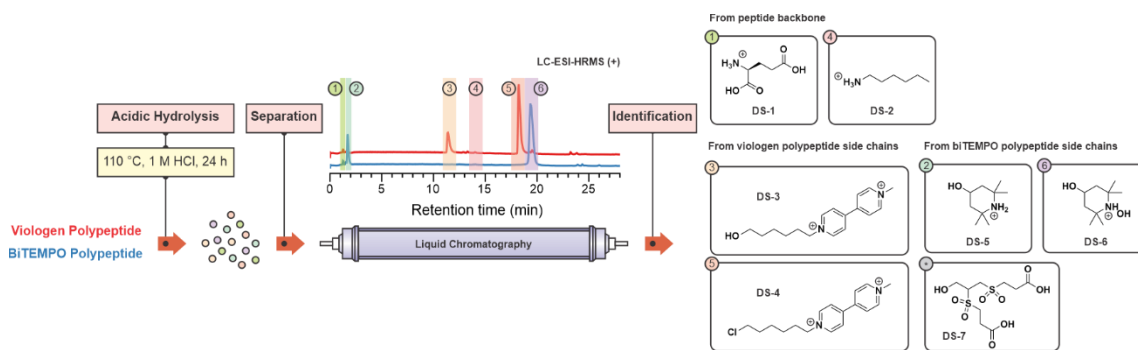


Figure 21. Liquid chromatography coupled with ESI-HRMS (LC-ESI-HRMS) was used to separate and identify the degradation products of the viologen and biTEMPO polypeptides (data from positive-ion mode shown).

Cell Viability Study

Cell viability testing with preosteoblast cells (MC3T3 cells), mouse fibroblast cells (NIH/3T3) and bovine coronary venular endothelial cells (CVECs) was conducted to evaluate the toxicity of the polypeptides, their repeat unit analogs and degradation products. In general, the viologen polypeptide was toxic towards MC3T3 and fibroblast cells due to its polycationic nature, whereas the biTEMPO polypeptide was deemed non-toxic towards all cell lines examined. The viologen polypeptide degradation products revealed lower toxicity effects towards all three cell lines tested compared to the original polypeptide, while the degradation products of the biTEMPO polypeptides exhibited no toxicity. A summary of the effect of the polypeptides, small-molecule analogs and their degradation products on cell viability can be found in **Figure 22** and **Appendix Figure 73** to **Appendix Figure 76**.

The viologen polypeptide exhibited no cytotoxicity towards CVECs ($IC_{50} > 100 \mu\text{g}\cdot\text{mL}^{-1}$), but showed cytotoxicity towards MC3T3 cells and fibroblasts at 1.52 and 2.68 $\mu\text{g}\cdot\text{mL}^{-1}$, respectively (**Figure 22** and **Appendix Figure 73**). In contrast, the viologen analog revealed no loss in cell viability towards MC3T3 cells and CVECs, showing IC_{50} values higher than 100 $\mu\text{g}\cdot\text{mL}^{-1}$ for both cell lines, but revealed some adverse effect on fibroblasts at 34.9 $\mu\text{g}\cdot\text{mL}^{-1}$ (**Figure 22** and **Appendix Figure 75**). This difference is hypothesized to originate from the polycationic nature of the viologen polypeptide that promoted cell membrane disruption and cell death. The higher IC_{50} values against CVECs may be complicated by the addition of heparin to the cell media, which is polyanionic and may complex to differing extents with the cationic viologen-based polypeptides, analogs

and degradation products. The biTEMPO polypeptide exhibited little to no cytotoxicity towards all three cell lines ($IC_{50} = 88.9, 63.2$ and $> 100 \mu\text{g}\cdot\text{mL}^{-1}$ towards MC3T3 cells, fibroblasts and CVECs, respectively) (**Figure 22** and **Appendix Figure 73**). While the small-molecule biTEMPO analog exhibited limited cytotoxicity towards MC3T3 and fibroblast cells ($IC_{50} = 55.9, 47.3 \mu\text{g}\cdot\text{mL}^{-1}$, respectively), it expressed a greater effect towards CVECs, having an IC_{50} value *ca.* three times lower ($IC_{50} = 17.3 \mu\text{g}\cdot\text{mL}^{-1}$) (**Figure 22** and **Appendix Figure 75**).

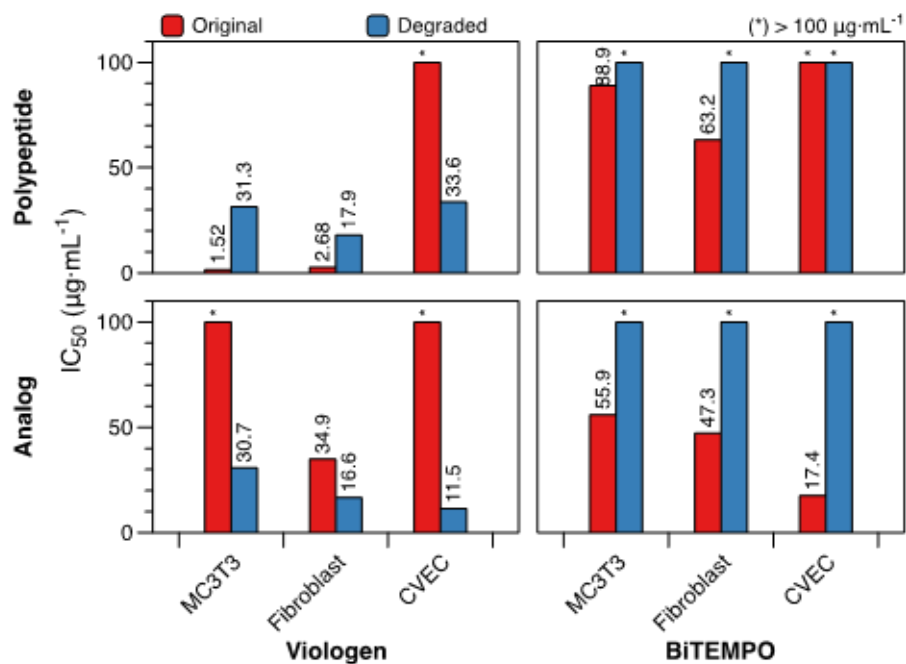


Figure 22. Cell viability study of viologen polypeptide, biTEMPO polypeptide, viologen analog, biTEMPO analog and their degradation products.

The degradation products for both polypeptides exhibited lower toxic effects compared to their original, undegraded forms and similar effects to the degradation

products of their corresponding small-molecule analogs (**Figure 22**, **Appendix Figure 74** and **Appendix Figure 76**). The viologen polypeptide degradation products expressed lower cytotoxicity at higher IC_{50} towards MC3T3 cells and fibroblasts ($IC_{50} = 31.3$ and $17.9 \mu\text{g}\cdot\text{mL}^{-1}$, respectively), when compared to the original polycationic viologen polypeptide ($IC_{50} = 1.52$ and $2.52 \mu\text{g}\cdot\text{mL}^{-1}$, respectively). Meanwhile, again, the toxicity for the degradation products being at much lower concentration towards CVECs ($IC_{50} = 33.6 \mu\text{g}\cdot\text{mL}^{-1}$, compared to higher than $100 \mu\text{g}\cdot\text{mL}^{-1}$ of the original viologen polypeptide) may be complicated by increased positive charge density of the degradation compounds in addition to the effect of heparin in the cell media. The degradation products of biTEMPO polypeptide and biTEMPO analog showed no toxicity towards all three cell lines ($IC_{50} > 100 \mu\text{g}\cdot\text{mL}^{-1}$) (**Appendix Figure 74** and **Appendix Figure 76**).

Conclusion

In summary, we designed an all-polypeptide organic radical battery comprised of redox-active amino-acid macromolecules that degrade on-demand. This concept represents an early step toward addressing sustainable, recyclable batteries for a circular economy and minimizing global dependence on strategic metals. Viologen and biTEMPO polypeptide anodes and cathodes, respectively, were synthesized *via* ROP of highly reactive cyclic NCAs, followed by sequential post-polymerization modifications to incorporate the redox-active groups. The polypeptide battery reached a maximum charge capacity of $33.0 \text{ mA}\cdot\text{h}\cdot\text{g}^{-1}$ (out of the theoretical $38.9 \text{ mA}\cdot\text{h}\cdot\text{g}^{-1}$) at 1 C. The active components degraded on demand in the presence of acid to regenerate the starting amino

acids and other building blocks. Looking to the future, the main challenges here are to prevent dissolution of the active material and to boost the overall cell capacity. Future studies will focus on preventing dissolution of both polypeptides by crosslinking¹³⁵ or post-processing modification¹³⁶ or by taking advantage of the polypeptide's solubility in flow battery cells.

CHAPTER IV

POLYPEPTIDE REDOX FLOW BATTERIES

Introduction

Redox flow batteries (RFBs) are considered to be the future of large-scale energy storage for their safety features, high energy density and long cycle life.^{80,81} However, current RFB technologies rely heavily on the use of vanadium and other mineral resources, which are facing a surge in price due to supply scarcity. Organic redox-active materials in general and small-molecule redox species in particular are constructed from renewable and zero-emission sources and have been emerging as greener alternatives to tackle the issues of inorganic counterparts. Unlike vanadium-based RFBs which depend on aqueous electrolytes, small-molecule organic molecules can be used in either aqueous or non-aqueous systems.^{84–86} The operation of aqueous organic RFBs (AORFBs) take advantage of the use of water, the ideal green chemistry solvent, but is often faced with the adverse effect caused by excessive protons and hydroxides in acidic and alkaline condition, respectively. The non-aqueous organic RFBs (NAORFBs), even though eliminating the dependence on pH, remain in need of new material designs that address the low solubility of active materials during charge transfer processes.

In either system, crossover of the redox active centers remains a major challenge that inhibits the widespread application of redox flow batteries.^{84–86} Recently, significant efforts were made to tackle this issue, ranging from the use of ion-exchange membranes and porous membranes to the oligomerization/polymerization of redox-active

moieties.^{79,81,89-94} Some examples include the use of viologen- and TEMPO-containing polymethacrylates by Janoschka *et al.* for aqueous RFBs and polystyrenes carrying similar redox-active centers by Montoto *et al.* for non-aqueous RFBs.^{123,137} One disadvantage, however, of these systems is the use non-degradable polymer backbones. In Chapter II, we reported the use of viologen- and TEMPO-containing polypeptides as redox-active materials for secondary batteries. This system, though demonstrating the first report of batteries with naturally-derived, degradable materials, was still faced with fast capacity fading due to the dissolution of active materials into electrolytes during cell cycling. In this project, we exploited this high solubility of the redox-active polypeptides, viologen and biTEMPO polypeptides, in organic solvents for non-aqueous organic RFBs (**Figure 23A**), while imparting the degradability of the polymer backbones, as a promising candidate for large-scale storage with enhanced sustainability feature. Small-molecule analogs of the polypeptides (**Figure 23B**) were also employed as active materials as a control.

Experimental Section

Materials

1. For Chemical Processes

3,3-Dithiodipropionic acid, 4,4'-dipyridine, *meta*-chloroperoxybenzoic acid (*m*-CPBA, $\leq 77\%$), dichloromethane (DCM), *N,N'*-dicyclohexylcarbodiimide (DCC), 4-dimethylaminopyridine (DMAP), 2,2-dimethoxy-2-phenylacetophenone (DMPA),

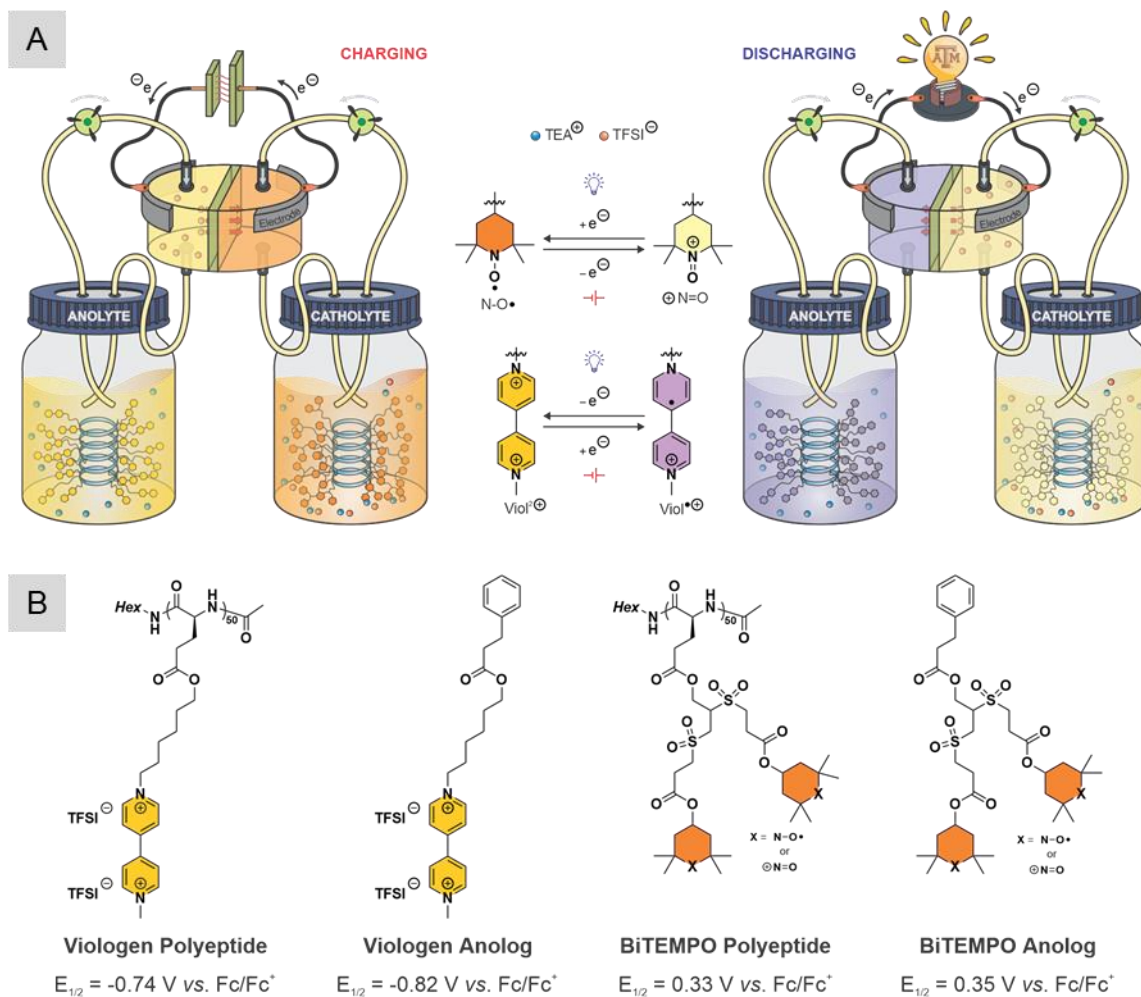


Figure 23: (A) Illustrative design of peptide-based redox flow battery during charging and discharging. (B) Molecular structures of the redox-active polypeptides and their small-molecule analogs.

N,N-dimethylformamide (DMF), dimethylsulfoxide (DMSO), 4-hydroxy-2,2,6,6-tetramethylpiperidine-1-oxyl (4-OH-TEMPO, TEMPOL), diphosgene, hexanes, *n*-hexylamine, hydrocinnamic acid, iodomethane, iron (II) sulfate heptahydrate (FeSO₄•7H₂O), L-glutamic acid, methanol, propargyl alcohol, sodium iodide (NaI), triethylamine (TEA), trifluoroethanol (TFE), trimethylsilyl chloride (TMSCl) and triphosgene were purchased from Sigma-Aldrich. DL-Dithiothreitol (DTT) was purchased

from Tokyo Chemical Industry (Japan). 6-Chloro-1-hexanol and acetic anhydride were purchased from Alfa-Aesar (USA). All reagents were used as received, except for propargyl alcohol, which was distilled under an atmosphere of N₂ prior to use. Ultrapure water (water) was collected from a Milli-Q® integral water purification system (18 MΩ·cm). Lithium bis(trifluoromethane)sulfonamide (LiTFSI) was purchased from Alfa Aesar (USA).

2. For Electrochemical Processes

Tetraethylammonium bis(trifluoromethane)sulfonamide (TEATFSI, 99%) was purchased from IoLiTec (Germany). Acetonitrile (ACN, 99.98%) was purchased from BASF (USA). The flow cell membranes Daramic 175 and FAPQ-375-PP were purchased from Daramic LLC (USA) and Fumatech BWT GmbH (Germany). The Daramic 175 membrane was used as received. The FAPQ 375 PP membrane was immersed in 0.5 M TEATFSI/ACN for a minimum of three days to ensure full ion exchange and swelling prior to use according to previous reports.¹³⁸ The glassy carbon macroelectrode, 11 μm diameter carbon fiber microelectrode and gold coil were purchased from CH Instruments, Inc (USA). Ferrocene (98%) was purchased from Sigma-Aldrich (USA). The fritted Ag/Ag⁺ electrode was filled with 0.1 M AgBF₄ (99%, Alfa Aesar, USA) solution, 0.5 M TEATFSI and propylene carbonate (99.98%, BASF, USA).

An H-type small-volume flow cell with interdigitated flow fields was custom-built with the backing plates machined from polypropylene and flow fields machined in-house from 3.18 mm thick impregnated graphite (product G347B, MWI, Inc., USA).¹³⁹ The

electrodes were cut to 1.7 cm × 1.5 cm dimensions from 190 ± 30 μm thick carbon paper (SGL 29 AA, SGL group, Wiesbaden, Germany) and used as received. Two pieces of carbon paper were layered on each side of the flow cell and compressed by *ca.* 20% during cell assembly. The two sides of the cell were separated with an FAPQ 375 PP membrane and sealed using a polytetrafluoroethylene gasket tape (Goretex Tape, Gallagher Fluid Seals, Inc., USA) with a geometric area of 2.55 cm². All flow cell assemblies were done on the laboratory bench prior to immediate transfer into an argon-filled glovebox (Innovative Technology, Inc., USA, O₂ < 10 ppm, H₂O < 0.1 ppm).

The electrolytes were stored in perfluoroalkoxy alkane (PFA) jars (10 mL, Savillex, USA). Peristaltic pumps (Masterflex, Germany, L/S series) recirculated the electrolytes at a constant volumetric flow rate of 10 mL·min⁻¹ *via* Norprene tubing (1.6 mm I.D., Masterflex, Germany) inside the pump head and PFA tubing (1.6 mm I.D., Swagelok, USA) from the reservoirs to the flow cell. The two types of tubing were connected using stainless steel compression fittings (Swagelok, USA).

Syntheses of Redox-active Polypeptides and their Small-molecule Analogs

The viologen-iodide and biTEMPO polypeptides and their small-molecule analogs were synthesized as reported in Chapter III. To enhance the solubility of the viologen species in ACN, iodide anions of the viologen-iodide polypeptide and analog were exchanged for TFSI prior to testing. The anion exchange was done upon mixing a solution of each viologen species with an equal volume of LiTFSI (6 eq), both in H₂O. The precipitate was collected *via* centrifugation, dissolved into ACN and precipitated into 0.5

M LiTFSI in H₂O (× 3), followed by precipitation into H₂O (× 3). The viologen-TFSI polypeptide was obtained as a brown solid and the viologen-TFSI analog as a brown viscous oil.

Chemical Characterization

Attenuated total reflectance-Fourier transform infrared (ATR-FTIR) spectra were recorded for powder samples on an IR Prestige 21 system (Shimadzu Corp., Japan) and analyzed using IRsolution v. 1.40 software.

Electrochemical Characterization

All electrochemical measurements were performed in an argon-filled glovebox with a VSP-300 potentiostat (Bio-Logic, France) unless otherwise noted. All calculations for polymers were done based on the molecular weight of the repeat units.

1. Cyclic Voltammetry

All cyclic voltammetry (CV) measurements were performed in an argon-filled glovebox at ambient glovebox temperature. CV measurements were performed in 0.5 M TEATFSI/ACN with either a 3 mm diameter glassy carbon macroelectrode or an 11 μm diameter carbon fiber microelectrode. Before each measurement, both working electrodes were polished on a MicroCloth pad containing an aqueous slurry of 0.05 μm alumina powder (Buehler Ltd., USA), rinsed with deionized water, and wiped with lens paper. For all experiments, a gold coil and a fritted Ag/Ag⁺ electrode were used as the counter

electrode and the pseudo reference electrode, respectively. To reference the measured redox potentials to the ferrocene/ferrocenium (Fc/Fc^+) redox couple, before each measurement, an additional CV was taken in the electrolyte containing 5 mM ferrocene. The viologen-TFSI polypeptide exhibited two redox processes at $E_{1/2} = -0.74$ V ($\text{Viol}^{2+}/\text{Viol}^{+\bullet}$) and -1.22 V ($\text{Viol}^{+\bullet}/\text{Viol}^0$) vs. Fc/Fc^+ , while the biTEMPO polypeptide exhibited one redox process at $E_{1/2} = 0.33$ V ($\text{N-O}^\bullet/{}^+\text{N=O}$) vs. Fc/Fc^+ . Similarly, the viologen-TFSI analog exhibited two redox processes at $E_{1/2} = -0.82$ V ($\text{Viol}^{2+}/\text{Viol}^{+\bullet}$) and -1.22 V ($\text{Viol}^{+\bullet}/\text{Viol}^0$) vs. Fc/Fc^+ , while the biTEMPO analog exhibited one redox process at $E_{1/2} = 0.35$ V ($\text{N-O}^\bullet/{}^+\text{N=O}$) vs. Fc/Fc^+ . For the scope of this project, only the first redox process of the viologen moieties ($\text{Viol}^{2+}/\text{Viol}^{+\bullet}$) was assessed for both systems, resulting in an open circuit voltage of 1.07 and 1.17 V for the polypeptide cell and viologen cell, respectively.

2. Crossover Tests

The crossover test of the redox-active polypeptides and their analogs was performed in the flow cell using two types of membranes, Daramic 175 and FAPQ 375 PP. One side of the flow cell was filled with the electrolyte solution (3.5 mL, 0.5 M TEATFSI/ACN) containing the tested species (20 mM) and the other with the electrolyte solution (3.5 mL, 0.5 M TEATFSI/ACN). Aliquots of the latter were taken after 6, 12, 24, 48, 72 and 96 h for microelectrode CV. As a result, FAPQ 375 PP was selected for flow cell cycling studies.

3. Flow Cell Cycling

The anolyte used in the flow cell studies consisted of 0.5 M viologen polypeptide/analog and the catholyte 0.25 mM BiTEMPO polypeptide/analog in 0.5 M TEATFSI in ACN. The theoretical capacity of these electrolytes was calculated using **Equation 6** to be $1.34 \text{ A}\cdot\text{h}\cdot\text{L}^{-1}$ ($10.1 \text{ mA}\cdot\text{h}$), assuming one electron transfer event and 7.5 mL of electrolyte *per side* (15 mL total). All cycling experiments were performed by applying a constant current density, which was determined from the geometric electrode area (2.55 cm^2). For the rate study, the current density was varied from 5 to $25 \text{ mA}\cdot\text{cm}^{-2}$, in increments of $5 \text{ mA}\cdot\text{cm}^{-2}$, for 5 cycles at each current density, with a potential window between 0.60-1.60 V. The cell was then returned to its initial current density of $10 \text{ mA}\cdot\text{cm}^{-2}$ for 5 additional cycles. For the stability study, the flow cells underwent constant current cycling for 500 cycles (109 h and 94 h for the polypeptide and analog cells, respectively) at a current density of $10 \text{ mA}\cdot\text{cm}^{-2}$, with a potential window between 0.60-1.60 V.

Results and Discussion

Syntheses of Redox-active Polypeptides and their Small-molecule Analogs

The viologen and biTEMPO polypeptides were prepared similarly as reported in Chapter III, both starting with L-glutamic acid as a common starting amino acid. The two divergent five-step synthetic pathways began with esterification of L-glutamic acid to install a chloro or alkynyl group through an alkyl spacer selectively at the γ -position, followed by reaction with phosgene to produce the *N*-carboxyanhydride (NCA)

monomers, which were then subjected to ROP to afford the corresponding chloro- or alkynyl-functionalized poly(L-glutamate)s. They then diverged with different strategies of sequential post-polymerization modifications to incorporate a single pendant viologen and dual TEMPO moieties. On one hand, the chloro-containing polypeptide underwent activation, replacing chlorine atoms with iodine atoms *via* Finkelstein reaction to obtain the iodo-containing polypeptide followed by installation of the redox-active moieties. On the other hand, the alkynyl-containing polypeptide was installed with inactive precursors followed by a subsequent activation step to generate the redox-active TEMPO moieties. Synthesis details of the viologen and biTEMPO polypeptides can be found in **Figure 17**. To enhance the solubility of the former polymer in organic solvent, its iodide counterions were exchanged for TFSI to afford viologen-TFSI polypeptide. Detailed synthetic procedures, characterization and the yield for each synthetic step can be found in **Chapter III** and the **Appendix B**.

The viologen and biTEMPO analogs were synthesized in a similar manner, as compared to their polypeptide counterparts. The two four-step synthetic pathways began with esterification of hydrocinnamic acid, a compound widely used in the food and beauty industries, to incorporate the chloro- and alkynyl-functionalities. Similar to the syntheses of the redox-active polypeptides, the synthesis pathways of the two analogs also diverged with different strategies of sequential modifications to incorporate a single pendant viologen and dual TEMPO moieties. While the chloro-containing hydrocinnamate underwent activation, replacing chlorine atoms with iodine atoms *via* Finkelstein reaction to obtain the iodo-containing hydrocinnamate followed by installation of the redox-active

moieties, the alkynyl-containing hydrocinmate was installed with inactive precursors followed by a subsequent activation step to generate the redox-active TEMPO moieties. Synthesis details of the viologen-iodide and biTEMPO analogs can be found in **Appendix Figure 17** and **Appendix Figure 18**. The iodide counterions of the former species were also exchanged for TFSI to afford the viologen-TFSI analog. Detailed synthetic procedures, characterization and the yield for each synthetic step can be found in **Chapter III** and **Appendix B**.

Crossover Tests

To determine the proper separator for the flow cell assembly, two different types of membranes, FAPQ 375 PP - an anion-exchange membrane (AEM) - and Daramic 175 - a porous membrane - were subject to crossover testing. The H-shaped flow cell was filled with each redox-active species in electrolyte solution in one side, connected *via* a membrane to the other side containing the electrolyte solution of equal volume. Aliquots of the latter solution were taken after 6, 12, 24, 48, 72 and 96 h for microelectrode CV. As expected, significant crossover was observed for both the redox-active polypeptides and their small-molecule analogs using the Daramic 175 membrane due to its large pore size.^{138,140} Compared to the porous membrane, the FAPQ 375 PP membrane allowed for considerably lower crossover of the small molecules over multiple days while no membrane permeation was observed for the polypeptides. As a result, this AEM was chosen for flow cell cycling studies.

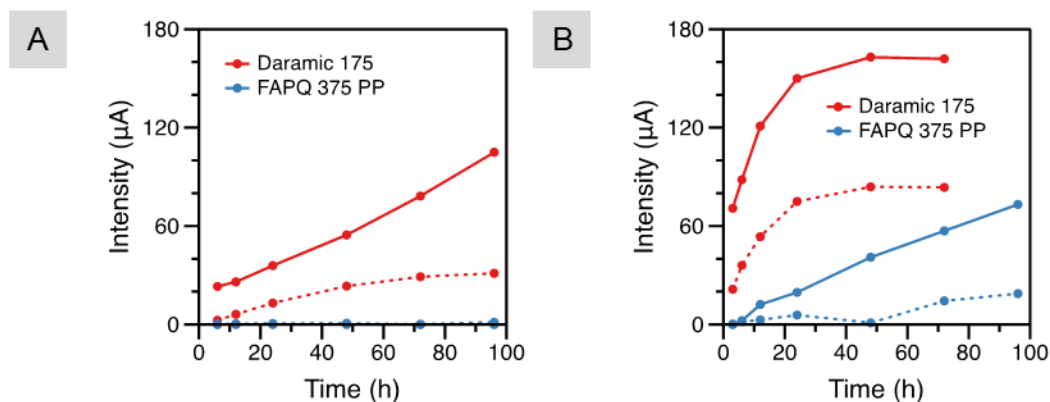


Figure 24. Crossover study of (A) the redox-active polypeptides and (B) their small-molecule analogs using Daramic 175 and FAPQ 375 PP membranes. Solid lines = viologen species, dashed lines = biTEMPO species.

Flow Cell Cycling

Although the redox-active species exhibit a solubility in excess of 1 M, for the scope of this project as proof of concept of peptide-based NARFBs, two flow cells with 50 mM effect concentration of active centers in 0.5 M TEATFSI in ACN were assembled, one with the viologen-TFSI and biTEMPO polypeptides as negolytes and posolytes, respectively, and the other with their small-molecule analogs. The two flow cells were cycled within the potential windows between 0.6 to 1.6 V. Each reservoir contained 7.5 mL of the redox-active species solution, giving the theoretical capacity of the flow cells to be $1.34 \text{ A}\cdot\text{h}\cdot\text{L}^{-1}$.

The variable rate experiment was first performed to determine the trade-off between applied current density, overpotential and accessed capacity, in addition to identifying an appropriate current density. The two flow cells were cycled at current densities of 5, 10, 15 and $20 \text{ mA}\cdot\text{cm}^{-2}$ for five cycles each, followed by five more cycles at $5 \text{ mA}\cdot\text{cm}^{-2}$. The charge and discharge capacities with the Coulombic efficiencies at

each current density are shown in **Figure 25**. As expected, the accessed capacities decreased as current densities increase, which is due to the larger cell polarization present at high current densities. At $5 \text{ mA}\cdot\text{cm}^{-2}$, the polypeptide flow cell presented a capacity utilization of 59% (out of the theoretical $1.34 \text{ A}\cdot\text{h}\cdot\text{L}^{-1}$), which decreased to 38% at $10 \text{ mA}\cdot\text{cm}^{-2}$, 13% at $10 \text{ mA}\cdot\text{cm}^{-2}$ and completely faded at $20 \text{ mA}\cdot\text{cm}^{-2}$. The analog flow cell presented a lower capacity utilization of 47% at $5 \text{ mA}\cdot\text{cm}^{-2}$, then faded to 34% at $10 \text{ mA}\cdot\text{cm}^{-2}$, 20% at $15 \text{ mA}\cdot\text{cm}^{-2}$ and *ca.* 0% at $20 \text{ mA}\cdot\text{cm}^{-2}$. As evidenced by the first and last sets of $10 \text{ mA}\cdot\text{cm}^{-2}$, the capacity of both the flow cells assembled faded by less than 5%, demonstrating that high current densities did not have significantly adverse impacts on cell performance.

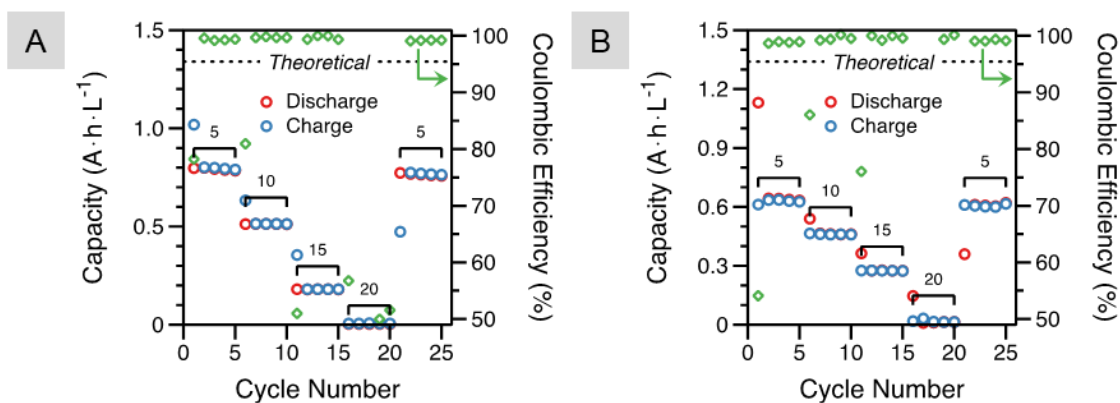


Figure 25. Rate study of the (A) polypeptide and (B) small-molecule analog NAORFBs.

Constant current cycling was then performed to evaluate the long-term stability of the polypeptide and analog flow cells at $10 \text{ mA}\cdot\text{cm}^{-2}$ (**Figure 26**). This current density

was chosen to balance experimental runtime and the impact of charge/discharge overpotential on accessed capacity. In this cycling experiment, the polypeptide flow cell started with a capacity utilization of $0.39 \text{ A}\cdot\text{h}\cdot\text{L}^{-1}$ (29% of the theoretical capacity) and reached its maximum of $0.53 \text{ A}\cdot\text{h}\cdot\text{L}^{-1}$ (39% of the theoretical capacity) at cycle 12 (**Figure 26A**). From this point on, the capacity faded to 93% and 60% of the original value after 250 and 500 cycles, respectively. The entire experiment ran for 109 h, with the capacity

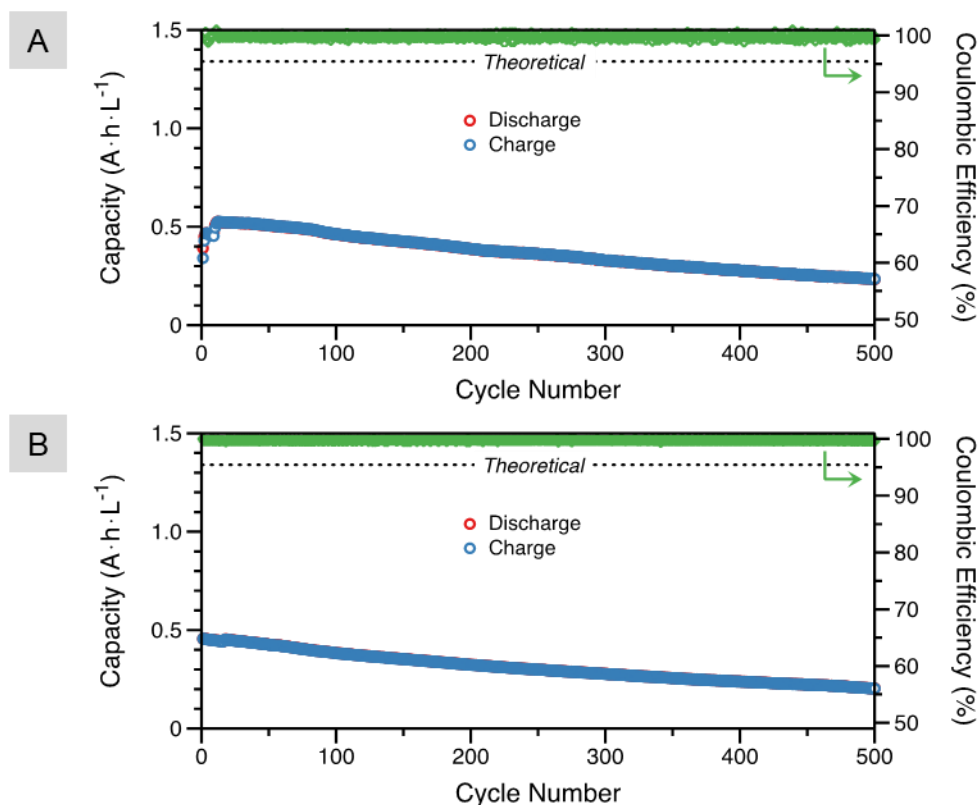


Figure 26. Constant current cycling of the (A) polypeptide and (B) small-molecule analog NAORFBs.

fading 0.06% *per h*. In a similar manner, the analog flow cell started with a capacity utilization of $0.44 \text{ A}\cdot\text{h}\cdot\text{L}^{-1}$ (33% of the theoretical capacity) and reached its maximum of

0.50 A·h·L⁻¹ (37% of the theoretical capacity) at cycle 3 (**Figure 26B**). From this point on, the capacity then faded to 60% and 36% of the original value at 250 and 500 cycles, respectively, with a total runtime of 94 h. Compared to the polypeptide counterpart, the capacity of the analog flow cell faded with much faster rate (0.59% *per h*). The performance decay of the two systems was possibly due to a combination of cell polarization and active material crossover and degradation. Attenuated total reflection Fourier-transform infrared spectra of the polypeptide electrolyte solutions before and after cycling demonstrated that the polypeptide backbones remained in their α -helical form (**Appendix Figure 79** and **Appendix Figure 80**), suggesting that the capacity fading was indeed due to the degradation of the redox-active centers.

Conclusion

In summary, we designed and tested an all-polypeptide NAORFB with the active materials that had been shown to degrade on demand. This concept represents an early step toward developing large-scale energy storage with enhanced sustainability of active materials and alleviating global dependence on strategic metals. The viologen-TFSI and biTEMPO polypeptide electrolytes were synthesized *via* ROP of highly reactive cyclic NCAs, followed by sequential post-polymerization modifications to incorporate the redox-active groups. The small-molecule analogs of the polypeptides were also prepared and tested in an NAORFB for comparison purposes. At 10 mA·cm⁻², the polypeptide flow cell started with a capacity of 0.39 A·h·L⁻¹ (29% of the theoretical capacity), its maximum of 0.53 A·h·L⁻¹ (38% of the theoretical capacity) at cycle 12 and faded to 60% of the

original value after 500 cycles (109 h). In a similar manner, the analog cell started with a capacity of $0.46 \text{ A}\cdot\text{h}\cdot\text{L}^{-1}$ (34% of the theoretical capacity) then faded to 45% of the original value after 500 cycles (94 h). In overall, the analog cell faded at faster rate compared to the polypeptide cell due to higher rate of crossover. Potential capacity fading mechanism can be a combination of cell polarization and active material crossover and degradation, and will be the scope a future study.

CHAPTER V

CONCLUSIONS

Synthetic polypeptides constitute an interesting class of polyamides. Their beauty lays not only in their on-demand degradation to generate the starting building blocks for recycling and upcycling purposes, but also in their potential tunability of structure-property-performance parameters. Exploiting the inherent degradability and conformations of peptides to direct the properties of the polymer networks, this dissertation is focused on the development of advanced functional polypeptides for use as extracellular matrices for cell therapeutics and as electroactive materials for battery applications.

Supramolecularly-assembled hydrogels constructed from synthetic peptides have emerged as an attractive option for three-dimensional (3D) cell cultures due their intrinsic biocompatibility and feasible tunability of structure-property-performance parameters. An alkenyl-functionalized amino acid, DL-allylglycine (DLAG), was cyclized *via in situ* phosgenation to produce *N*-carboxyanhydride (NCA) monomers. Subsequent ring-opening polymerization (ROP) with PEGylated amines yielded poly(ethylene glycol)₄₅-*block*-poly(DLAG)_n (PEG₄₅-*b*-PDLAG_n) with varying lengths of the PDLAG segments (**P-20** with $n = 20$ and **P-30** with $n = 30$) to establish different hydrophilic-hydrophobic ratios. Rheology measurements of the polypeptides in cell media suggested that the hydrogels formed from 4% w/v of **P-30** (**P-30-4%**) were deemed suitable for 3D cell cultures for achieving self-supporting strengths within 1 h. Cell cultures using **P-30-4%**

hydrogels demonstrated that this system indeed provided livable environments for cell growth. Follow-up studies will focus on the incorporation of fluorescence dyes onto the PEGylated polypeptides to track gel locations during cell cultures and the application of these supramolecularly-assembled hydrogels for the treatment of spinal cord injuries.

Peptide-based materials have been studied extensively for biomedical applications, yet there are limited precedents of their applicability in energy storage. The intrinsic degradability of peptides, in addition to the ability of their backbones to self-assemble into various 3D structures, makes them a promising candidate for battery applications to embed sustainability features into current energy storage systems that are in need of safer and more environmentally friendly active materials while enabling structure-property tunability for performance improvement. Over the past few decades, rechargeable lithium-ion batteries and metal-based redox flow batteries have revolutionized our modern life, addressing the increasing energy need at various scales and impacting the wealth and well-being of society. This rapid development has, however, outgrown the ability to tackle issues associated with the ethical mining, safe usage and non-hazardous disposal of precious strategic elements such as lithium, cobalt, vanadium and other mineral ore resources. Inspired by the properties of peptide-based materials, an all-polypeptide-based rechargeable secondary battery is demonstrated, in which redox-active viologens and nitroxide radicals are incorporated as redox-active groups along peptide backbones to function as anode and cathode materials, respectively. The polypeptide battery reached a maximum charge capacity of $33.0 \text{ mA}\cdot\text{h}\cdot\text{g}^{-1}$ (84% of the theoretical capacity) at 1 C. The anodic and cathodic active materials, viologen and biTEMPO polypeptides, respectively,

were synthesized *via* ROP of highly reactive cyclic NCAs, followed by sequential post-polymerization modifications to incorporate the redox-active groups. They were also demonstrated to degrade on demand in the presence of acid to regenerate the starting amino acids and other building blocks. This peptide-based rechargeable battery, though demonstrating that it is possible to fabricate batteries from with naturally-derived, degradable materials, was still faced with fast capacity fading due to the dissolution of active materials into electrolytes during cell cycling (8% capacity retention after 250 cycles). Thus, the high solubility of the redox-active polypeptides in organic solvents was exploited for use in non-aqueous organic redox flow batteries. The polypeptide flow cell started with a discharge capacity of $0.39 \text{ A}\cdot\text{h}\cdot\text{L}^{-1}$ (29% of the theoretical capacity) at $10 \text{ mA}\cdot\text{cm}^{-2}$, reached a maximum discharge capacity of $0.53 \text{ A}\cdot\text{h}\cdot\text{L}^{-1}$ (39% of the theoretical capacity) after 12 cycles and were able to maintain 60% of the initial value even after 500 cycles. These peptide-based batteries still have a long way to go before commercialization, but represent the first step in addressing the need for alternative chemistries for green and sustainable batteries in the future circular economy. Follow-up studies will focus on (1) preventing dissolution of both polypeptides in secondary batteries (by crosslinking or post-processing), (2) recycling the redox-active polypeptides from the constructed batteries to demonstrate material circularity, (3) alternative synthetic strategies to reduce the cost of production and (4) studying the effect of conformations (random coil *vs.* α -helix *vs.* β -sheet) on the kinetics of electron transfer of redox-active polypeptides in both secondary and flow configurations.

REFERENCES

- (1) Van Hest, J. C. M. Peptide Conjugates for Biological Applications. *Bioconjug. Chem.* **2017**, 28 (3), 689–690. <https://doi.org/10.1021/acs.bioconjchem.7b00102>.
- (2) Chen, J.; Zou, X. Self-Assemble Peptide Biomaterials and Their Biomedical Applications. *Bioact. Mater.* **2019**, 4, 120–131. <https://doi.org/10.1016/j.bioactmat.2019.01.002>.
- (3) Lovley, D. R. E-Biologics: Fabrication of Sustainable Electronics with “Green” Biological Materials. *MBio* **2017**, 8 (3). <https://doi.org/10.1128/mBio.00695-17>.
- (4) Ardoña, H. A. M.; Tovar, J. D. Peptide π -Electron Conjugates: Organic Electronics for Biology? *Bioconjug. Chem.* **2015**, 26 (12), 2290–2302. <https://doi.org/10.1021/acs.bioconjchem.5b00497>.
- (5) He, X.; Fan, J.; Zou, J.; Wooley, K. L. Reversible Photo-Patterning of Soft Conductive Materials via Spatially-Defined Supramolecular Assembly. *Chem. Commun.* **2016**, 52 (54), 8455–8458. <https://doi.org/10.1039/C6CC03579E>.
- (6) Huang, J.; Hastings, C. L.; Duffy, G. P.; Kelly, H. M.; Raeburn, J.; Adams, D. J.; Heise, A. Supramolecular Hydrogels with Reverse Thermal Gelation Properties from (Oligo)Tyrosine Containing Block Copolymers. *Biomacromolecules* **2013**, 14 (1), 200–206. <https://doi.org/10.1021/bm301629f>.
- (7) Fan, J.; Li, R.; Wang, H.; He, X.; Nguyen, T. P.; Letteri, R. A.; Zou, J.; Wooley, K. L. Multi-Responsive Polypeptide Hydrogels Derived from N-Carboxyanhydride Terpolymerizations for Delivery of Nonsteroidal Anti-Inflammatory Drugs. *Org.*

- Biomol. Chem.* **2017**, *15* (24), 5145–5154. <https://doi.org/10.1039/C7OB00931C>.
- (8) He, X.; Fan, J.; Zhang, F.; Li, R.; Pollack, K. A.; Raymond, J. E.; Zou, J.; Wooley, K. L. Multi-Responsive Hydrogels Derived from the Self-Assembly of Tethered Allyl-Functionalized Racemic Oligopeptides. *J. Mater. Chem. B* **2014**, *2* (46), 8123–8130. <https://doi.org/10.1039/C4TB00909F>.
- (9) Jeong, Y.; Joo, M. K.; Bahk, K. H.; Choi, Y. Y.; Kim, H.-T.; Kim, W.-K.; Jeong Lee, H.; Sohn, Y. S.; Jeong, B. Enzymatically Degradable Temperature-Sensitive Polypeptide as a New in-Situ Gelling Biomaterial. *J. Control. Release* **2009**, *137* (1), 25–30. <https://doi.org/10.1016/j.jconrel.2009.03.008>.
- (10) Park, M. H.; Joo, M. K.; Choi, B. G.; Jeong, B. Biodegradable Thermogels. *Acc. Chem. Res.* **2012**, *45* (3), 424–433. <https://doi.org/10.1021/ar200162j>.
- (11) Song, Z.; Fu, H.; Wang, R.; Pacheco, L. A.; Wang, X.; Lin, Y.; Cheng, J. Secondary Structures in Synthetic Polypeptides from *N*-Carboxyanhydrides: Design, Modulation, Association, and Material Applications. *Chem. Soc. Rev.* **2018**, *47* (19), 7401–7425. <https://doi.org/10.1039/C8CS00095F>.
- (12) Bonduelle, C. Secondary Structures of Synthetic Polypeptide Polymers. *Polym. Chem.* **2018**, *9* (13), 1517–1529. <https://doi.org/10.1039/C7PY01725A>.
- (13) Leuchs, H. Ueber Die Glycin-Carbonsäure. *Berichte der Dtsch. Chem. Gesellschaft* **1906**, *39* (1), 857–861. <https://doi.org/10.1002/cber.190603901133>.
- (14) Gradišar, Š.; Žagar, E.; Pahovnik, D. Ring-Opening Polymerization of *N*-Carboxyanhydrides Initiated by a Hydroxyl Group. *ACS Macro Lett.* **2017**, *6* (6), 637–640. <https://doi.org/10.1021/acsmacrolett.7b00379>.

- (15) Kricheldorf, H. R. Polypeptides and 100 Years of Chemistry of Alpha-Amino Acid N-Carboxyanhydrides. *Angew. Chem. Int. Ed. Engl.* **2006**, *45* (35), 5752–5784. <https://doi.org/10.1002/anie.200600693>.
- (16) Kricheldorf, H. Mechanism of the NCA-polymerization, 5. Catalysis by Secondary Amines. *Die Makromol. Chemie* **1977**. <https://doi.org/10.1002/macp.1977.021780710>.
- (17) Zou, J.; Fan, J.; He, X.; Zhang, S.; Wang, H.; Wooley, K. L. A Facile Glovebox-Free Strategy To Significantly Accelerate the Syntheses of Well-Defined Polypeptides by N -Carboxyanhydride (NCA) Ring-Opening Polymerizations. *Macromolecules* **2013**, *46* (10), 4223–4226. <https://doi.org/10.1021/ma4007939>.
- (18) Zhao, W.; Lv, Y.; Li, J.; Feng, Z.; Ni, Y.; Hadjichristidis, N. Fast and Selective Organocatalytic Ring-Opening Polymerization by Fluorinated Alcohol without a Cocatalyst. *Nat. Commun.* **2019**, *10* (1), 3590. <https://doi.org/10.1038/s41467-019-11524-y>.
- (19) Rasines Mazo, A.; Allison-Logan, S.; Karimi, F.; Chan, N. J.-A.; Qiu, W.; Duan, W.; O'Brien-Simpson, N. M.; Qiao, G. G. Ring Opening Polymerization of α -Amino Acids: Advances in Synthesis, Architecture and Applications of Polypeptides and Their Hybrids. *Chem. Soc. Rev.* **2020**, *49* (14), 4737–4834. <https://doi.org/10.1039/C9CS00738E>.
- (20) Lovell, S. C.; Davis, I. W.; Arendall, W. B.; de Bakker, P. I. W.; Word, J. M.; Prisant, M. G.; Richardson, J. S.; Richardson, D. C. Structure Validation by $C\alpha$ Geometry: ϕ, ψ and $C\beta$ Deviation. *Proteins Struct. Funct. Bioinforma.* **2003**, *50* (3),

- 437–450. <https://doi.org/10.1002/prot.10286>.
- (21) Robinson, S. W.; Afzal, A. M.; Leader, D. P. Bioinformatics: Concepts, Methods, and Data. In *Handbook of Pharmacogenomics and Stratified Medicine*; Elsevier, 2014; pp 259–287. <https://doi.org/10.1016/B978-0-12-386882-4.00013-X>.
- (22) Shepherd, N. E.; Hoang, H. N.; Abbenante, G.; Fairlie, D. P. Left- and Right- Handed Alpha-Helical Turns in Homo- and Hetero-Chiral Helical Scaffolds. *J. Am. Chem. Soc.* **2009**, *131* (43), 15877–15886. <https://doi.org/10.1021/ja9065283>.
- (23) Meijer, J. T.; Roeters, M.; Viola, V.; Löwik, D. W. P. M.; Vriend, G.; van Hest, J. C. M. Stabilization of Peptide Fibrils by Hydrophobic Interaction. *Langmuir* **2007**, *23* (4), 2058–2063. <https://doi.org/10.1021/la0625345>.
- (24) Wang, M.; Zhou, P.; Wang, J.; Zhao, Y.; Ma, H.; Lu, J. R.; Xu, H. Left or Right: How Does Amino Acid Chirality Affect the Handedness of Nanostructures Self-Assembled from Short Amphiphilic Peptides? *J. Am. Chem. Soc.* **2017**, *139* (11), 4185–4194. <https://doi.org/10.1021/jacs.7b00847>.
- (25) Bulheller, B. M.; Rodger, A.; Hirst, J. D. Circular and Linear Dichroism of Proteins. *Phys. Chem. Chem. Phys.* **2007**, *9* (17), 2020. <https://doi.org/10.1039/b615870f>.
- (26) Greenfield, N. J. Using Circular Dichroism Spectra to Estimate Protein Secondary Structure. *Nat. Protoc.* **2006**, *1* (6), 2876–2890. <https://doi.org/10.1038/nprot.2006.202>.
- (27) Miyazawa, T.; Blout, E. R. The Infrared Spectra of Polypeptides in Various Conformations: Amide I and II Bands 1. *J. Am. Chem. Soc.* **1961**, *83* (3), 712–719. <https://doi.org/10.1021/ja01464a042>.

- (28) Barth, A. Infrared Spectroscopy of Proteins. *Biochim. Biophys. Acta* **2007**, *1767* (9), 1073–1101. <https://doi.org/10.1016/j.bbabbio.2007.06.004>.
- (29) Li, J.; Xing, R.; Bai, S.; Yan, X. Recent Advances of Self-Assembling Peptide-Based Hydrogels for Biomedical Applications. *Soft Matter* **2019**, *15* (8), 1704–1715. <https://doi.org/10.1039/C8SM02573H>.
- (30) Worthington, P.; Pochan, D. J.; Langhans, S. A. Peptide Hydrogels – Versatile Matrices for 3D Cell Culture in Cancer Medicine. *Front. Oncol.* **2015**, *5*. <https://doi.org/10.3389/fonc.2015.00092>.
- (31) Tavakoli, J.; Tang, Y. Hydrogel Based Sensors for Biomedical Applications: An Updated Review. *Polymers (Basel)*. **2017**, *9* (12), 364. <https://doi.org/10.3390/polym9080364>.
- (32) Fan, T.; Yu, X.; Shen, B.; Sun, L. Peptide Self-Assembled Nanostructures for Drug Delivery Applications. *J. Nanomater.* **2017**, *2017*, 1–16. <https://doi.org/10.1155/2017/4562474>.
- (33) Lu, J.; Wang, X. Biomimetic Self-Assembling Peptide Hydrogels for Tissue Engineering Applications. In *Advances in Experimental Medicine and Biology*; Springer New York LLC, 2018; Vol. 1064, pp 297–312. https://doi.org/10.1007/978-981-13-0445-3_18.
- (34) Dimatteo, R.; Darling, N. J.; Segura, T. In Situ Forming Injectable Hydrogels for Drug Delivery and Wound Repair. *Adv. Drug Deliv. Rev.* **2018**, *127*, 167–184. <https://doi.org/10.1016/j.addr.2018.03.007>.
- (35) Liu, C.; Zhang, Q.; Zhu, S.; Liu, H.; Chen, J. Preparation and Applications of

- Peptide-Based Injectable Hydrogels. *RSC Adv.* **2019**, *9* (48), 28299–28311. <https://doi.org/10.1039/C9RA05934B>.
- (36) Dasgupta, A.; Das, D. Designer Peptide Amphiphiles: Self-Assembly to Applications. *Langmuir* **2019**, *35* (33), 10704–10724. <https://doi.org/10.1021/acs.langmuir.9b01837>.
- (37) He, X.; Fan, J.; Wooley, K. L. Stimuli-Triggered Sol-Gel Transitions of Polypeptides Derived from α -Amino Acid N -Carboxyanhydride (NCA) Polymerizations. *Chem. - An Asian J.* **2016**, *11* (4), 437–447. <https://doi.org/10.1002/asia.201500957>.
- (38) Löwik, D. W. P. M.; van Hest, J. C. M. Peptide Based Amphiphiles. *Chem. Soc. Rev.* **2004**, *33* (4), 234–245. <https://doi.org/10.1039/B212638A>.
- (39) Israelachvili, J. N.; Mitchell, D. J.; Ninham, B. W. Theory of Self-Assembly of Hydrocarbon Amphiphiles into Micelles and Bilayers. *Journal of the Chemical Society, Faraday Transactions 2: Molecular and Chemical Physics*. 1976. <https://doi.org/10.1039/F29767201525>.
- (40) Wang, C.; Wang, Z.; Zhang, X. Amphiphilic Building Blocks for Self-Assembly: From Amphiphiles to Supra-Amphiphiles. *Acc. Chem. Res.* **2012**, *45* (4), 608–618. <https://doi.org/10.1021/ar200226d>.
- (41) Hamley, I. W. PEG–Peptide Conjugates. *Biomacromolecules* **2014**, *15* (5), 1543–1559. <https://doi.org/10.1021/bm500246w>.
- (42) Dasgupta, A.; Mondal, J. H.; Das, D. Peptide Hydrogels. *RSC Adv.* **2013**, *3* (24), 9117. <https://doi.org/10.1039/c3ra40234g>.

- (43) Gravert, D. J.; Janda, K. D. Organic Synthesis on Soluble Polymer Supports: Liquid-Phase Methodologies. *Chem. Rev.* **1997**, *97* (2), 489–510. <https://doi.org/10.1021/cr960064l>.
- (44) Engler, A. C.; Lee, H.; Hammond, P. T. Highly Efficient “Grafting onto” a Polypeptide Backbone Using Click Chemistry. *Angew. Chemie Int. Ed.* **2009**, *48* (49), 9334–9338. <https://doi.org/10.1002/anie.200904070>.
- (45) Kharkar, P. M.; Rehmann, M. S.; Skeens, K. M.; Maverakis, E.; Kloxin, A. M. Thiol–Ene Click Hydrogels for Therapeutic Delivery. *ACS Biomater. Sci. Eng.* **2016**, *2* (2), 165–179. <https://doi.org/10.1021/acsbiomaterials.5b00420>.
- (46) Kim, J.; Kong, Y. P.; Niedzielski, S. M.; Singh, R. K.; Putnam, A. J.; Shikanov, A. Characterization of the Crosslinking Kinetics of Multi-Arm Poly(Ethylene Glycol) Hydrogels Formed via Michael-Type Addition. *Soft Matter* **2016**, *12* (7), 2076–2085. <https://doi.org/10.1039/C5SM02668G>.
- (47) Deming, T. J. Polypeptide and Polypeptide Hybrid Copolymer Synthesis via NCA Polymerization. In *Peptide Hybrid Polymers*; Springer-Verlag: Berlin/Heidelberg, 2006; pp 1–18. https://doi.org/10.1007/12_080.
- (48) Hadjichristidis, N.; Iatrou, H.; Pitsikalis, M.; Sakellariou, G. Synthesis of Well-Defined Polypeptide-Based Materials via the Ring-Opening Polymerization of α -Amino Acid N -Carboxyanhydrides. *Chem. Rev.* **2009**, *109* (11), 5528–5578. <https://doi.org/10.1021/cr900049t>.
- (49) Gkikas, M.; Iatrou, H.; Thomaidis, N. S.; Alexandridis, P.; Hadjichristidis, N. Well-Defined Homopolypeptides, Copolypeptides, and Hybrids of Poly(

- Proline). *Biomacromolecules* **2011**, *12* (6), 2396–2406.
<https://doi.org/10.1021/bm200495n>.
- (50) Zou, J.; Zhang, F.; Chen, Y.; Raymond, J. E.; Zhang, S.; Fan, J.; Zhu, J.; Li, A.; Seetho, K.; He, X.; Pochan, D. J.; Wooley, K. L. Responsive Organogels Formed by Supramolecular Self Assembly of PEG-Block-Allyl-Functionalized Racemic Polypeptides into β -Sheet-Driven Polymeric Ribbons. *Soft Matter* **2013**, *9* (25), 5951. <https://doi.org/10.1039/c3sm50582k>.
- (51) History Of Batteries: A Timeline - UPS Battery Center
<http://www.upsbatterycenter.com/blog/history-batteries-timeline/>.
- (52) History of batteries: their invention and development
<http://www.allaboutbatteries.com/history-of-batteries.html>.
- (53) Armand, M.; Tarascon, J.-M. Building Better Batteries. *Nature* **2008**, *451* (7179), 652–657. <https://doi.org/10.1038/451652a>.
- (54) The Evolution of Battery Technology <http://www.visualcapitalist.com/evolution-of-battery-technology/>.
- (55) Zeng, X.; Li, J.; Singh, N. Recycling of Spent Lithium-Ion Battery: A Critical Review. *Crit. Rev. Environ. Sci. Technol.* **2014**, *44* (10), 1129–1165.
<https://doi.org/10.1080/10643389.2013.763578>.
- (56) Olivetti, E. A.; Ceder, G.; Gaustad, G. G.; Fu, X. Lithium-Ion Battery Supply Chain Considerations: Analysis of Potential Bottlenecks in Critical Metals. *Joule* **2017**, *1* (2), 229–243. <https://doi.org/https://doi.org/10.1016/j.joule.2017.08.019>.
- (57) Sukegawa, T.; Sato, K.; Oyaizu, K.; Nishide, H. Efficient Charge Transport of a

- Radical Polyether/SWCNT Composite Electrode for an Organic Radical Battery with High Charge-Storage Density. *RSC Adv.* **2015**, 5 (20), 15448–15452. <https://doi.org/10.1039/C4RA15949G>.
- (58) Nishide, H. Radical Polymers toward an Organic-Based Rechargeable Battery and Photovoltaic Cell. In *Abstracts of Papers, 246th ACS National Meeting & Exposition, Indianapolis, IN, United States, September 8-12, 2013*; 2013.
- (59) Koshika, K.; Chikushi, N.; Sano, N.; Oyaizu, K.; Nishide, H. A TEMPO-Substituted Polyacrylamide as a New Cathode Material: An Organic Rechargeable Device Composed of Polymer Electrodes and Aqueous Electrolyte. *Green Chem.* **2010**, 12 (9), 1573–1575. <https://doi.org/10.1039/b926296b>.
- (60) Suga, T.; Konishi, H.; Nishide, H. Photocrosslinked Nitroxide Polymer Cathode-Active Materials for Application in an Organic-Based Paper Battery. *Chem. Commun.* **2007**, 0 (17), 1730. <https://doi.org/10.1039/b618710b>.
- (61) Nishide, H.; Suga, T.; Oyaizu, K. Radical Battery: A Paper-like Polymer-Based Rechargeable Device. In *ACS National Meeting Book of Abstracts*; 2007.
- (62) Nakahara, K.; Oyaizu, K.; Nishide, H. Organic Radical Battery Approaching Practical Use. *Chem. Lett.* **2011**, 40 (3), 222–227. <https://doi.org/10.1246/cl.2011.222>.
- (63) Nishide, H.; Iwasa, S.; Pu, Y.-J.; Suga, T.; Nakahara, K.; Satoh, M. Organic Radical Battery: Nitroxide Polymers as a Cathode-Active Material. *Electrochim. Acta* **2004**, 50 (2–3), 827–831. <https://doi.org/10.1016/j.electacta.2004.02.052>.
- (64) Janoschka, T.; Hager, M. D.; Schubert, U. S. Powering up the Future: Radical

- Polymers for Battery Applications. *Adv. Mater.* **2012**, *24* (48), 6397–6409.
<https://doi.org/10.1002/adma.201203119>.
- (65) Muench, S.; Wild, A.; Friebe, C.; Häupler, B.; Janoschka, T.; Schubert, U. S. Polymer-Based Organic Batteries. *Chem. Rev.* **2016**, *116* (16), 9438–9484.
<https://doi.org/10.1021/acs.chemrev.6b00070>.
- (66) Zhang, K.; Monteiro, M. J.; Jia, Z. Stable Organic Radical Polymers: Synthesis and Applications. *Polym. Chem.* **2016**, *7* (36), 5589–5614.
<https://doi.org/10.1039/C6PY00996D>.
- (67) Kim, J.; Kim, J. H.; Ariga, K. Redox-Active Polymers for Energy Storage Nanoarchitectonics. *Joule* **2017**, *1* (4), 739–768.
<https://doi.org/10.1016/j.joule.2017.08.018>.
- (68) Muench, S.; Wild, A.; Friebe, C.; Häupler, B.; Janoschka, T.; Schubert, U. S. Polymer-Based Organic Batteries. *Chem. Rev.* **2016**, *116* (16), 9438–9484.
<https://doi.org/10.1021/acs.chemrev.6b00070>.
- (69) Suga, T.; Sugita, S.; Ohshiro, H.; Oyaizu, K.; Nishide, H. P- and n-Type Bipolar Redox-Active Radical Polymer: Toward Totally Organic Polymer-Based Rechargeable Devices with Variable Configuration. *Adv. Mater.* **2011**, *23* (6), 751–754. <https://doi.org/10.1002/adma.201003525>.
- (70) Suga, T.; Ohshiro, H.; Sugita, S.; Oyaizu, K.; Nishide, H. Emerging N-Type Redox-Active Radical Polymer for a Totally Organic Polymer-Based Rechargeable Battery. *Adv. Mater.* **2009**, *21* (16), 1627–1630.
<https://doi.org/10.1002/adma.200803073>.

- (71) Koshika, K.; Sano, N.; Oyaizu, K.; Nishide, H. An Ultrafast Chargeable Polymer Electrode Based on the Combination of Nitroxide Radical and Aqueous Electrolyte. *Chem. Commun.* **2009**, No. 7, 836–838. <https://doi.org/10.1039/B818087C>.
- (72) Koshika, K.; Sano, N.; Oyaizu, K.; Nishide, H. An Aqueous, Electrolyte-Type, Rechargeable Device Utilizing a Hydrophilic Radical Polymer-Cathode. *Macromol. Chem. Phys.* **2009**, *210* (22), 1989–1995. <https://doi.org/10.1002/macp.200900257>.
- (73) Sano, N.; Tomita, W.; Hara, S.; Min, C.-M.; Lee, J.-S.; Oyaizu, K.; Nishide, H. Polyviologen Hydrogel with High-Rate Capability for Anodes toward an Aqueous Electrolyte-Type and Organic-Based Rechargeable Device. *ACS Appl. Mater. Interfaces* **2013**, *5* (4), 1355–1361. <https://doi.org/10.1021/am302647w>.
- (74) Tomlinson, E. P.; Hay, M. E.; Boudouris, B. W. Radical Polymers and Their Application to Organic Electronic Devices. *Macromolecules* **2014**, *47* (18), 6145–6158. <https://doi.org/10.1021/ma5014572>.
- (75) Qu, J.; Morita, R.; Satoh, M.; Wada, J.; Terakura, F.; Mizoguchi, K.; Ogata, N.; Masuda, T. Synthesis and Properties of DNA Complexes Containing 2,2,6,6-Tetramethyl-1-Piperidinoxy (TEMPO) Moieties as Organic Radical Battery Materials. *Chem. - A Eur. J.* **2008**, *14* (11), 3250–3259. <https://doi.org/10.1002/chem.200800021>.
- (76) Hiejima, T.; Kaneko, J. Spiral Configuration of Nitroxide Radicals Along the Polypeptide Helix and Their Magnetic Properties. *Macromolecules* **2013**, *46* (5), 1713–1722. <https://doi.org/10.1021/ma302256c>.

- (77) Wild, A.; Strumpf, M.; Häupler, B.; Hager, M. D.; Schubert, U. S. All-Organic Battery Composed of Thianthrene- and TCAQ-Based Polymers. *Adv. Energy Mater.* **2017**, 7 (5), 1601415. <https://doi.org/10.1002/aenm.201601415>.
- (78) Oka, K.; Kato, R.; Oyaizu, K.; Nishide, H. Poly(Vinyldibenzothiophenesulfone): Its Redox Capability at Very Negative Potential Toward an All-Organic Rechargeable Device with High-Energy Density. *Adv. Funct. Mater.* **2018**, 28 (50), 1805858. <https://doi.org/10.1002/adfm.201805858>.
- (79) Soloveichik, G. L. Flow Batteries: Current Status and Trends. *Chem. Rev.* **2015**, 115 (20), 11533–11558. <https://doi.org/10.1021/cr500720t>.
- (80) Lai, Y. Y.; Li, X.; Zhu, Y. Polymeric Active Materials for Redox Flow Battery Application. *ACS Appl. Polym. Mater.* **2020**, 2 (2), 113–128. <https://doi.org/10.1021/acsapm.9b00864>.
- (81) Zhong, F.; Yang, M.; Ding, M.; Jia, C. Organic Electroactive Molecule-Based Electrolytes for Redox Flow Batteries: Status and Challenges of Molecular Design. *Front. Chem.* **2020**, 8. <https://doi.org/10.3389/fchem.2020.00451>.
- (82) Prifti, H.; Parasuraman, A.; Winardi, S.; Lim, T. M.; Skyllas-Kazacos, M. Membranes for Redox Flow Battery Applications. *Membranes (Basel)*. **2012**, 2 (2), 275–306. <https://doi.org/10.3390/membranes2020275>.
- (83) Wang, W.; Luo, Q.; Li, B.; Wei, X.; Li, L.; Yang, Z. Recent Progress in Redox Flow Battery Research and Development. *Adv. Funct. Mater.* **2013**, 23 (8), 970–986. <https://doi.org/10.1002/adfm.201200694>.
- (84) Pan, F.; Wang, Q. Redox Species of Redox Flow Batteries: A Review. *Molecules*

- 2015**, *20* (11), 20499–20517. <https://doi.org/10.3390/molecules201119711>.
- (85) Leung, P.; Shah, A. A.; Sanz, L.; Flox, C.; Morante, J. R.; Xu, Q.; Mohamed, M. R.; Ponce de León, C.; Walsh, F. C. Recent Developments in Organic Redox Flow Batteries: A Critical Review. *J. Power Sources* **2017**, *360*, 243–283. <https://doi.org/10.1016/j.jpowsour.2017.05.057>.
- (86) Winsberg, J.; Hagemann, T.; Janoschka, T.; Hager, M. D.; Schubert, U. S. Redox-Flow Batteries: From Metals to Organic Redox-Active Materials. *Angew. Chemie Int. Ed.* **2017**, *56* (3), 686–711. <https://doi.org/10.1002/anie.201604925>.
- (87) Wei, X.; Cosimbescu, L.; Xu, W.; Hu, J. Z.; Vijayakumar, M.; Feng, J.; Hu, M. Y.; Deng, X.; Xiao, J.; Liu, J.; Sprenkle, V.; Wang, W. Towards High-Performance Nonaqueous Redox Flow Electrolyte Via Ionic Modification of Active Species. *Adv. Energy Mater.* **2015**, *5* (1), 1400678. <https://doi.org/10.1002/aenm.201400678>.
- (88) Chai, J.; Lashgari, A.; Wang, X.; Williams, C. K.; Jiang, J. “Jimmy.” All-PEGylated Redox-Active Metal-Free Organic Molecules in Non-Aqueous Redox Flow Battery. *J. Mater. Chem. A* **2020**, *8* (31), 15715–15724. <https://doi.org/10.1039/D0TA02303E>.
- (89) Nagarjuna, G.; Hui, J.; Cheng, K. J.; Lichtenstein, T.; Shen, M.; Moore, J. S.; Rodríguez-López, J. Impact of Redox-Active Polymer Molecular Weight on the Electrochemical Properties and Transport Across Porous Separators in Nonaqueous Solvents. *J. Am. Chem. Soc.* **2014**, *136* (46), 16309–16316. <https://doi.org/10.1021/ja508482e>.

- (90) Schmidt, D.; Häupler, B.; Hager, M. D.; Schubert, U. S. Poly(DCAQI): Synthesis and Characterization of a New Redox-Active Polymer. *J. Polym. Sci. Part A Polym. Chem.* **2016**, *54* (13), 1998–2003. <https://doi.org/10.1002/pola.28066>.
- (91) Hendriks, K. H.; Robinson, S. G.; Braten, M. N.; Sevov, C. S.; Helms, B. A.; Sigman, M. S.; Minter, S. D.; Sanford, M. S. High-Performance Oligomeric Catholytes for Effective Macromolecular Separation in Nonaqueous Redox Flow Batteries. *ACS Cent. Sci.* **2018**, *4* (2), 189–196. <https://doi.org/10.1021/acscentsci.7b00544>.
- (92) Baran, M. J.; Braten, M. N.; Montoto, E. C.; Gossage, Z. T.; Ma, L.; Chénard, E.; Moore, J. S.; Rodríguez-López, J.; Helms, B. A. Designing Redox-Active Oligomers for Crossover-Free, Nonaqueous Redox-Flow Batteries with High Volumetric Energy Density. *Chem. Mater.* **2018**, *30* (11), 3861–3866. <https://doi.org/10.1021/acs.chemmater.8b01318>.
- (93) Hagemann, T.; Strumpf, M.; Schröter, E.; Stolze, C.; Grube, M.; Nischang, I.; Hager, M. D.; Schubert, U. S. (2,2,6,6-Tetramethylpiperidin-1-Yl)Oxyl-Containing Zwitterionic Polymer as Catholyte Species for High-Capacity Aqueous Polymer Redox Flow Batteries. *Chem. Mater.* **2019**, *31* (19), 7987–7999. <https://doi.org/10.1021/acs.chemmater.9b02201>.
- (94) Hagemann, T.; Winsberg, J.; Grube, M.; Nischang, I.; Janoschka, T.; Martin, N.; Hager, M. D.; Schubert, U. S. An Aqueous All-Organic Redox-Flow Battery Employing a (2,2,6,6-Tetramethylpiperidin-1-Yl)Oxyl-Containing Polymer as Catholyte and Dimethyl Viologen Dichloride as Anolyte. *J. Power Sources* **2018**,

- 378, 546–554. <https://doi.org/10.1016/j.jpowsour.2017.09.007>.
- (95) Wang, H.; Cai, L.; Paul, A.; Enejder, A.; Heilshorn, S. C. Hybrid Elastin-like Polypeptide–Polyethylene Glycol (ELP-PEG) Hydrogels with Improved Transparency and Independent Control of Matrix Mechanics and Cell Ligand Density. *Biomacromolecules* **2014**, *15* (9), 3421–3428. <https://doi.org/10.1021/bm500969d>.
- (96) Lee, J.; Cuddihy, M. J.; Kotov, N. A. Three-Dimensional Cell Culture Matrices: State of the Art. *Tissue Eng. Part B Rev.* **2008**, *14* (1), 61–86. <https://doi.org/10.1089/teb.2007.0150>.
- (97) Doyle, A. D.; Wang, F. W.; Matsumoto, K.; Yamada, K. M. One-Dimensional Topography Underlies Three-Dimensional Fibrillar Cell Migration. *J. Cell Biol.* **2009**, *184* (4), 481–490. <https://doi.org/10.1083/jcb.200810041>.
- (98) Zaman, M. H.; Trapani, L. M.; Sieminski, A. L.; MacKellar, D.; Gong, H.; Kamm, R. D.; Wells, A.; Lauffenburger, D. A.; Matsudaira, P. Migration of Tumor Cells in 3D Matrices Is Governed by Matrix Stiffness along with Cell-Matrix Adhesion and Proteolysis. *Proc. Natl. Acad. Sci.* **2006**, *103* (29), 10889–10894. <https://doi.org/10.1073/PNAS.0604460103>.
- (99) Baker, B. M.; Chen, C. S. Deconstructing the Third Dimension – How 3D Culture Microenvironments Alter Cellular Cues. *J. Cell Sci.* **2012**, *124* (8), 1183–1193. <https://doi.org/10.1242/jcs.064618>.
- (100) Langhans, S. A. Three-Dimensional in Vitro Cell Culture Models in Drug Discovery and Drug Repositioning. *Front. Pharmacol.* **2018**, *9*, 6.

<https://doi.org/10.3389/fphar.2018.00006>.

- (101) Bairagi, D.; Biswas, P.; Basu, K.; Hazra, S.; Hermida-Merino, D.; Sinha, D. K.; Hamley, I. W.; Banerjee, A. Self-Assembling Peptide-Based Hydrogel: Regulation of Mechanical Stiffness and Thermal Stability and 3D Cell Culture of Fibroblasts. *ACS Appl. Bio Mater.* **2019**, *2* (12), 5235–5244. <https://doi.org/10.1021/acsabm.9b00424>.
- (102) Luo, J.; Liu, X.; Yang, Z.; Sun, F. Synthesis of Entirely Protein-Based Hydrogels by Enzymatic Oxidation Enabling Water-Resistant Bioadhesion and Stem Cell Encapsulation. *ACS Appl. Bio Mater.* **2018**, *1* (5), 1735–1740. <https://doi.org/10.1021/acsabm.8b00541>.
- (103) Liyanage, W.; Vats, K.; Rajbhandary, A.; Benoit, D. S. W.; Nilsson, B. L. Multicomponent Dipeptide Hydrogels as Extracellular Matrix-Mimetic Scaffolds for Cell Culture Applications. *Chem. Commun.* **2015**, *51* (56), 11260–11263. <https://doi.org/10.1039/C5CC03162A>.
- (104) Escuder, B.; Rodríguez-Llansola, F.; Miravet, J. F. Supramolecular Gels as Active Media for Organic Reactions and Catalysis. *New J. Chem.* **2010**, *34* (6), 1044. <https://doi.org/10.1039/b9nj00764d>.
- (105) Hirst, A. R.; Escuder, B.; Miravet, J. F.; Smith, D. K. High-Tech Applications of Self-Assembling Supramolecular Nanostructured Gel-Phase Materials: From Regenerative Medicine to Electronic Devices. *Angew. Chem. Int. Ed. Engl.* **2008**, *47* (42), 8002–8018. <https://doi.org/10.1002/anie.200800022>.
- (106) Branco, M. C.; Schneider, J. P. Self-Assembling Materials for Therapeutic

- Delivery. *Acta Biomater.* **2009**, *5* (3), 817–831.
<https://doi.org/10.1016/J.ACTBIO.2008.09.018>.
- (107) Wang, H.; Yang, Z. Short-Peptide-Based Molecular Hydrogels: Novel Gelation Strategies and Applications for Tissue Engineering and Drug Delivery. *Nanoscale* **2012**, *4* (17), 5259–5267. <https://doi.org/10.1039/c2nr31149f>.
- (108) Aggeli, A.; Nyrkova, I. A.; Bell, M.; Harding, R.; Carrick, L.; McLeish, T. C. B.; Semenov, A. N.; Boden, N. Hierarchical Self-Assembly of Chiral Rod-like Molecules as a Model for Peptide β -Sheet Tapes, Ribbons, Fibrils, and Fibers. *Proc. Natl. Acad. Sci.* **2001**, *98* (21), 11857–11862.
<https://doi.org/10.1073/pnas.191250198>.
- (109) Yamada, Y.; Patel, N. L.; Kalen, J. D.; Schneider, J. P. Design of a Peptide-Based Electronegative Hydrogel for the Direct Encapsulation, 3D Culturing, in Vivo Syringe-Based Delivery, and Long-Term Tissue Engraftment of Cells. *ACS Appl. Mater. Interfaces* **2019**, *11* (38), 34688–34697.
<https://doi.org/10.1021/acsami.9b12152>.
- (110) Zanna, N.; Focaroli, S.; Merlettini, A.; Gentilucci, L.; Teti, G.; Falconi, M.; Tomasini, C. Thixotropic Peptide-Based Physical Hydrogels Applied to Three-Dimensional Cell Culture. *ACS Omega* **2017**, *2* (5), 2374–2381.
<https://doi.org/10.1021/acsomega.7b00322>.
- (111) Qi, X.; Zhang, M.; Su, T.; Pan, W.; Tong, X.; Zeng, Q.; Xiong, W.; Jiang, N.; Qian, Y.; Li, Z.; He, X.; Shen, L.; Zhou, Z.; Shen, J. Biocompatible Hydrogels Based on Food Gums with Tunable Physicochemical Properties as Scaffolds for Cell Culture.

- J. Agric. Food Chem.* **2020**, *68* (12), 3770–3778.
<https://doi.org/10.1021/acs.jafc.9b06120>.
- (112) Jayasinghe, H. G.; Madihally, S. V.; Vasquez, Y. Formation of Stem Cell Aggregates and Their Differentiation on Surface-Patterned Hydrogels Based on Poly(2-Hydroxyethyl Methacrylate). *ACS Appl. Bio Mater.* **2019**, *2* (11), 4911–4921. <https://doi.org/10.1021/acsabm.9b00661>.
- (113) Paez, J. I.; Farrukh, A.; Valbuena-Mendoza, R.; Włodarczyk-Biegun, M. K.; del Campo, A. Thiol-Methylsulfone-Based Hydrogels for 3D Cell Encapsulation. *ACS Appl. Mater. Interfaces* **2020**, *12* (7), 8062–8072. <https://doi.org/10.1021/acsami.0c00709>.
- (114) Li, P.; Yin, Z.; Dou, X.-Q.; Zhou, G.; Feng, C.-L. Convenient Three-Dimensional Cell Culture in Supramolecular Hydrogels. *ACS Appl. Mater. Interfaces* **2014**, *6* (10), 7948–7952. <https://doi.org/10.1021/am501275t>.
- (115) Zou, J.; He, X.; Fan, J.; Raymond, J. E.; Wooley, K. L. Supramolecularly Knitted Tethered Oligopeptide/Single-Walled Carbon Nanotube Organogels. *Chem. - A Eur. J.* **2014**, *20* (29), 8842–8847. <https://doi.org/10.1002/chem.201403027>.
- (116) Caliari, S. R.; Burdick, J. A. A Practical Guide to Hydrogels for Cell Culture. *Nat. Methods* **2016**, *13* (5), 405–414. <https://doi.org/10.1038/nmeth.3839>.
- (117) Engler, A. J.; Sen, S.; Sweeney, H. L.; Discher, D. E. Matrix Elasticity Directs Stem Cell Lineage Specification. *Cell* **2006**, *126* (4), 677–689. <https://doi.org/10.1016/j.cell.2006.06.044>.
- (118) Rowlands, A. S.; George, P. A.; Cooper-White, J. J. Directing Osteogenic and

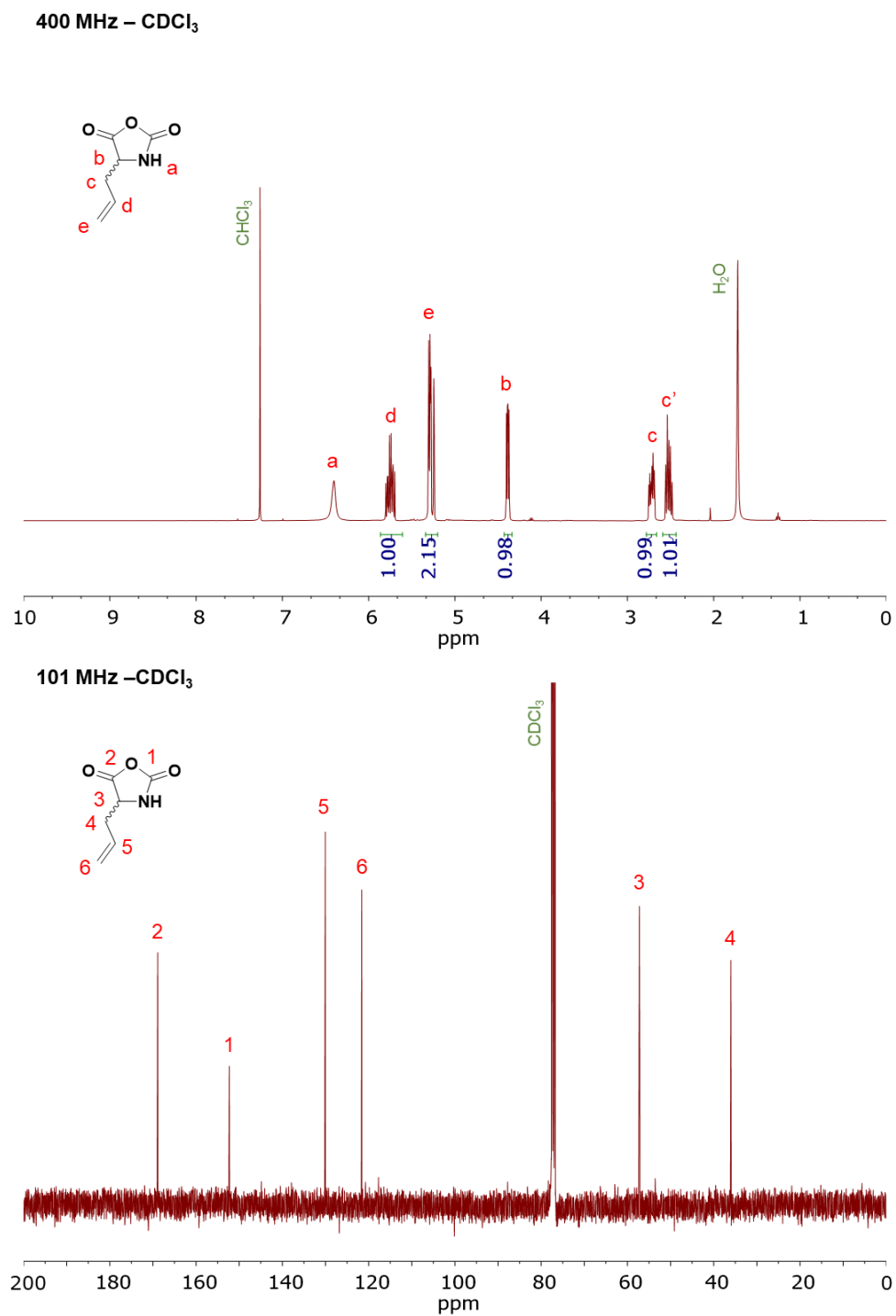
- Myogenic Differentiation of MSCs: Interplay of Stiffness and Adhesive Ligand Presentation. *Am. J. Physiol. Physiol.* **2008**, 295 (4), C1037–C1044. <https://doi.org/10.1152/ajpcell.67.2008>.
- (119) Friebe, C.; Lex-Balducci, A.; Schubert, U. S. Sustainable Energy Storage: Recent Trends and Developments toward Fully Organic Batteries. *ChemSusChem* **2019**, 12 (18), 4093–4115. <https://doi.org/10.1002/cssc.201901545>.
- (120) Joo, Y.; Agarkar, V.; Sung, S. H.; Savoie, B. M.; Boudouris, B. W. A Nonconjugated Radical Polymer Glass with High Electrical Conductivity. *Science* **2018**, 359 (6382), 1391–1395. <https://doi.org/10.1126/science.aao7287>.
- (121) Lutkenhaus, J. A Radical Advance for Conducting Polymers. *Science* **2018**, 359 (6382), 1334. <https://doi.org/10.1126/science.aat1298>.
- (122) Coates, G. W.; Getzler, Y. D. Y. L. Chemical Recycling to Monomer for an Ideal, Circular Polymer Economy. *Nat. Rev. Mater.* **2020**, 5 (7), 501–516. <https://doi.org/10.1038/s41578-020-0190-4>.
- (123) Janoschka, T.; Martin, N.; Martin, U.; Friebe, C.; Morgenstern, S.; Hiller, H.; Hager, M. D.; Schubert, U. S. An Aqueous, Polymer-Based Redox-Flow Battery Using Non-Corrosive, Safe, and Low-Cost Materials. *Nature* **2015**, 527 (7576), 78–81. <https://doi.org/10.1038/nature15746>.
- (124) Qu, J.; Fujii, T.; Katsumata, T.; Suzuki, Y.; Shiotsuki, M.; Sanda, F.; Satoh, M.; Wada, J.; Masuda, T. Helical Polyacetylenes Carrying 2,2,6,6-Tetramethyl-1-Piperidinyloxy and 2,2,5,5-Tetramethyl-1-Pyrrolidinyloxy Moieties: Their Synthesis, Properties, and Function. *J. Polym. Sci. Part A Polym. Chem.* **2007**, 45

- (23), 5431–5445. <https://doi.org/10.1002/pola.22288>.
- (125) Ibe, T.; Frings, R. B.; Lachowicz, A.; Kyo, S.; Nishide, H. Nitroxide Polymer Networks Formed by Michael Addition: On Site-Cured Electrode-Active Organic Coating. *Chem. Commun.* **2010**, *46* (20), 3475–3477. <https://doi.org/10.1039/c002797a>.
- (126) Hatakeyama-Sato, K.; Wakamatsu, H.; Katagiri, R.; Oyaizu, K.; Nishide, H. An Ultrahigh Output Rechargeable Electrode of a Hydrophilic Radical Polymer/Nanocarbon Hybrid with an Exceptionally Large Current Density beyond 1 A cm⁻². *Adv. Mater.* **2018**, *30* (26), 1800900. <https://doi.org/10.1002/adma.201800900>.
- (127) Otaki, M.; Goto, H. Helical Spin Polymer with Magneto-Electro-Optical Activity. *Macromolecules* **2019**, *52* (9), 3199–3209. <https://doi.org/10.1021/acs.macromol.9b00274>.
- (128) Belshaw, P. J.; Mzengeza, S.; Lajoie, G. A. Chlorotrimethylsilane Mediated Formation of ω-Allyl Esters of Aspartic And Glutamic Acids. *Synth. Commun.* **1990**, *20* (20), 3157–3160. <https://doi.org/10.1080/00397919008051540>.
- (129) Deming, T. J. Noodle Gels for Cells. *Nat. Mater.* **2010**, *9* (7), 535–536. <https://doi.org/10.1038/nmat2789>.
- (130) Lalatsa, A.; Schätzlein, A. G.; Mazza, M.; Le, T. B. H.; Uchegbu, I. F. Amphiphilic Poly(L-Amino Acids) — New Materials for Drug Delivery. *J. Control. Release* **2012**, *161* (2), 523–536. <https://doi.org/https://doi.org/10.1016/j.jconrel.2012.04.046>.

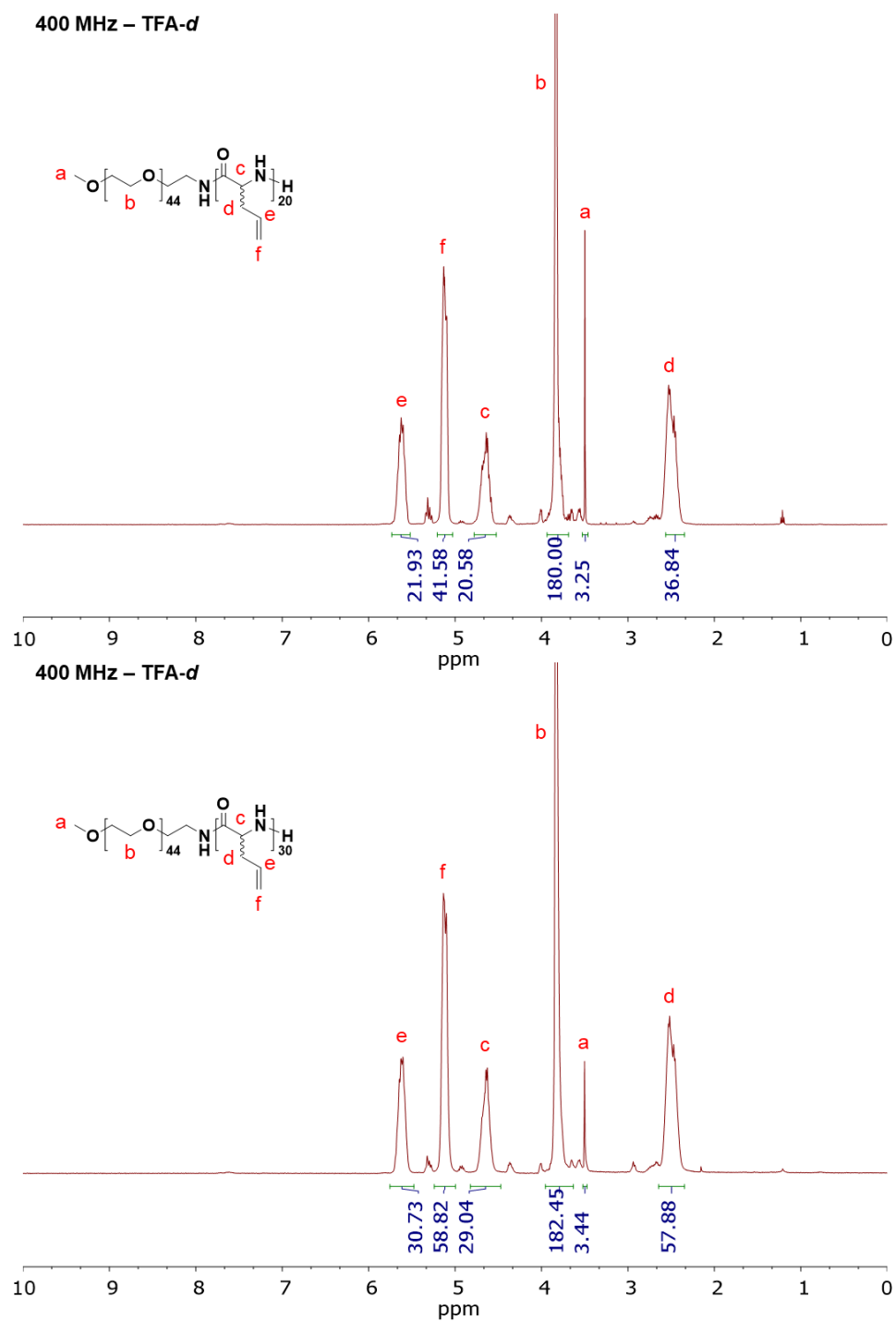
- (131) Matson, J. B.; Stupp, S. I. Self-Assembling Peptide Scaffolds for Regenerative Medicine. *Chem. Commun.* **2012**, *48* (1), 26–33. <https://doi.org/10.1039/C1CC15551B>.
- (132) Bard, A. J.; Faulkner, L. R. *Electrochemical Methods: Fundamentals and Applications, 2nd Edition*; Wiley Textbooks, 2000.
- (133) Bugnon, L.; Morton, C. J. H.; Novak, P.; Vetter, J.; Nesvadba, P. Synthesis of Poly(4-Methacryloyloxy-TEMPO) via Group-Transfer Polymerization and Its Evaluation in Organic Radical Battery. *Chem. Mater.* **2007**, *19* (11), 2910–2914. <https://doi.org/10.1021/cm063052h>.
- (134) Janoschka, T.; Teichler, A.; Häupler, B.; Jähnert, T.; Hager, M. D.; Schubert, U. S. Reactive Inkjet Printing of Cathodes for Organic Radical Batteries. *Adv. Energy Mater.* **2013**, *3* (8), 1025–1028. <https://doi.org/10.1002/aenm.201300036>.
- (135) Vlad, A.; Rolland, J.; Hauffman, G.; Ernould, B.; Gohy, J.-F. Melt-Polymerization of TEMPO Methacrylates with Nano Carbons Enables Superior Battery Materials. *ChemSusChem* **2015**, *8* (10), 1692–1696. <https://doi.org/10.1002/cssc.201500246>.
- (136) Wang, S.; Park, A. M. G.; Flouda, P.; Easley, A. D.; Li, F.; Ma, T.; Fuchs, G. D.; Lutkenhaus, J. L. Solution-Processable Thermally Crosslinked Organic Radical Polymer Battery Cathodes. *ChemSusChem* **2020**, *13* (9), 2371–2378. <https://doi.org/10.1002/cssc.201903554>.
- (137) Montoto, E. C.; Cao, Y.; Hernández-Burgos, K.; Sevov, C. S.; Braten, M. N.; Helms, B. A.; Moore, J. S.; Rodríguez-López, J. Effect of the Backbone Tether on the Electrochemical Properties of Soluble Cyclopropenium Redox-Active

- Polymers. *Macromolecules* **2018**, *51* (10), 3539–3546.
<https://doi.org/10.1021/acs.macromol.8b00574>.
- (138) Montoto, E. C.; Nagarjuna, G.; Moore, J. S.; Rodríguez-López, J. Redox Active Polymers for Non-Aqueous Redox Flow Batteries: Validation of the Size-Exclusion Approach. *J. Electrochem. Soc.* **2017**, *164* (7), A1688–A1694.
<https://doi.org/10.1149/2.1511707jes>.
- (139) Milshtein, J. D.; Barton, J. L.; Darling, R. M.; Brushett, F. R. 4-Acetamido-2,2,6,6-Tetramethylpiperidine-1-Oxyl as a Model Organic Redox Active Compound for Nonaqueous Flow Batteries. *J. Power Sources* **2016**.
<https://doi.org/10.1016/j.jpowsour.2016.06.125>.
- (140) Nagarjuna, G.; Hui, J.; Cheng, K. J.; Lichtenstein, T.; Shen, M.; Moore, J. S.; Rodríguez-López, J. Impact of Redox-Active Polymer Molecular Weight on the Electrochemical Properties and Transport across Porous Separators in Nonaqueous Solvents. *J. Am. Chem. Soc.* **2014**, *136* (46), 16309–16316.
<https://doi.org/10.1021/ja508482e>.

Nuclear Magnetic Resonance Spectroscopy

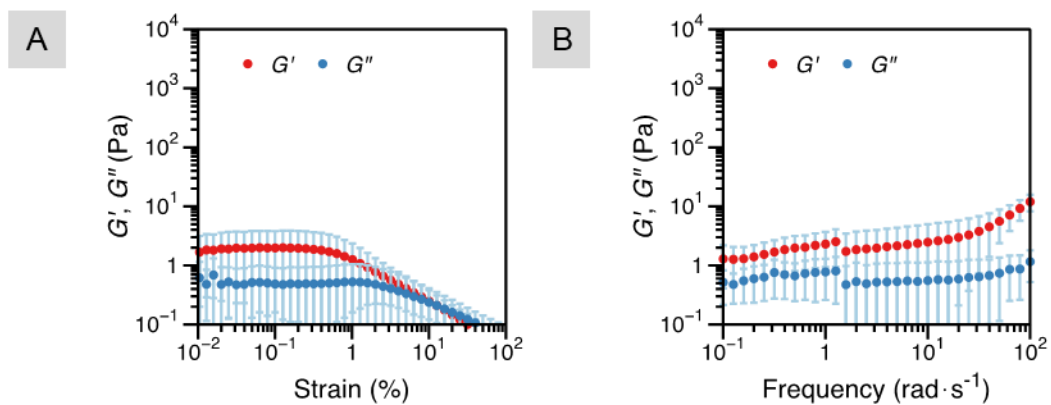


Appendix Figure 2. ¹H NMR and ¹³C NMR spectra of DLAG NCA.

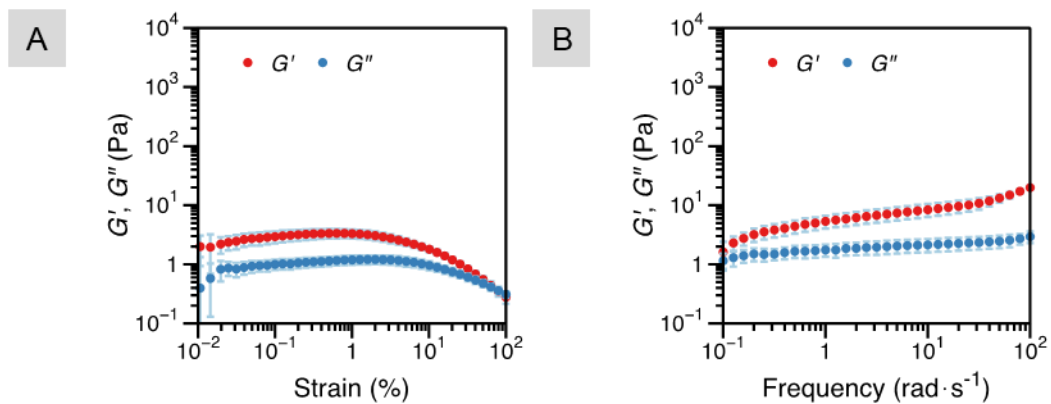


Appendix Figure 3. ^1H NMR spectra of PEG₄₅-*b*-PDLA₂₀ (P-20)

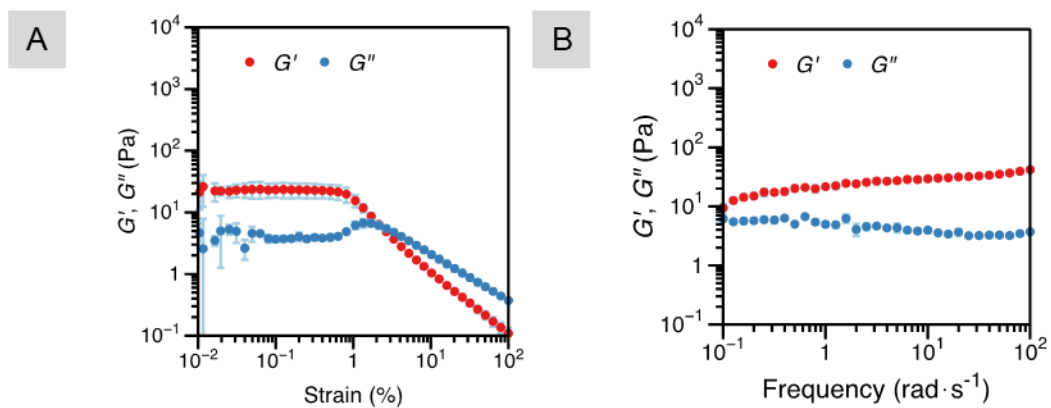
Rheology



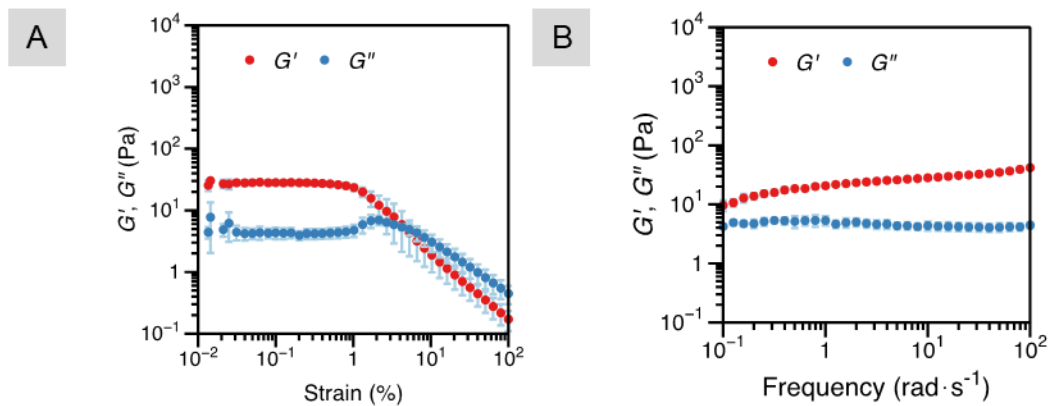
Appendix Figure 4. (A) Strain sweep ($T = 37$ °C, $\omega = 10$ $\text{rad}\cdot\text{s}^{-1}$) and (B) frequency sweep tests ($T = 37$ °C, $\gamma = 0.2\%$) of **P-20-1%** hydrogels.



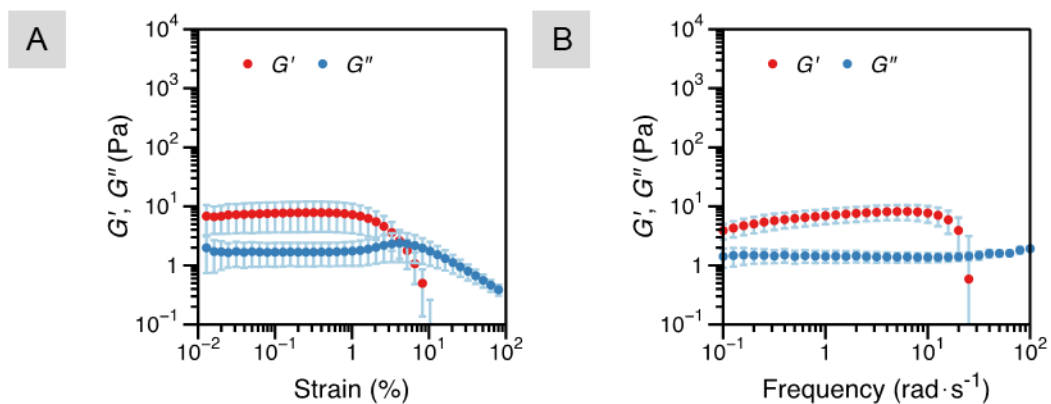
Appendix Figure 5. (A) Strain sweep ($T = 37$ °C, $\omega = 10$ $\text{rad}\cdot\text{s}^{-1}$) and (B) frequency sweep tests ($T = 37$ °C, $\gamma = 0.2\%$) of **P-20-2%** hydrogels.



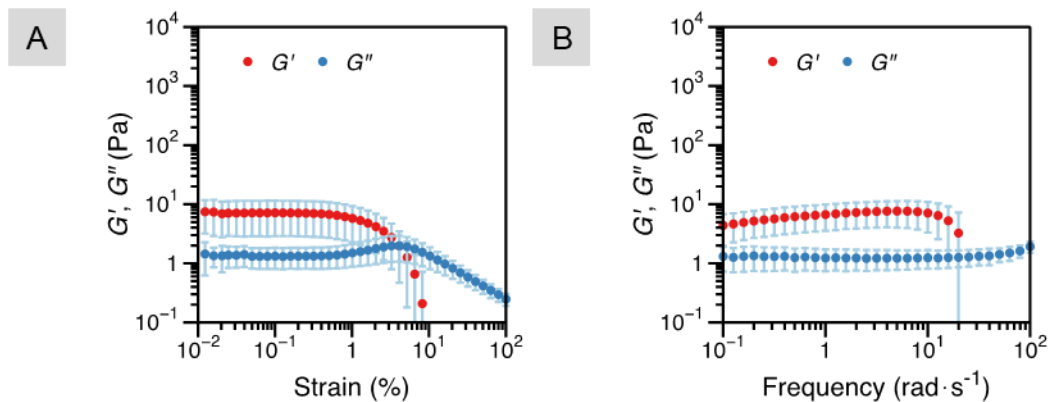
Appendix Figure 6. (A) Strain sweep ($T = 37\text{ }^{\circ}\text{C}$, $\omega = 10\text{ rad}\cdot\text{s}^{-1}$) and (B) frequency sweep tests ($T = 37\text{ }^{\circ}\text{C}$, $\gamma = 0.2\%$) of **P-20-4%** hydrogels.



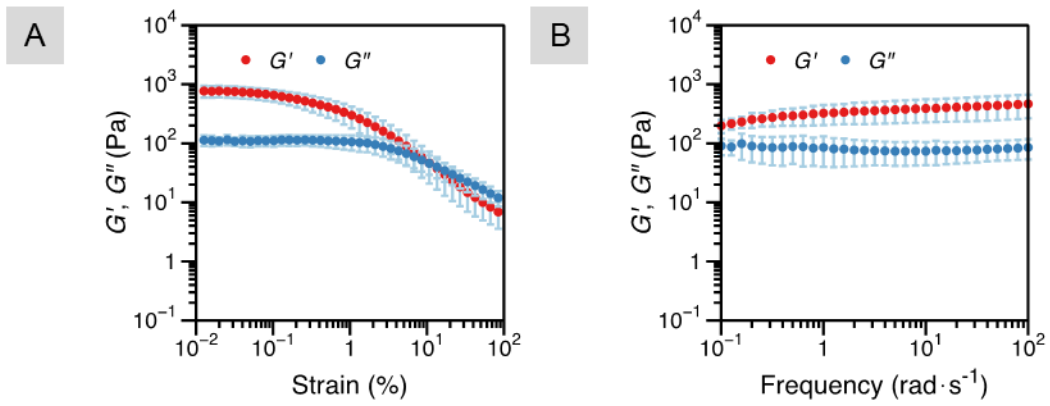
Appendix Figure 7. (A) Strain sweep ($T = 37\text{ }^{\circ}\text{C}$, $\omega = 10\text{ rad}\cdot\text{s}^{-1}$) and (B) frequency sweep tests ($T = 37\text{ }^{\circ}\text{C}$, $\gamma = 0.2\%$) of **P-20-8%** hydrogels.



Appendix Figure 8. (A) Strain sweep ($T = 37\text{ }^{\circ}\text{C}$, $\omega = 10\text{ rad}\cdot\text{s}^{-1}$) and (B) frequency sweep tests ($T = 37\text{ }^{\circ}\text{C}$, $\gamma = 0.2\%$) of **P-30-1%** hydrogels.

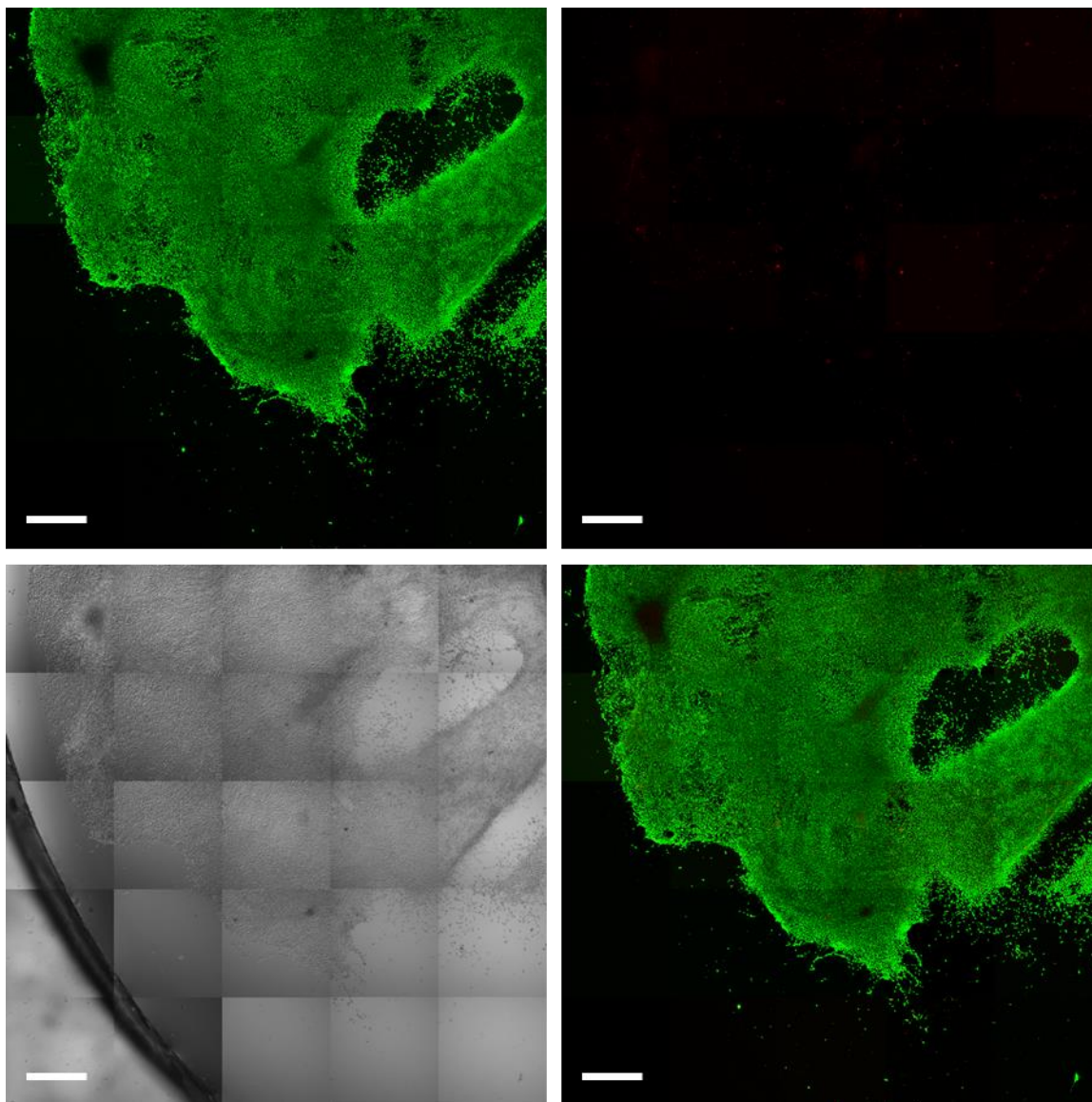


Appendix Figure 9. (A) Strain sweep ($T = 37\text{ }^{\circ}\text{C}$, $\omega = 10\text{ rad}\cdot\text{s}^{-1}$) and (B) frequency sweep tests ($T = 37\text{ }^{\circ}\text{C}$, $\gamma = 0.2\%$) of **P-30-2%** hydrogels.

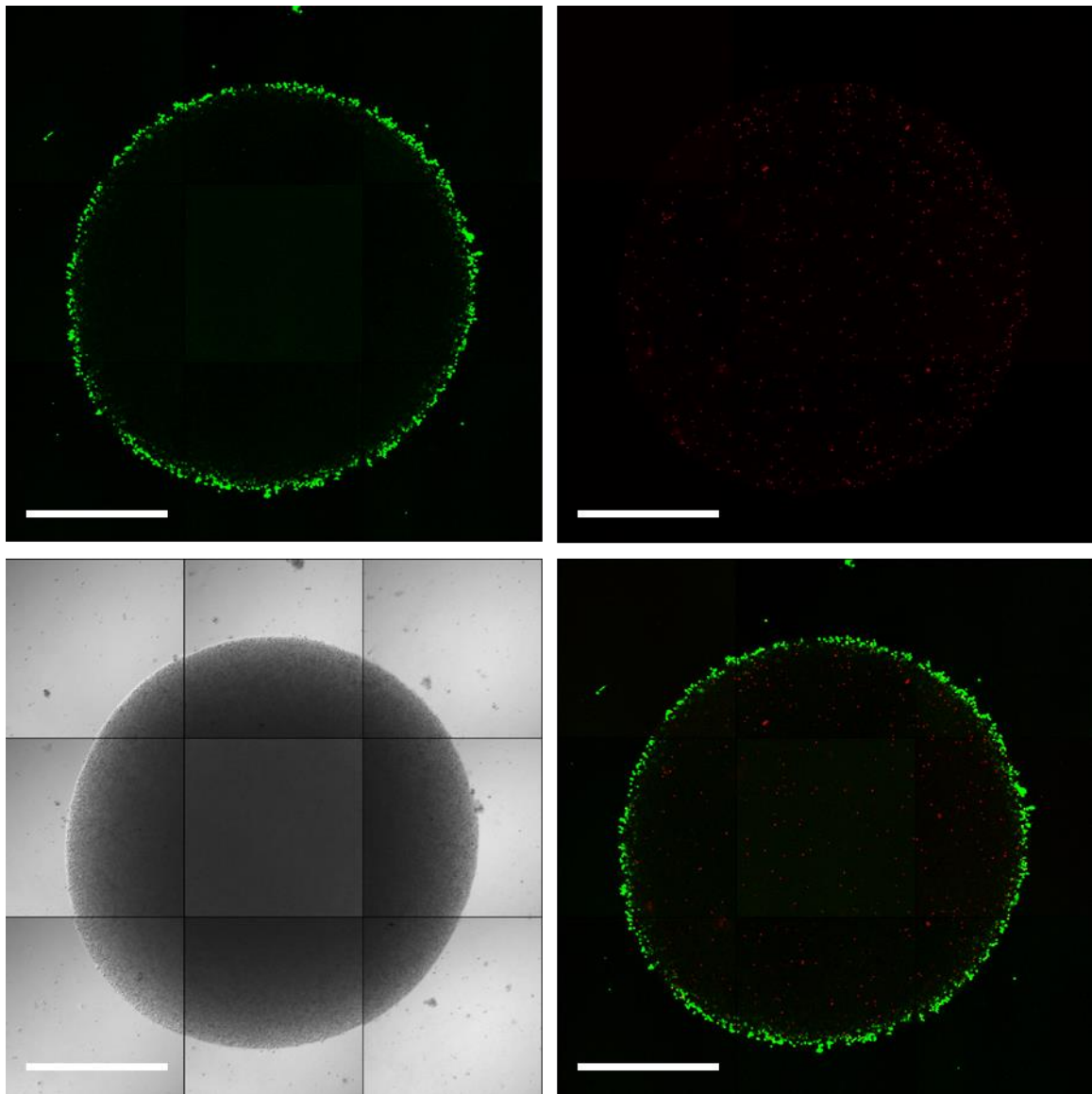


Appendix Figure 10. (A) Strain sweep ($T = 37\text{ }^\circ\text{C}$, $\omega = 10\text{ rad}\cdot\text{s}^{-1}$) and (B) frequency sweep tests ($T = 37\text{ }^\circ\text{C}$, $\gamma = 0.2\%$) of **P-30-8%** hydrogels.

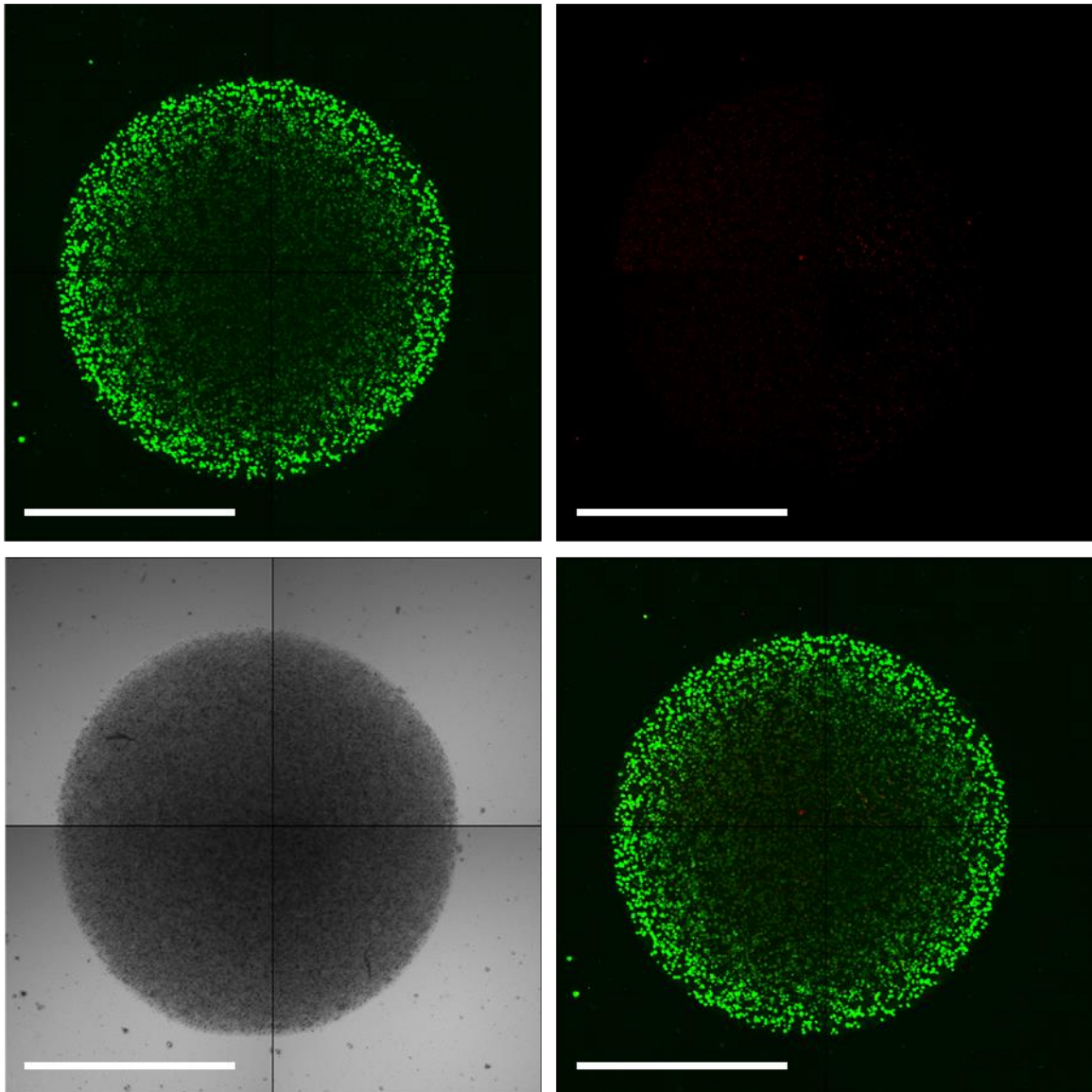
Fluorescence Confocal Microscopy



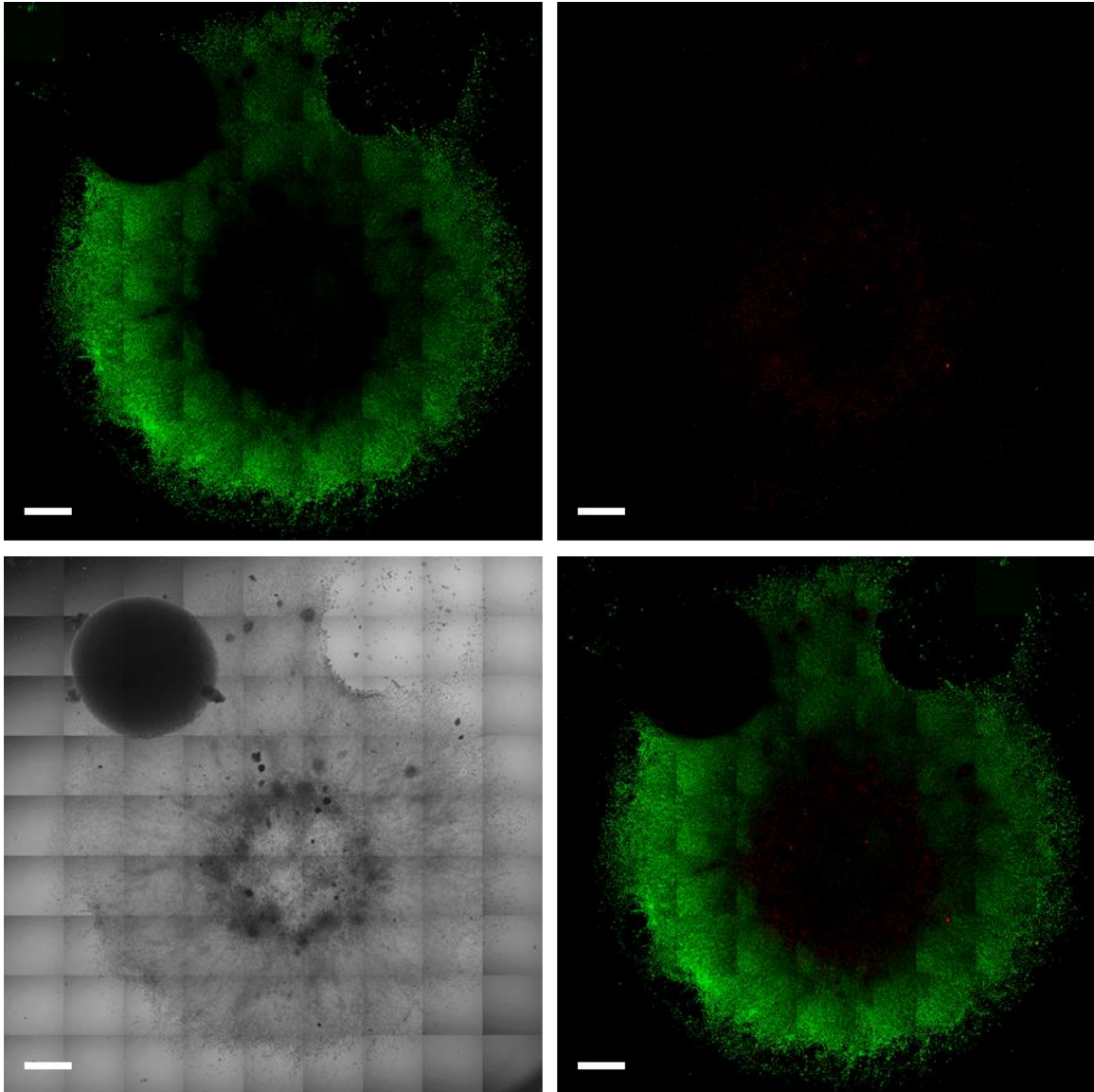
Appendix Figure 11. Images (10×) of P-20-4% hydrogel cell culture after 7 d of incubation, including a green fluorescence (*top-left*), brightfield (*bottom-left*), red fluorescence (*top-right*) and merged fluorescence image (*bottom-right*). Scale bars = 1 mm.



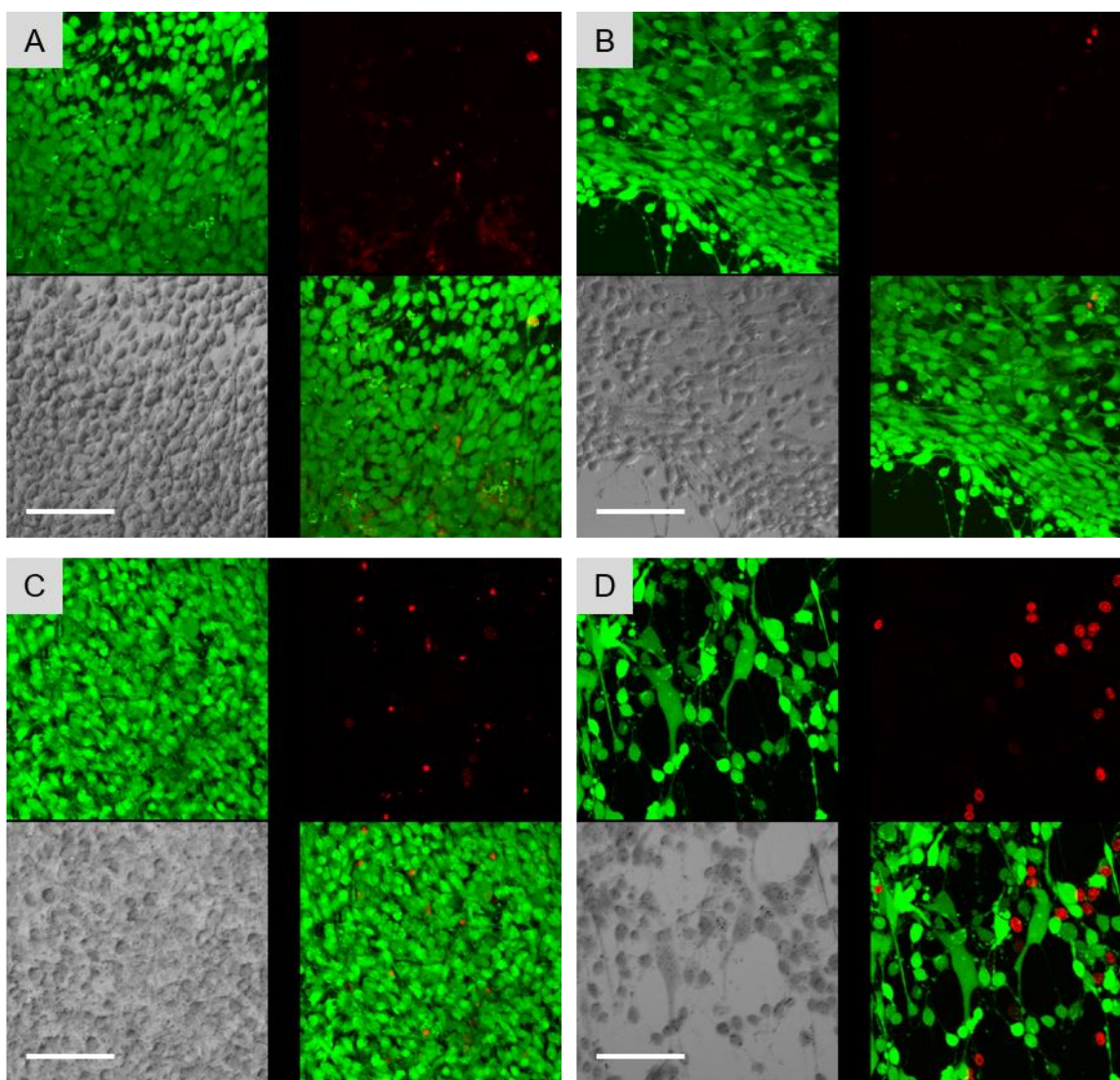
Appendix Figure 12. Images (10 \times) of P-30-4% hydrogel cell culture after 1 h of incubation, including a green fluorescence (*top-left*), brightfield (*bottom-left*), red fluorescence (*top-right*) and merged fluorescence image (*bottom-right*). Scale bars = 1 mm.



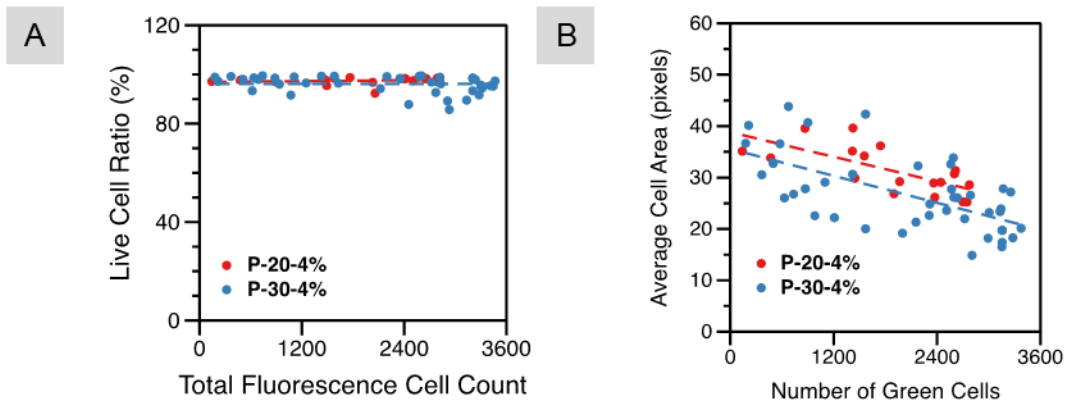
Appendix Figure 13. Images (10×) of **P-30-4%** hydrogel cell culture after 5 d of incubation, including a green fluorescence (*top-left*), brightfield (*bottom-left*), red fluorescence (*top-right*) and merged fluorescence image (*bottom-right*). Scale bars = 1 mm.



Appendix Figure 14. Images (10×) of **P-30-4%** hydrogel cell culture after 7 d of incubation, including a green fluorescence (*top-left*), brightfield (*bottom-left*), red fluorescence (*top-right*) and merged fluorescence image (*bottom-right*). Scale bars = 1 mm.



Appendix Figure 15. High magnification images (40 \times) of P-20-4% (top) and P-30-4% (bottom) hydrogel cell cultures after 7 d in gel-dense areas (**A** and **C**) and at gel-glass interfaces (**B** and **D**). Scale bars = 100 μ m. Each figure includes a green fluorescence (*top-left*), brightfield (*bottom-left*), red fluorescence (*top-right*) and merged fluorescence image (*bottom-right*).

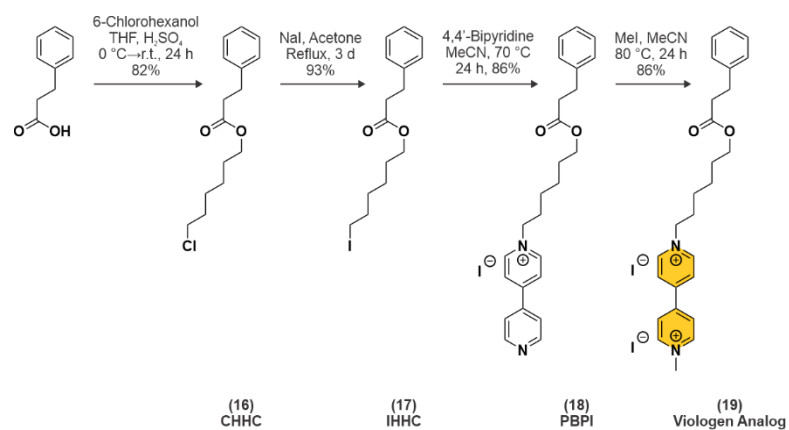


Appendix Figure 16. Cell quantification of P-20-4% and P-30-4% hydrogel cell cultures after 7 d.

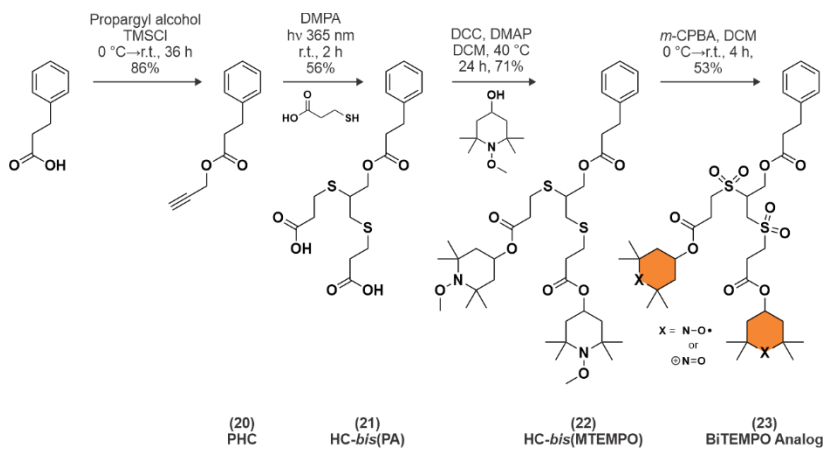
APPENDIX B

SUPPLEMENTARY DATA FOR CHAPTER III

Syntheses of Small-molecule Analogs

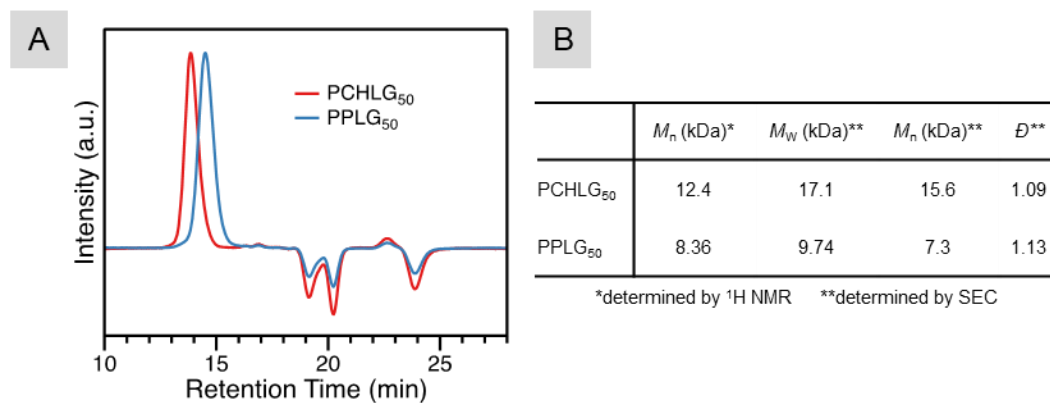


Appendix Figure 17. Synthesis of viologen analog.



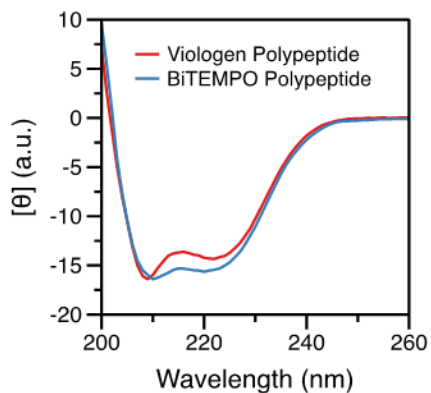
Appendix Figure 18. Synthesis of biTEMPO analog.

Size Exclusion Chromatography



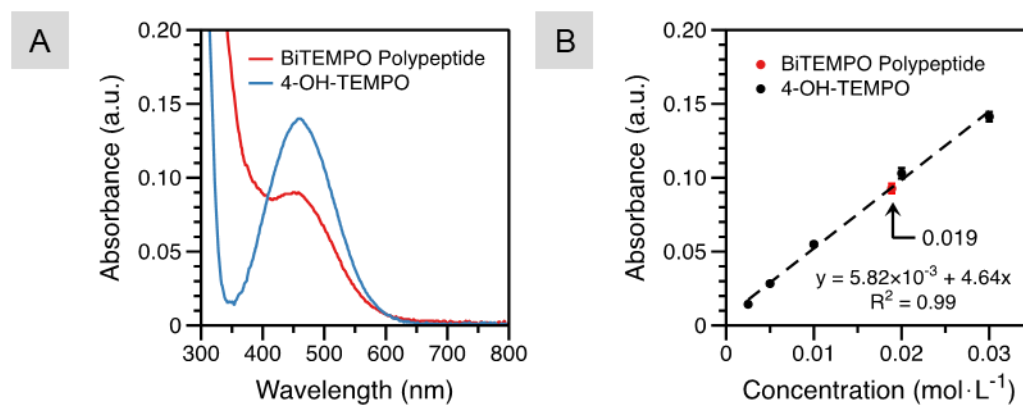
Appendix Figure 19. (A) SEC traces of PCHLG₅₀ (**4**) and PPLG₅₀ (**12**), and (B) their tabulated dispersity and molar mass values.

Circular Dichroism



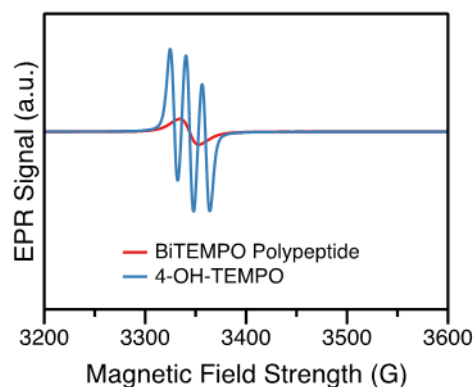
Appendix Figure 20. Normalized CD spectra of viologen polypeptide (**6**) and biTEMPO polypeptide (**14**) in ACN (0.1 mg·mL⁻¹).

Ultraviolet-visible Spectroscopy



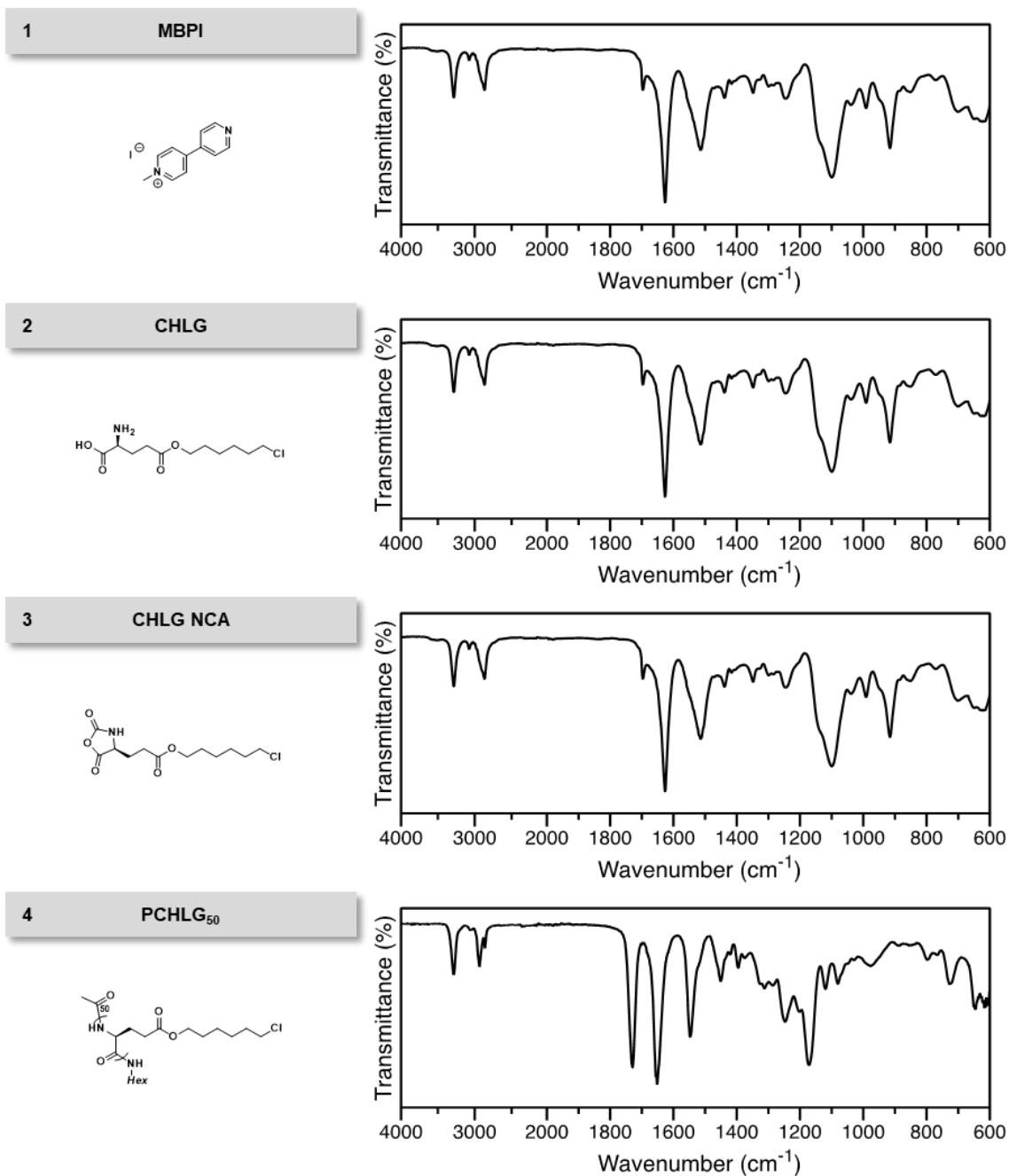
Appendix Figure 21. (A) UV-vis spectra of biTEMPO polypeptide (1 mM of repeating unit) and 4-OH-TEMPO (1 mM) in CHCl₃. (B) UV-vis calibration curve of 4-OH-TEMPO in CHCl₃.

Electron Paramagnetic Resonance Spectroscopy

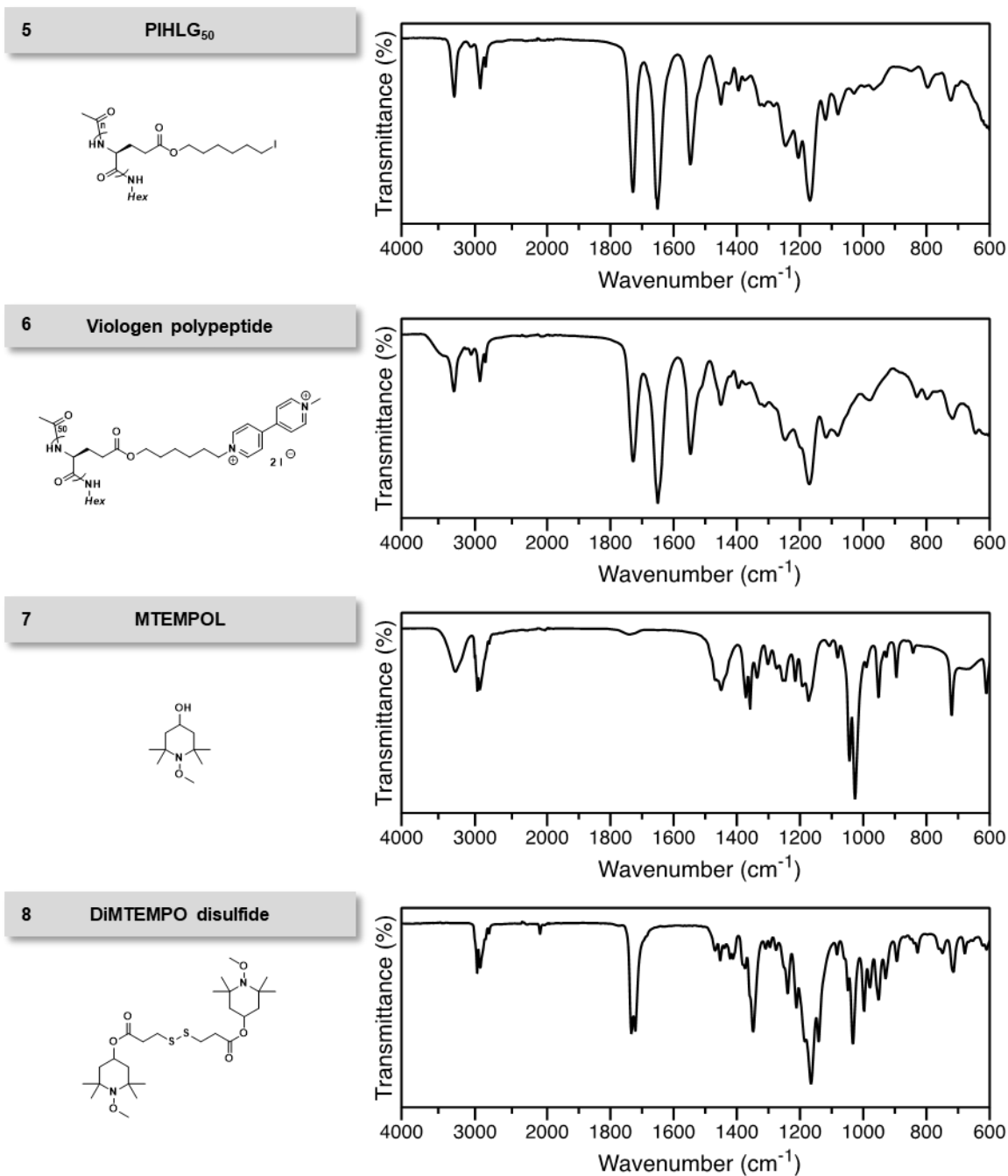


Appendix Figure 22. EPR spectra of biTEMPO polypeptide (1 mM of repeating unit) and 4-OH-TEMPO (1 mM) in CHCl₃.

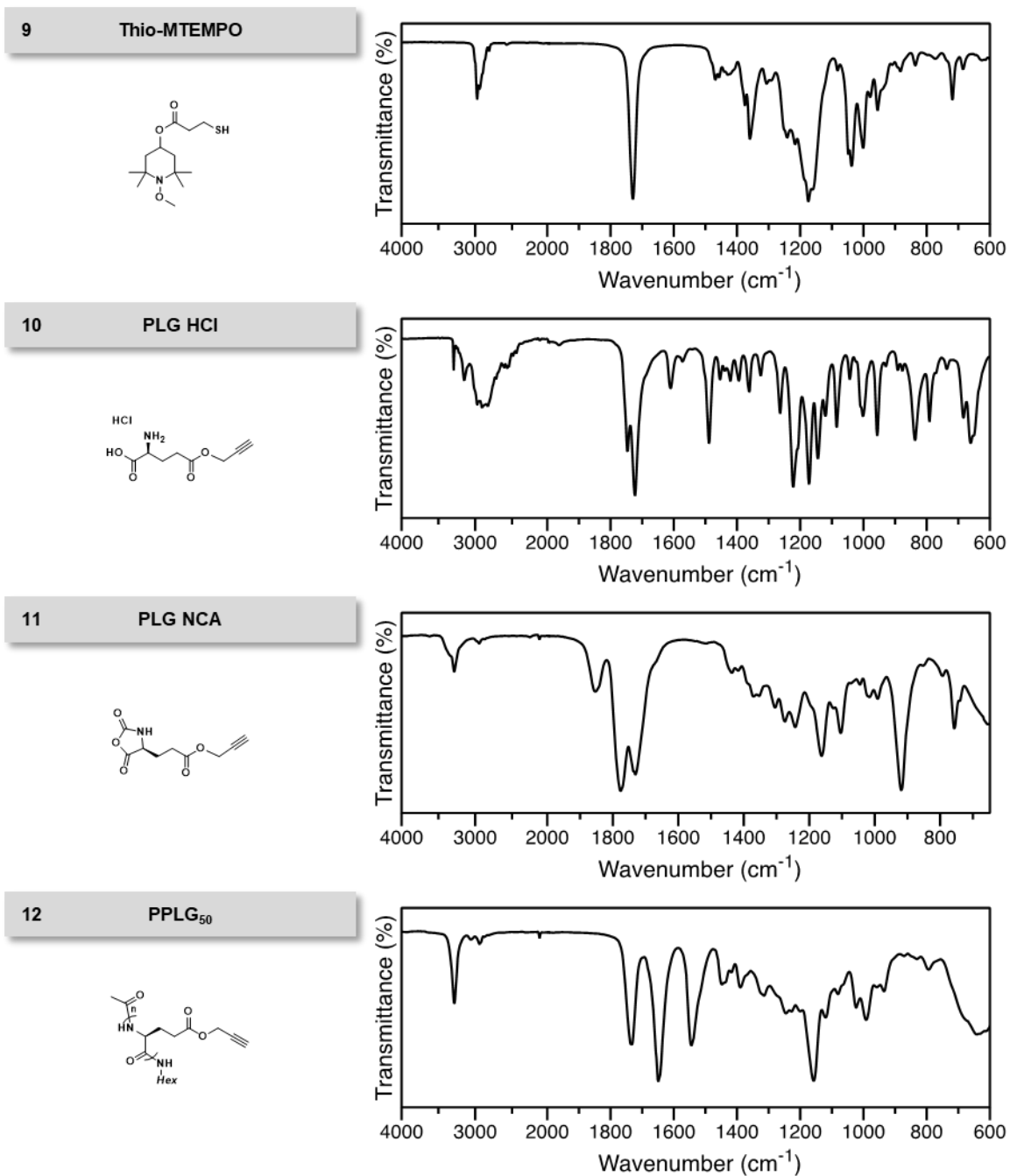
Attenuated Total Reflection-Fourier Transform Infrared Spectroscopy



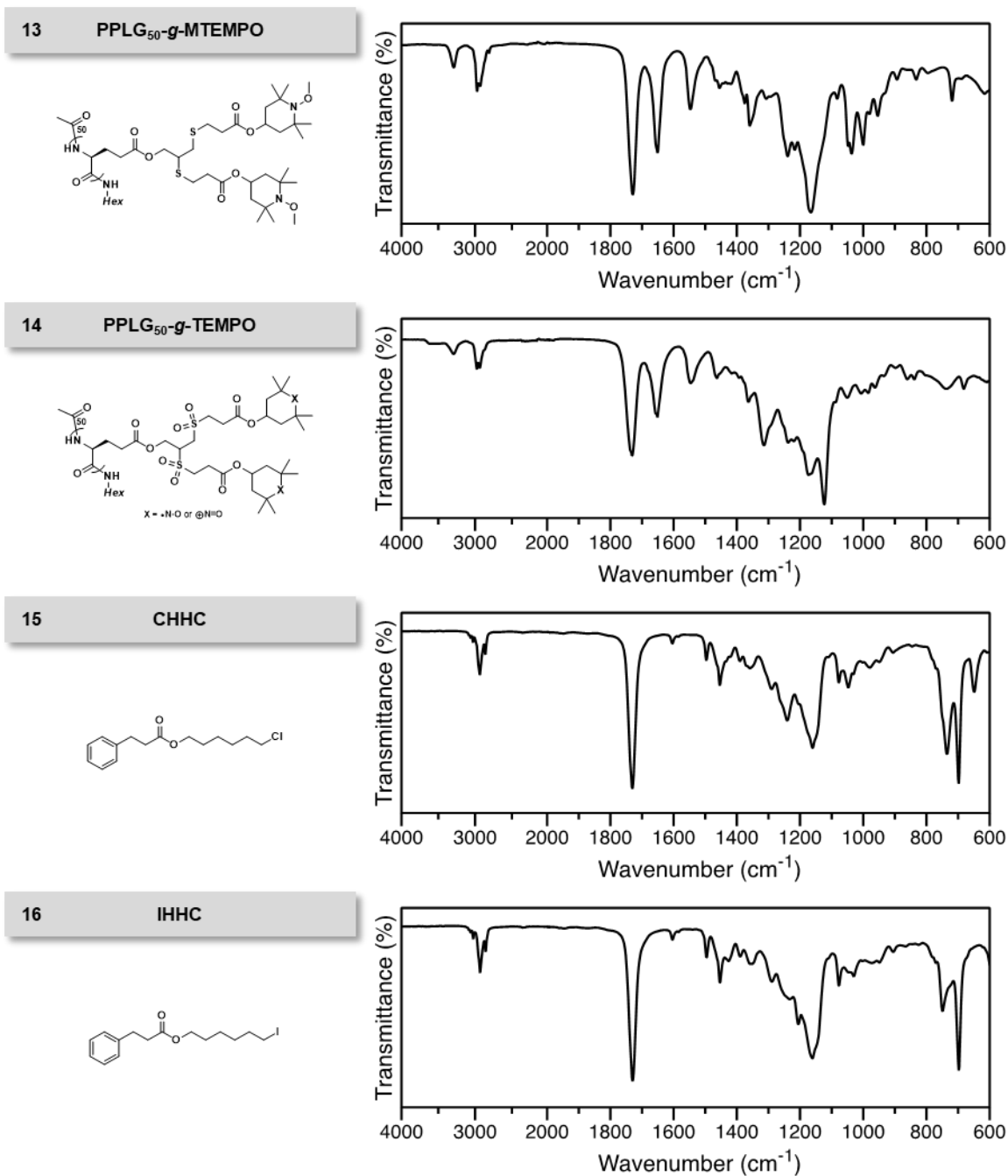
Appendix Figure 23. ATR-FTIR spectra of the synthesized species.



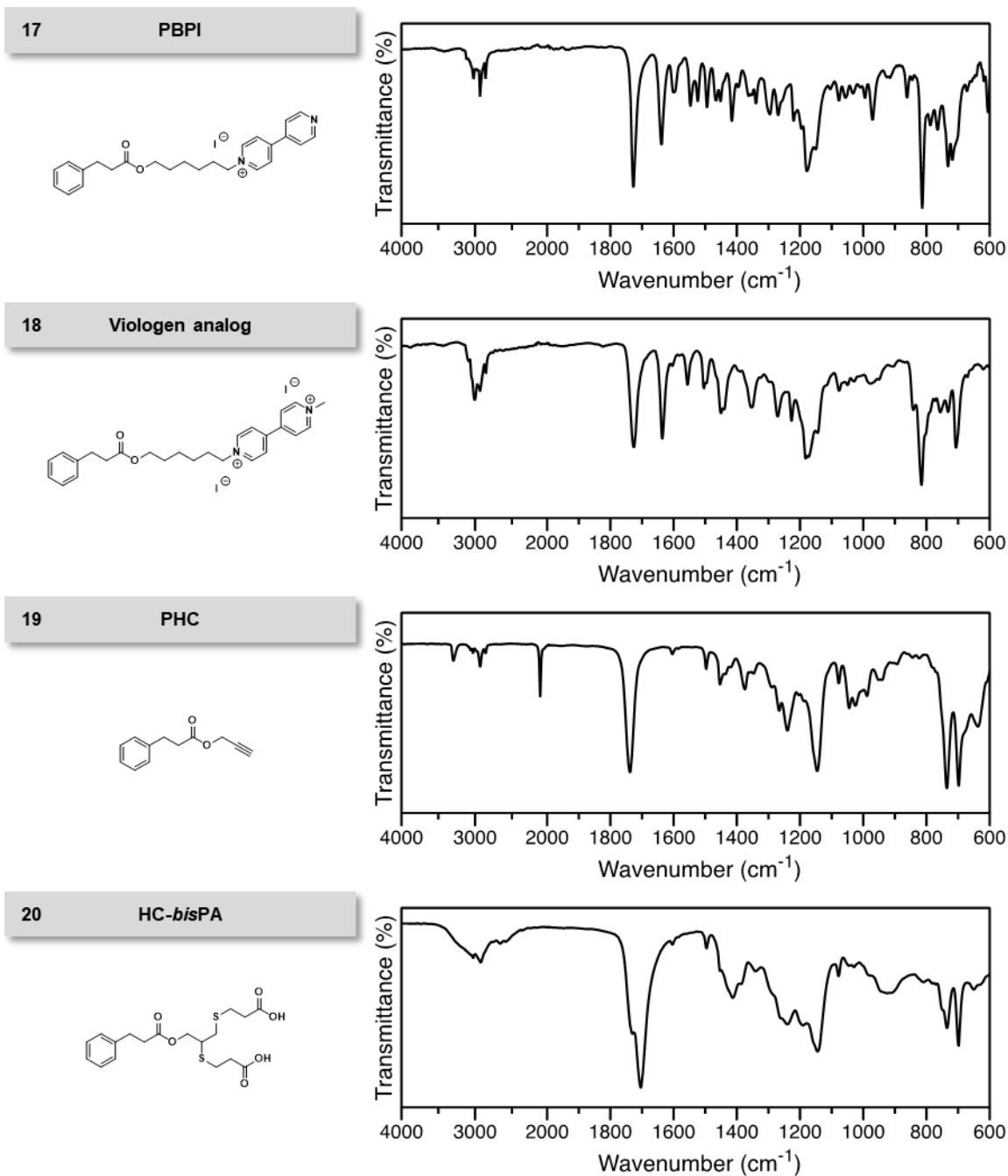
Appendix Figure 24. ATR-FTIR spectra of the synthesized species (cont'd).



Appendix Figure 25. ATR-FTIR spectra of the synthesized species (cont'd).

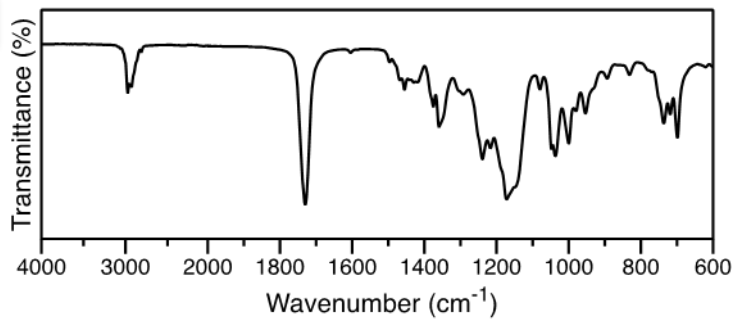
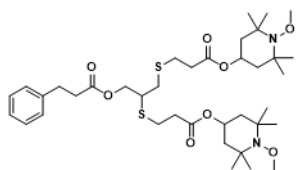


Appendix Figure 26. ATR-FTIR spectra of the synthesized species (cont'd).

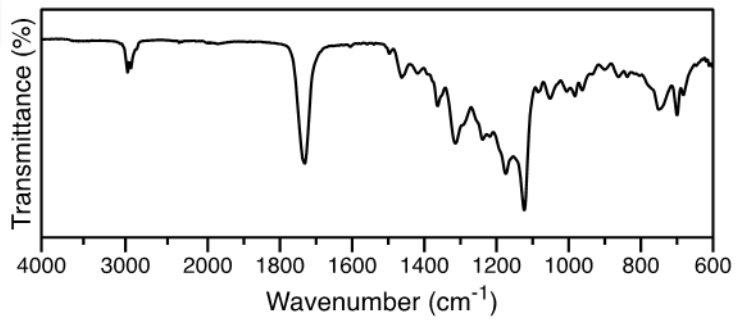
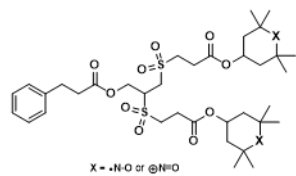


Appendix Figure 27. ATR-FTIR spectra of the synthesized species (cont'd).

21 HC-bis(MTEMPO)

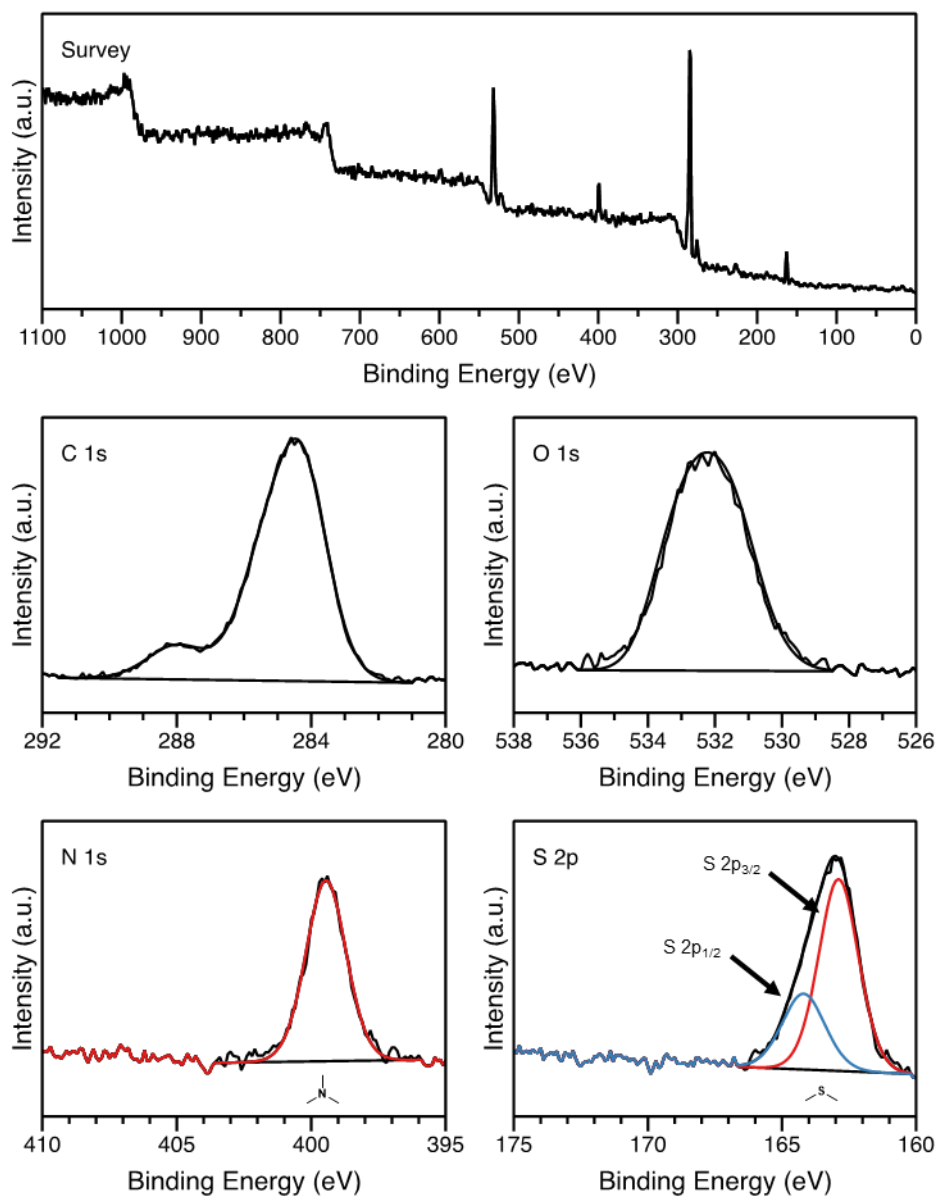


22 BiTEMPO analog

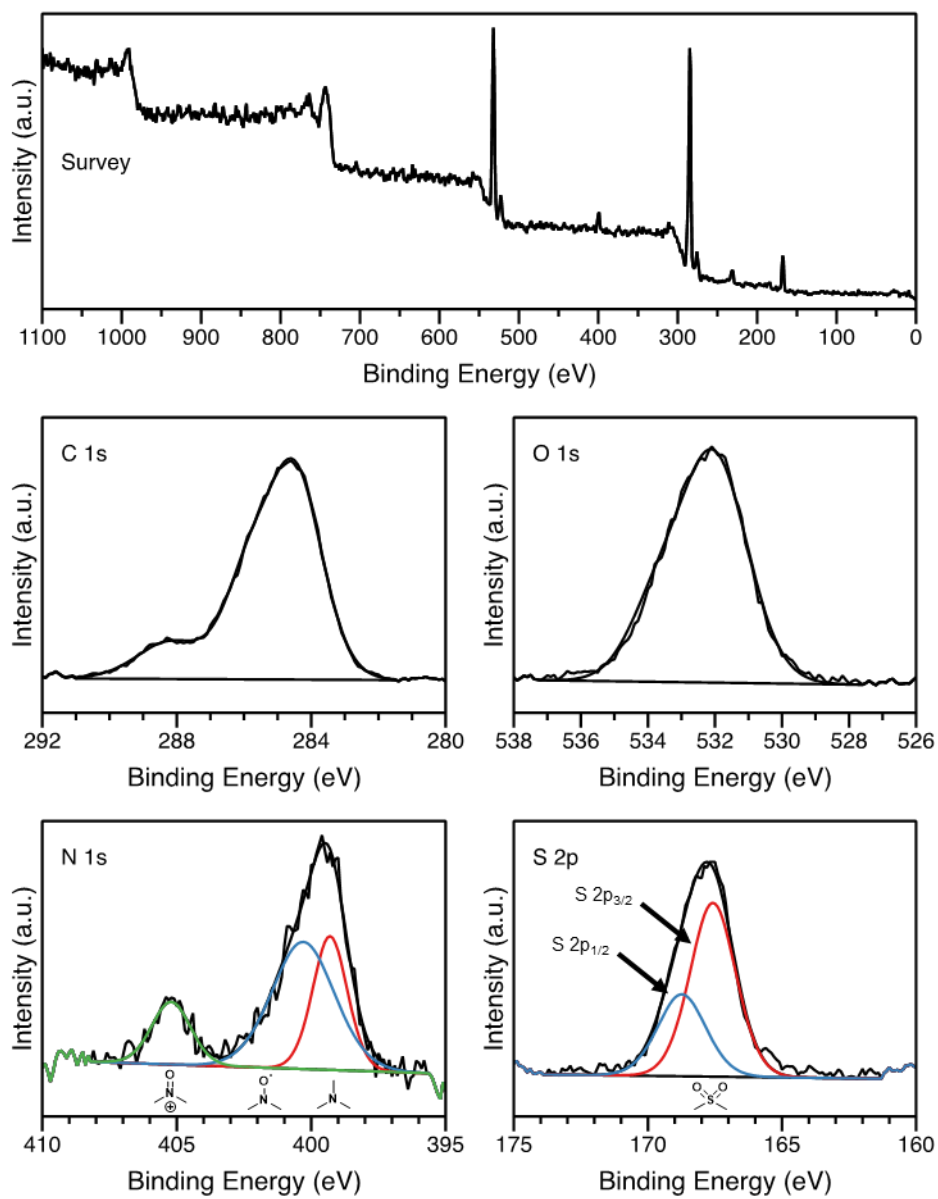


Appendix Figure 28. ATR-FTIR spectra of the synthesized species (cont'd).

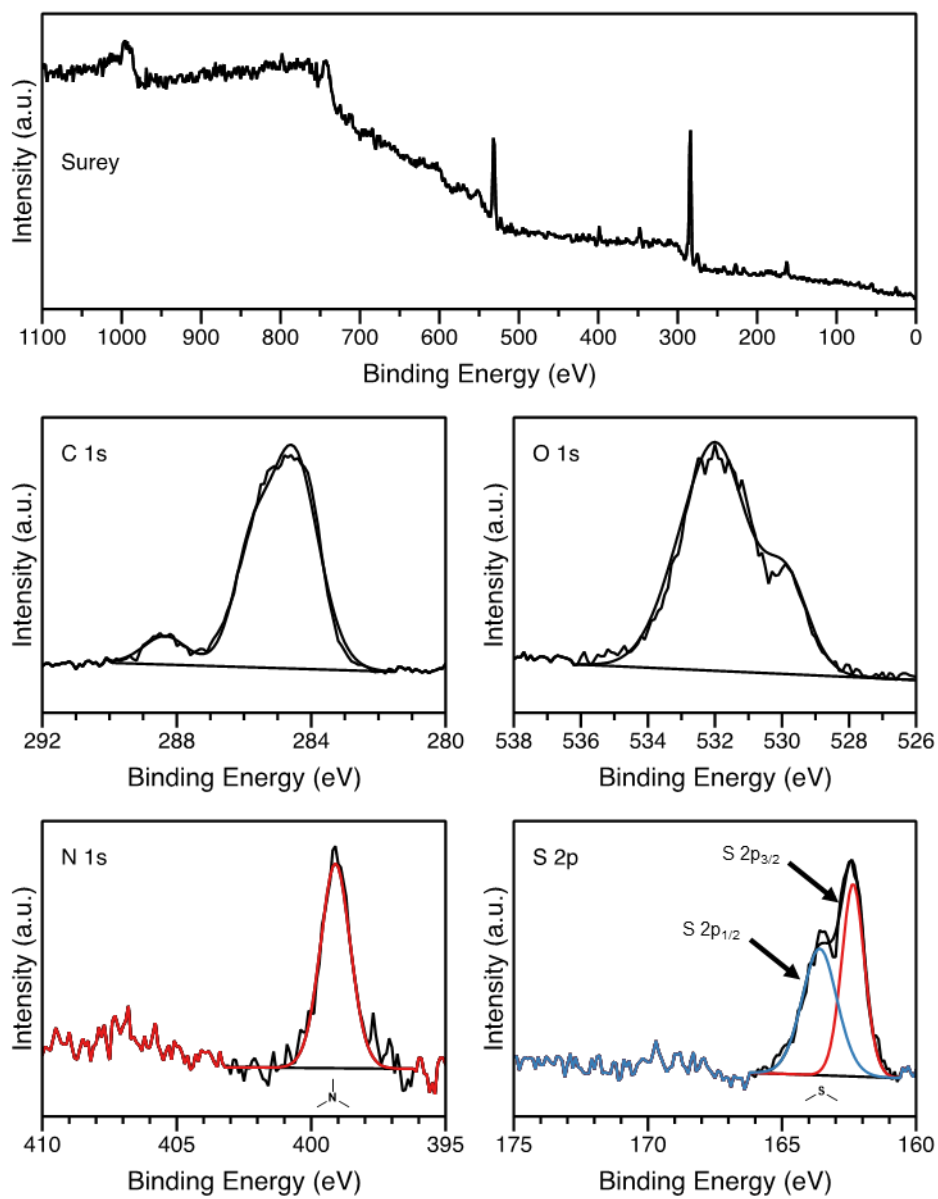
X-ray Photoelectron Spectroscopy



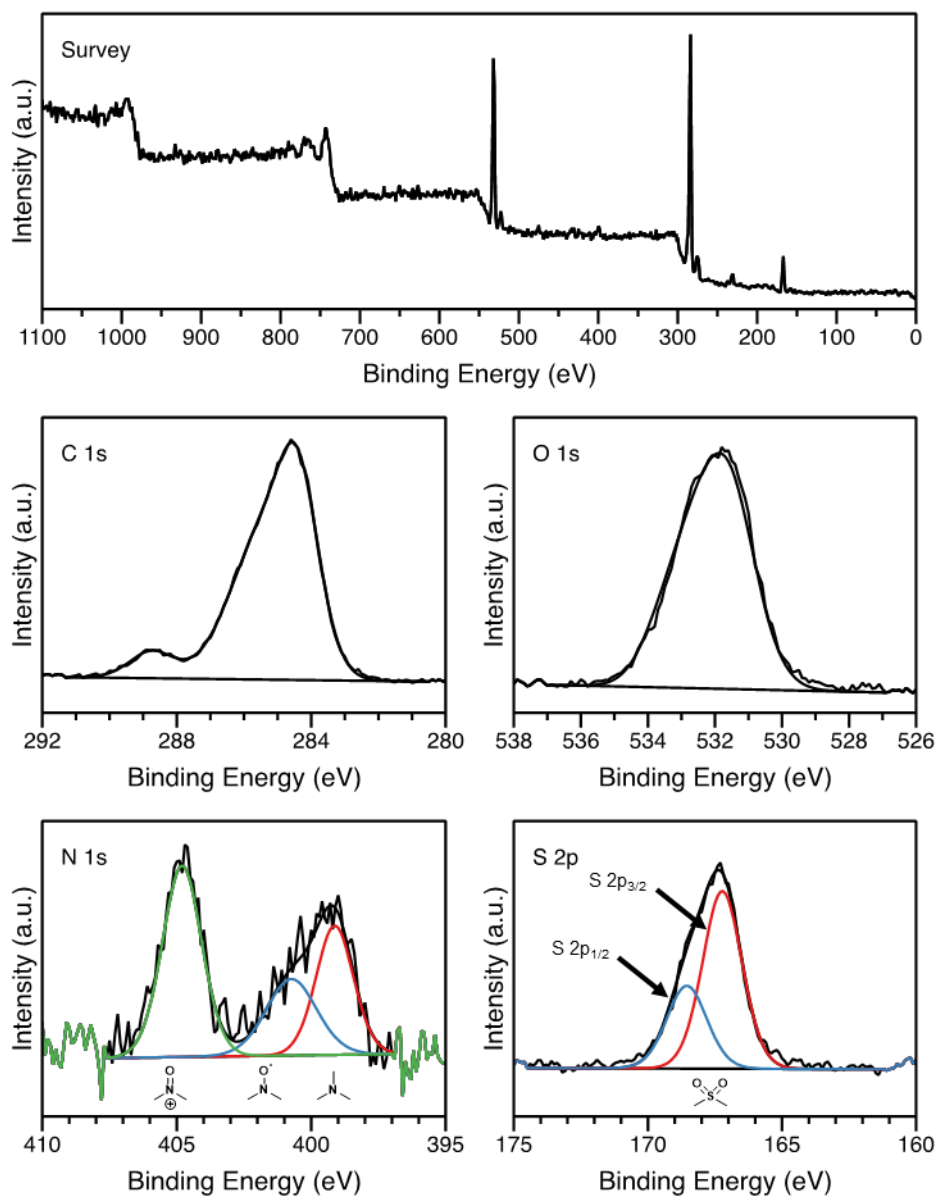
Appendix Figure 29. XPS spectra of PPLG₅₀-g-MTEMPO (13).



Appendix Figure 30. XPS spectra of biTEMPO polypeptide (**14**).

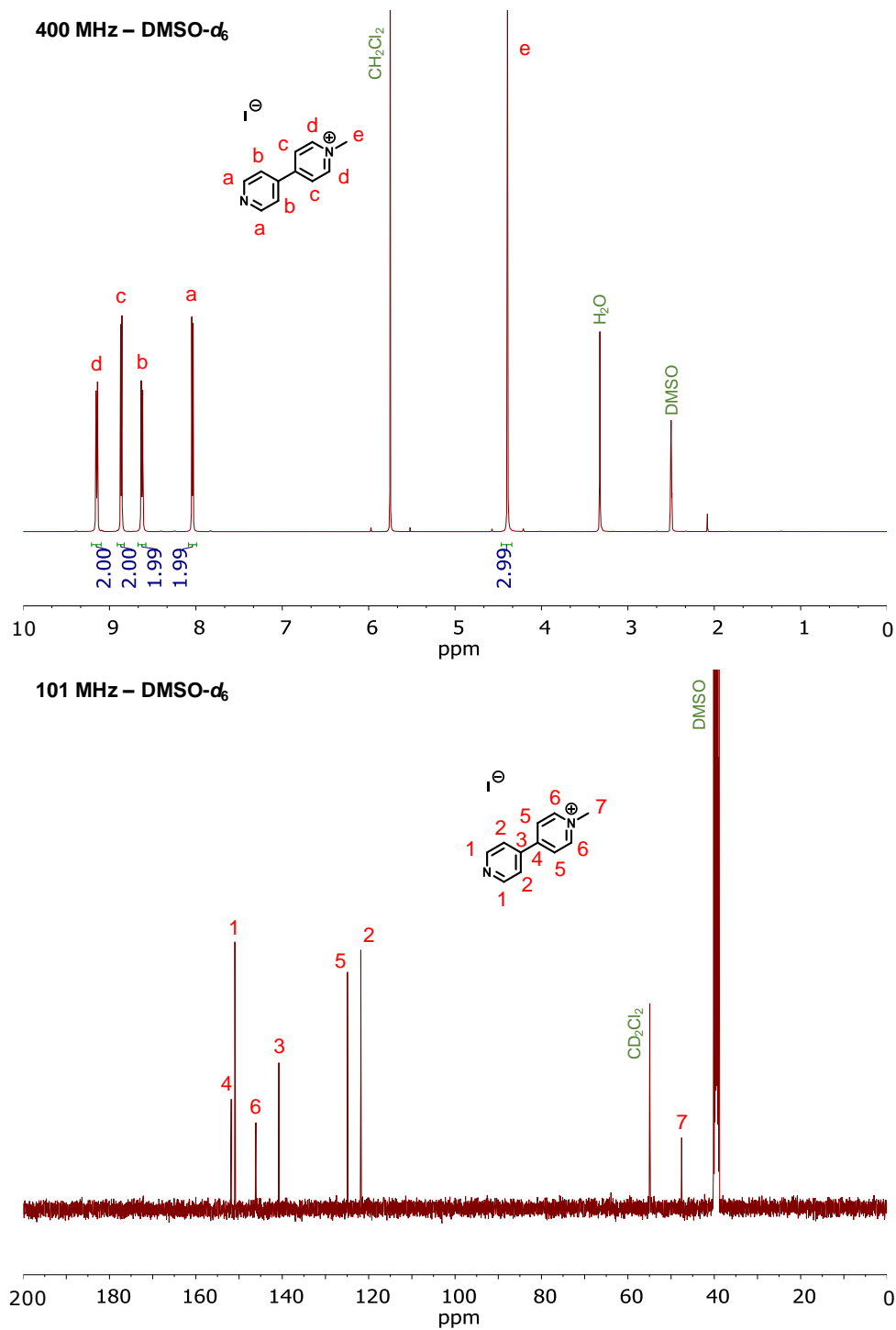


Appendix Figure 31. XPS spectra of HC-*bis*(MTEMPO) (**21**).

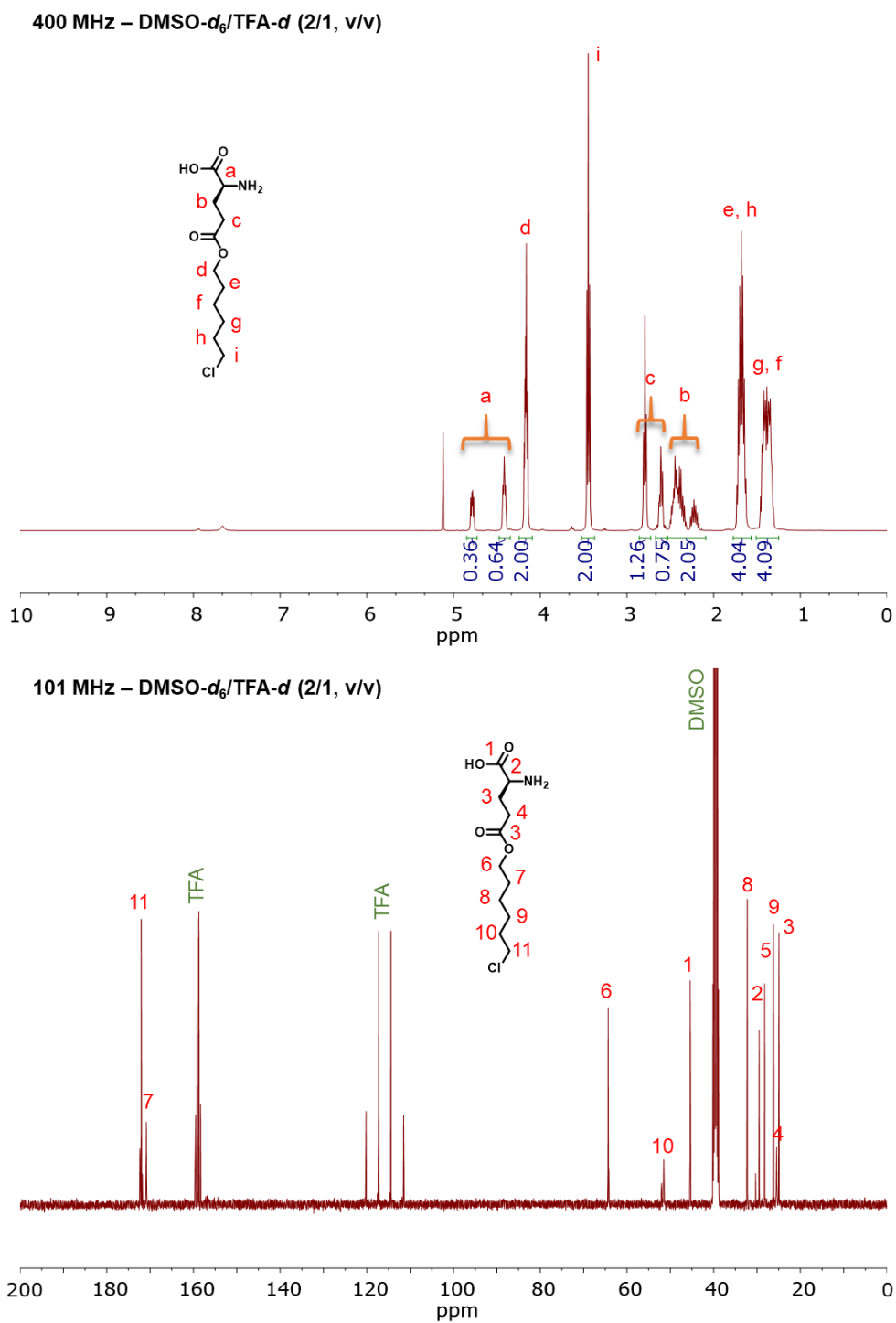


Appendix Figure 32. XPS spectra of biTEMPO analog (22).

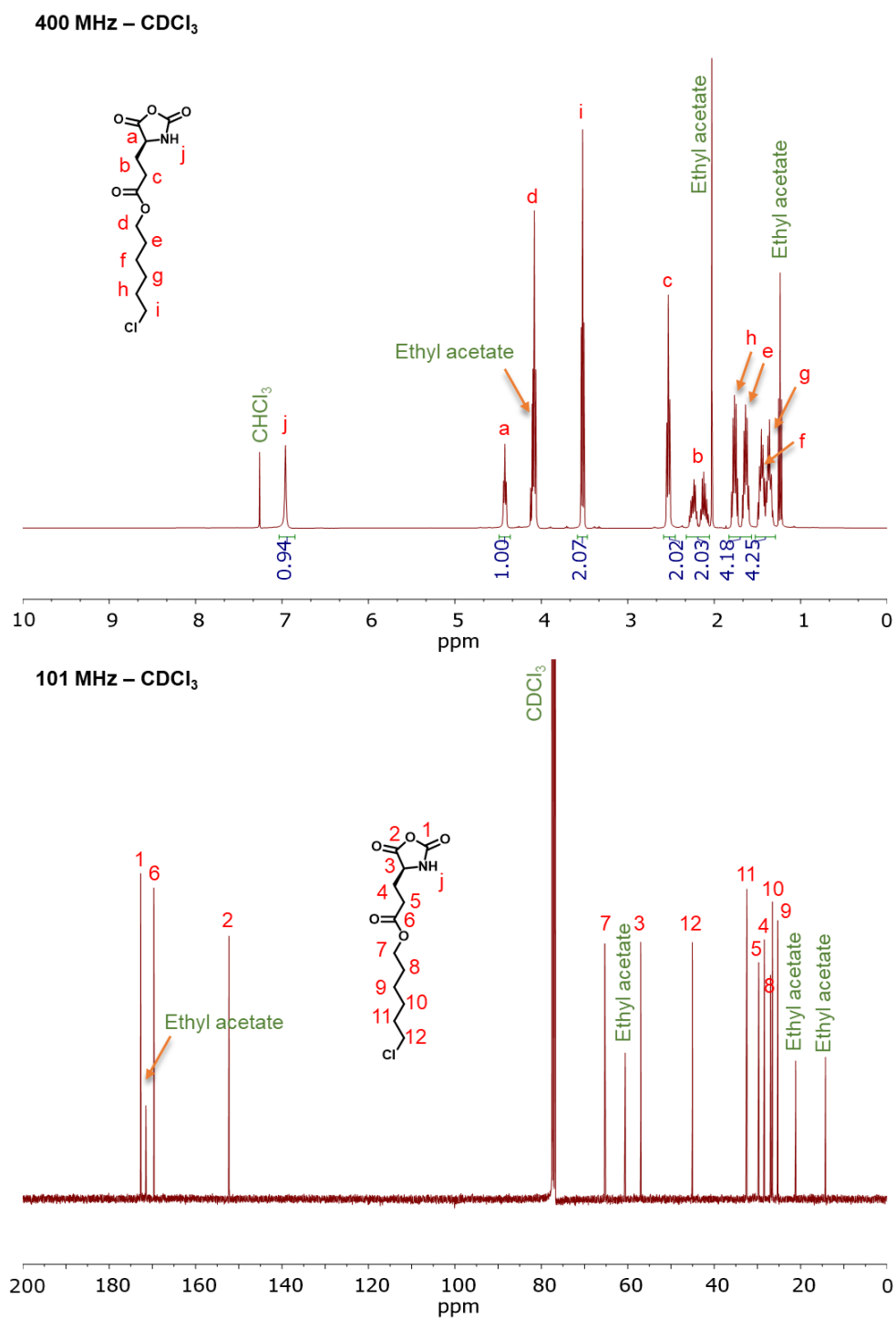
Nuclear Magnetic Resonance Spectroscopy



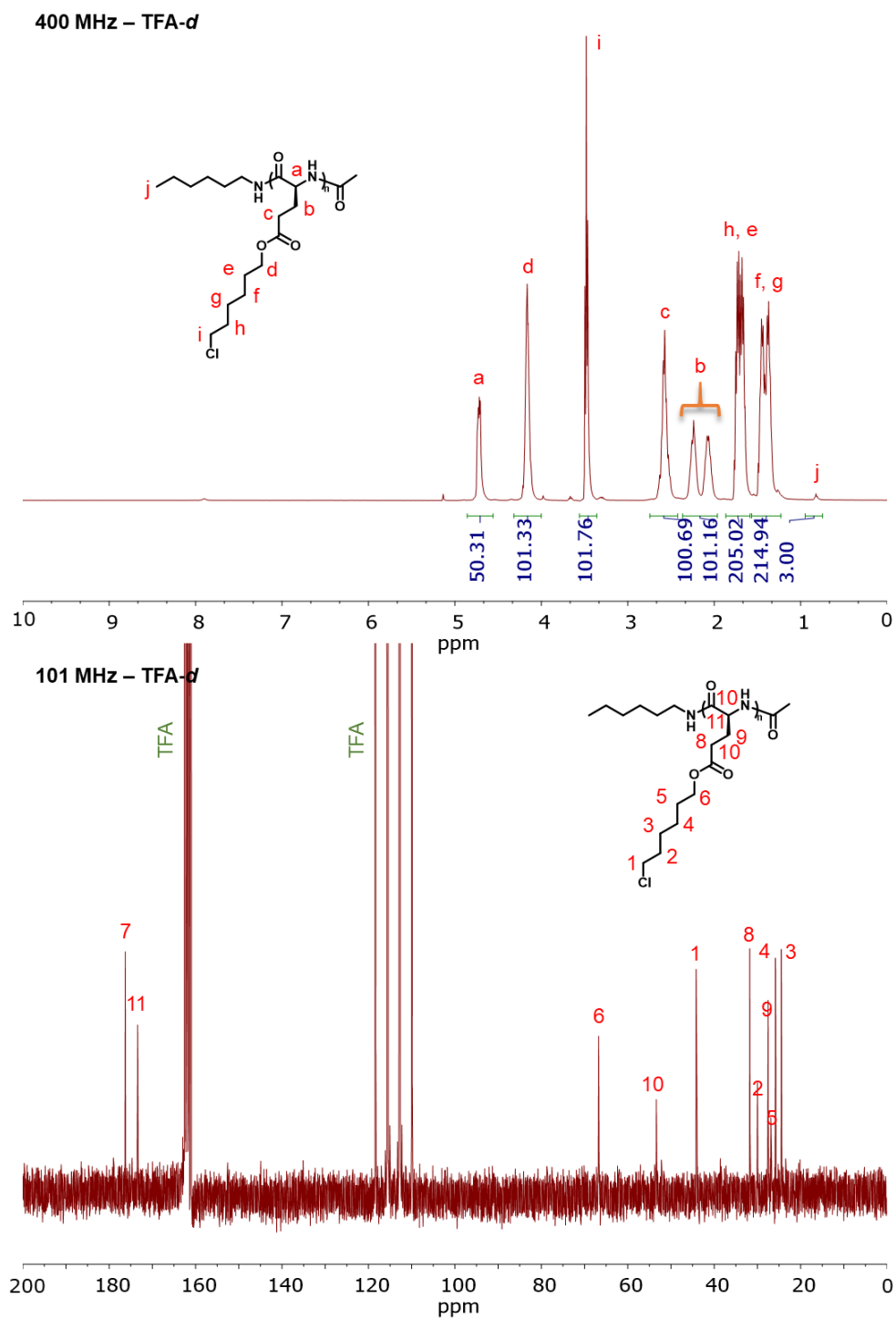
Appendix Figure 33. ¹H NMR and ¹³C NMR spectra of MBPI (2).



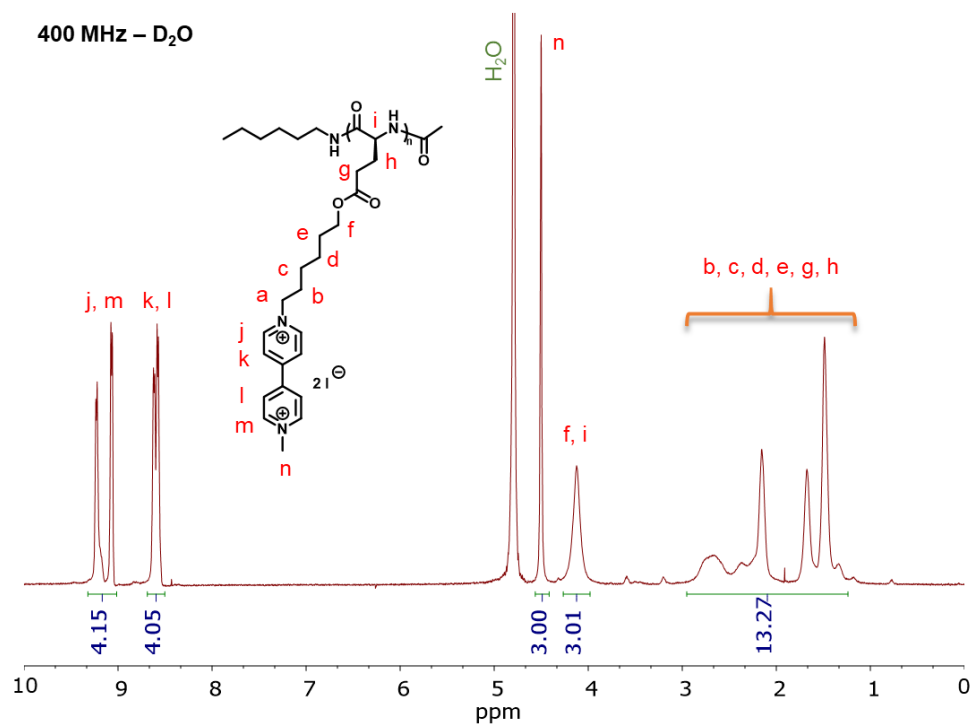
Appendix Figure 34. ¹H NMR and ¹³C NMR spectra of CHLG (3).



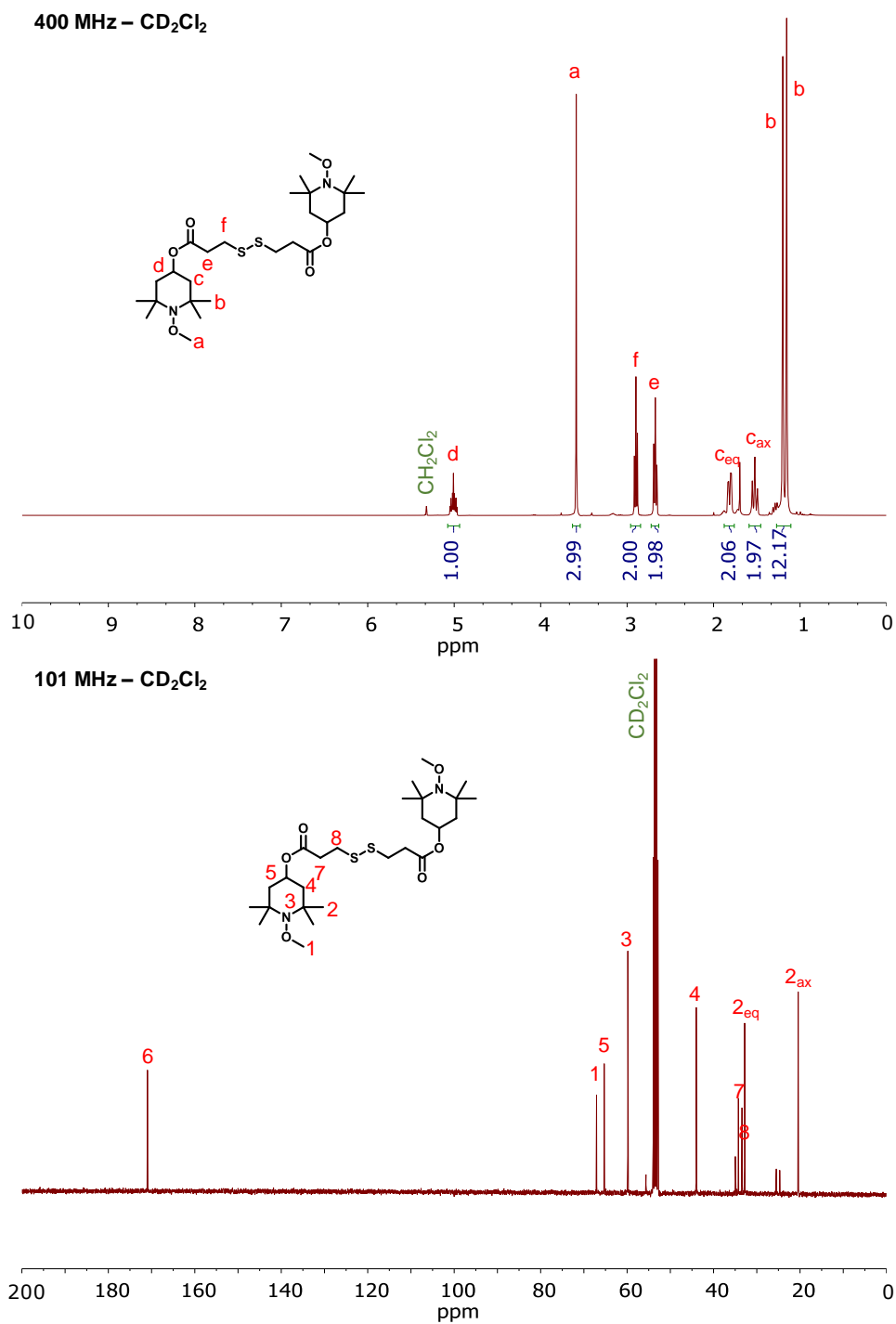
Appendix Figure 35. ¹H NMR and ¹³C NMR spectra of CHLG NCA (**4**).



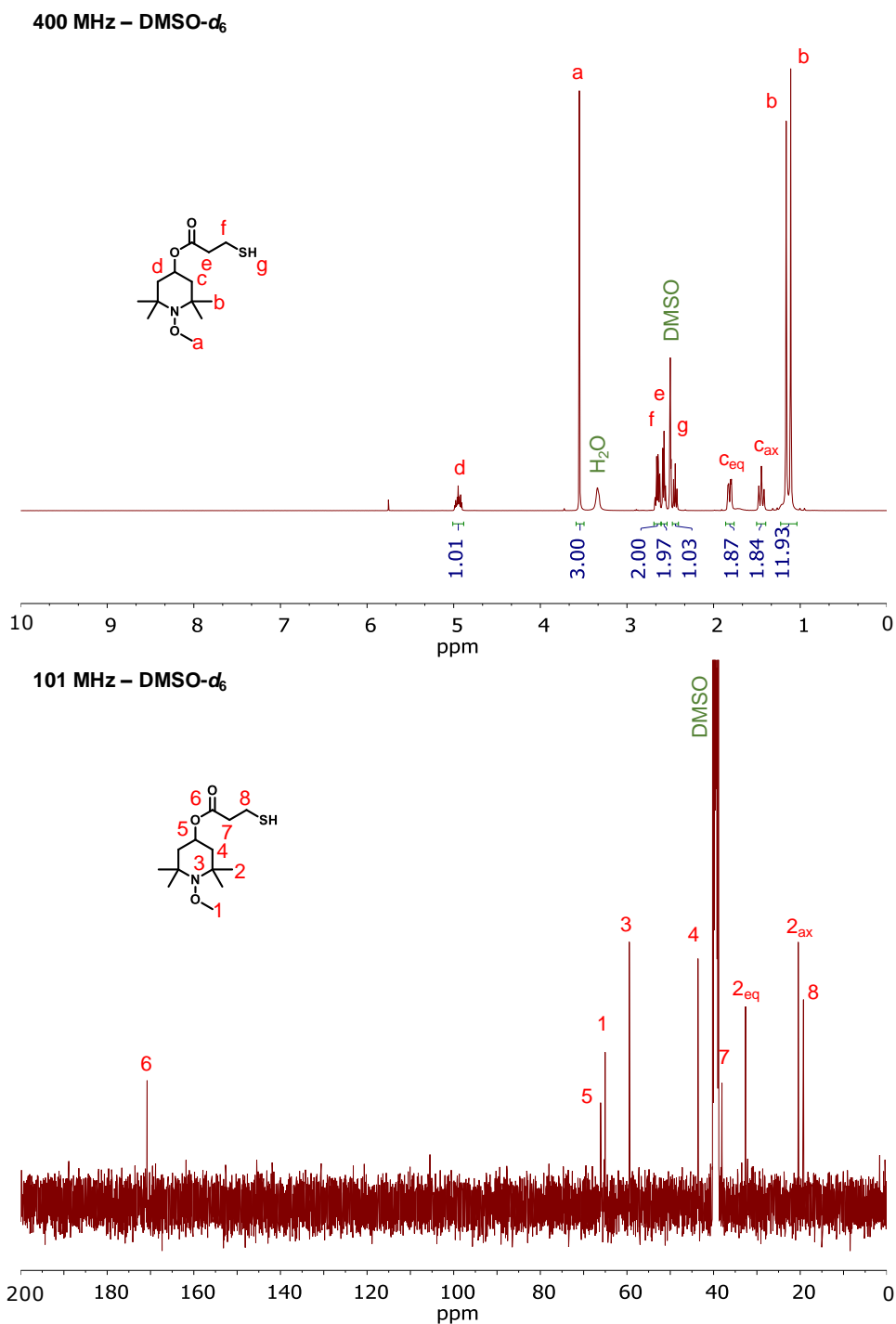
Appendix Figure 36. ¹H NMR and ¹³C NMR spectra of PCHLG₅₀ (5).



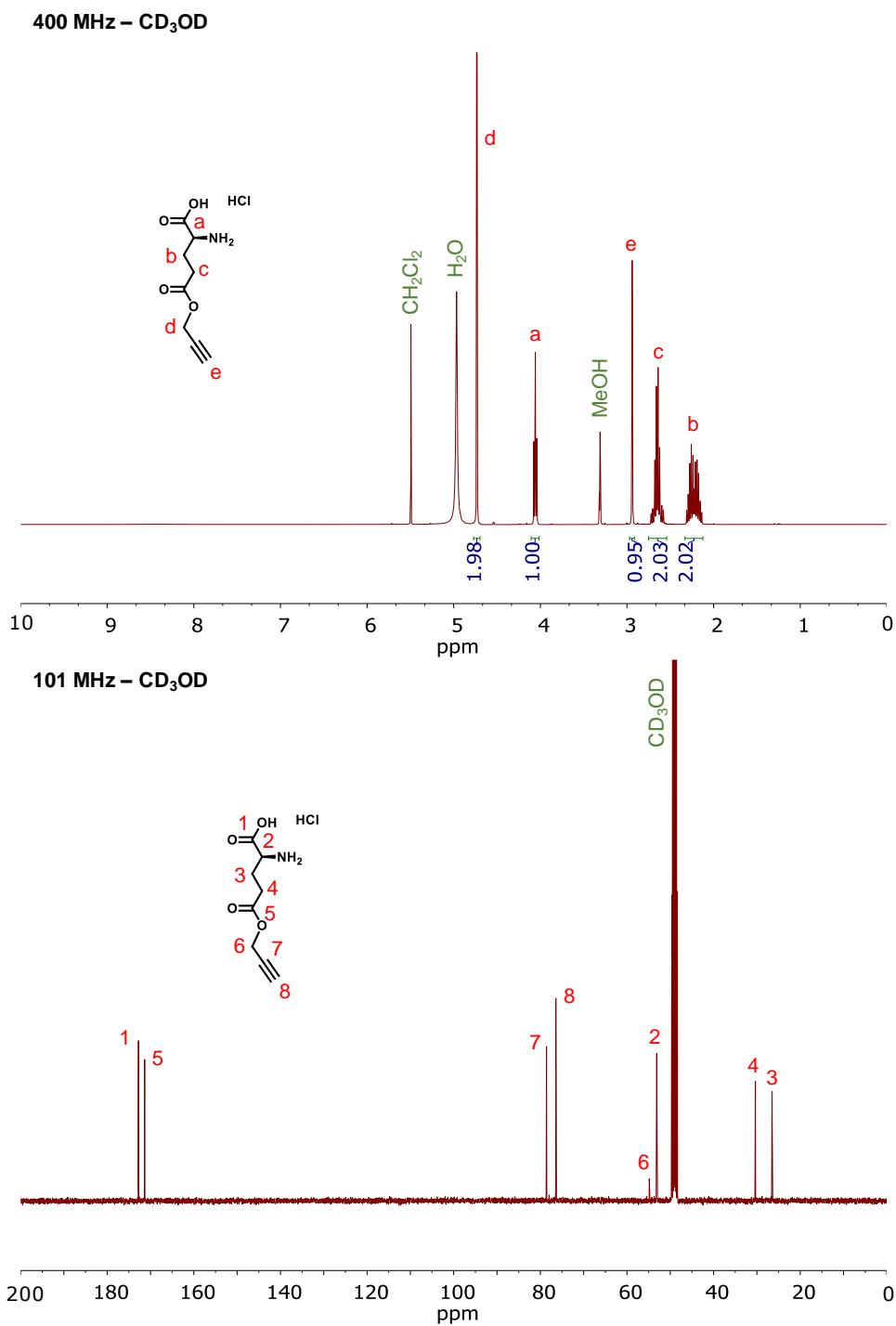
Appendix Figure 38. ¹H NMR and ¹³C NMR spectra of viologen polypeptide (7).



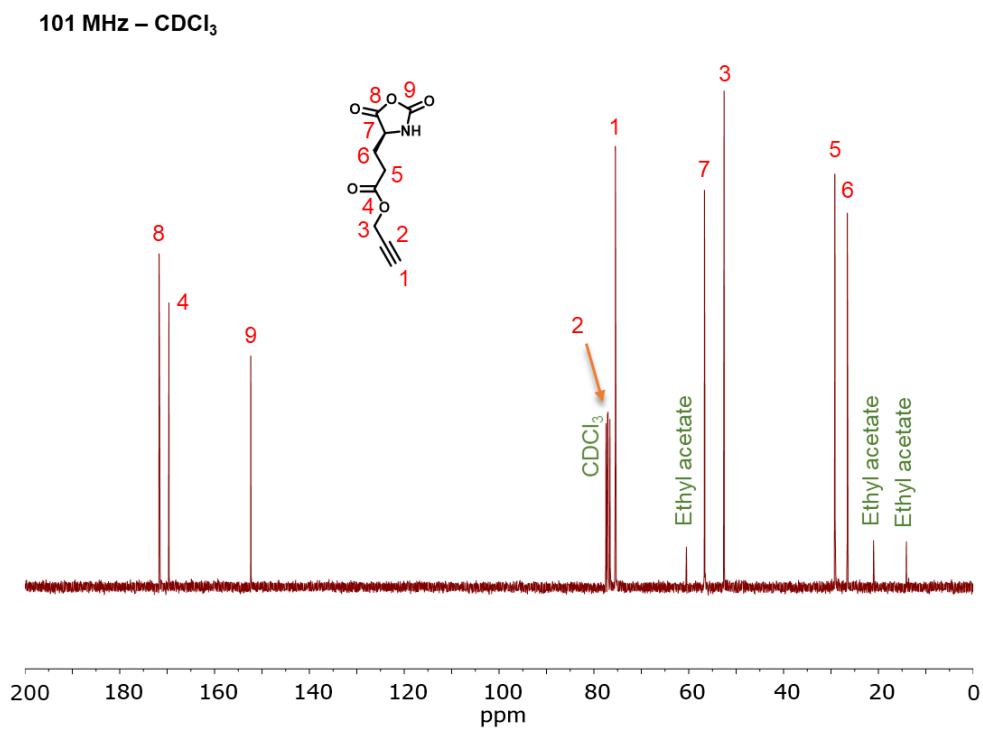
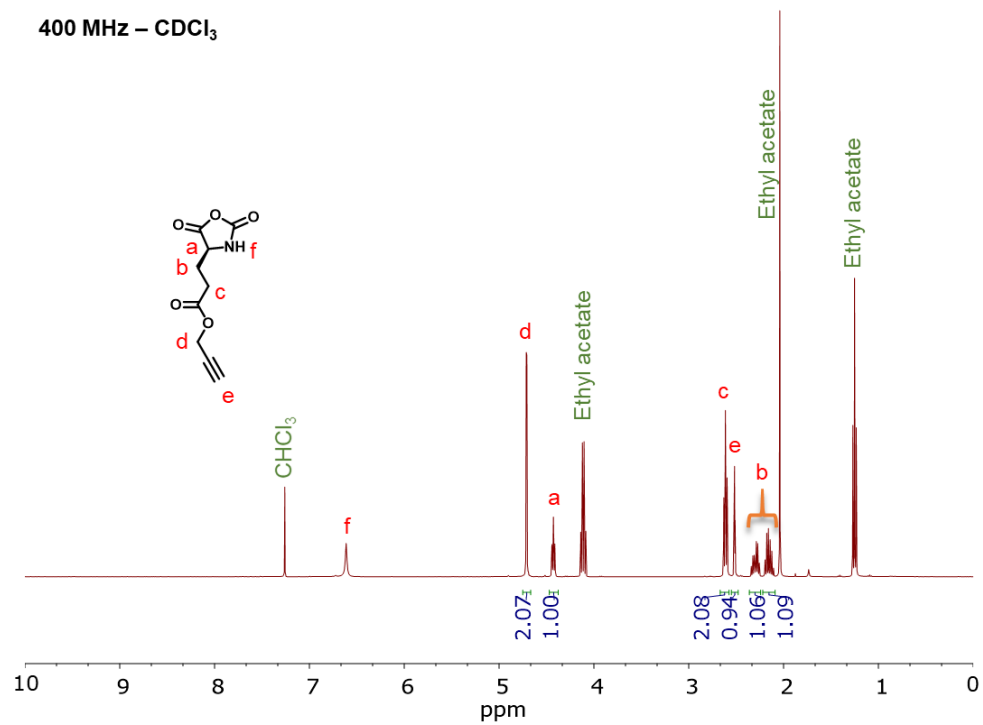
Appendix Figure 40. ¹H NMR and ¹³C NMR spectra of diMTEMPO disulfide (9).



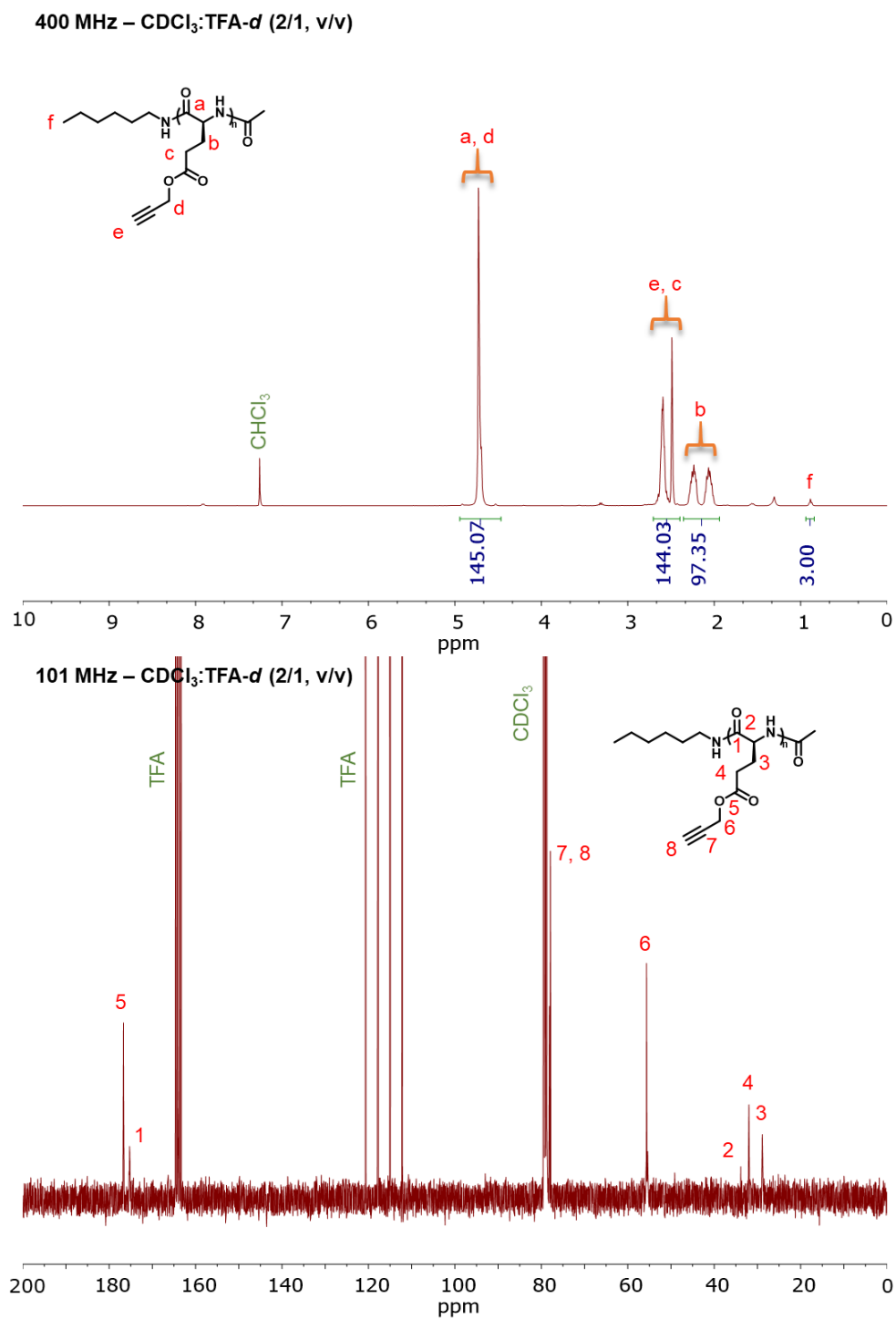
Appendix Figure 41. ^1H NMR and ^{13}C NMR spectra of Thio-MTEMPO (**10**).



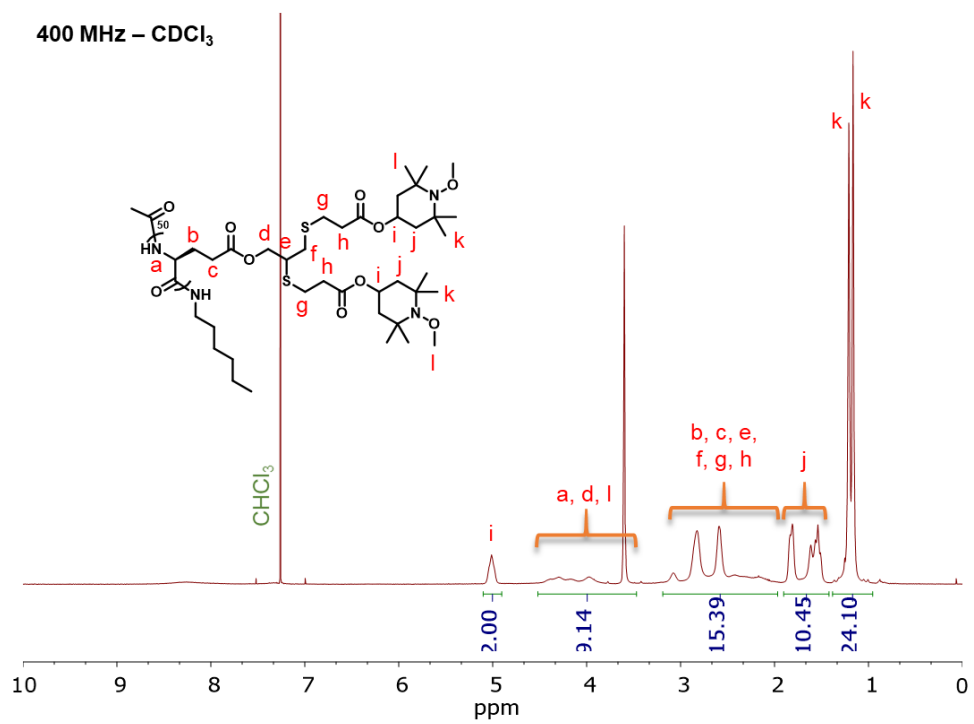
Appendix Figure 42. ¹H NMR and ¹³C NMR spectra of PLG HCl (**11**).



Appendix Figure 43. ¹H NMR and ¹³C NMR spectra of PLG NCA (12).

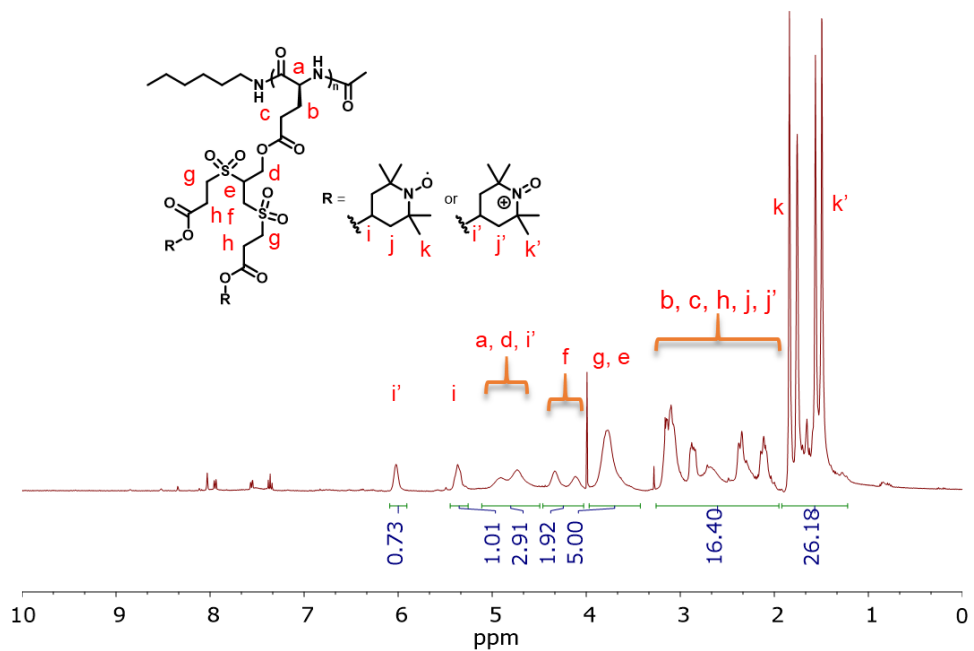


Appendix Figure 44. ¹H NMR and ¹³C NMR spectra of PPLG₅₀ (13).

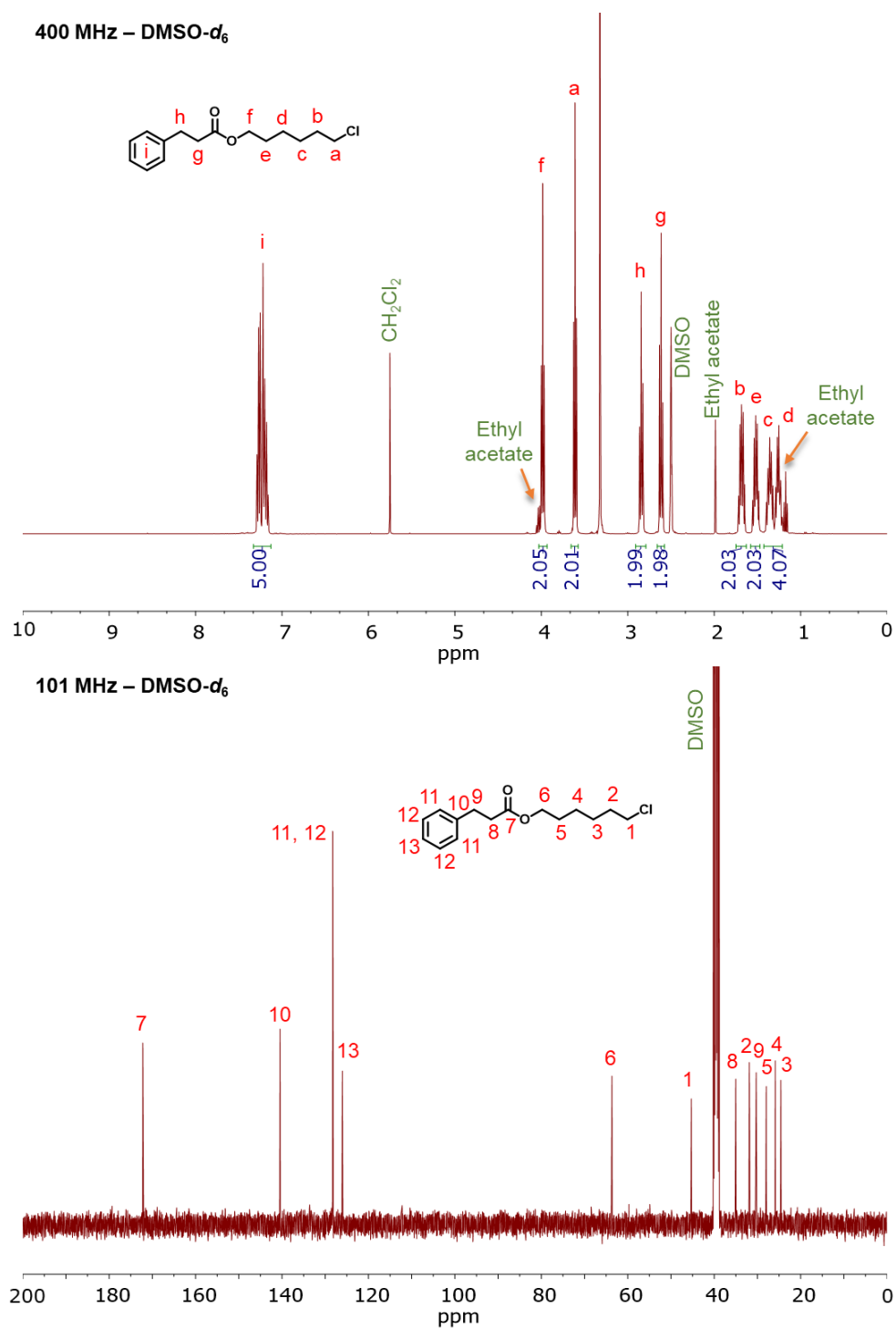


Appendix Figure 45. ¹H NMR spectrum of PPLG₅₀-g-MTEMPO (**14**).

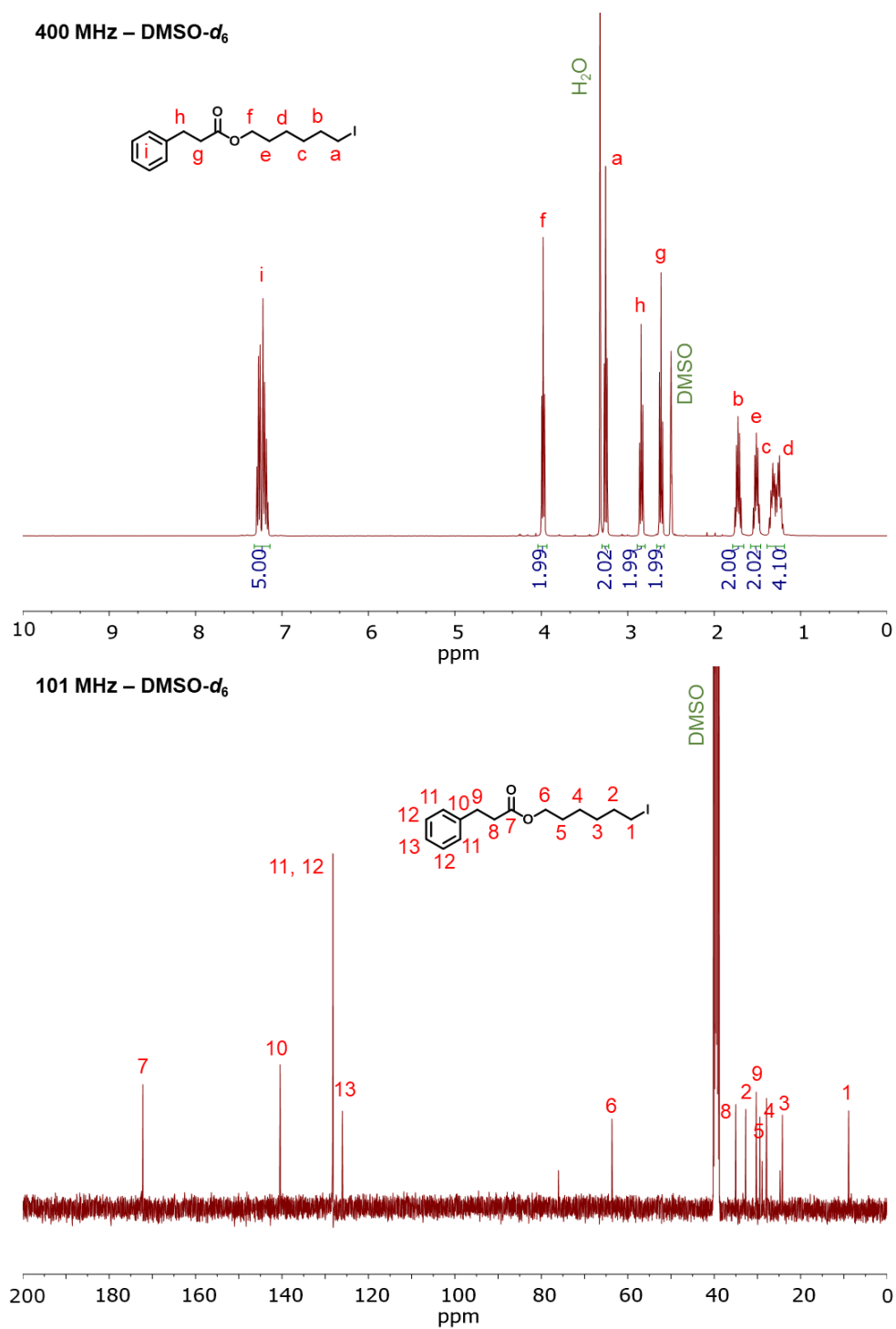
400 MHz -TFA-d



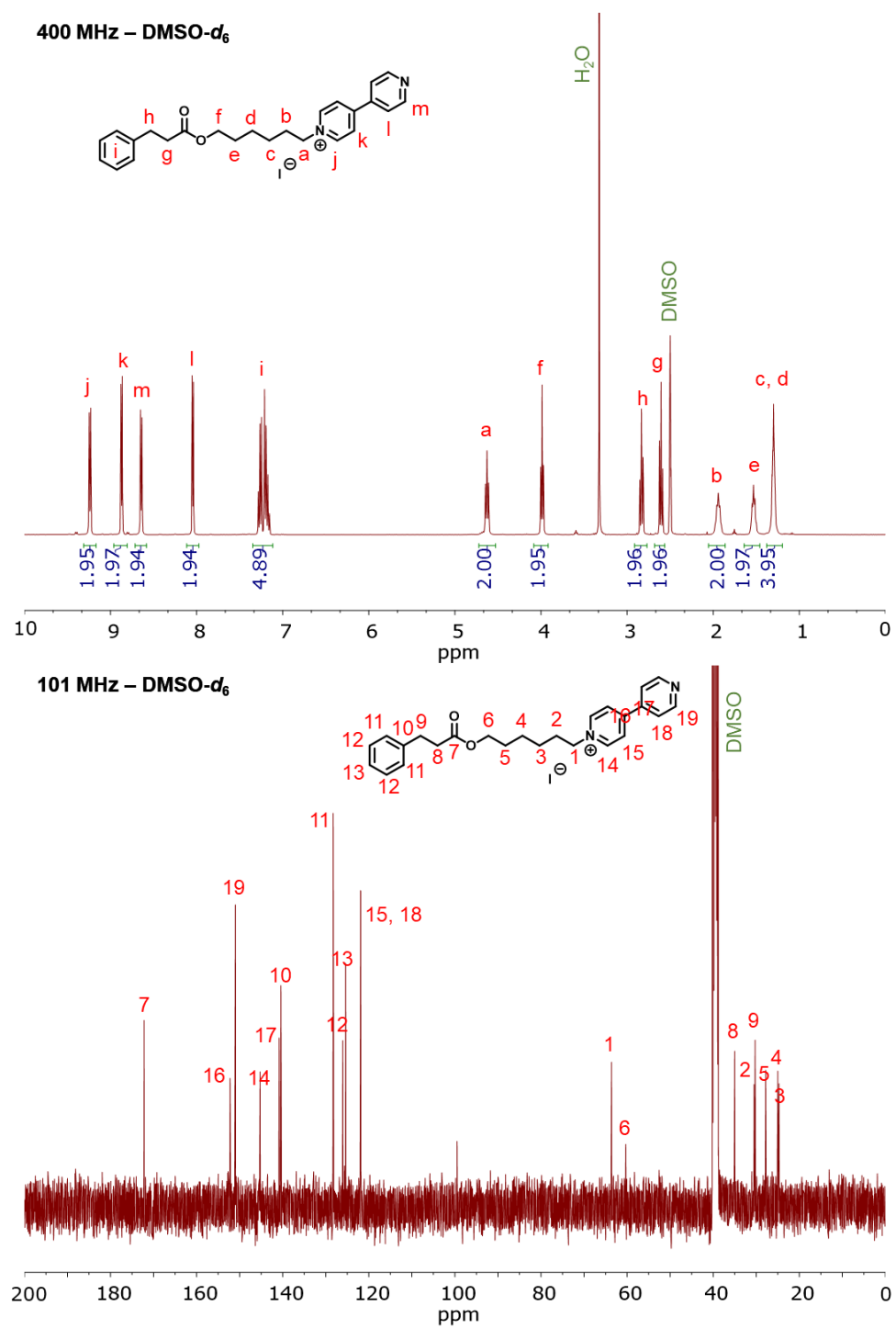
Appendix Figure 46. ¹H NMR spectrum of biTEMPO polypeptide (15).



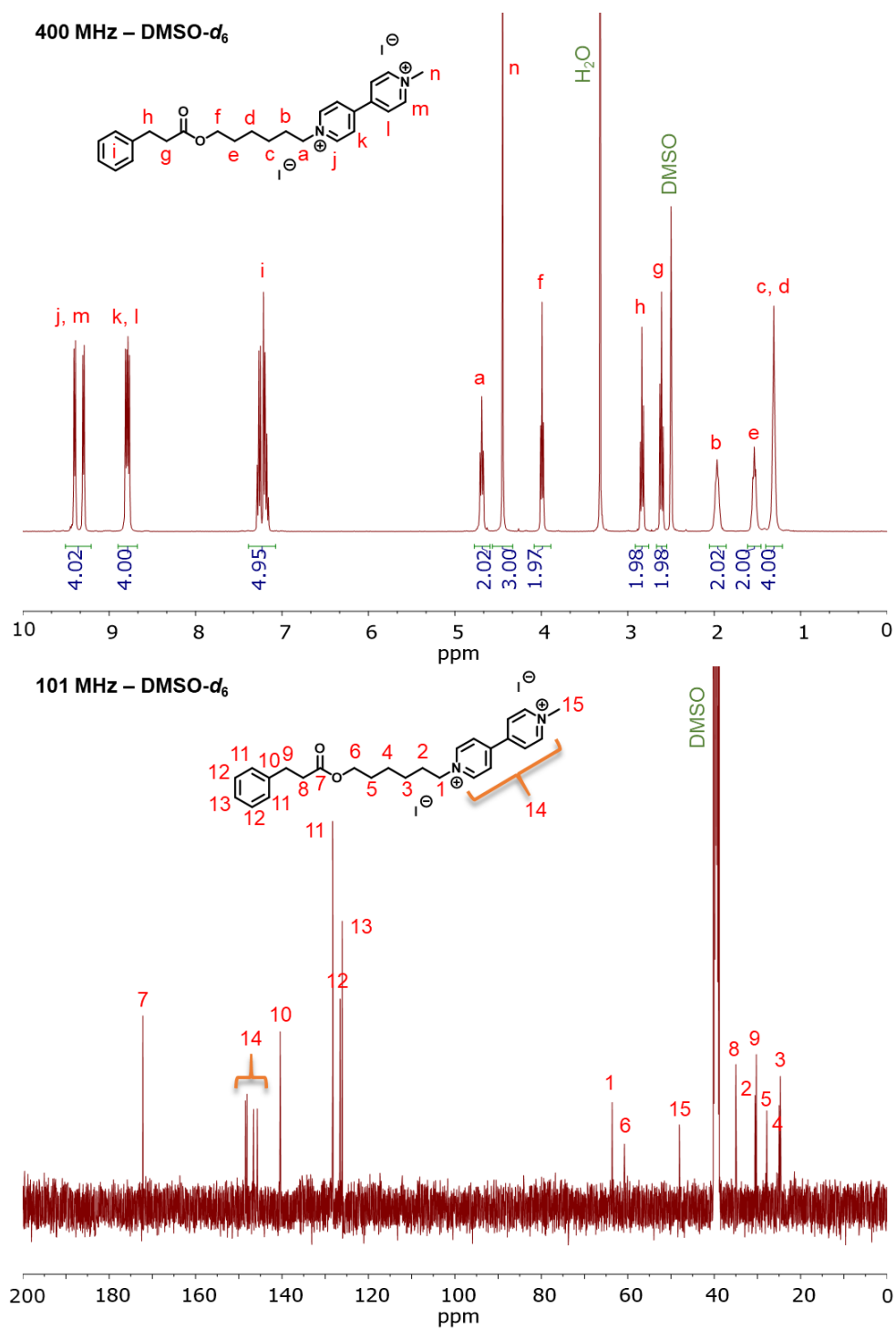
Appendix Figure 47. ^1H NMR and ^{13}C NMR spectra of CHHC (16).



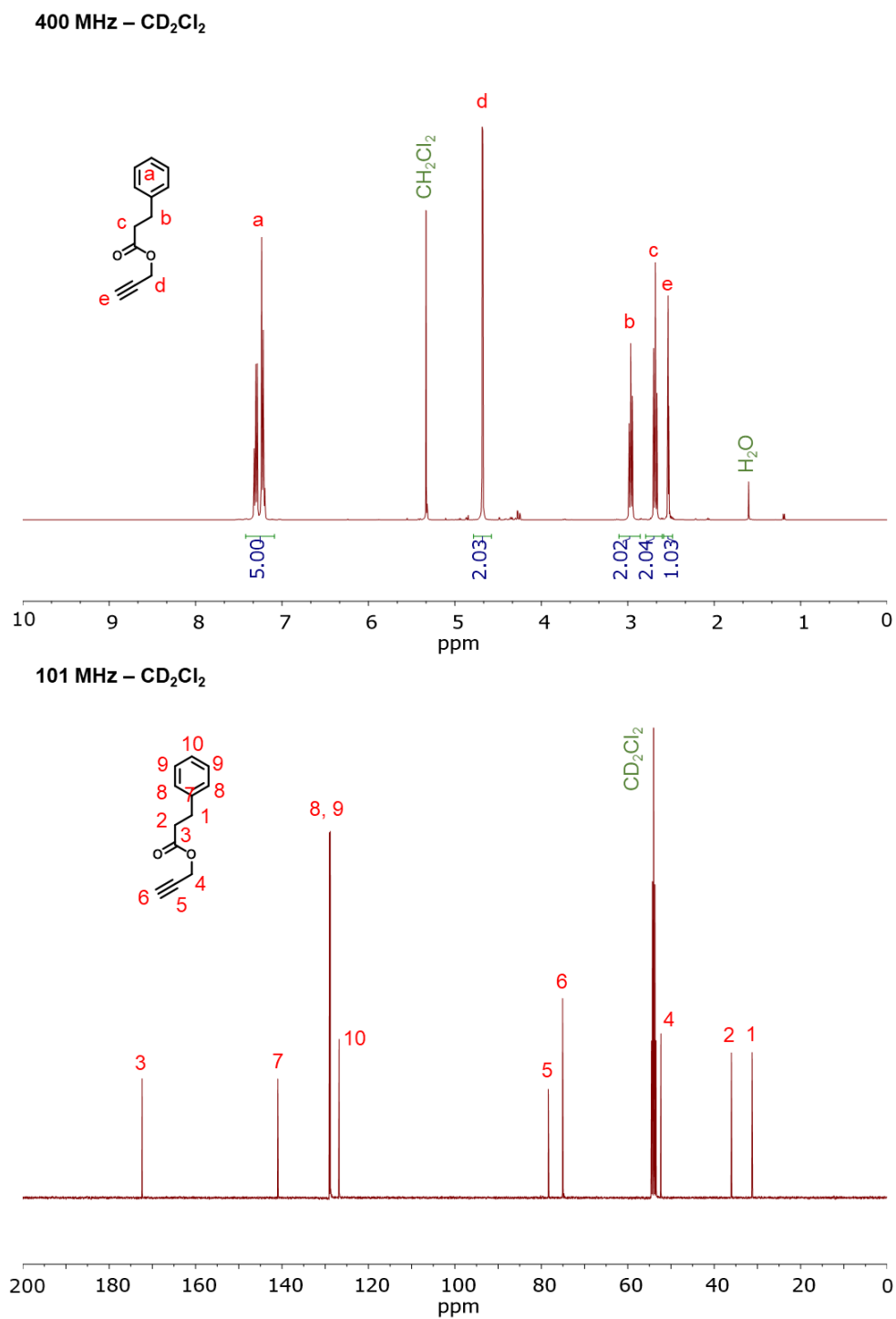
Appendix Figure 48. ^1H NMR and ^{13}C NMR spectra of IHHC (17).

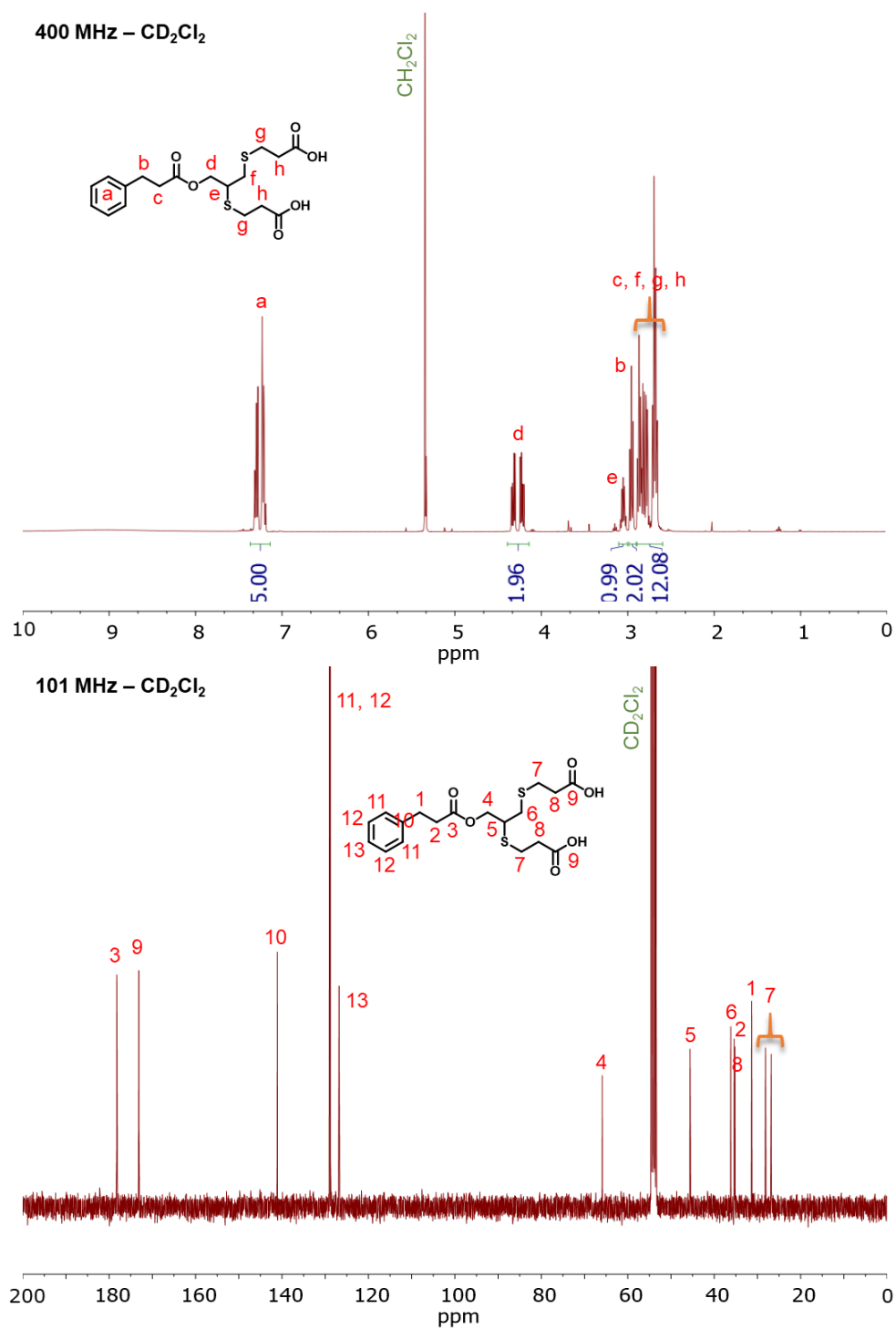


Appendix Figure 49. ^1H NMR and ^{13}C NMR spectra of PBPI (18).

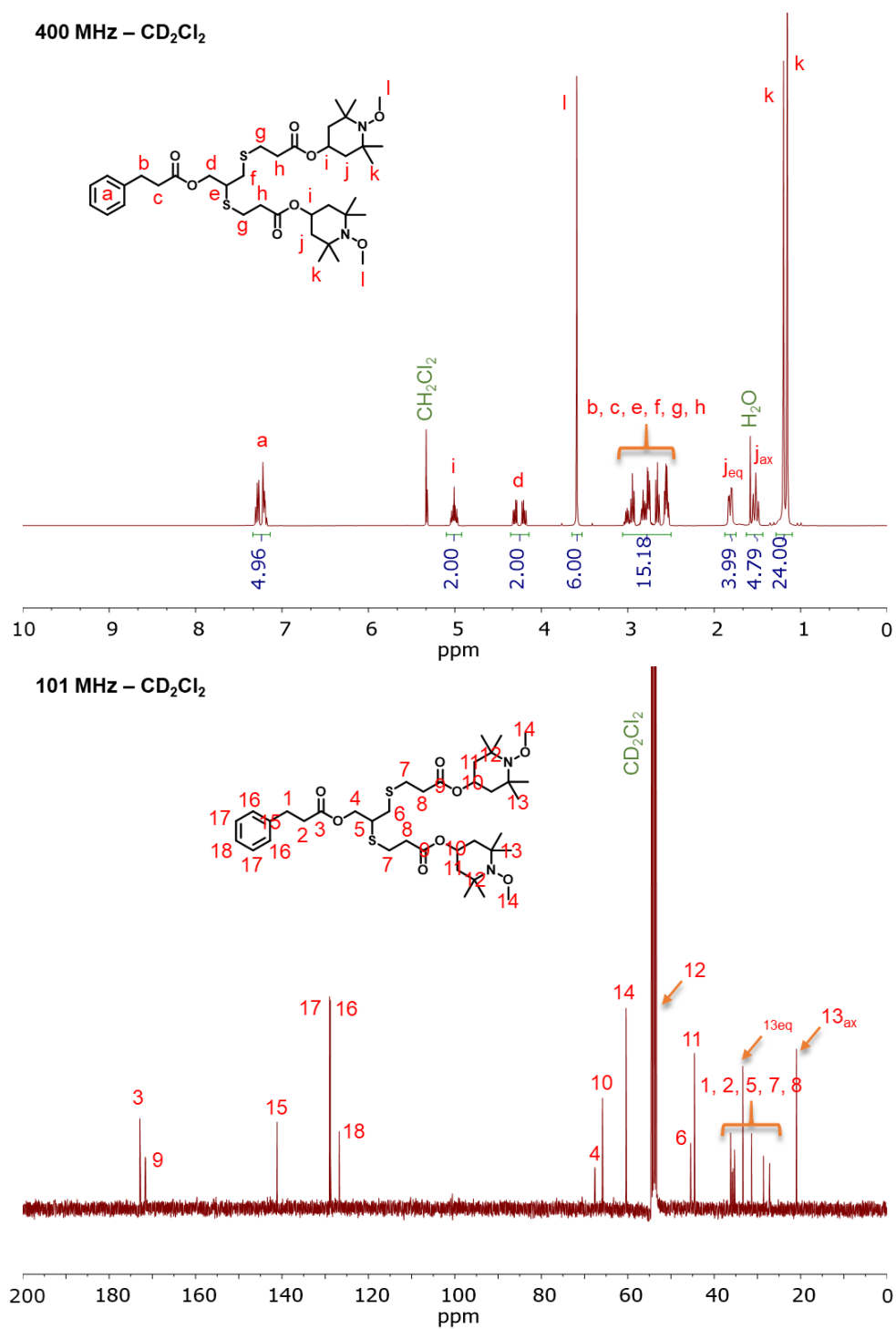


Appendix Figure 50. ^1H NMR and ^{13}C NMR spectra of viologen analog (**19**).

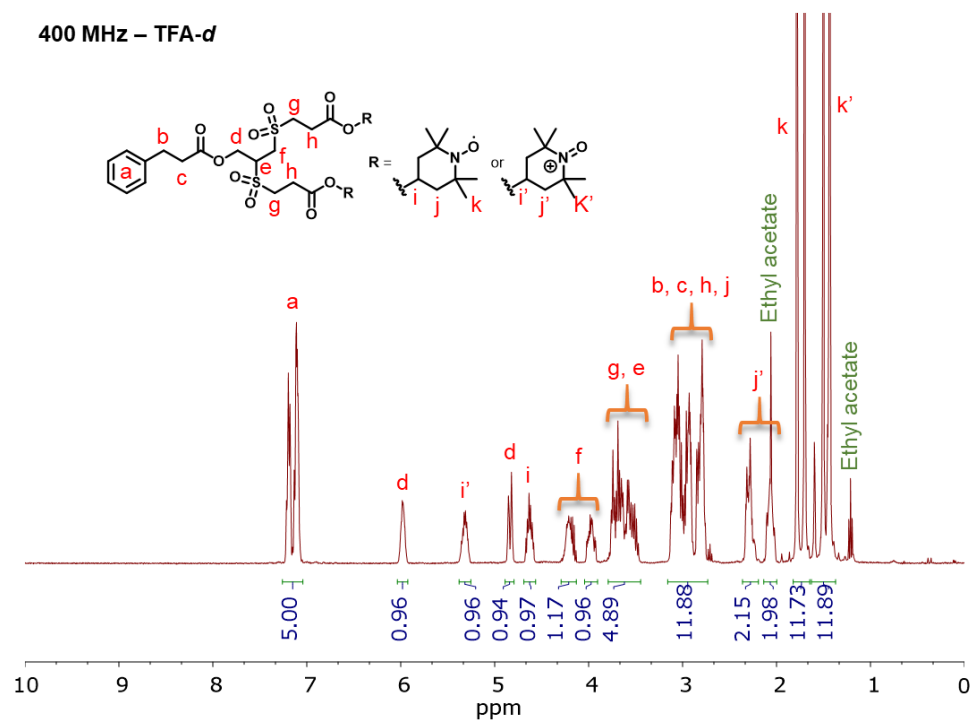




Appendix Figure 52. ¹H NMR and ¹³C NMR spectra of HC-*bis*PA (**21**).

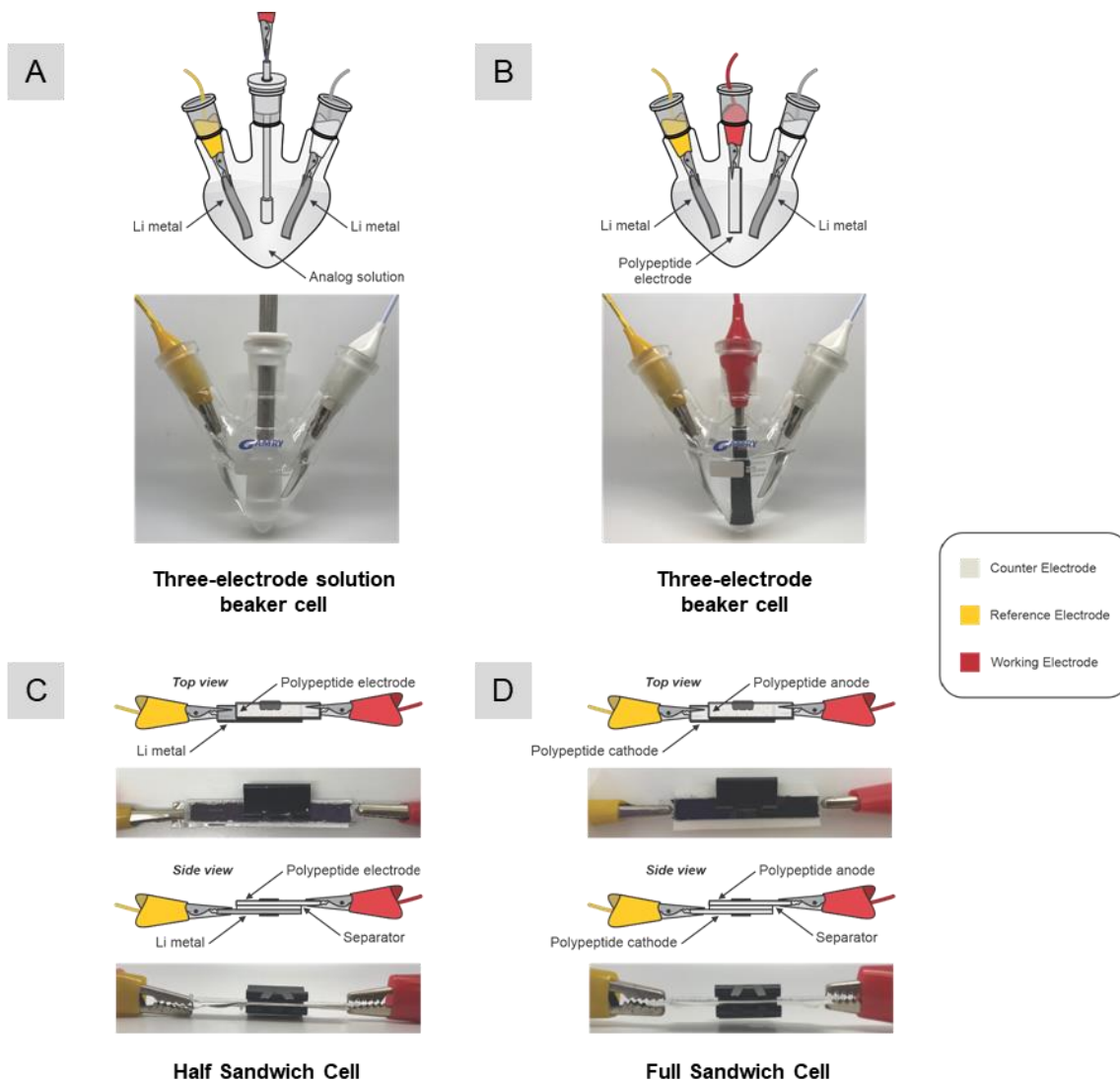


Appendix Figure 53. ¹H NMR and ¹³C NMR spectra of HC-*bis*(MTEMPO) (**22**).

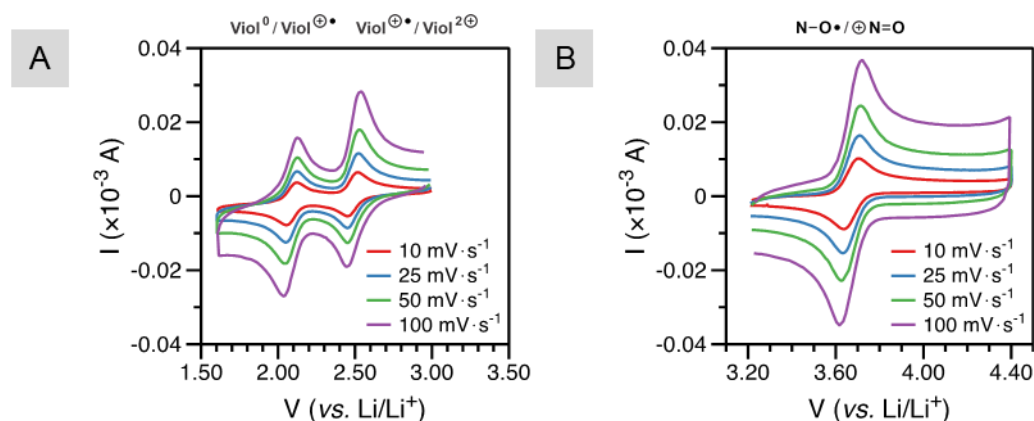


Appendix Figure 54. ^1H NMR and ^{13}C NMR spectra of biTEMPO analog (23).

Electrochemical Characterization



Appendix Figure 55. Electrochemical characterization set-ups discussed in the manuscript. **(A)** The three-electrode solution beaker cell: glassy carbon working electrode and lithium metal counter/reference electrodes. **(B)** The three-electrode beaker cell: polypeptide composite working electrode and lithium metal counter/reference electrodes. **(C)** The half sandwich cell: viologen or biTEMPO polypeptide composite working electrode and lithium metal reference electrode with a filter paper separator. **(D)** The full sandwich cell: viologen polypeptide composite working electrode and biTEMPO polypeptide composite reference electrode with a filter paper separator.



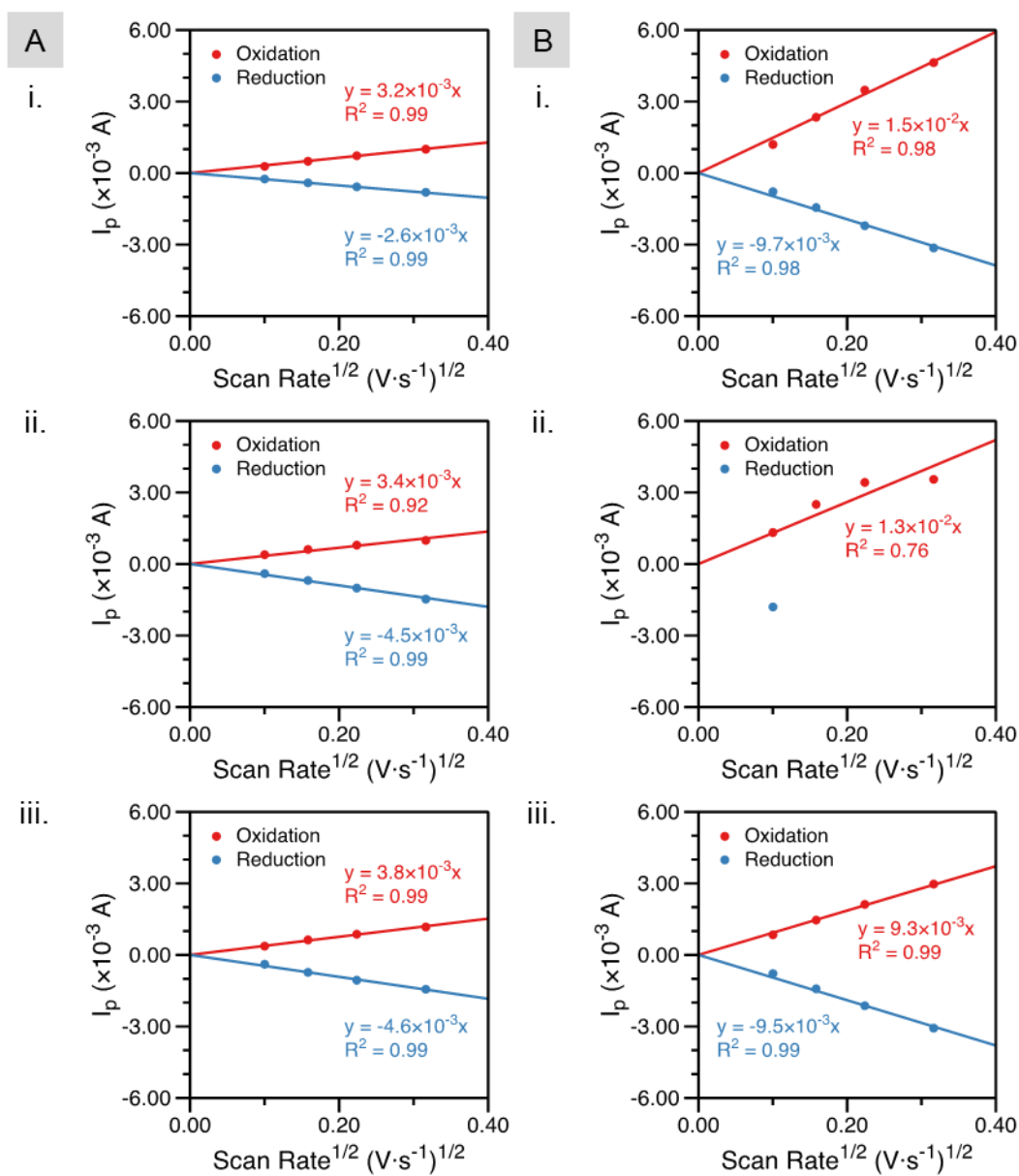
Appendix Figure 56. Solution state cyclic voltammetry of (A) viologen analog and (B) biTEMPO analog at 1 mM in 0.5 M LiCF₃SO₃ in PC electrolyte. A glassy carbon electrode was utilized as the working electrode in a three-electrode beaker cell with lithium metal reference and counter electrodes.

Appendix Table 1. Comparison of the oxidation/reduction peak potential (E_o/E_R), the peak separation (ΔE_p), half-wave potential ($E_{1/2}$), oxidation/reduction peak width (W_o/W_R), and oxidation/reduction peak area (A_o/A_R) for the biTEMPO analog, biTEMPO polypeptide thin film and biTEMPO polypeptide composite electrode.

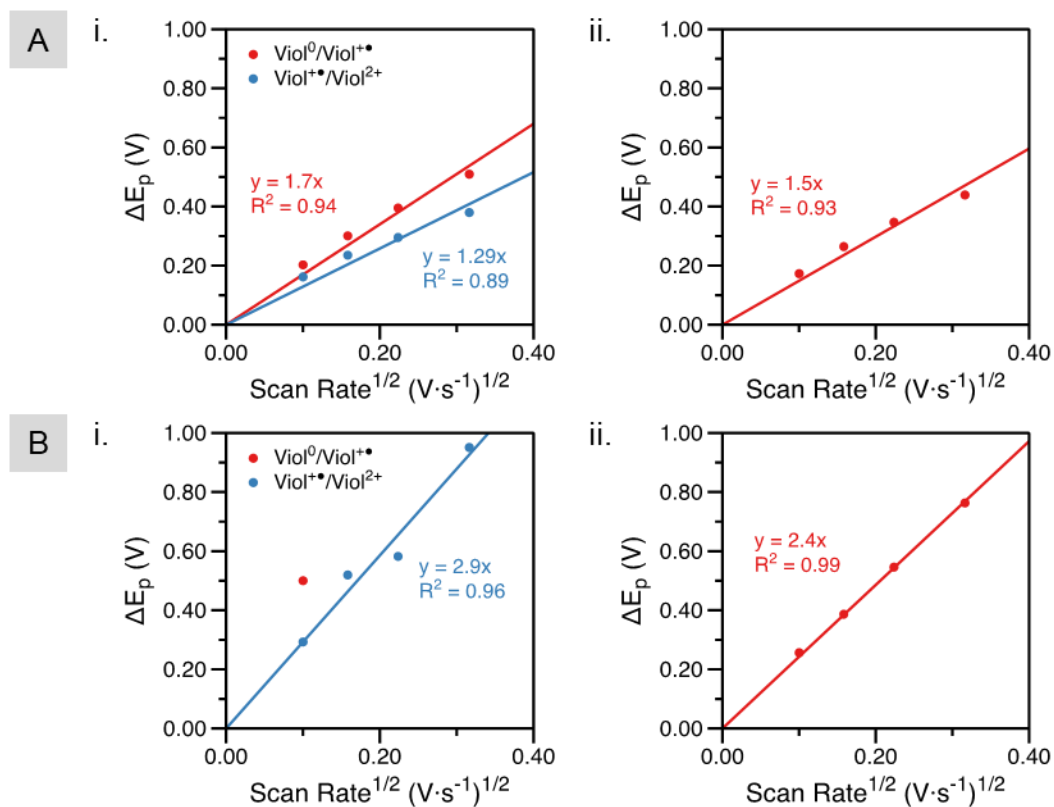
Parameter	BiTEMPO Analog Solution	BiTEMPO Polypeptide Thin Film	BiTEMPO Polypeptide Composite Electrode
E_o (V)	3.70	3.77	3.80
E_R (V)	3.69	3.60	3.56
ΔE_p (V)	0.06	0.17	0.24
$E_{1/2}$ (V)	3.67	3.69	3.68
W_o (V)	0.26	0.24	0.26
W_R (V)	0.19	0.19	0.24
A_o (W)	4.13×10^{-6}	1.23×10^{-4}	2.36×10^{-4}
A_R (W)	2.07×10^{-6}	8.43×10^{-5}	1.46×10^{-4}

Appendix Table 2. Comparison of the oxidation/reduction peak potential (E_o/E_R), the peak separation (ΔE_p), half-wave potential ($E_{1/2}$), oxidation/reduction peak width (W_o/W_R), and oxidation/reduction peak area (A_o/A_R) for both peaks of the viologen analog, viologen polypeptide thin film and viologen polypeptide composite electrode.

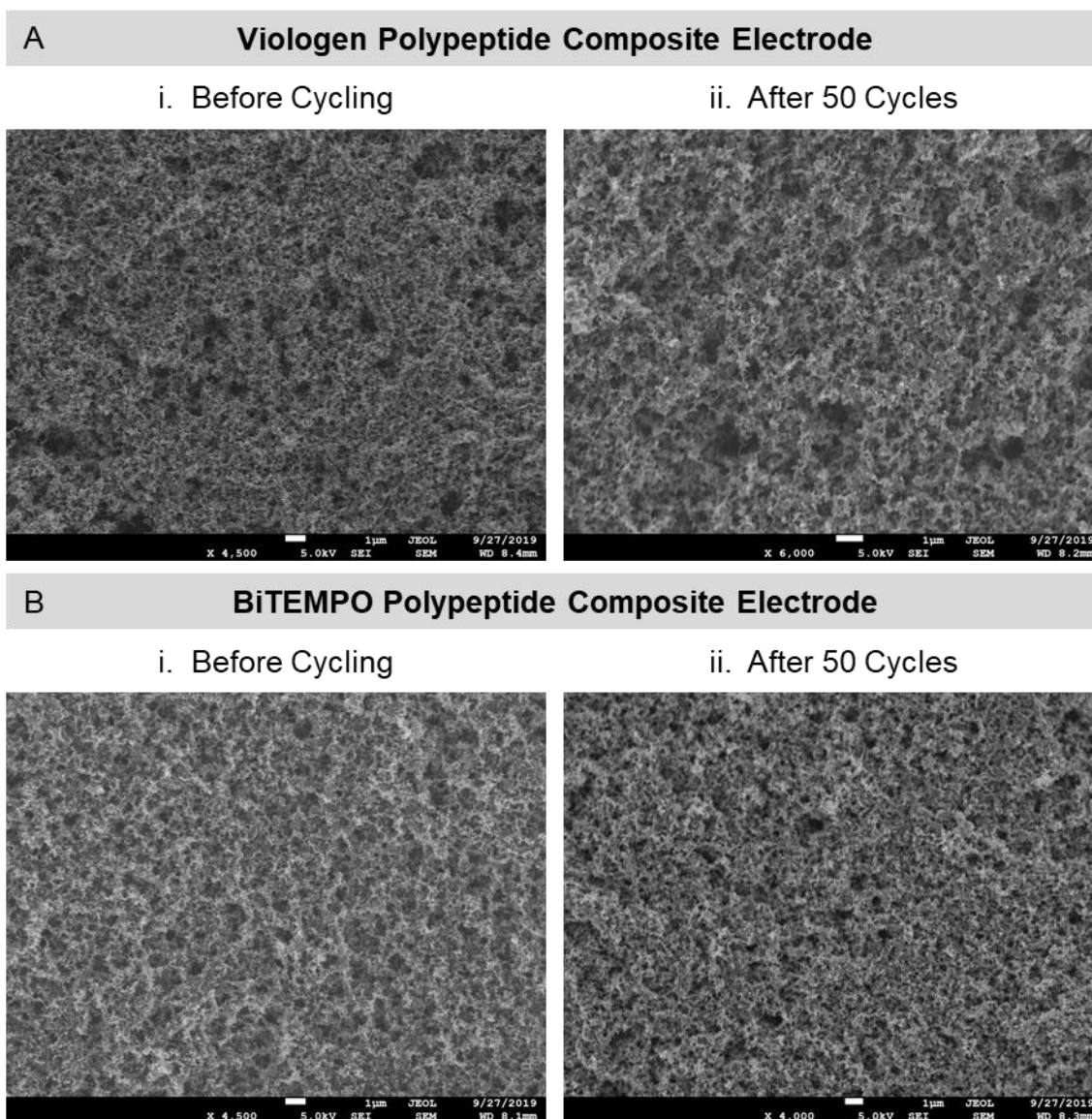
Reaction	Parameter	Viologen Analog Solution	Viologen Polypeptide Thin Film	Viologen Polypeptide Composite Electrode
Viol⁺/Viol²⁺	E_o (V)	2.51	2.62	2.70
	E_R (V)	2.46	2.46	2.42
	ΔE_p (V)	0.05	0.16	0.28
	$E_{1/2}$ (V)	2.49	2.54	2.56
	W_o (V)	0.17	0.18	0.43
	W_R (V)	0.15	0.18	0.15
	A_o (W)	1.31×10^{-6}	7.69×10^{-5}	3.29×10^{-4}
	A_R (W)	8.20×10^{-7}	5.06×10^{-5}	6.73×10^{-5}
Viol⁰/Viol⁺	E_o (V)	2.12	2.19	2.31
	E_R (V)	2.06	1.99	1.84
	ΔE_p (V)	0.06	0.20	0.47
	$E_{1/2}$ (V)	2.09	2.09	2.08
	W_o (V)	0.15	0.19	0.43
	W_R (V)	0.18	0.21	0.33
	A_o (W)	8.57×10^{-7}	9.05×10^{-5}	4.85×10^{-4}
	A_R (W)	1.18×10^{-6}	8.55×10^{-5}	2.67×10^{-4}



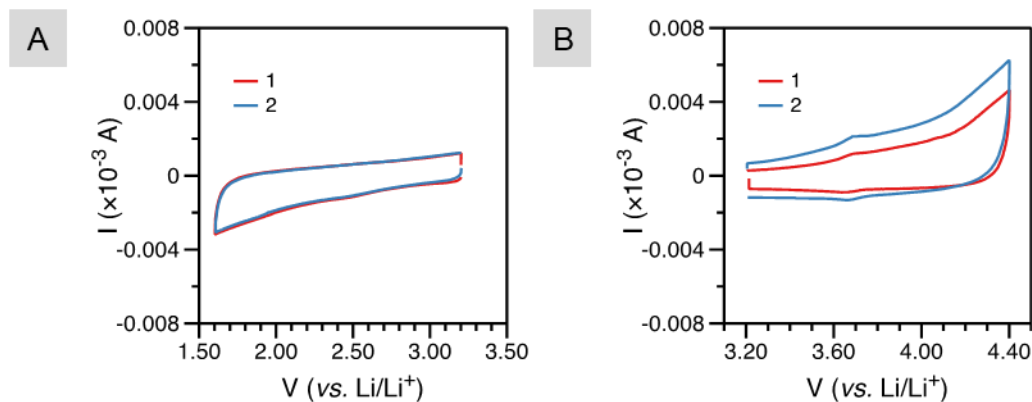
Appendix Figure 57. Peak current vs. square-root of scan rate from the cyclic voltammograms for (A) polypeptide thin film electrodes and (B) polypeptide composite electrodes of **i.** $Viol^{+•}/Viol^{2+}$ and **ii.** $Viol^0/Viol^{+•}$ for the viologen polypeptide and **iii.** for the biTEMPO polypeptide. The viologen polypeptide composite electrode did not exhibit a lower redox peak at scan rates greater than $10 \text{ mV} \cdot \text{s}^{-1}$.



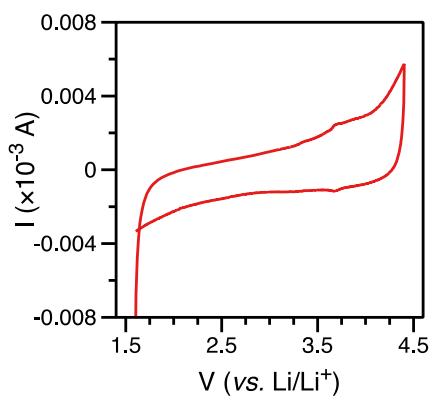
Appendix Figure 58. Peak separation vs. square-root of scan rate from the cyclic voltammograms for (A) polypeptide thin film electrodes and (B) polypeptide composite electrodes of i. the viologen polypeptide and ii. the biTEMPO polypeptide. The viologen polypeptide composite electrode did not exhibit a lower redox peak at scan rates greater than $10 \text{ mV}\cdot\text{s}^{-1}$.



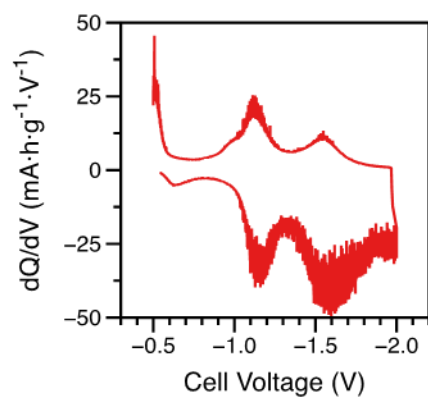
Appendix Figure 59. Scanning electron micrographs of **(A)** the viologen polypeptide composite electrode and **(B)** the biTEMPO polypeptide composite electrode **i.** before and **ii.** after 50 charge-discharge cycles in the full sandwich cell configuration (viologen polypeptide composite electrode | 0.5 M LiCF₃SO₃ in PC + filter paper | biTEMPO polypeptide composite electrode).



Appendix Figure 60. Solution state CV of the electrolyte (1) after soaking the electrode in the electrolyte solution, and after electrochemical testing of (2) PVDF/CB composite electrodes. The tests were carried out for the electrolyte tested with (A) the viologen polypeptide composite electrodes and (B) the biTEMPO polypeptide composite electrodes.

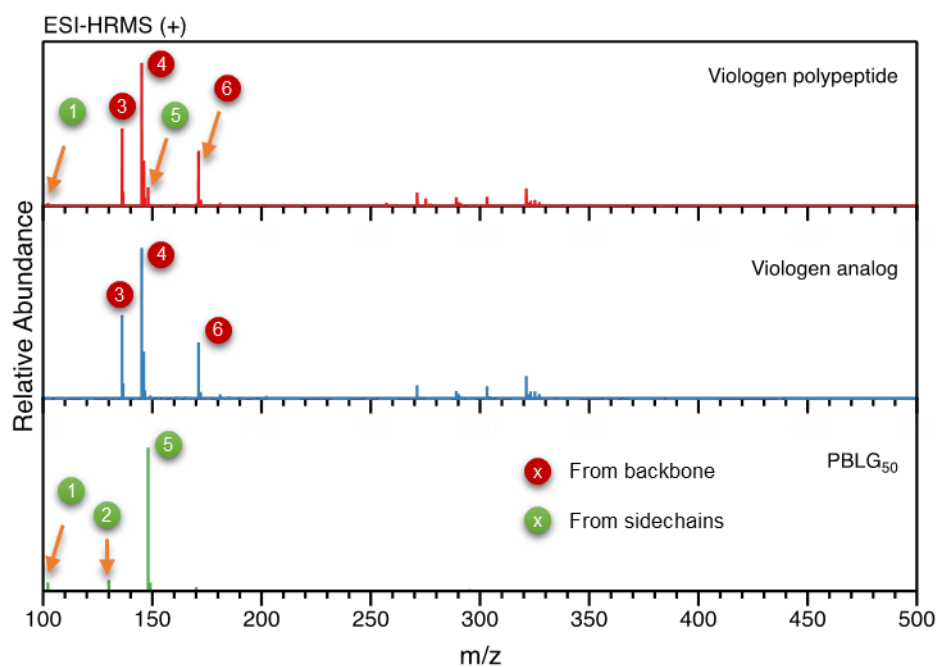


Appendix Figure 61. Solution state CV of the electrolyte after testing the full cells (with both composite electrodes). The CV was conducted in a three-electrode beaker cell with a glassy carbon working electrode and lithium metal counter and reference electrodes. The electrolyte was 0.5 M LiCF_3SO_3 in PC unless otherwise stated. For the full sandwich cell, the separator was soaked in 15 mL of electrolyte after electrochemical testing and the resulting solution was used for solution state CV testing.



Appendix Figure 62. Differential capacity curves from galvanostatic cycling curves filter paper sandwich cell at 1C. An adjacent-averaging filter with a 5-point window was applied in OriginPro 2020 to remove noise in the data.

Degradation Study



1

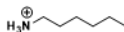
Calc'd: 102.1282
Found: 102.1282

2

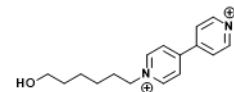
Calc'd: 130.0500
Found: 130.0501

3

Calc'd: 136.0944
Found: 136.0940



[Glu-H₂O+H]⁺



4

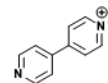
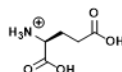
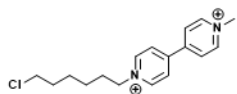
Calc'd: 145.0775
Found: 145.0770

5

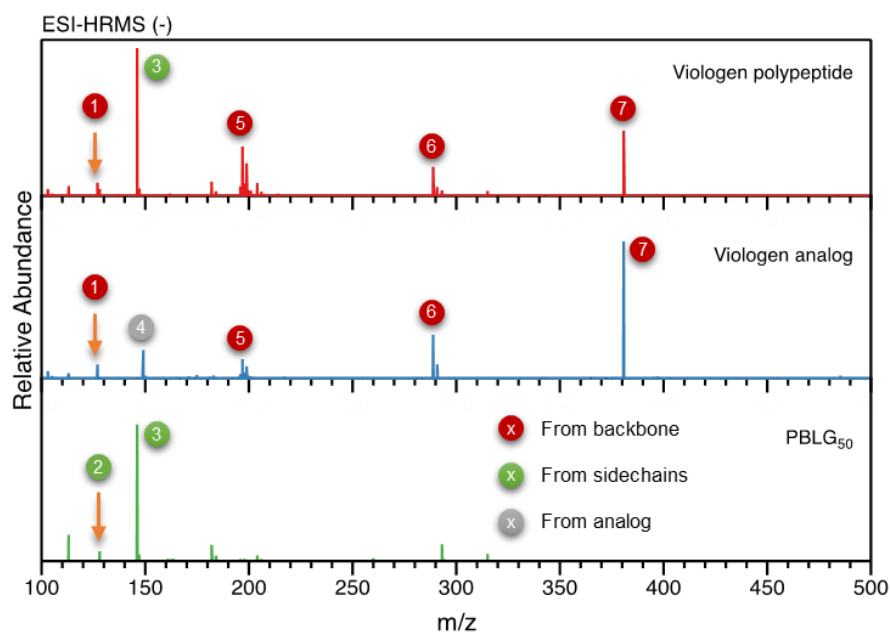
Calc'd: 148.0610
Found: 148.0640

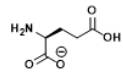
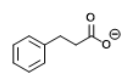
6

Calc'd: 171.0922
Found: 171.0917

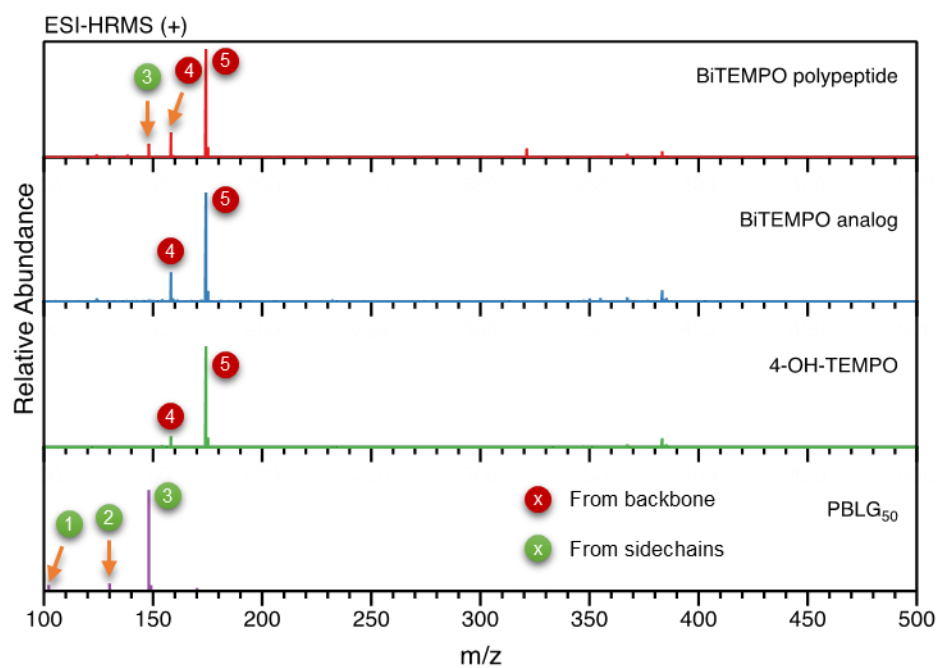


Appendix Figure 63. High resolution mass spectrometry (HRMS, positive ESI) of the degradation products of (from top to bottom) viologen polypeptide, viologen analog and PBLG₅₀.



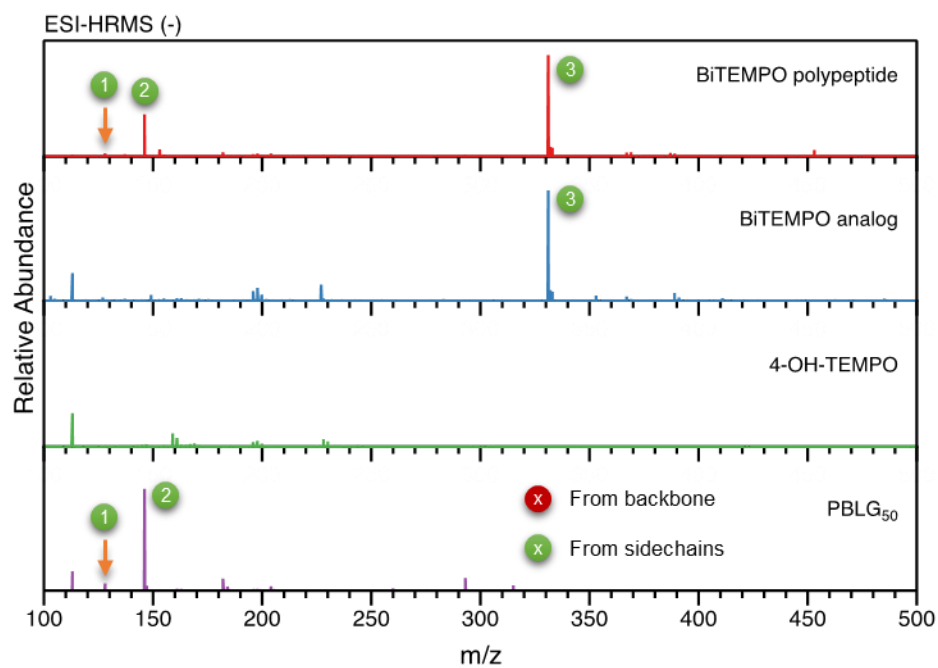
1	Calc'd: 126.9045 Found: 126.9039	2	Calc'd: 128.0348 Found: 128.0341	3	Calc'd: 146.0453 Found: 146.0447
	I^-		[Glu-H ₂ O-H] ⁻		
4	Calc'd: 149.0603 Found: 149.0599	5	Calc'd: 196.8422 Found: 196.8423	6	Calc'd: 288.7778 Found: 288.7790
			ICl_2^-		I_2Cl^-
4	Calc'd: 380.7134 Found: 380.7148				
	I_3^-				

Appendix Figure 64. HRMS (negative ESI) of the degradation products of (from top to bottom) viologen polypeptide, viologen analog and PBLG₅₀.



1	Calc'd: 102.1282 Found: 102.1282	2	Calc'd: 130.0500 Found: 130.0501	3	Calc'd: 148.0610 Found: 148.0640
	<chem>CCCCCCCC[NH3+]</chem>		[Glu-H ₂ O+H] ⁺		<chem>CC(O)C(C(=O)O)C(=O)O[NH3+]</chem>
4	Calc'd: 158.1545 Found: 158.1540	5	Calc'd: 174.1494 Found: 174.1489		
	<chem>CC1(C)C(O)C(N)C1</chem>		<chem>CC1(C)C(O)C(O)C1[NH2+]</chem>		

Appendix Figure 65. HRMS (positive ESI) of the degradation products of (from top to bottom) biTEMPO polypeptide, biTEMPO analog, 4-OH-TEMPO and PBLG₅₀.



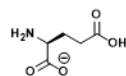
1

Calc'd: 128.0348
Found: 128.0341

[Glu-H₂O-H]⁻

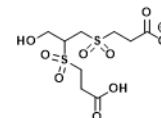
2

Calc'd: 146.0453
Found: 146.0447

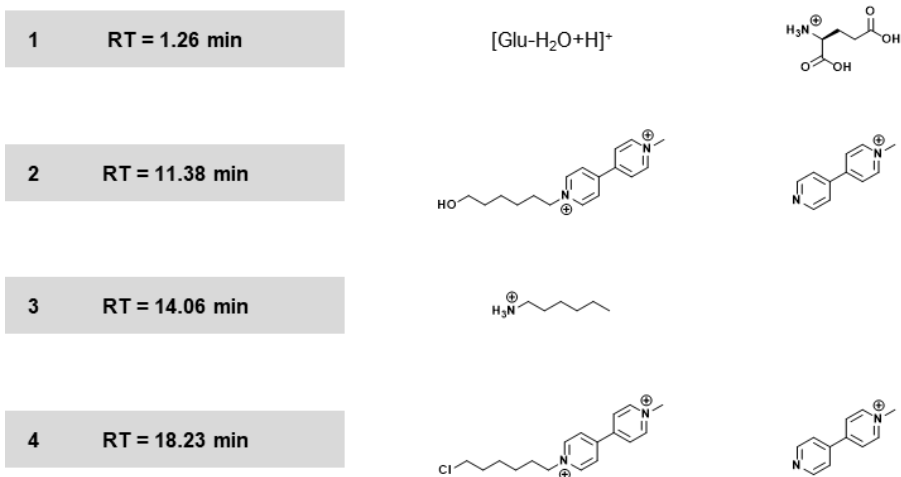
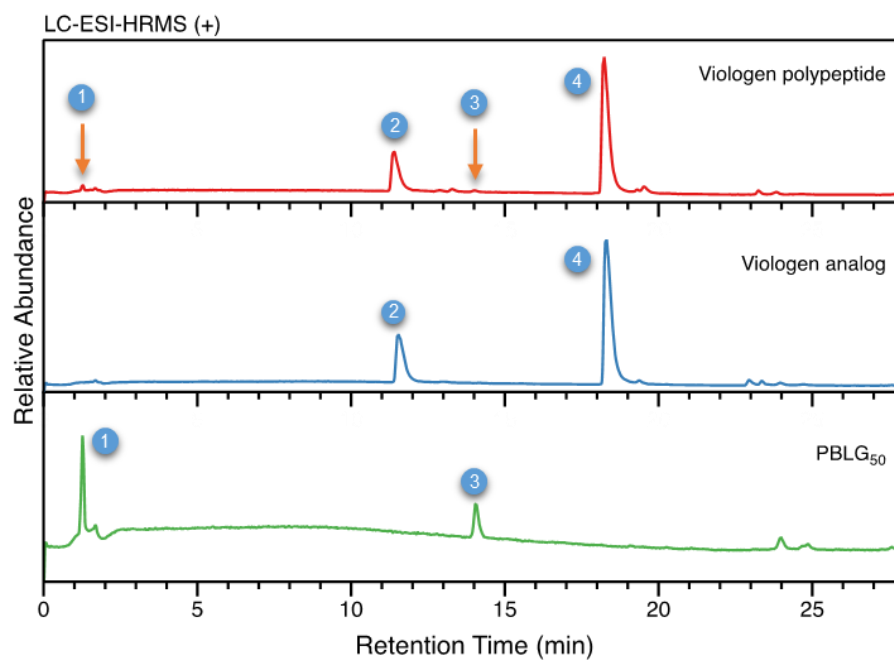


3

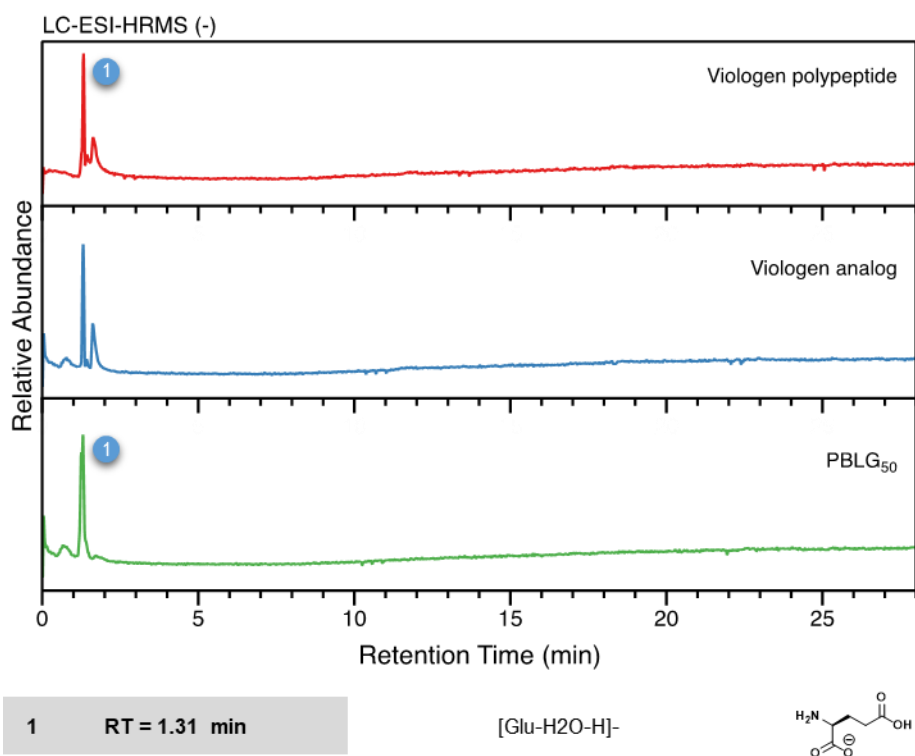
Calc'd: 331.0158
Found: 331.0169



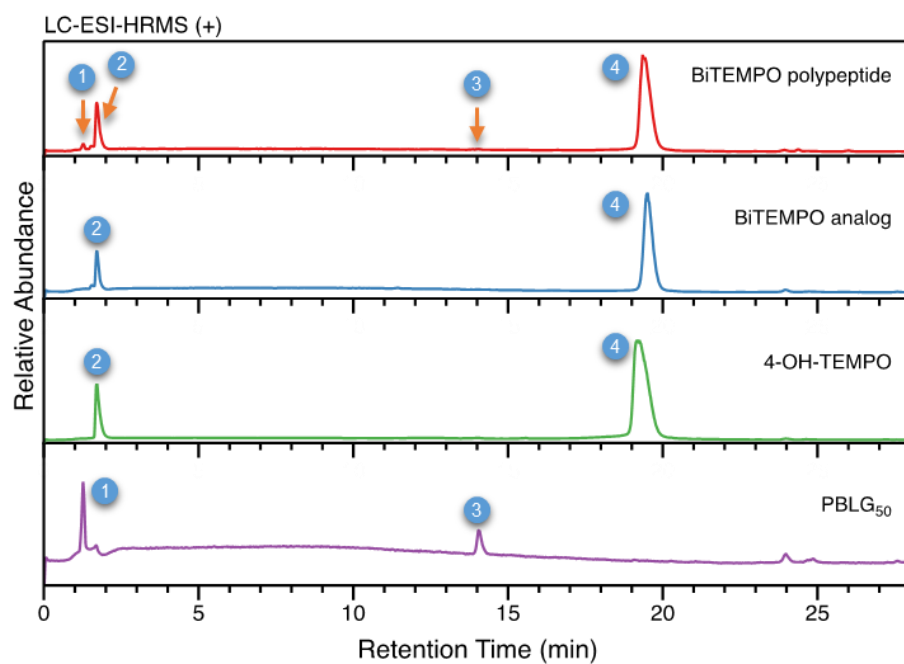
Appendix Figure 66. HRMS (negative ESI) of the degradation products of (from top to bottom) biTEMPO polypeptide, biTEMPO analog, 4-OH-TEMPO and PBLG₅₀.



Appendix Figure 67. Separation of the degradation products of (from top to bottom) viologen polypeptide, viologen analog and PBLG₅₀ using liquid chromatography-mass spectrometry (LC-HRMS, positive ESI).

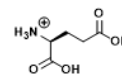


Appendix Figure 68. Separation of the degradation products of (from top to bottom) viologen polypeptide, viologen analog and PBLG₅₀ using LC-HRMS (negative ESI). FeCl₄⁻ contaminants eluted at 1.31 min in all samples. I⁻ and I₃⁻ residues eluted at 1.62 min for viologen polypeptide and viologen analog.



1 RT = 1.27 min

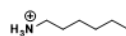
[Glu-H₂O+H]⁺



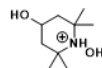
2 RT = 1.71 min



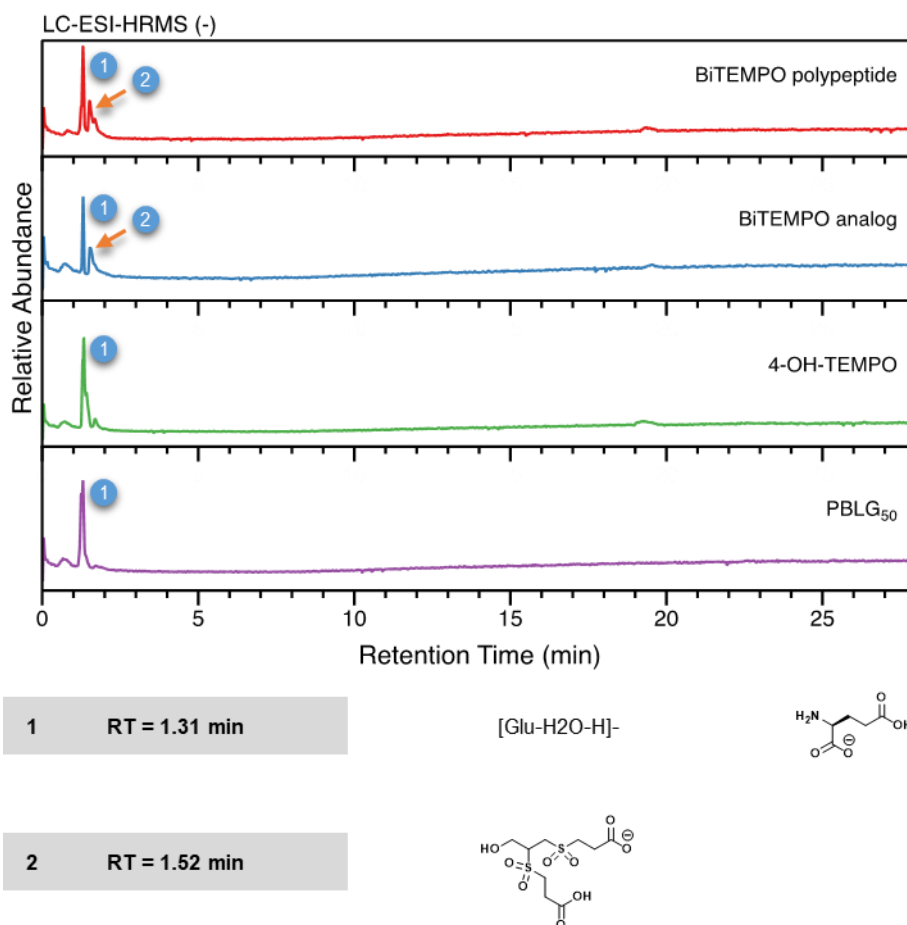
3 RT = 14.06 min



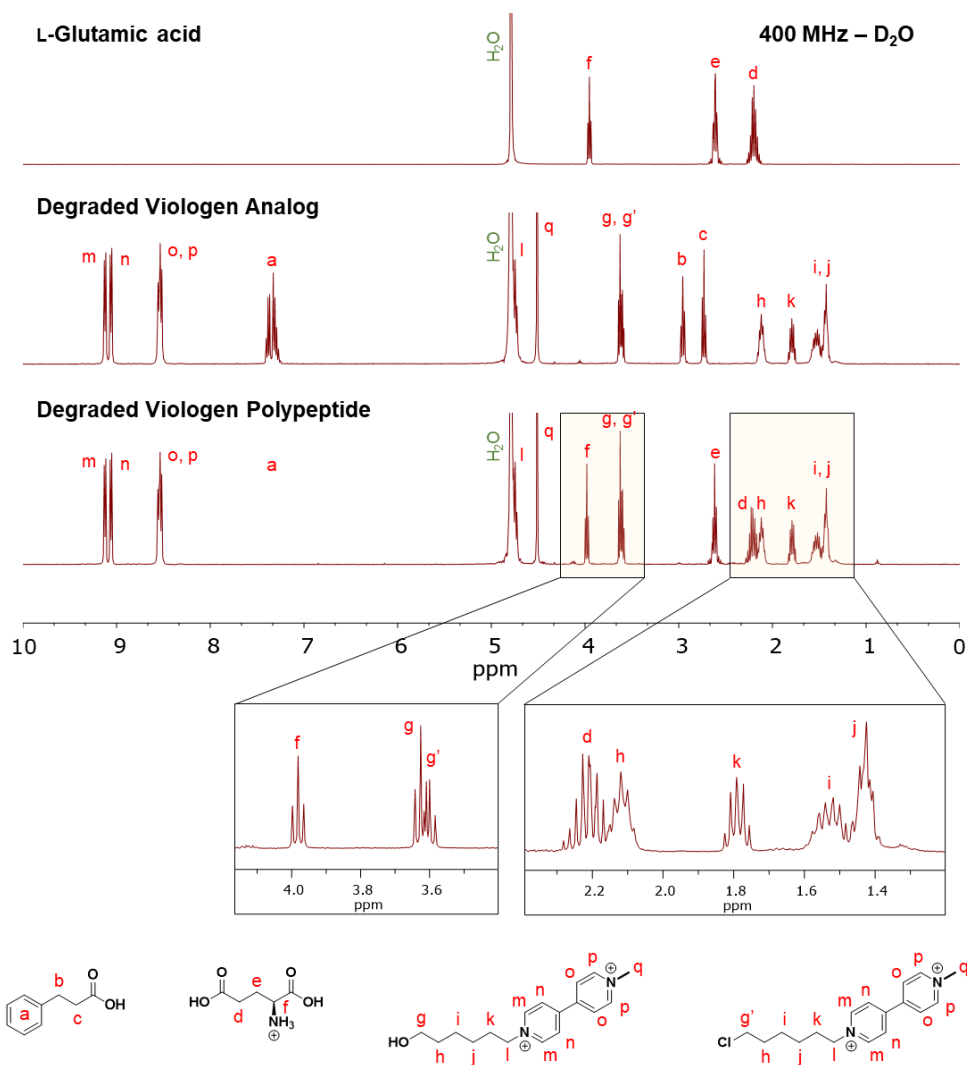
4 RT = 19.35 min



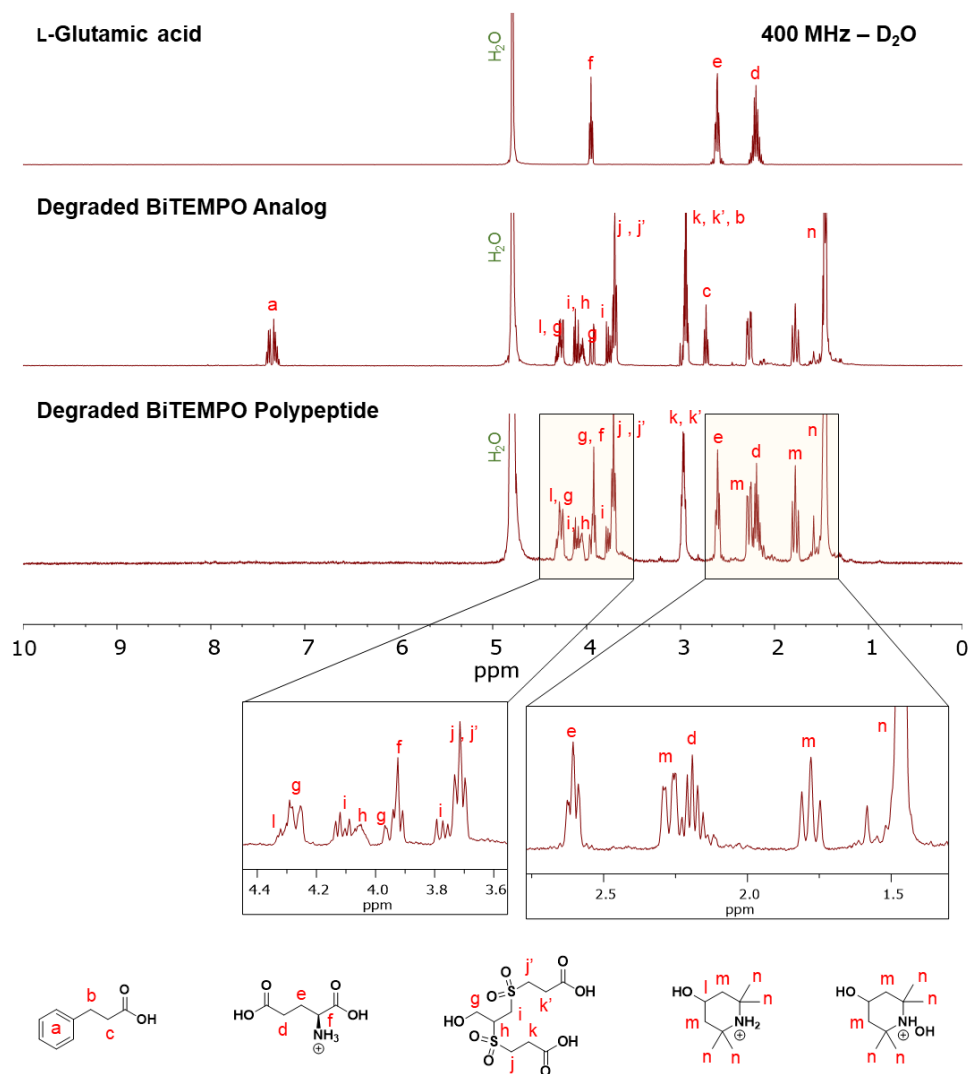
Appendix Figure 69. Separation of the degradation products of (from top to bottom) biTEMPO polypeptide, biTEMPO analog, 4-OH-TEMPO and PBLG₅₀ using LC-HRMS (positive ESI).



Appendix Figure 70. Separation of the degradation products of (from top to bottom) biTEMPO polypeptide, biTEMPO analog, 4-OH-TEMPO and PBLG₅₀ using LC-HRMS (negative ESI). FeCl₄⁻ contaminants eluted at 1.31 min in all samples.

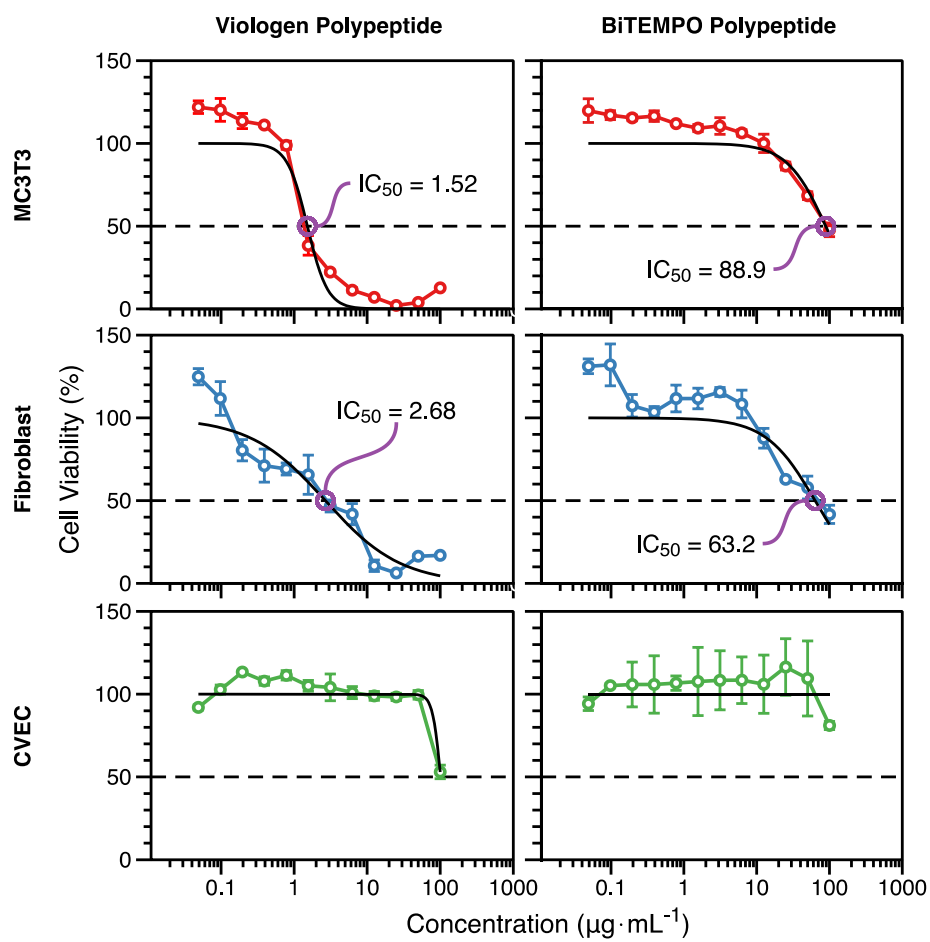


Appendix Figure 71. ¹H NMR spectra of L-glutamic acid, viologen analog and viologen polypeptide after acid degradation with 1 M HCl at 110 °C.

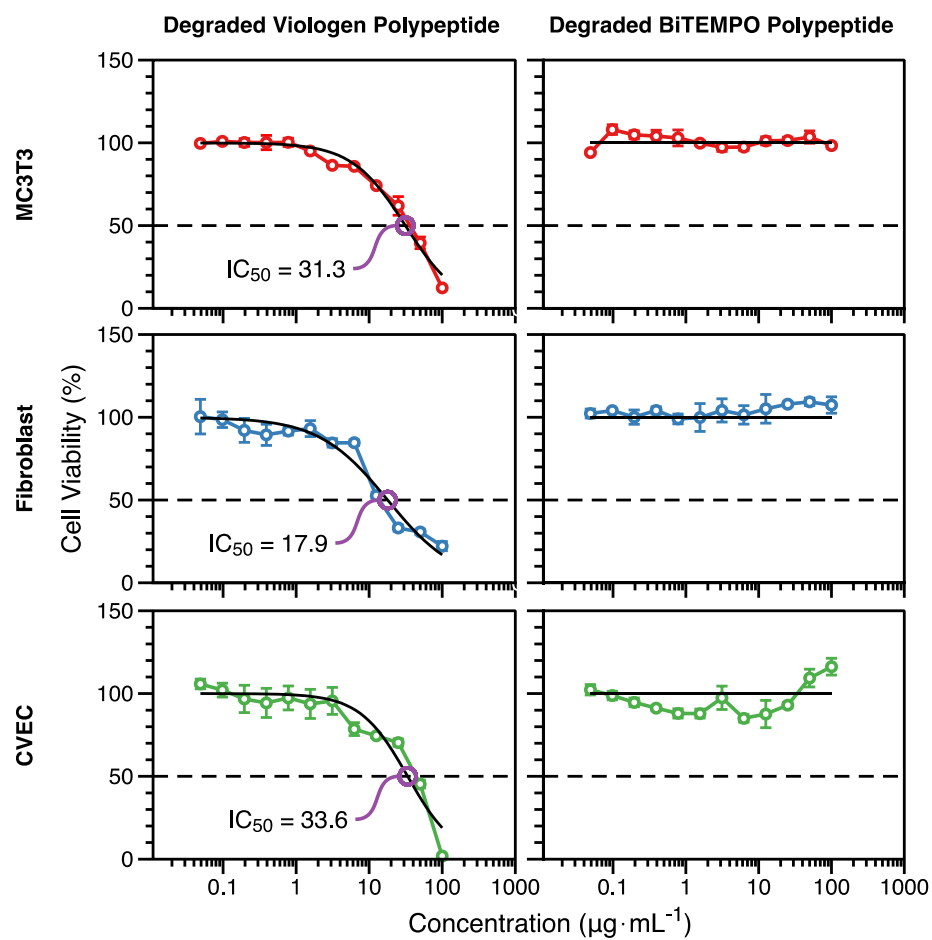


Appendix Figure 72. ¹H NMR spectra of L-glutamic acid, biTEMPO analog and biTEMPO polypeptide after acid degradation with 1 M HCl at 110 °C.

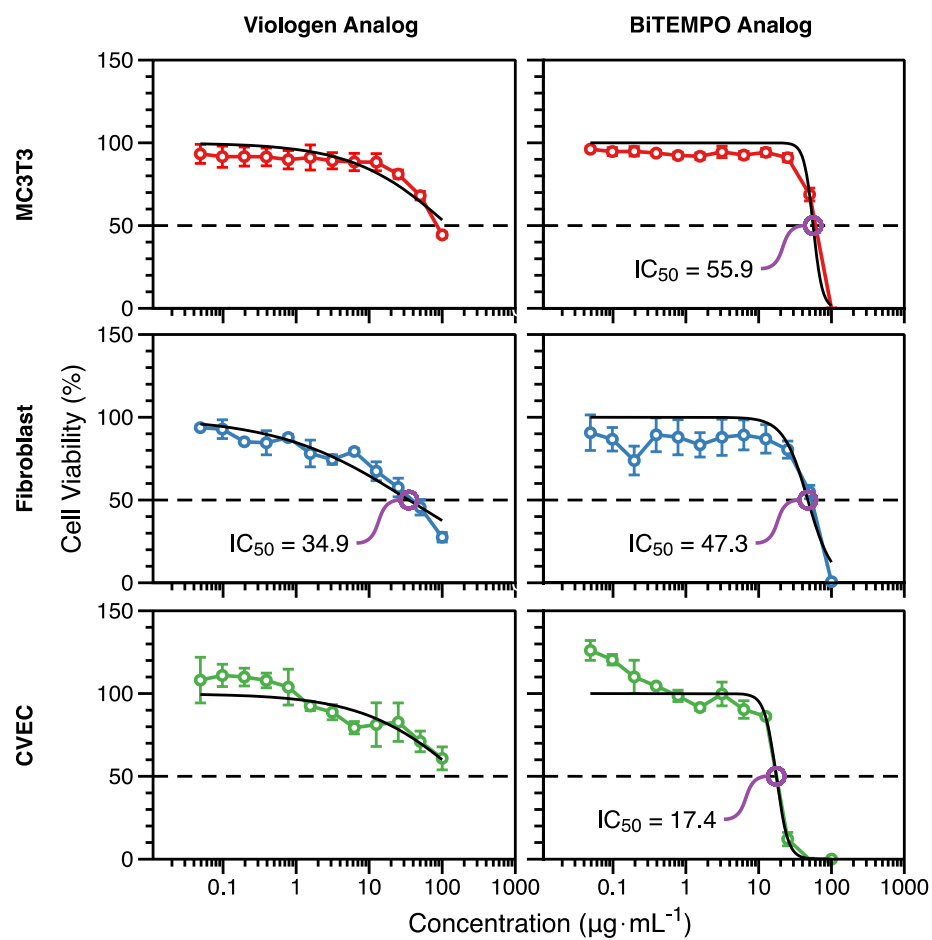
Cell Viability Study



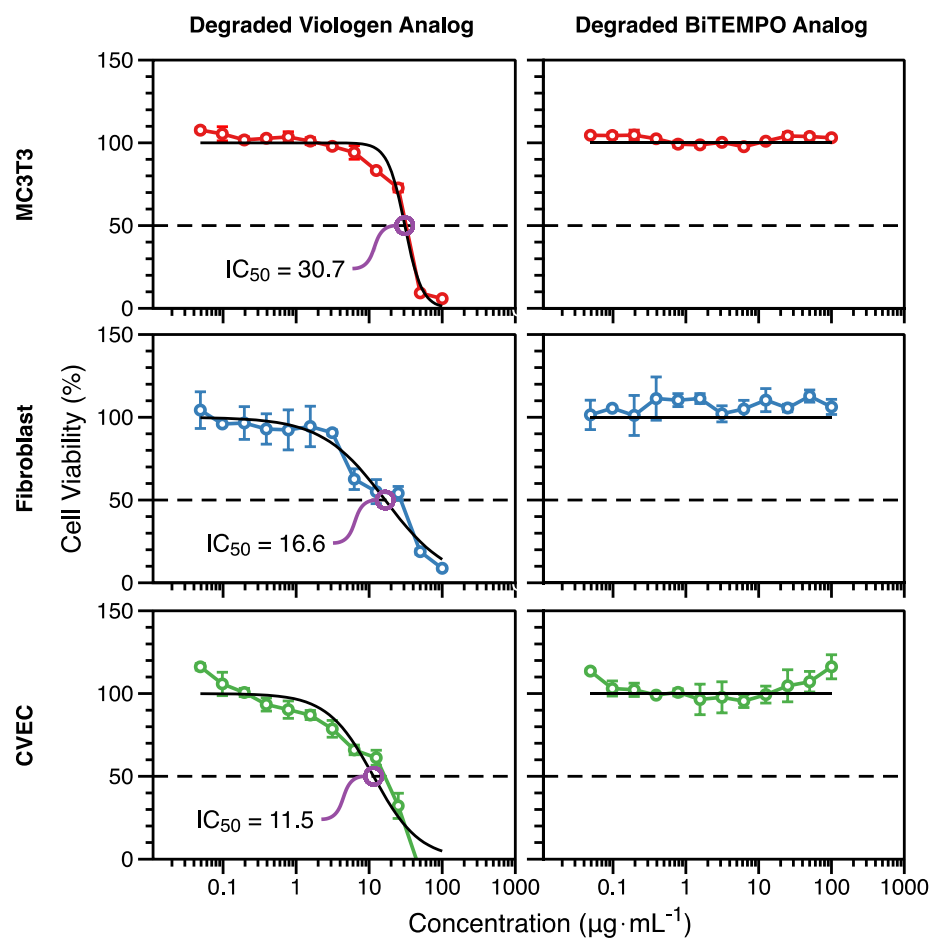
Appendix Figure 73. Cytotoxicity effects of viologen and biTEMPO polypeptides on MC3T3 cells, fibroblast cells and coronary venular endothelial cells (CVECs).



Appendix Figure 74. Cytotoxicity effects of the degradation products of viologen and biTEMPO polypeptides on MC3T3 cells, fibroblast cells and CVECs.



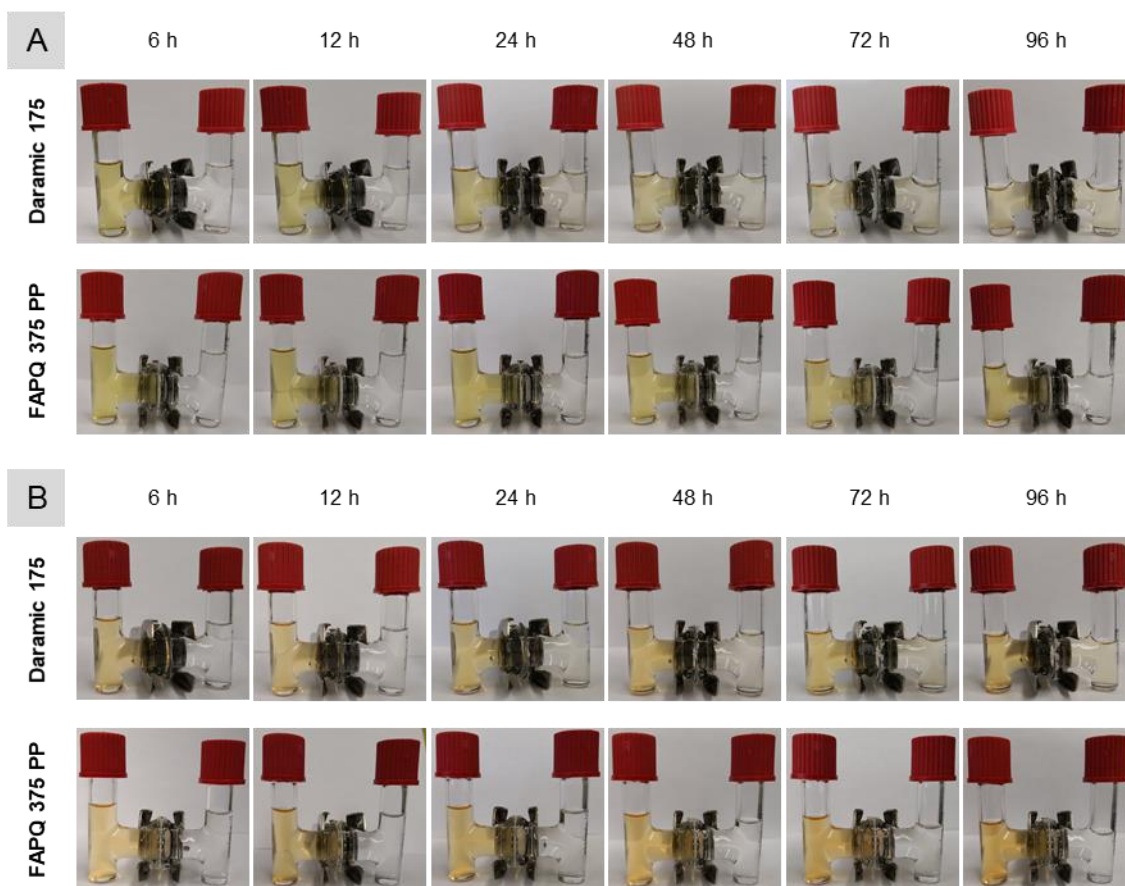
Appendix Figure 75. Cytotoxicity effects of viologen and biTEMPO analogs on MC3T3 cells, fibroblast cells and coronary venular endothelial cells (CVECs).



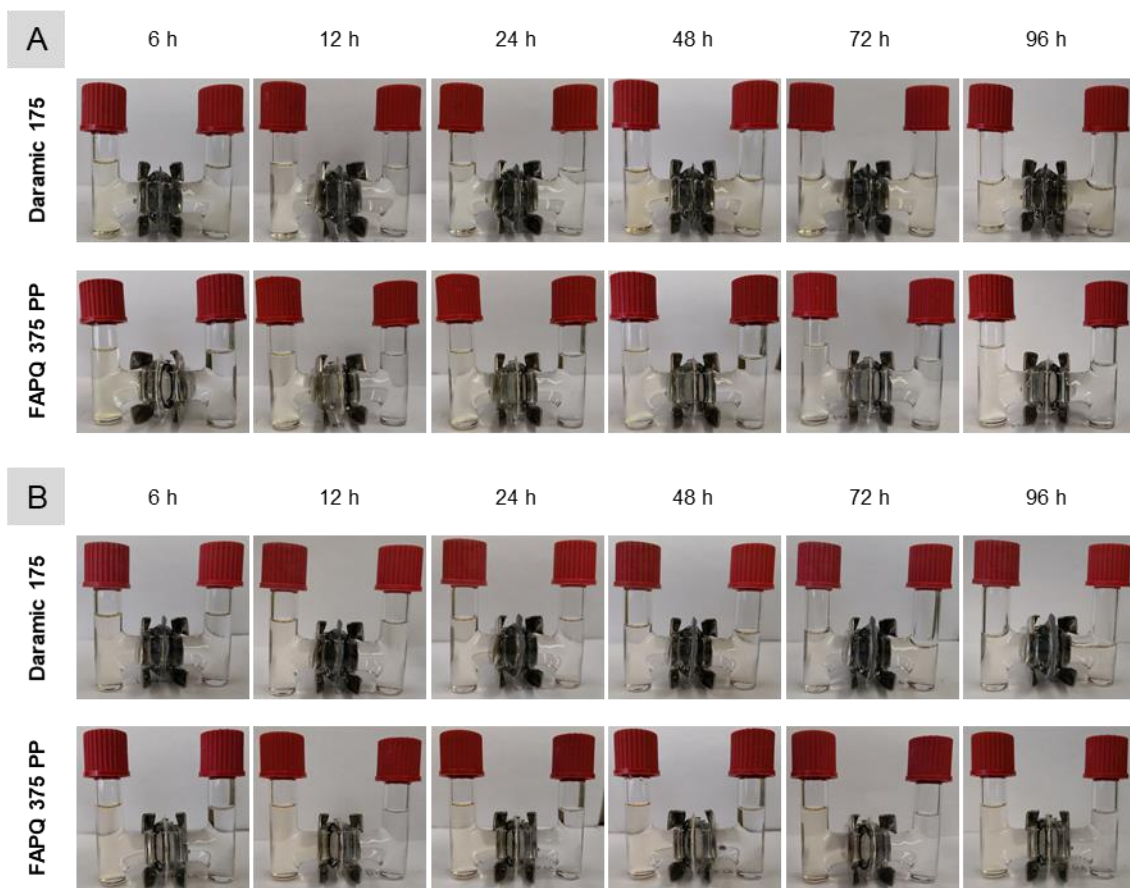
Appendix Figure 76. Cytotoxicity effects of the degradation products of viologen and biTEMPO analogs on MC3T3 cells, fibroblast cells and CVECs.

APPENDIX C

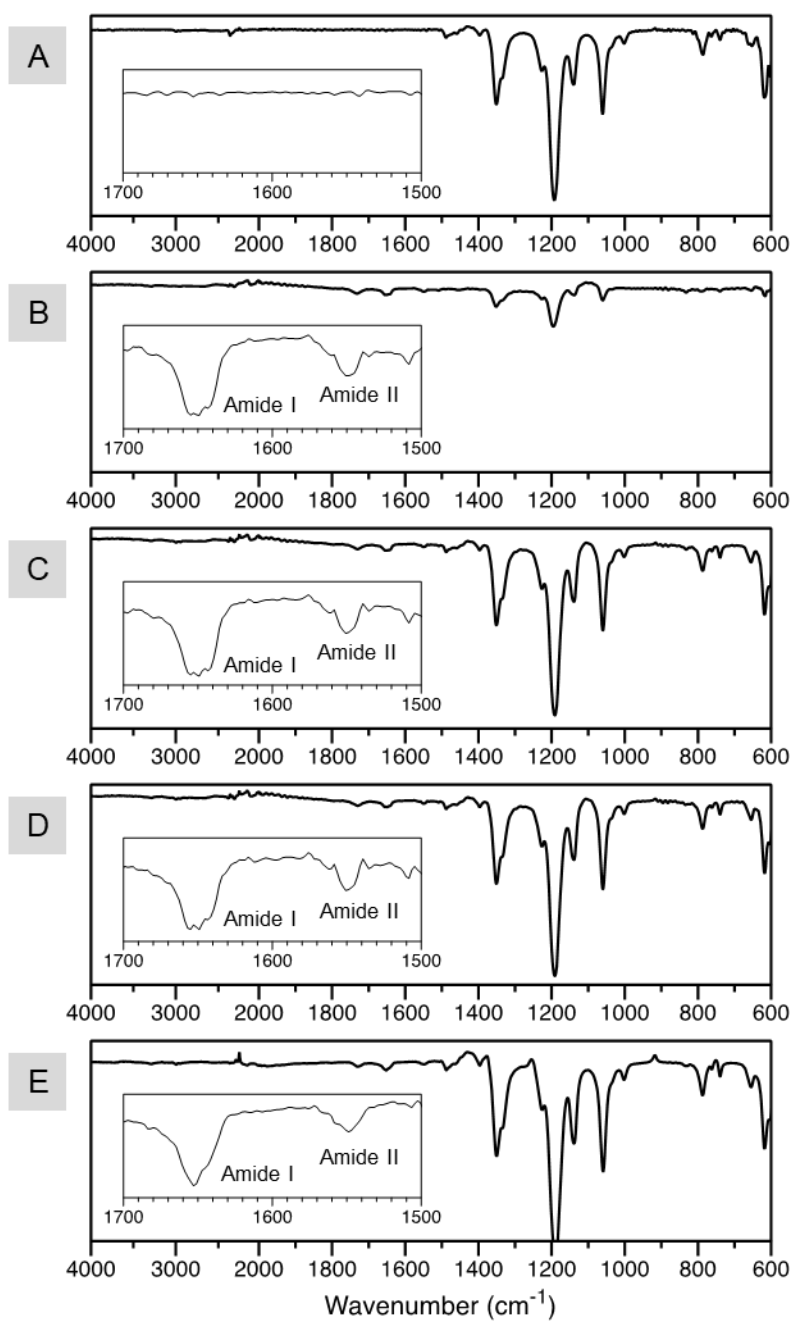
SUPPLEMENTARY DATA FOR CHAPTER IV



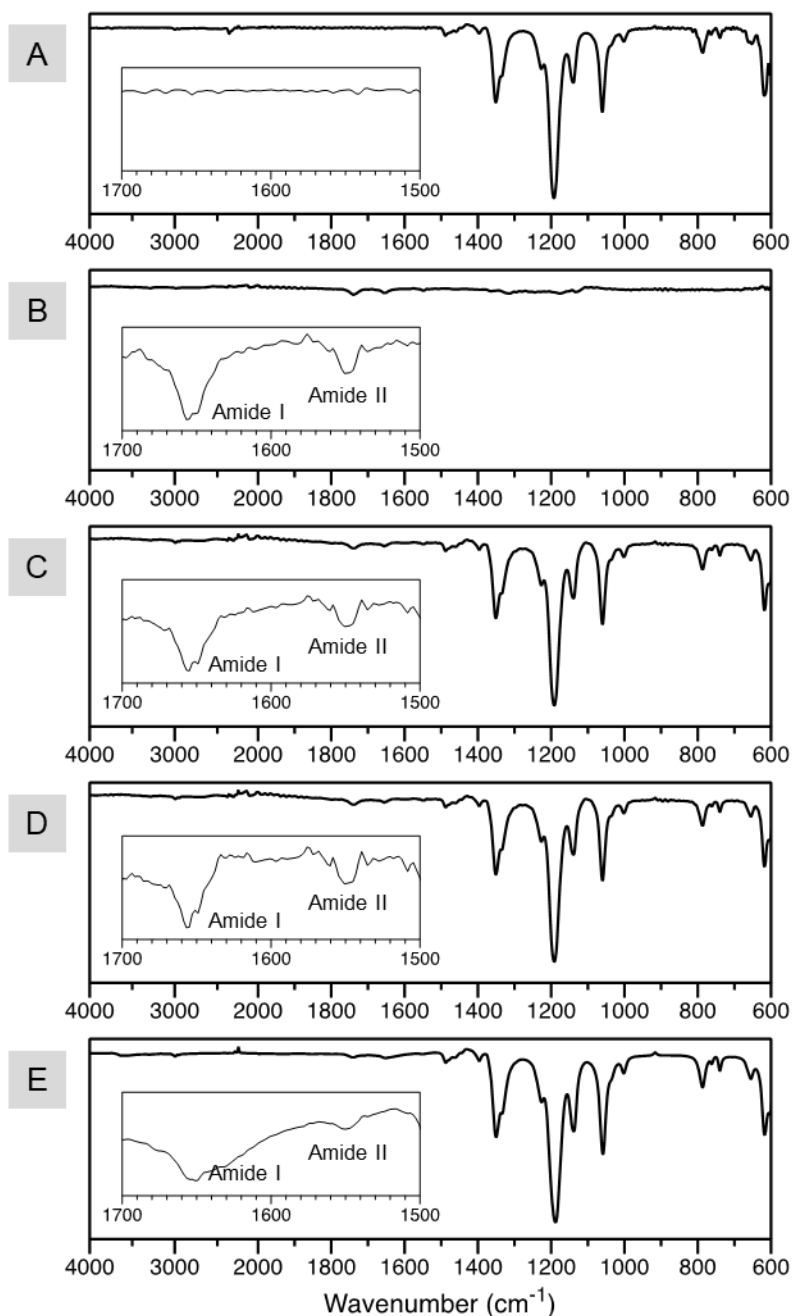
Appendix Figure 77. Crossover study of (A) viologen-TFSI and (B) biTEMPO polypeptides using Daramic 175 and FAPQ 375 PP membranes.



Appendix Figure 78. Crossover study of (A) viologen-TFSI and (B) biTEMPO analogs using Daramic 175 and FAPQ 375 PP membranes.



Appendix Figure 79. ATR-FTIR spectra of (A) 0.5 M TEATFSI/ACN, (B) 50 mM viologen-TFSI polypeptide/ACN, and 50 mM viologen-TFSI polypeptide in 0.5 M TEATFSI/ACN (C) before cycling, (D) after rate study and (E) after 500 cycles at $10 \text{ mA}\cdot\text{cm}^{-2}$. The y-axis of the spectra is transmittance (%).



Appendix Figure 80. ATR-FTIR spectra of (A) 0.5 M TEATFSI/ACN, (B) 50 mM biTEMPO polypeptide/ACN, and 50 mM biTEMPO polypeptide in 0.5 M TEATFSI/ACN (C) before cycling, (D) after rate study and (E) after 500 cycles at $10 \text{ mA}\cdot\text{cm}^{-2}$. The y-axis of the spectra is transmittance (%).